STRUCTURAL, OPTICAL, AND ELECTRONIC PROPERTIES OF Gd_2TiO_5

Ph.D. Thesis

By

Ritu Nain

DISCIPLINE OF PHYSICS

INDIAN INSTITUTE OF TECHNOLOGY INDORE

JANUARY 2026

STRUCTURAL, OPTICAL, AND ELECTRONIC PROPERTIES OF Gd_2TiO_5

A THESIS

Submitted in partial fulfillment of the requirements for the award of the degree
of
DOCTOR OF PHILOSOPHY

by
Ritu Nain

DISCIPLINE OF PHYSICS
INDIAN INSTITUTE OF TECHNOLOGY INDORE
January 2026

INDIAN INSTITUTE OF TECHNOLOGY INDORE

I hereby certify that the work which is being presented in the thesis entitled **STRUCTURAL, OPTICAL, AND ELECTRONIC PROPERTIES OF Gd_2TiO_5** in the partial fulfillment of the requirements for the award of the degree of **DOCTOR OF PHILOSOPHY** and submitted in the **DEPARTMENT/SCHOOL OF PHYSICS, Indian Institute of Technology Indore**, is an authentic record of my own work carried out during the time period from December 2020 to January 2026 under the supervision of Professor Pankaj R. Sagdeo, Professor, Department of Physics, IIT Indore.

The matter presented in this thesis has not been submitted by me for the award of any other degree of this or any other institute.

01-04-2026

signature of the student with date

(Ritu Nain)

This is to certify that the above statement made by the candidate is correct to the best of my/our knowledge.

प्रो. पंकज र. संगदेव / Prof. Pankaj R. Sagdeo
भौतिक शास्त्र विभाग / Department of Physics
भारतीय प्रौद्योगिकी संस्थान इन्दौर
Indian Institute of Technology Indore

07-04-2026

Signature of Thesis Supervisor with date

(Prof. Pankaj R. Sagdeo)

Certificate

Ritu Nain has successfully given his/her Ph.D. Oral Examination held on

Signature of Thesis Supervisor with date
07-04-2026
(Prof. Pankaj R. Sagdeo)

Signature of Chairperson (OEB)	Signature of External Examiner	Signature of Thesis Supervisor Prof. Pankaj R. Sagdeo
Date:	Date:	Date: 07-04-2026

Signature of PSPC Member #1	Signature of PSPC Member #2
Date:	Date:

Signature of Convener, DPGC	Signature of Head of Discipline
Date:	Date:

ACKNOWLEDGEMENTS

I would like to express my profound gratitude to my thesis supervisor, Prof. Pankaj R. Sagdeo [Dean of Infrastructure Development Office], for providing me the opportunity to work under his guidance through invaluable guidance and support throughout the research work. Their scientific expertise, insightful suggestions, and constant encouragement have been an essential part in shaping this thesis and developing a critical outlook in my understanding of the research work. I will be forever grateful for the motivation and the support provided at every stage of my research work.

I would like to express my immense gratitude to my PSPC members, Prof. Rupesh Devan and Prof. Somaditya Sen, for their continuous encouragement, support, critical evaluation, and valuable suggestions provided during the PhD work. Their motivation and suggestions have significantly improved my research work.

I sincerely acknowledge my research collaborators for their technical discussions, meaningful contributions, and scientific cooperation during the research work, which substantially aided in the successful completion of the thesis. I sincerely thank Prof Rajesh Kumar and Dr. Vinayak Mishra for their scientific efforts, expertise, and providing assistance during the collaborative work. I extend heartfelt thanks to my respected seniors, as well as collaborators Dr. Vikas Mishra and Dr. Omkar Rambadey, for their scientific discussions, analytical approach, and continuous support throughout the research work.

I would like to sincerely thank Dr. Archna Sagdeo (Scientific Officer-F) from Indus Synchrotron Utilization Division, Raja Ramanna Centre for Advanced Technology, Indore (RRCAT) (BL-12), India, for their assistance during X-ray diffraction measurements.

I would like to thank all faculty members of the Department of Physics, IIT Indore. I sincerely thank the Sophisticated Instrumentation Centre,

IIT Indore, most specifically Mr. Nitin Upadhyay and Mr. Kinny Pandey, for their support during XRD and SEM measurements, respectively.

I would like to express my deep gratitude to not only my seniors but also being my mentors, Dr. Vikas Mishra, Dr. Anil Kumar, Dr. Minal Gupta, Dr. Omkar Rambadey, and Dr Kailash Kumar, for providing me with constant motivation guidance, encouragement, and insightful advice, which helped me navigate both academic and research challenges, which has significantly contributed in my research journey.

I sincerely thank all my respected seniors of the Materials Research Laboratory (MRL Lab) and all beloved juniors, Nikita, Payal, Unnati, Dibya, Ansh and Akash for their love, care, and support.

My sincere appreciation goes to my colleagues and friends (Sheetal, Vandana, and Kamlajeet Singh) for their encouragement, moral support, and companionship throughout this journey. Their presence made the research experience enjoyable and memorable. Moreover, several people have knowingly and unknowingly contributed to the successful completion of my thesis.

Last but not least, I would like to express my heartfelt gratitude to my family for their unconditional love, patience, and unwavering support, which have been a constant source of strength and motivation throughout my academic journey. Lastly, I want to thank the superpower/almighty, the creator and Guardian, and to whom I owe my existence.

SYNOPSIS

1. Introduction

Rare-earth titanates exhibit unique structural, physical, and optical properties, making them highly suitable for applications in the nuclear and radiation industries [1–2]. These materials are known for their high mechanical strength, as well as their excellent chemical and temperature resistance, which makes them effective in environments with high radiation flux, such as energy and nuclear settings [3]. This group of materials includes lanthanide perovskites ($LnTiO_3$), pyrochlore-related structures ($Ln_2Ti_2O_7$), and $Ln_4Ti_9O_{24}$ compositions (where Ln is a lanthanide element from La to Lu) [4, 5]. A particularly interesting member of this class is Ln_2TiO_5, in which the Ti atom adopts a rare five-fold coordination geometry, a geometry rarely observed in most titanium-based transition metal oxides [4]. Most titanium-based oxides are found to exist in four-fold or six-fold coordination, possessing tetrahedral and octahedral geometries, and a significant amount of work in this regard has been done on perovskite ($LnTiO_3$) and pyrochlore ($Ln_2Ti_2O_7$) type structures.

Our work primarily focuses on Gd_2TiO_5, a compound within this category, which exhibits remarkable chemical and optical properties [2]. Being a wide-bandgap material, Gd_2TiO_5 absorbs most of the light in the UV range, which limits its applicability in light-emission processes. Hence, reducing its bandgap with doping or other means can be useful in light-emitting devices, photocatalytic, and solar cell applications. The tuning of the bandgap can be achieved by doping or substituting a suitable element, which alters the composition and structure, and subsequently modifies the orbital overlap and, consequently, the electronic bandgap structure of the material. Keeping this in mind, pristine Eu and Fe have been substituted at the Gd and Ti sites, respectively. For this purpose, Optical absorption spectroscopy and Raman spectroscopy have been employed, as these are widely used techniques for characterizing and providing valuable information about

the electronic band structure and lattice dynamics of the system [6]. These techniques offer significant potential for investigating the interplay between electronic and lattice dynamical properties in materials, making them powerful tools for advancing research in this field.

2. Methodology

2.1 Synthesis techniques

The polycrystalline samples of Eu- and Fe-substituted Gd_2TiO_5, including the pristine one, have been synthesized using the solid-state reaction route. For the synthesis process, the gadolinium oxide (Gd_2O_3), titanium oxide (TiO_2), europium oxide (Eu_2O_3), and iron oxide (Fe_3O_4), all with a purity of 99.99% have been taken in stoichiometric amounts to obtain the respective compositions of $Gd_{2-x}Eu_xTiO_5$ and $Gd_2Ti_{1-x}Fe_xO_5$, where x = 0.03, 0.05, 0.07, and 0.10. The stoichiometric amounts of the powders mentioned above were mixed thoroughly in an isopropyl alcohol medium and grounded in an agate mortar pestle. A maximum heat treatment of 1350 °C was given for the formation of pure Gd_2TiO_5, while 1300 °C and 1250 °C were given for the formation of $Gd_{2-x}Eu_xTiO_5$ and $Gd_2Ti_{1-x}Fe_xO_5$ series, respectively.

2.2 X-ray Diffraction Characterization

For characterizing the phase purity of the synthesized samples, a Bruker D8 diffractometer equipped with a Cu target and a K_α wavelength of 1.5405 Å was used to collect the X-ray diffraction data. [7]. The XRD pattern was taken in an angular range of 20–80° with a step size of 0.02°. For extracting the structural information, Rietveld refinement of all the samples was performed using the FullProf software, considering the *Pnam* space group of the synthesized samples [8], and a pseudo-Voigt function was used for fitting the peaks. For extracting crystallographic information, the VESTA (Visualization for Electronic Structure Analysis) software was used.

Furthermore, UV–visible absorption spectroscopy was employed to conduct the optical absorption measurements, and the optical absorption spectra were collected using the UV–Vis-NIR spectrophotometer in the wavelength range of 200–900 nm at a scan rate of 60 nm/min. The $BaSO_4$ (barium sulphate) was chosen as a reference material for the baseline due to its high reflectance properties, reproducible baseline, and low cost. Raman spectroscopy was employed to study the phonon and lattice dynamics of the system using a LABRAM HR dispersive spectrometer equipped with a CCD detector in backscattered mode. An excitation laser source with an excitation wavelength of 633 nm and a laser power of less than 5 mW was used to collect the data, along with a grating having 600 grooves per millimetre.

3. Results

3.1 Influence of Fe Substitution on the Structural and Optical Properties of Gd_2TiO_5 Ceramic

Rare-earth titanates with the composition Ln_2TiO_5 have been found to possess interesting structural and physical properties due to their remarkable properties of high thermal and chemical resistance against irradiation. Most titanium-based binary oxides and other perovskite oxides of varying compositions have been found to exist in the most common tetrahedral and octahedral configurations. However, in the case of the Ln_2TiO_5 system, titanium exists in the five-fold coordination number, which is very rarely observed in nature [9]. As the crystal field splitting varies differently corresponding to different geometries of the polyhedra in oxides, their chemical, physical, and structural properties will differ, which will in turn affect their optical and electronic properties. To see the effect of the square pyramidal geometry of Ti-O5 polyhedra in the Ln_2TiO_5 system, and how the structural and optical properties of these materials differ from the conventional oxide systems, Fe was substituted at the Ti-site in Gd_2TiO_5. The X-ray diffraction confirmed the phase purity and the orthorhombic phase of the synthesised samples. For extracting structural information, such as

crystal structure, lattice parameters, and bond lengths, Rietveld refinement was carried out using the Full Proof software with pseudo-Voigt peak fitting. The crystal structure of Gd_2TiO_5 was found to possess TiO5 and GdO7 polyhedra units, where the titanium atom is surrounded by five oxygen atoms, forming a distorted square pyramidal geometry. The Gd-O7 polyhedra form the capped trigonal prismatic geometry. To explain the structural distortion in these complexes, Addison's model was used, in which the distortion in five-fold coordinate metal complexes is defined by a geometric parameter 'τ_5', which is called the 'index of degree of trigonality'. According to Addison's model, the expression for the τ_5 is given by

$$\boldsymbol{\tau_5 = \frac{(\beta-\alpha)}{60}} \quad (1)$$

where τ_5 is equal to '0' for an ideal square pyramidal geometry and is equal to '1' for a perfectly trigonal bipyramidal structure, and the geometry of other distorted structural complexes lies on the continuum defined by these two extreme geometries. In pure Gd_2TiO_5, τ_5 was found to be ~0.30, indicating that the geometry of the TiO5 polyhedron is a distorted square pyramid. Additionally, the Gd-O and Ti/Fe-O bond lengths were extracted from the Rietveld results, which showed that one of the Gd-O and Ti/Fe-O bond lengths (Ti-O(4)) varied systematically with the Fe-substitution as shown in **Figures 1a** and **b**. To further explore the optical and electronic properties of these materials, Diffuse reflectance spectroscopy was performed on the sample series, where the diffuse reflectance data were converted into absorption spectra using the Kubelka-Munk function *F*(R) [10]. Kubelka-Munk function is proportional to the absorption coefficient and is related to reflectance by the relation

$$\boldsymbol{F(R_\infty)\ or\ \alpha \approx \frac{K}{S} \approx \frac{(1-R_\infty)^2}{2R_\infty}}, \quad (2)$$

where *K* and *S* are defined as the K–M absorption and scattering coefficients, respectively. The band gap of the Fe-substituted samples was calculated using the Tauc equation, defined as

$$(\boldsymbol{\alpha hv})^{\boldsymbol{n}} = \boldsymbol{A}\left(\boldsymbol{hv} - \boldsymbol{E_g}\right), \quad (3)$$

where 'n' is ½ for the indirect band gap transitions. The band gap of the sample series exhibited a drastic yet systematic decrease with increasing Fe content in Gd_2TiO_5, as shown in **Figure 2**. This decreasing trend in the band gap was speculated to be related to the systematic variation in the changes in Gd-O or Ti-O bond lengths, hinting that the Gd-5*d* or Ti-3*d* orbitals may be dominating at the band edges and governing the systematic variations in the band gap. To account for this behavior and facilitate further analysis, band structure and density of states calculations were performed on the prepared samples using the Quantum Espresso (QE) software [11]. From the band structure results, the computed value of the bandgap was found to be 4.0 eV, which decreased to 3.05 eV upon 10% Fe substitution, as expected from the experimental results. From the partial density of states (PDOS) plots in both the cases of pristine Gd_2TiO_5 and 10% Fe-substituted GTO (Gd_2TiO_5), the conduction band minima were found to be dominated by the O-2*p* orbitals, and the valence band maxima by the Ti-3*d* orbitals, as shown in **Figures 3a** and **b**. This indicates that the band structure and band gap properties in the rare-earth titanates of Ln_2TiO_5 are governed by the orbital overlap between the Ti-3*d* and O-2*p* orbitals. Hence, the Ti/Fe-O(4) bond length contributes significantly to altering the band gap. This work concludes that by engineering the Ti-O bond length, the band gap and optical properties can be tuned accordingly, which has numerous applications in the field of band gap engineering.

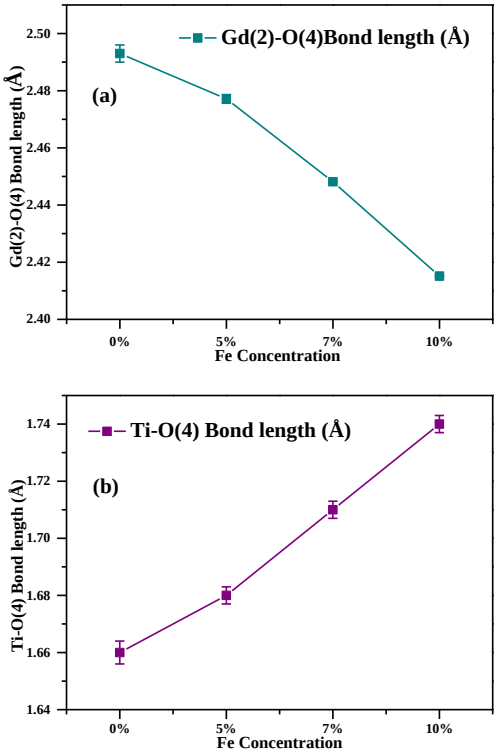

Figure 1a and **b** The systematic variation of Gd(2)-O(4) and Ti–O(4) bond lengths with the increased amount of Fe in Gd_2TiO_5

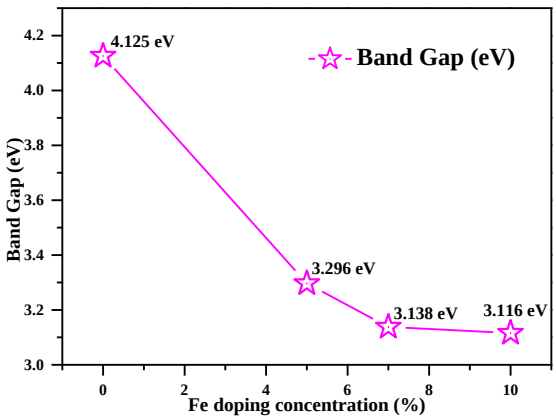

Figure 2 Variation of optical band gap (E_g) with Fe substitution in Gd_2TiO_5, obtained from the diffuse reflectance measurements

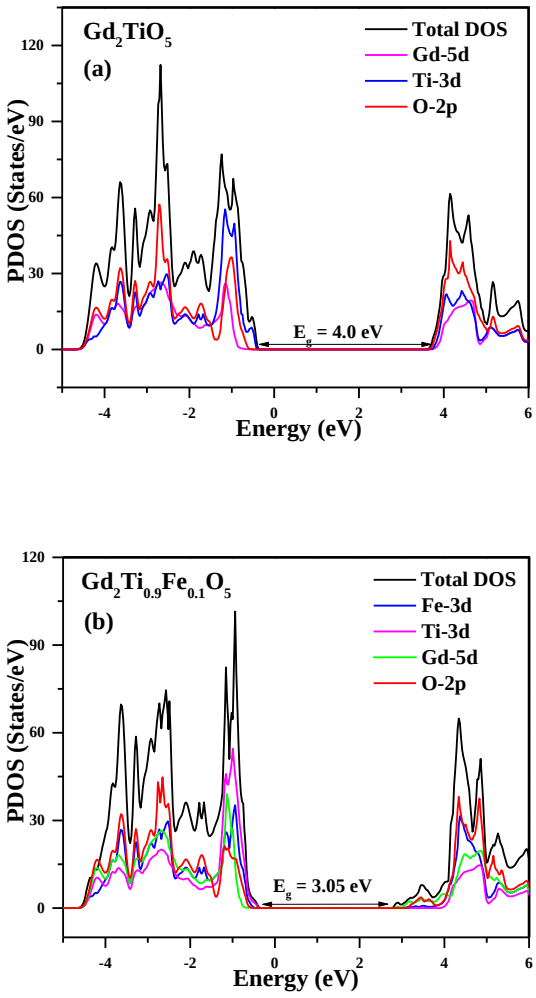

Figure 3 Partial density of states of **a** pristine and **b** 10% Fe-substituted Gd_2TiO_5

3.2 Experimental and First-principles Investigation on the Optical Properties of Eu and Fe-substituted Gd_2TiO_5

This work primarily explores the predominant contribution of 3*d* and 5*d* orbitals at the Fermi level and in the band structure of the rare-earth complex oxides of composition Ln_2TiO_5, where Ln is the lanthanide element. For this purpose, rare-earth titanate Gd_2TiO_5 has been synthesized using the conventional solid-state reaction method, which has been found to exist in the orthorhombic phase under ambient temperature conditions. To explore the optical and electronic characteristics and to find the contributions of Ti-3*d* and Gd-5*d* orbitals

at the Fermi edges of this rare-earth titanate, Eu and Fe are substituted at the Gd- and Ti-sites, respectively, with concentration percentages of 3%,5%,7% and 10% to get the respective compositions $Gd_{2-x}Eu_xTiO_5$ and $Gd_2Ti_{1-x}Fe_xO_5$. X-ray diffraction (XRD) measurements and Rietveld refinement were performed using the *Pnam* space group to verify the phase purity and extract the crystallographic information of the synthesized series samples.

To study the optical and band gap properties, UV–visible absorption spectroscopy was performed in the diffuse reflectance (DR) mode. The optical absorption data of the prepared samples were analyzed by converting the obtained diffuse reflectance data into the Kubelka-Munk function *F*(R) using the Kubelka–Munk equation (**equation 2**)**,** where *F*(R) is proportional to the absorption coefficient. The optical absorbance data for both the sample series are shown in **Figures 4a** and **b**. The optical band gap was extracted using the Tauc plot and **equation 3,** where it showed a gradual decrease with increasing Eu concentration, resulting in a change of approximately 0.14 eV. Whereas a substantial decrease in the band gap was noted in the case of increasing amount of Fe at the Ti-site, exhibiting an approximate change of ~ 1 eV, as shown in **Figure 5**. The decrease was much more drastic in the case of Fe substitution as compared to the case of Eu substitution.

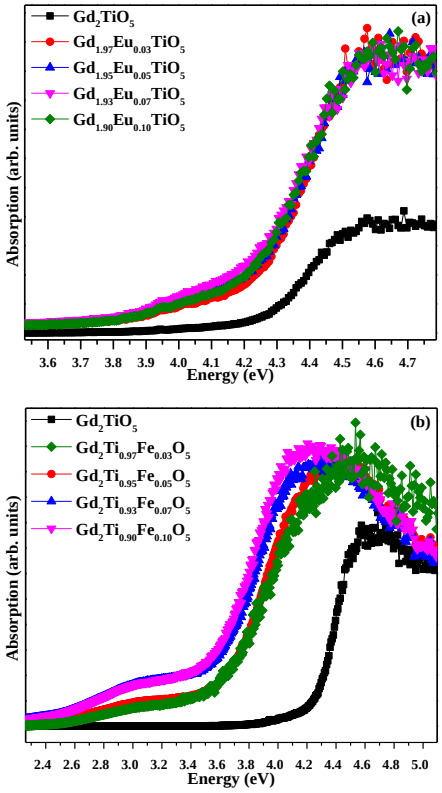

Figure 4 The optical absorption spectra of **a** Eu- and **b** Fe-substituted series samples ($Gd_{2-x}Eu_xTiO_5$, and $Gd_2Ti_{1-x}Fe_xO_5$, x = 0, 0.03, 0.05, 0.07, and 0.10) along with the pristine Gd_2TiO_5, carried out in the diffuse reflectance (DR) mode

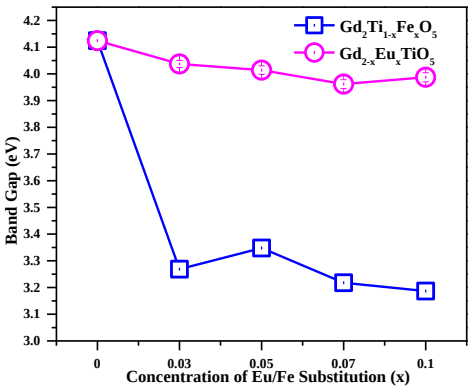

Figure 5 The bandgap variation observed in Eu- and Fe-substituted samples ($Gd_{2-x}Eu_xTiO_5$ and $Gd_2Ti_{1-x}Fe_xO_5$, x = 0, 0.03, 0.05, 0.07, and 0.10)

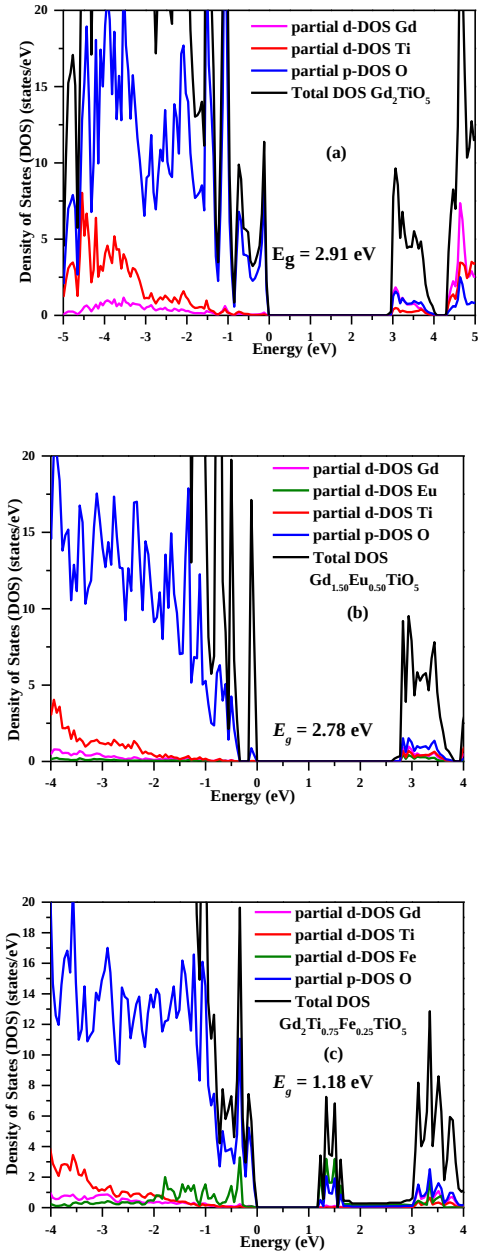

Figure 6 Density of states results obtained from the VASP calculations. Figures **a**, **b**, and **c** show the total and partial density of states of pure Gd_2TiO_5, $Gd_{1.75}Eu_{0.25}TiO_5$, and $Gd_2Ti_{0.75}Fe_{0.25}O_5$ samples, respectively

To further support the results, first-principles calculations were carried out using Density Functional Theory, implemented with the GGA + U methodology in the VASP software [12]. From the density of states plots (DOS), it was found that the valence band maximum was mainly composed of O *p*-states, with minor contributions from the *d*-

states of Gd and Ti. The conduction band minimum was formed by a mixture of Gd and Ti *d*-states, as well as O *p*-states, all of which were contributing significantly. In the case of $Gd_{1.50}Eu_{0.5}TiO_5$, the Eu *d*-states were also contributing to both the valence band and conduction band edges; however, the introduction of Eu caused a slight decrease in the bandgap (~ 0.13 eV), as can be observed in **Figures 6a** and **b**. A contrasting behaviour was observed in the case of Fe-substituted Gd_2TiO_5 ($Gd_2Ti_{0.75}Fe_{0.25}O_5$ composition), where a significant reduction was observed in the optical bandgap (~ 1.18 eV) due to the appearance of new *p-d* hybridized states, as can be seen in **Figure 6c**. By combining the results with experimental observations, it is concluded that Fe substitution at the Ti-site majorly affects the bandgap properties than the Eu substitution at the Gd-site, and significant changes occur in the band structure and band gap properties with substitution at the Ti-site. Therefore, it is stated that the bandgap structure of these rare-earth titanates can be modified and tuned accordingly by making the substitution of a suitable element at the Ti-site in comparison with the Gd-site. The above results will be helpful in exploring the band structure and engineering the bandgap properties in the rare-earth titanates of the Ln_2TiO_5 system.

3.3 Interplay of Electron−Phonon Coupling and Lattice Dilation in Band Gap Tuning of $Gd_2Ti_{1-x}Fe_xO_5$

The fundamental absorption edge in many semiconductors exhibits a red or blue shift, depending on the material and external stimuli such as temperature, pressure, and disorder within the system. To date, numerous rigorous studies have been conducted to investigate the role of electron-phonon interactions and lattice dilation (Volume effect) in semiconductors and oxide materials [13-15]. The contribution of the electron-phonon (e-ph) interaction has been calculated by considering the Debye-Waller and self-energy terms using rigid-ion pseudopotential models [16-18].

The Electron–phonon coupling (EPC) and lattice dilation effects are crucial in understanding material properties, particularly at higher temperatures, as they play a significant role in phenomena such as thermal expansion. This work explicitly calculates the contribution of the lattice dilation effect and e-ph interactions in complex oxide materials, where the disorder has been considered analogous to temperature and other thermal effects coming into the system. As several material properties (including band gap) can be tuned by chemical substitution, also, in this respect, a cumulative study of charge-lattice coupling and lattice dilation effect has been carried out as a result of chemical substitution, which is not explored as extensively as temperature or pressure effects. Keeping this in consideration, in this study, we have attempted to find the cause of the variance of the band gap with respect to the general disorder coming from doping or other substitutional effects, which are analogous to temperature, causing the perturbation in the electronic levels of the solid, and giving rise to disorder in the system.

For the case of temperature-induced variations, this disorder in the system leads to thermal expansion or contraction, depending on the material's properties, and an increase in electron-phonon interactions within the system, which together are responsible for the disorder-dependent variation of the band gap in semiconductors. That is, if temperature is taken as a specific case of disorder present in the system, then this generally will have contributions from the two effects: thermal expansion and electron-phonon interactions in the system. The well-known equation of temperature dependence of the energy band gap with temperature is given by **equation 4** as

$$\left(\frac{\partial E_g}{\partial T}\right)_P = \left(\frac{\partial E_g}{\partial T}\right)_V + \left(\frac{\partial E_g}{\partial lnV}\right)_T \left(\frac{\partial lnV}{\partial T}\right)_P \quad (4)$$

where the first term in the above expression gives the contribution of the electron-phonon interactions, whose explicit contribution has been calculated using electron self-energy terms and Debye-Waller (DW) factors by many researchers [19-20]. The second term on the right-hand

side represents the contribution of thermal expansion (lattice dilation) and can be determined both theoretically and experimentally through band structure calculations and the pressure dependence of the band gap, respectively.

In the case of Fe-substituted Gd_2TiO_5, XRD and refinement results indicated an expansion in the system. According to previous scientific reports, electron-phonon interactions lead to a decrease in the band gap, whereas the dominance of lattice dilation (the second term) is responsible for the increase in the band gap with increasing temperature. It should be noted that temperature variation introduces modifications to the lattice via unit cell expansion, affecting the electron-vibration interaction strength. Consequently, the electronic levels themselves and the Fermi level can change significantly, resulting in a variation in the material's band gap. The underlying chemical potential that is altered in such processes may also be influenced by other physical conditions, such as chemical substitution, which can affect the thermodynamic behavior of the system and induce variations in the band gap. This is due to the obvious effects on the lattice volume (dilation) and the Fermi level shifts resulting from modified orbital hybridizations (electron−phonon coupling). This is scientifically significant in view of tuning the optical properties for use at even room temperatures. Thus, an explicit understanding of the LD and EPC effects is of importance.

In this work, thermal and structural disorder have been considered analogues to cause the lattice volume changes, eventually affecting the optical band gap (but to different extents). Hence, rewriting **equation 4** of the temperature dependence of the band gap by considering only the substitution-induced structural disorder present in the system, **equation 5** can be rewritten as

$$\left(\frac{\partial E_g}{\partial c}\right)_P = \left(\frac{\partial E_g}{\partial c}\right)_V + \left(\frac{\partial E_g}{\partial \ln V}\right)_c \left(\frac{\partial \ln V}{\partial c}\right)_P \quad (5)$$

where c represents the concentration of the Fe content in Gd_2TiO_5, and d*c* gives the change in the consecutive values of the Fe concentration.

One can directly observe the variation of E_g with Fe content at ambient pressure, which would give the term on the LHS in **equation 5**, i.e., the rate of variation of band gap with change in the Fe concentration, as can be seen in **Figure 4b.** Similarly, the contribution of the second term (lattice dilation term) has been experimentally determined via the parallel analysis of the unit cell and electronic band structures using X-ray diffraction and UV−vis spectroscopy measurements. Although the explicit calculation has not been done for the first term (e-ph interaction contribution), it has been derived from the contribution of the other two terms, which are known. Thus, we are able to resolve the effects of lattice dilation and electron-phonon coupling in these systems, and the obtained results are presented in **Figure 5**.

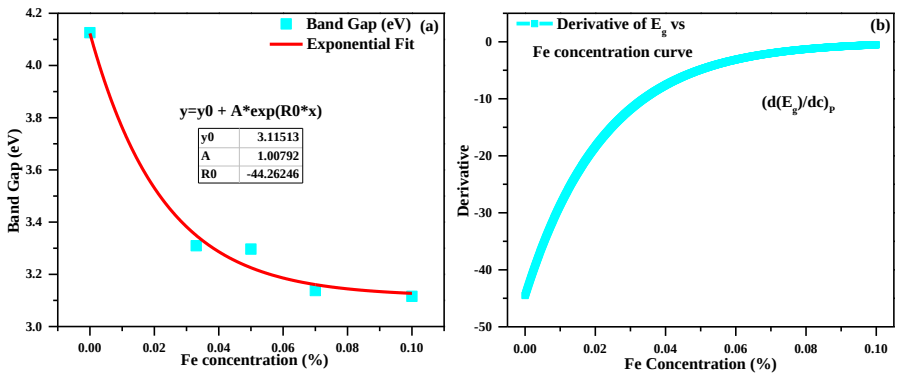

Figure 4a The optical band gap shows a systematic decrement with the increasing Fe amount and shows a good agreement with the exponential fit. **b** shows the derivative of the curve of the band gap (Eg) vs Fe concentration at constant pressure, i.e., $(\partial E_g/\partial c)_P$

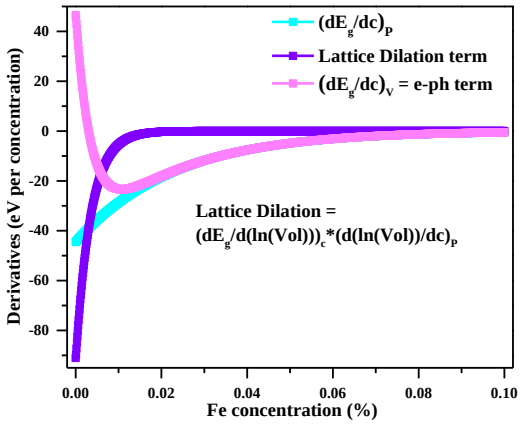

Figure 5 The total contribution to the band gap variation with Fe concentration is represented by the sky-blue dotted curve ($(\boldsymbol{\partial E_g/\partial c})_p$) The magenta- and purple-colored curves define the contribution of electron-phonon interactions ($(\boldsymbol{\partial E_g/\partial c})_V$) and lattice dilation terms, respectively, in the band gap variation

From the plot (**Figure 5**), it is inferred that the concentration derivative of the band gap is negative for Fe content ≤10%; however, it becomes less negative (tends to 0) with increasing Fe content. This is because the band gap reduces exponentially with the Fe concentration and attains an asymptotic behavior, as observed from the experimental data in **Figure 4a**. The obtained plot for the LD effects can be understood to represent the part of the band gap variation as the cell volume changes, which is stronger only at lower concentrations, and for Fe% >1%, this contribution seems to decrease significantly and asymptotically approach zero. Similarly, the plot of the EPC versus Fe concentration represents the contribution of charge lattice interaction to the variation in band gap as the Fe content varies. The curve initially is positive and traces a sharp drop to negative values within 1% Fe variation. However, at higher Fe content, the EPC interaction appears to contribute to the band gap shrinkage and ultimately achieves saturation, as evidenced by the asymptotic value of zero. From temperature-dependent band gap studies on semiconductors, it is known that the gap decreases with increasing temperature due to enhanced electron-phonon

interactions. However, here we are dealing with a stimulus of chemical origin, rather than temperature. Although the contribution to the band gap variation due to the LD effects rapidly approaches zero, the nonzero values of the same for the derived EPC contribution suggest EPC-dominated variation of the overall band gap as a result of Fe substitution in the Fe-substituted Gd_2TiO_5 system.

Hence, it is concluded that in the rare-earth materials of the Ln_2TiO_5 type, the overall contribution from the substitution disorder in the band gap variation primarily comes from the e-ph interaction term, and the lattice dilation effect (volume effect) contributes significantly only at lower concentrations. To further support the results and estimation of e-ph strength in the system with Fe substitution, Raman spectroscopy was performed to obtain composition-dependent Raman data. Some of the singly observed modes were fitted with the Fano model, which showed broadening (FWHM) and an increasing asymmetric line shape of the phonon states, indicating an increase in structural disorder in the system, which favors electron-phonon interactions with increasing Fe substitution. Thus, our work aims to understand the chemical perturbation-induced band gap variation in the Gd_2TiO_5 system.

4. Bibliography

1. Liu, X.; Yang, D.; Liu, C.; Liu, H.; Ji, S.; Mu, P.; Wu, Y.; Li, Y. Insights into the Radiation Behavior of Ln2TiO5 (Ln = La-Y) from Defect Energetics. *Comput. Mater. Sci.* 2017, *139*, 295−300.
2. Austin, D. A.; Cole, M.; Stennett, M. C.; Corkhill, C. L.; Hyatt, N. C. A Preliminary Investigation of the Molten Salt Mediated Synthesis of Gd2TiO5 ‘Stuffed’ Pyrochlore. *MRS Adv.* 2021, *6* (4−5), 149−153.
3. Aughterson, R. D.; Lumpkin, G. R.; Ionescu, M.; Reyes, M. D. L.; Gault, B.; Whittle, K. R.; Smith, K. L.; Cairney, J. M. Ion-Irradiation Resistance of the Orthorhombic Ln2TiO5 (Ln = La, Pr, Nd, Sm, Eu, Gd, Tb, and Dy) Series. *J. Nucl. Mater.* 2015, *467*, 683−691.
4. Petrova, M. A.; Grebenshchikov, R. G. Specific Features of the Phase Formation in the Titanate Systems Ln 2TiO5-Ln′2TiO5 (Ln

=La, Gd, Tb, Er; Ln′ = Tb, Lu). *Glass Phys. Chem.* 2008, *34* (5), 603−607.
5. Xu, J.; Xi, R.; Xu, X.; Zhang, Y.; Feng, X.; Fang, X.; Wang, X. A2B2O7 Pyrochlore Compounds: A Category of Potential Materials for Clean Energy and Environment Protection Catalysis. *J. Rare Earths* 2020, *38* (8), 840−849.
6. Kortüm, G. Regular and Diffuse Reflection. In *Reflectance Spectroscopy: Principles, Methods, Applications*; Kortüm, G., Ed.; Springer Berlin Heidelberg: Berlin, Heidelberg, 1969; pp 5−71.
7. Adams, F. X-ray absorption and diffraction -overview. In *Encyclopaedia of Analytical Science*, 2 ed.; Worsfold, P., Townshend, A., Poole, C., Eds.; Elsevier: Oxford, 2005; pp 365−377.
8. McCusker, L. B.; Von Dreele, R. B.; Cox, D. E.; Louer, D.; Scardi, P. Rietveld Refinement Guidelines. *J. Appl. Crystallogr.* 1999, *32* (1), 36−50.
9. Blackman A. G.; Schenk E.B.; Jelley R.E.; Krenske E. H.; Gahan L.R. Five-coordinate transition metal complexes and the value of τ 5: observations and caveats. *Dalton Trans.* 2020, *49* (42), 14798–14806.
10. UV-Visible-NIR Reflectance Spectrophotometry in Cultural Heritage: Background Paper. *Anal. Methods* 2016, *8* (30), 5894−5896.
11. Giannozzi P.; Andreussi O.; Brumme T.; Bunau O.; Nardelli, M.B.; Calandra, M.; Car, R.; Cavazzoni, C.; Ceresoli, D.; Cococcioni, M. et al. Advanced capabilities for materials modelling with Quantum ESPRESSO. *J. Phys. Condens. Matter.* 2017, *29*(46), 465901.
12. Kresse, G. and Joubert, D. From ultrasoft pseudopotentials to the projector augmented-wave method. D. *Phys. Rev. B* 1999, 59(3), 1758.
13. Moglich, P.; Rompe, R. Uber Energieumwandlung im Festkörper. *Z. Phys.* 1940, *115* (11−12), 707-728.
14. Seiwert, R. Thermische Verschiebung Der Langwelligen Grenze Der Grundgitterbasorption von Cadmiumsulfid. *Ann. Phys.* 1950, *441*(1), 241−252.
15. Fan, H. Y. Temperature Dependence of the Energy Gap in Semiconductors. *Phys. Rev.* 1951, *82* (6), 900−905.
16. Bardeen, J.; Shockley, W. Deformation Potentials and Mobilities in Non-Polar Crystals. *Phys. Rev.* 1950, *80* (1), 72−80.
17. Cheeseman, I. C. The Structure of the Long Wave Absorption Edge of Insulating Crystals. *Proc. Phys. Soc., London, Sect. A* 1952, *65*(1), 25−32.
18. Keffer, C.; Hayes, T. M.; Bienenstock, A. Debye-Waller Factors and the PbTe Band-Gap Temperature Dependence. *Phys. Rev. B* 1970, *2* (6), 1966−1976.
19. Olguin, D.; Cardona, M.; Cantarero, A. Electron−Phonon Effects on the Direct Band Gap in Semiconductors: LCAO Calculations. *Solid State Commun.* 2002, *122* (11), 575−589.
20. Varshni, Y. P. Temperature Dependence of the Energy Gap in Semiconductors. *Physica* 1967, *34* (1), 149−154.

LIST OF PUBLICATIONS

List of Publications from Thesis Work:

1. Nain, R.; Mishra, V.; Sagdeo, P. R. Influence of Fe Substitution on the Structural and Optical Properties of Gd2TiO5 Ceramic. *J. Mater. Sci. Mater. Electron.* 2024, *35* (17), 1172. (Impact factor: 2.8)
   DOI: 10.1007/s10854-024-12954-1

2. Nain, R.; Mishra, V.; Mishra, V.; Sagdeo, P. R. Experimental and First-Principles Investigation on the Optical Properties of Eu and Fe-Substituted Gd2TiO5. *J. Mater. Sci. Mater. Electron.* 2025, *36* (8), 466. (Impact factor: 2.8)
   DOI: 10.1007/s10854-025-14543-2

3. Nain, R., Rambadey, O.V., and Sagdeo, P.R. Interplay of Electron–Phonon Coupling and Lattice Dilation in Band Gap Tuning of Gd2Ti1-xFexO5. *The J. Phys. Chem. C.* 2025, *129* (43), 19656–19671. (Impact factor: 3.3)
   DOI: 10.1021/acs.jpcc.5c06381

Contributing and other Work than the Thesis:

1. Nain, R.; Bansal, L.; Sagdeo, P. R.; Kumar, R. Utilizing Rare Earth Titanates to Improve Performance of Solid-State Electrochromic Device. *Nano Express* 2024, *5* (2), 025016. (Impact factor: 2.5)
   DOI: 10.1088/2632-959X/ad4795

2. Rambadey O. V.; Kumar K., Nain R., Kumar A.; Sagdeo P.R.; Chamberlin P. M., Adu K. W. Shedding light on evolution of Raman line shape with probing laser power: Light-induced perturbation in electron–phonon coupling. *J. Chem. Phys.* 2024, *161* (3), 034202. (Impact factor: 3.1)
   DOI: 10.1063/5.0189327

List of Conferences, Workshop presentations/attended during Ph.D.

1. Theme Meeting: Spectroscopy using Indus Synchrotron Radiation (SISR-2023), organized by Bhabha Atomic Research Centre (BARC) and Raja Ramana Centre for Advanced Technology (RRCAT), held at RRCAT, Indore, India.

2. IUMRS- ICA 2024, UGC-DAE Indore, India

3. DAE-Solid State Physics Symposium 2024, DAE Convention Centre, Anushaktinagar, Mumbai

TABLE OF CONTENTS

LIST OF FIGURES

LIST OF TABLES

ACRONYMS (if any)

TEM Transmission Electron Microscopy

XRD X-Ray Diffraction

MOT Molecular Orbital Theory

LFT Ligand Field Theory

CFT Crystal Field Theory

CFSE Crystal Field Stabilization Energy

SAED Selected Area Electron Diffraction Pattern

EIS Electrolyte-Insulator-Semiconductor

LED Light Emitting Diode

IRS Infrared Spectroscopy

LD Lattice Dilation And

EPC Electron-Phonon Coupling

DW Debye-Waller

UV-VIS-NIR Ultraviolet-Visible-Near Infrared

MIR Mid-Infra-Red

FWHM Full Width at Half Maximum

PWHM Peak Width at Half Maximum

DRA Diffuse Reflectance Assembly

IRS Internal Reflection Spectroscopy

ATR Attenuated Total Reflection

IRRAS Infrared Reflection-Absorption Spectroscopy

K-M Kubelka-Munk

QE Quantum Espresso

VASP Vienna *Ab Initio* Simulation Package

HSE Heyd–Scuseria–Ernzerhof

PBE Exchange Functionals

DFT Density Functional Theory

DRS Diffuse Reflectance Spectroscopy

DOS Density of States

ISFET Ion-Sensitive Field-Effect Transistors

TDOS Total density of states

PDOS Total density of states

SCF self-consistent field

PBE Perdew-Burke-Ernzerhof

GGA generalized gradient approximation

PAW projector-augmented wave

OAS optical absorption spectroscopy

LO Longitudinal Optical

SQUID Superconducting Quantum Interference Device

SAED Selected Area Electron Diffraction

GTO Gd_2TiO_5

GTFO Gd_2TiFeO_5

Chapter 1

Introduction

The coexistence of seven- and five-fold coordination in Gd_2TiO_5 represents a structurally unique and geometrically uncommon geometry that is rarely encountered in materials science. In particular, the presence of a square-pyramidal coordination environment introduces a distinct local geometry of significant structural relevance. Generally, titanium in most transition-metal oxides predominantly occupies an octahedral or tetrahedral coordination environment. This unusual coordination framework gives rise to modified crystal field effects, making Gd_2TiO_5 an attractive system for investigating structure-property correlations. The material therefore offers valuable insight into how geometrical distortions and atypical coordination environments influence the structural, optical, and electronic properties of complex oxides. This introductory chapter provides a brief overview of the material, highlighting the diverse properties of the crystal structure, crystal field effect and optical properties.

1.1 Origin of the Problem (Rare-Earth Titanates of Ln_2TiO_5)

In recent years, rare-earth titanates [1, 2] with the general formula Ln_2TiO_5 have attracted increasing scientific attention owing to their remarkable structural, optical, and thermal properties, which make them highly relevant for advanced nuclear technologies [3]. Historically, rare-earth titanates, including lanthanide perovskites (ABO_3-type), pyrochlores ($Ln_2Ti_2O_7$), $LnTiO_3$ compounds, and complex oxides such as $Ln_4Ti_9O_{24}$, have been extensively investigated due to their wide-ranging applications in spintronics, photonic devices, radiation-tolerant materials, and energy storage and harvesting systems [4–6]. Within this

broader family, the Ln_2TiO_5 phase has recently emerged as a promising yet comparatively underexplored class of materials [7, 8]. Early studies suggest that these compounds may exhibit unique structural flexibility and radiation resistance, positioning them as strong candidates for use in next-generation nuclear waste immobilization, inert matrix fuels, and other extreme-environment applications [1, 9]. However, systematic research on their fundamental properties remains limited, underscoring the need for more comprehensive experimental and theoretical investigations.

1.1.1 Historical Overview

In a study of 1965, Collongues and other authors (Collongues *et al.*, 1965) [10] reported a number of compounds containing Ti and Zr and rare-earth elements of different and varying compositions, such as $A_2B_2O_7$ (pyrochlore structure in cubic phase), Sc_4ZrO_{12}, Rhombohedral phase $A_4B_3O_{12}$ (UY_6O_{12}-type), a very unique family of A_2BO_5-type in which B atoms was possessing a rare coordination number as compared to conventional structures explored before. They were found to exhibit different phases corresponding to different temperature ranges. The diffraction patterns of Y_2TiO_5, Gd_2TiO_5, and Dy_2TiO_5 were indexed in terms of the monoclinic phase. Later in 1967, W.G. Mumme and A.D. Wadsley [11] reported the same low-temperature phase of Y_2TiO_5, which was formed through the thermal decomposition of $NaYTiO_4$ synthesized using the solid-state reaction method followed by a 1300 °C heat treatment, and was overlooked in a study by *Ault and Welch (1966)* [12]. The identity of the diffraction pattern was similar to that of the compositions Gd_2TiO_5, Eu_2TiO_5, and Sm_2TiO_5 (first noted by Waring & Schneider, 1965) [13], which were indexed using an orthorhombic unit cell with the *Pnam* space group, with cell parameters a, b, and c as 10.48, 3.76, and 11.33 Å, respectively. In the same year, G.J. McCarthy, W.B. White, and R. Roy [14] studied the phase equilibrium in the Eu-Ti-O and Sm-Ti-O system, which revealed the existence of Eu_2TiO_5 and

Sm_2TiO_5 along with other compositions belonging to this family. Although the existence of both the compounds was first reported by Waring and Schneider [13], the structure type was not identified. In this work, Eu_2TiO_5 was indexed according to the monoclinic cell on similar grounds to Gd_2TiO_5 and Sm_2TiO_5, with an orthorhombic structure analogous to Y_2TiO_5, by comparing the data results reported by Queyroux [15]. Further, Müller-*Buschbaum et al.* prepared and analyzed the single crystal structures of Nd_2TiO_5 and Eu_2TiO_5, finding Nd_2TiO_5 to be isotypic with La_2TiO_5 [16, 17]. After this, until the 1980s, in the in-between era, many oxide materials were synthesized with tetragonal and octahedral coordination, containing rare-earth elements as well as other elements. After this, for the first time, a rigorous study of the crystal morphology and polymorphic properties of these materials was conducted by *Petrova et al.* [18]. In a systematic study conducted in 1982 and 1986, they reported polymorphism in the general Ln_2TiO_5 system and investigated the solid-solution phases in the Ln_2TiO_5-Lu_2TiO_5 (Ln = Gd, Tb, Er) system to determine the structural changes and stable phases in the corresponding oxide system. Later, starting from 2002 to 2010, they reported and published various studies on the crystal structure phases and polymorphic properties, providing rigorous analysis of the physical and chemical synthesis conditions, structural composition, and temperature stability of different phases. For the first time, a phase relationship was established in compositions of end members La_2TiO_5-Lu_2TiO_5 and intermediate Gd_2TiO_5-Tb_2TiO_5 compositions within the Ln_2TiO_5 Family [19, 20]. Their findings highlighted the possibility of a correlation between ionic radii and atomic numbers in the rare-earth titanates (Ln_2TiO_5 system), leading to similar morphological and structural properties. The solid-solutions of La_2TiO_5 and Lu_2TiO_5 confirmed the existence of a new composition LaLuTiO5, showing stability up to 1480 °C. The Gd_2TiO_5-Tb_2TiO_5 systems, having close ionic radii (0.938 and 0.923 Å, respectively), were found to form a continuous series of solid solutions of orthorhombic and hexagonal phases, with partial solid solutions of cubic Tb_2TiO_5 and 58 mol% Gd_2TiO_5. Having a large difference in ionic radii, the La_2TiO_5-

Lu_2TiO_5 system was found to have partial solid-solutions of La_2TiO_5 and Lu_2TiO_5 with an ordered phase of $LaLuTiO_5$. In another study, the researchers reported that Gd_2TiO_5 exists in two polymorphic forms: the low-temperature orthorhombic phase and the high-temperature hexagonal phase, exhibiting a polymorphic phase transition at approximately 1700 °C and a melting point of 1790 °C. The crystal structure was found to be isostructural with the orthorhombic structural phase of La_2TiO_5 [17, 21]. In their study, they found that the stoichiometric mixing of Gd_2O_3 and TiO_2, achieved via the solid-optical zone melting technique, yields only the orthorhombic phase of the Gd_2TiO_5 single crystal structure. However, if a replacement of Gd_2O_3 is made with 10-20 mol% of Gd_2O_3 by Lu_2O_3, single crystals of the hexagonal phase are found to evolve, having a composition of $Gd_{1.8}Lu_{0.2}TiO_5$. Using the same structural model, the hexagonal modification of Dy_2TiO_5 was solved, and the synthesis and stability of crystal structure phases with temperature were also reported in a study carried out by *Sinha and Sharma (2005)* [22]. In the study by Sinha and Sharma et al., the synthesis of Dy_2TiO_5 was reported using the conventional solid-state route method. During the heat treatment hours, the $Dy_2Ti_2O_7$ phase forms first. Subsequently, $Dy_2Ti_2O_7$ reacts with the remaining Dy_2O_3 to form the orthorhombic polymorph of Dy_2TiO_5 at 1100 °C, followed by the hexagonal phase around 1150 °C. By doping molybdenum trioxide (MoO_3), the high-temperature fluorite (Cubic) was found to be stable, which is the most suitable phase for being a control rod material for neutron absorption in the nuclear industry. *Shepelev and Petrova* [20] studied the single crystals of Dy_2TiO_5 that were grown by the optical zone melting technique, which resulted in the main composition being in cubic form with a minor modification of the monoclinic phase.

Although these Ln_2TiO_5-type materials are rarely explored, a significant amount of work has been done in this regard by 2-3 researchers. Over the last two decades, *Aughterson et al.* [23–25] conducted a series of works involving the synthesis, characterization,

and testing of the radiation tolerance of the complete Ln_2TiO_5 series, which includes the Lanthanide elements La, Pr, Nd, Eu, Gd, and Tb, from 2008 to 2018.

In 2008, an attempt was made to synthesize the Ln_2TiO_5 series, comprising lanthanide elements La, Pr, Nd, Eu, Gd, and Tb, using a nitrate-alkoxide route [26]. The samples were shear-mixed and then fine-ground to a powder form, followed by calcination and sintering for 48 hours at 1400 ºC. Except La, all samples were found to be almost (95%) in a single orthorhombic phase with *Pnam* symmetry, with a 5% secondary phase having a pyrochlore structural form of $Ln_2Ti_2O_7$ at room temperature. A further temperature-dependent study was conducted on Tb_2TiO_5, which revealed a structural phase transition from an orthorhombic to a hexagonal phase in the range of 1200-1520 ºC, in agreement with the *Petrova et al.* results of 1520 ºC. The change in cell parameters with temperature was found to be non-linear, with an expansion in the cell volume [7, 19, 20].

Further to see the effect of substitutional disorder and structural-property relationship, and to study already known different crystal structure phases, *Aughterson et al. (2014),* [27] synthesized the $Sm_xYb_{2-x}TiO_5$ (x = 0, 0.6, 1,1.4, and 2) bulk series first time and characterized them using the well-known techniques of X-ray diffraction, neutron diffraction, and transmission electron microscopy (TEM). From the characterization, Yb_2TiO_5 and $Sm_{0.6}Yb_{1.4}TiO_5$ were found to exist in a cubic crystal structure with two types of symmetries, where the majority of peaks belonged to long-range defect fluorite structure (*Fm*-3*m* symmetry) with some minor peaks of short-range pyrochlore structure (*Fd*-3*m* symmetry). The Sm_2TiO_5 was found in the orthorhombic phase with the *Pnam* space group. The compositions $Sm_{1.4}Yb_{0.6}TiO_5$ and $SmYbTiO_5$ existed in the hexagonal phase with $P6_3/mmc$ symmetry. For the precise determination and getting detailed insight into the existing crystal phases, both polycrystalline and single-crystal X-ray diffraction techniques were employed to characterize the synthesized samples in this work. Again, in a 2015 study (*Aughterson et al.,2015*), they reported

the synthesis and structural properties of these rare-earth titanates, which contain the lanthanide elements La, Pr, Nd, Sm, Gd, and Dy [28]. Notably, this study provided the first systematic structural data for Pr_2TiO_5. This study improved upon previously reported lab source XRD data and was characterized using the 10-BM-1 synchrotron beamline in Australia in 2015. The synthesis method was reported as a solid-state reaction route, involving intermixing, grinding by Ball Milling, and a final sintering process at 1330 °C to 1550 °C for 48 hours, with a heating and cooling rate of 5 °C/min. For the synthesis of the bulk Sm_2TiO_5 sample, an optical floating zone furnace was used instead of the conventional solid-state synthesis method to achieve the desired material composition. From the XRD and structural refinement, compositions Gd_2TiO_5, Tb_2TiO_5, and Sm_2TiO_5 were found to be in single phase, whereas La_2TiO_5, Pr_2TiO_5, Nd_2TiO_5, and Dy_2TiO_5 exhibited a secondary pyrochlore phase ($Ln_2Ti_2O_7$) with a percentage of 2%, 3.5%, 4% and 5% respectively. For the descriptive structural analysis and bonding characteristics, Rietveld refinement and bond valence sum approaches were used to correlate the structural parameters, and UV-Vis absorbance spectroscopy was used for the band gap analysis. With increasing lanthanide size (from Dy to La), density and cell volume showed a systematic increase, corresponding to the larger ionic radii and cell sizes. No systematic trend was observed in the band gap values with increasing size and lanthanide element. However, the refined coordinates and cell parameters were quite consistent with the previous experimental results reported by Shepelev and Petrova, as well as those of other authors [11, 17, 19, 21, 29–31]. The lanthanide-oxygen bond lengths, Ln(1)-O and Ln(2)-O, exhibited linear and exponential trends, respectively, with increasing lanthanide ionic radii. The titanium-oxygen bond lengths also exhibited a mixed behaviour, with both linear and exponential variations, except for Dy_2TiO_5 and Tb_2TiO_5, where some deviation was observed from the expected trend, which was anticipated to be the destabilizing mechanism in their orthorhombic phase. This was the first comparative and extensive study of crystallographic structural parameters, where rigorous analysis of

refinement and bond valence sum analysis were performed to extract and correlate cell parameter and bond length information. The results revealed a systematic trend among these rare-earth titanates, which was in clear agreement with the stability diagram provided by Shepelev and Petrova [20, 32, 33].

Over the past several decades, substantial progress has been made in the rigorous analysis of the Ln_2TiO_5 system, largely driven by the work of researchers Y. F. Shepelev, M. A. Petrova, R. D. Aughterson, and F. X. Zhang [25, 27, 34–36]. Their contributions include detailed investigations of crystal structure dynamics, polymorphic transitions, and responses to ion irradiation. Collectively, these studies highlight the promising structural stability and radiation tolerance of Ln_2TiO_5 compounds, positioning them as strong candidates for further research. Owing to these properties, the Ln_2TiO_5 family holds considerable potential for advanced applications in optical technologies and the development of nuclear materials.

1.1.2 Rare Earth Titanates of Ln_2TiO_5-type

In recent years, Rare-earth titanates of the Ln_2TiO_5 (Ln = La, Pr, Nd, Sm, Eu, Gd, Dy, Er, and Y) composition have garnered considerable interest due to their remarkable structural, optical, and thermal properties, which are of significant importance in today's nuclear world [8, 9, 27, 37]. Over the years, rare-earth titanates, including lanthanide perovskites (ABO_3-type), pyrochlore structures ($Ln_2Ti_2O_7$), $LnTiO_3$, and complex oxides of the $Ln_4Ti_9O_{24}$ type, have been rigorously researched and studied [1, 6, 38–40], with broad applications in the fields of spintronics, photonics, and energy harvesting. In this category, a new composition, Ln_2TiO_5, has emerged, which hasn't been extensively researched [8, 16, 41]. However, recent studies have shown its potential use in the fields of optical and nuclear industries due to its unique and interesting structural properties, making it a highly stable and radiation-resistant material. It belongs to a class of mixed-metal

oxides, where Ln represents the lanthanide element, which can be La, Pr, Nd, Sm, Gd, Tb, or Dy. These materials have garnered significant interest and attention due to their complex structural features and exceptional thermal and chemical stability, which surpass those of other existing oxide materials.

Their tunable structural properties and phase relationships, along with their ability to form complex solid solutions, make these titanates relevant for both fundamental research and technological applications, particularly in the fields of ceramics, nuclear and material industry, and the world of solid-state physics.

1.2 Ln_2TiO_5: The key to Their Uniqueness

Rare-earth titanates with the general composition Ln_2TiO_5, where Ln is the lanthanide element, represent a unique class of materials characterized by unusual structural coordination and distinct structural, electronic, and optical properties [28, 42]. The special feature that sets them apart is the rare five-fold coordination of Ti^{4+} and the distorted square pyramidal geometry of the TiO_5 polyhedral, which is generally not seen in conventional oxides of Ti^{4+} (Like $ATiO_3$ perovskites) and other compositions in the materials world [11, 13, 43, 44]. Generally, Ti^{4+} prefers to possess the most common octahedral geometry or, in less common cases, a tetrahedral cage, which makes the Ln_2TiO_5 composition structurally, optically, and electronically unique among all well-researched titanates and oxides.

1.2.1 Structural Uniqueness and Coordination Chemistry

Rare-earth titanates with the general formula Ln_2TiO_5 represent a structurally unique class of oxides distinguished by the presence of five-fold coordinated Ti^{4+} in a distorted square-pyramidal TiO_5 geometry. This coordination is extremely uncommon because Ti^{4+} (d^0)

typically stabilizes in six-coordinate octahedral (TiO_6) environments due to strong electrostatic preferences [31, 45–48]. The presence of TiO_5 units results in pronounced structural asymmetry, lowered site symmetry, and the emergence of unusual local electric fields not encountered in conventional Ti-based oxides. These features make Ln_2TiO_5 compounds exceptional candidates for studying low-coordination titanium chemistry and structure-property relationships that are fundamentally different from the enormous class of standard Ti-based perovskites [49, 49–51].

1.2.2 Crystal Field Splitting and Electronic Structure

The five-fold coordination induces a non-octahedral crystal-field splitting of the Ti-3*d* orbitals, which is fundamentally different from the conventional t_{2g}/e_g splitting in octahedral TiO_6 units and tetrahedral configurations [52]. As a result, Ln_2TiO_5 compounds exhibit distinct band-edge configurations, modified O-2*p* and Ti-3*d* hybridization, and unique optical and dielectric behaviour, which cannot be replicated in perovskite titanates having rutile or anatase-type structures.

1.2.3 Importance of Gd_2TiO_5

Among the Ln_2TiO_5 family members, Gd_2TiO_5 hold a significant place due to the possession of a half-filled $4f^7$ electronic configuration by the Gd^{3+}, which gives rise to strong spin-only magnetic moments with negligible spin-orbit coupling [15, 53, 54]. This places Gd_2TiO_5 in a special position for studying 4*f*-lattice coupling, magneto-dielectric interactions, and distortion arising from the magnetic field of rare-earth ions. Moreover, Gd_2TiO_5 composition lies in the middle of the lanthanide titanates series of the Ln_2TiO_5 composition, due to having intermediate ionic radii possessed by the Gd atom, which makes Gd_2TiO_5 an ideal candidate for the investigation from a structurally

balanced structure viewpoint and a widely accepted standard member of the lanthanide titanates series.

1.2.4 Implications for Material Science and Applications

Rare-earth titanates of Ln_2TiO_5 composition hold a crucial position in material science due to their rarely observed coordination geometry, tunable structural properties and the presence of optically and magnetically active rare-earth ions, which makes the system an interesting model for understanding the structure-property relationships in complex oxides. Due to their possession of unusual coordination numbers, electronic configurations, and high thermal stability, as well as tunable bonding characteristics, these materials are emerging as promising candidates for photonic devices, dielectric components, catalytic applications, and platforms for fundamental research in solid-state chemistry [55–57]. The tunable and adjustable nature of Ln_2TiO_5 titanates motivates researchers to employ new methodologies and novel approaches for conducting more rigorous investigations, generating new functionalities and characteristics [5, 57–59] that can hold technological importance and significance in material science.

1.3 Crystal Field Splitting

Crystal Field theory [52, 60] explains the nature of the interaction and bonding between the metal and the ligand in complex coordination compounds, which is crucial for understanding the important properties of metal coordination complexes, such as colour and magnetism. Valence band theory [61, 62], which was based on the formation of a coordinate-covalent bond (dative bond) by the interaction between the Lewis base (ligand) and the Lewis acid (metal ion), which acts as electron donor and acceptor, respectively, was unable to distinguish whether the geometry of 4-coordinated complexes would be square planar or tetrahedral. To account for the limitations of the VBT

(Valence band Theory), the crystal field theory was given by Hans Bethe in 1929, and subsequent modifications were done by J.H. Van Vleck (1935), named as Molecular Orbital Theory (MOT) or Ligand Field Theory (LFT) [63–65]. The crystal field theory considers that there also exist repulsive forces between the d electrons of the metal ion and the ligand, in addition to strong forces of attraction between the donor electrons of the ligand and the empty orbitals of the metal ion. The following assumptions are taken in the crystal field theory:

1. The crystal field theory (CFT) is purely an electrostatic model, which considers the interaction between the ligand atom and the metal ion to be ionic in nature without any covalent interaction. However, it is practically impossible to neglect covalent interactions thoroughly when explaining the results of some coordination complexes.
2. Here, the ligand atoms are considered as point charge particles, which is not always true. In most of cases, the size of the electron-donating ligand is found to be comparable to the metal ion is almost the same.

In the hypothetical model of CFT, the field of the ligand atom is considered to be spherical while approaching the metal ion, and due to repulsion between the ligand and metal electrons, energy is raised a little bit, resulting in the barycentre, but the degeneracy of d orbitals is still maintained. However, in transition metal complexes, the ligand field does not always possess perfect spherical symmetry because the metal ions can adopt different geometries, such as tetrahedral, square planar, or octahedral. As a result, the d orbitals interact differently with the surrounding ligands, causing their degeneracy to be removed and resulting in energy-level splitting in the t_{2g} and e_g orbitals.

1.3.1 Crystal Field Splitting in Octahedral Complexes

To understand the crystal field splitting in octahedral complexes, it is essential to comprehend the shapes and electron density distribution in d-orbitals. It is known that electron density lobes in $d_{x^2-y^2}$ and d_{z^2}

orbitals lie along the axes, while the electron density distribution in the lobes of d_{xy}, d_{yz}, and d_{zx} lies between the axes. In octahedral complexes, the ligands approach the metal orbitals along the axes; hence, more repulsion is felt by the $d_{x^2-y^2}$ and d_{z^2} orbitals by the ligand atoms, while they are repelled less comparatively. These results splitting of energy levels of these d-orbitals into t_{2g} and e_g levels, where the energy of $d_{x^2-y^2}$ and d_{z^2} (e_g) orbitals gets raised or repelled by 0.60 Δ_o (Δ_{oct}), and the energy of d_{xy}, d_{yz}, and d_{zx} (t_{2g}) orbitals gets lowered or stabilized by 0.4 Δ_o (Δ_{oct}) in comparison to the energy of the Barycentre, which represents the crystal field energy of a hypothetical spherical field. Here, the Δ_o or 10Dq represents the crystal field splitting energy, which is given by the difference between the energies of the e_g and t_{2g} orbitals. The schematic for the crystal field splitting in octahedral complexes is shown in **Figure 1.1**.

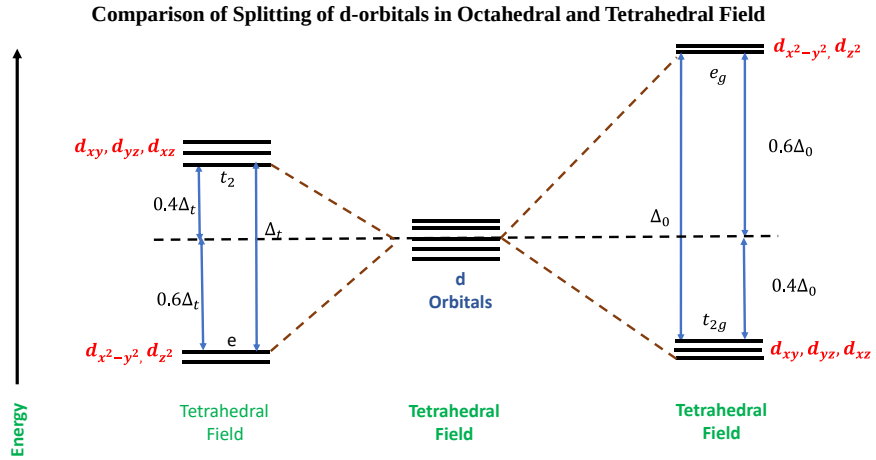

Figure 1.1 The schematic shows the crystal field splitting of *d*-orbitals in Octahedral and tetrahedral field environments

1.3.2 Crystal Field Stabilization Energy (CFSE)

The crystal field energy [66] is the stable energy resulting from the redistribution of atomic orbitals by placing a transition metal ion in a particular crystal field of ligand atoms. This energy results when the *d*-orbitals are split by the influence of the ligand field, where some of

the orbitals are raised in energy and some become lower in energy with respect to the spherical field of the ligand atom (Barycentre). As seen in the above case of octahedral complexes, where the e_g orbitals are raised and the t_{2g} orbitals are lowered energetically, this provides the system with extra stability due to the rearrangement of d electrons. The consequent gain in bonding energy is referred to as crystal field stabilization.

In other words, we can say it is the difference between the energy of the electronic configuration in the ligand field and the energy of the electronic configuration in the isotropic or spherical field.

$$\text{CFSE} = \Delta E = E_{\text{Ligand field}} - E_{\text{Isotropic field}} \quad (1.1)$$

CFSE (Octahedral Complexes):

$$\textbf{CFSE} = -0.4 \times n(t_{2g}) + 0.6 \times n(e_g) \times \Delta_o \quad (1.2)$$

Where $n(t_{2g})$ and $n(e_g)$ represent the number of electrons occupying the t_{2g} and e_g orbitals, respectively.

CFSE (Tetrahedral Complexes):

The tetrahedral crystal field stabilization energy is calculated in the same way as the octahedral case. The magnitude of the tetrahedral splitting energy is only $\frac{4}{9}$ of the octahedral splitting energy:

$$\Delta_t = \tfrac{4}{9}\,\Delta_o \quad (1.3)$$

$$\textbf{CFSE} = 0.4 \times n(t_2) - 0.6 \times n(e) \times \Delta_t \quad (1.4)$$

where $n(t_{2g})$ and $n(e_g)$ are the number of electrons occupying the respective levels. Some of the important factors that affect the crystal field energy (SFSE) are listed below:

1. **Metal Ion Oxidation State**: A Higher oxidation state of the metal ion results in a larger crystal field energy (Δ).

2. **Nature of the Metal Ion**: Crystal field energy gets increased by progressing from 3d…..> 4d…..> 5d within a given group.

3. **Geometry of the Complex Ion:** The splitting of the crystal field depends upon the geometry of the complex. For example, corresponding to the same metal ion and the same ligand, splitting

in octahedral complexes is found to be twice as strong as in the case of tetrahedral complexes.

4. **Nature of the Ligand**: Different amount of splitting occurs in the case of different ligands.

The crystal field splitting strength varies from strong to weak, depending on the oxidation state, charge, and nature of the metal ion or ligand. As the oxidation state of the central atom increases, the size of the central metal ion decreases, accompanied by a significant increase in charge. This results in a shorter metal-ligand distance and a stronger interaction energy, leading to an increase in the crystal field energy as the oxidation number increases. To account for these effects, different ligands and metal ions can be listed in a spectrochemical series, ordered by their increasing ability to stabilize a complex. In the decreasing strength, important ligands and metal ions can be written as:

- **Spectrochemical series for ligands**

  Co≈ CN-> Phen> Bpy > en > NO2-> NH3> NCS-> H2O= [ox]2-> OH-> F-, SCN-> Cl-> Br-> I-

- **Spectrochemical Series for metal ions**

  Pt4+> Ir3+>pd4+>Ru3+>Rh3+> Mo3+> Co3+> Cr3+> Fe3+> V2+> Fe2+> Co2+> Ni2+> Mn2+

1.3.3 Crystal Field Splitting in Tetrahedral Complexes

The ligand-metal interaction in tetrahedral complexes, and its distinction from that in octahedral complexes, can be explained using a cubic model. In an octahedral arrangement, ligands are located at the centres of the cube's faces, while in a tetrahedral arrangement, they occupy the corners of the cube. In tetrahedral complexes, four ligands are bonded to the central metal ion, but their directions do not align directly with the metal's *d*-orbitals. Instead, they are positioned closer to the t_{2g} orbitals than the e_g orbitals, causing greater repulsion of the t_{2g}

set. As a result, the d-orbital splitting pattern observed in tetrahedral complexes is the reverse of that in octahedral complexes, as shown in **Figure 1.1.** Because of the weaker overlap between metal and ligand orbitals in tetrahedral coordination, the energy splitting is smaller, about half of that in octahedral complexes. Therefore, tetrahedral complexes usually exhibit high-spin configurations. A comparison of the crystal field splitting of *d*-orbitals in Tetrahedral and Octahedral complexes is shown in a schematic in **Figure 1.2**.

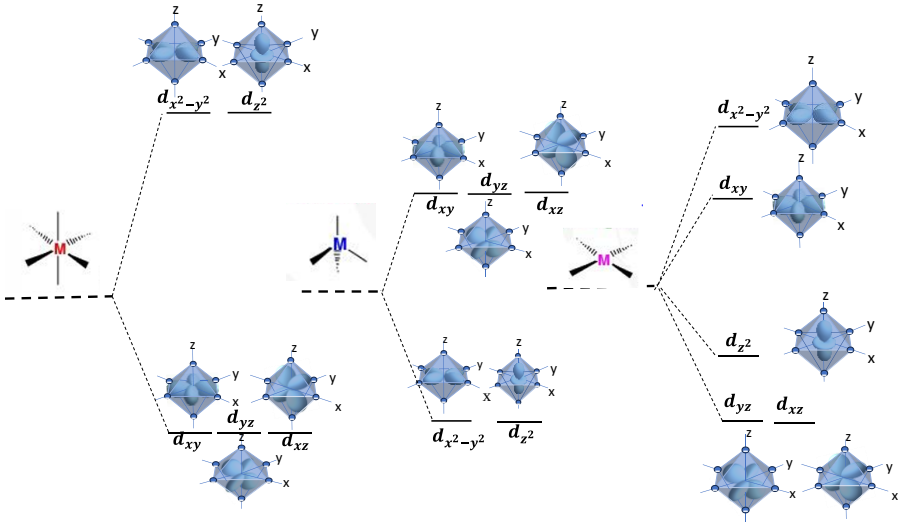

Figure 1.2 The schematic shows the comparison of crystal field splitting of d-orbitals in Octahedral, tetrahedral, and square planar fields, respectively

The crystal field splitting energy in a tetrahedral coordination environment is inherently smaller than that observed in an octahedral field. Generally, this relationship can be expressed as $\Delta_t = (4/9)\,\Delta_o$.

1.3.4 Tetragonal Distortion of Octahedral Complexes (Jahn-Teller Distortion)

The splitting of degenerate d-orbitals within a crystal field leads to enhanced stability of the complex through crystal field stabilization energy (CFSE). In certain cases, the removal of degeneracy may proceed further, resulting in additional stabilization. Specifically, when the

electron occupancy of degenerate d-orbitals is asymmetric, the unequal electron repulsion with surrounding ligands can induce distortions in what would otherwise be highly symmetric geometries [67]. This phenomenon particularly occurs in octahedral complexes, where distortion arises mainly from the uneven occupancy of the e_g orbitals, whose lobes directly point towards the ligands. However, odd filling of the t_{2g} orbitals, which are oriented between the ligands, generally do not result in noticeable distortion due to less direct interaction with ligands. Therefore, electronic configurations such as high-spin $d^4(t_{2g}^3 e_g^1)$, low-spin $d^7(t_{2g}^6 e_g^1)$, and $d^9(t_{2g}^6 e_g^3)$ characteristically exhibit Jahn-Teller distortions, which are driven by asymmetrically filled e_g orbitals.

Among the e_g set of orbitals, the electron in the d_{z^2} experiences repulsion from the two ligands along the z-axis, whereas the electron in the $d_{x^2-y^2}$ orbital encounters repulsion from four ligands in the xy-plane. As a result, the electron preferentially occupies the d_{z^2} orbital to minimizes the energy. This occupancy leads to the elongation of two bonds along the z-axis as compared to the other four bonds, resulting in the distortion, which is called tetragonal elongation or 'Z-out' distortion. Conversely, if the electron occupies the $d_{x^2-y^2}$ orbital, the bonds along the z-axis contract, producing a tetragonal compression or 'Z-in' distortion. These distortions result the lowering of the overall symmetry and energy of the complex by removing the orbital degeneracy associated with the electronic occupancy, hence stabilizes the system. The schematic for the Jahn-Teller distortion is shown in **Figure 1.3**. The Jahn-Teller effect exemplifies how asymmetries in electronic configurations can drive significant structural changes that optimise the energy landscape in transition metal complexes.

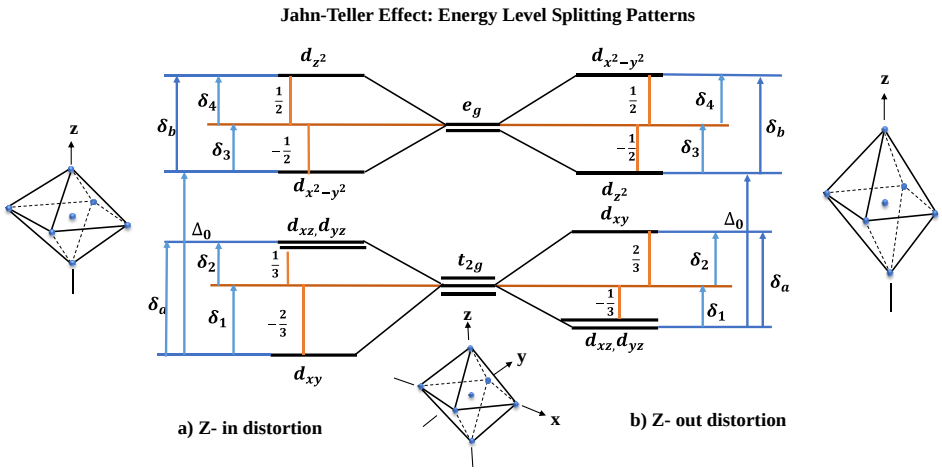

Figure 1.3: The schematic shows the Jahn-Teller effect: Tetragonal distortion in octahedral complexes

1.3.5 Crystal Field Splitting in Square Planar Complexes

Square planar coordination can be understood as a structural modification which is derived from the octahedral geometry. It can be visualized as a result of the removal of two ligands located along the z-axis of the octahedral complex, thereby leaving the four ligands arranged in the x-y plane around the central metal ion. When the axial ligands are displaced, the remaining four planar ligands tend to move slightly closer to the metal centre and thereby results the alteration of the crystal field environment.

This change in geometry leads to the redistribution of energy obtained from the octahedral crystal field, among the metal d-orbitals, as shown in the splitting diagram of Figure **1.2**. As the ligands along the z-axis move away, the energy of the d-orbitals that possess a z-component decreases. Among these, the d_{z^2} orbital experiences the greatest stabilization because its electron density is concentrated along the z-axis. The d_{xz} and d_{yz} orbitals also decrease in energy, but in a lesser extent. In contrast, the dxy and $d_{x^2-y^2}$ orbitals, which lie in the plane of the ligands and experience greater electrostatic repulsion, increase in energy.

Overall, the resulting crystal field splitting in square planar complexes is more complex than in octahedral or tetrahedral systems. The significant stabilization of orbitals with the z-component and the high energy of the $d_{x^2-y^2}$ orbital gives rise to the distinct energy-level arrangement and characteristics of square planar geometries, as shown in **Figure 1.2**. This pattern plays a crucial role in determining the electronic configuration, magnetic properties, and overall stability of such complexes.

1.4 Introduction to the Ln_2TiO_5 System and its Properties

1.4.1 Polymorphism in Ln_2TiO_5 Materials

Rare-earth titanates of compositions $Ln_2T_2O_7$ and Ln_2TiO_5 are the most important and well-researched family among all the rare-earth titanates, which have vast applications in the nuclear industry due to their fascinating characteristics of high mechanical strength, radiation stability, chemical and irradiation resistance [3, 23, 24, 27, 37, 68, 69]. These rare-earth titanates exhibit interesting properties of polymorphism, showing phase transitions depending on the temperature, pressure, and size of the rare-earth cation atom. The rare-earth titanates of the composition of $Ln_2Ti_2O_7$ are generally found in cubic phase and adopt pyrochlore-type structure having the *F*d3*m* space group, except rare-earth titanate of Lanthanum, Praseodymium, and Neodymium, which exhibit either orthorhombic phase with the $Pna2_1$ space group or a monoclinic phase with the $P2_1$ space group. The Ln_2TiO_5 composition, however, exists in three polymorphic conditions, namely orthorhombic, cubic, and hexagonal, depending upon the temperature and ionic radii of the lanthanide element. Titanates, starting from lanthanum to Samarium (with a large ionic radius), crystallize into an orthorhombic structure with the *Pnam* symmetry (Z = 4). The

intermediate rare-earth titanates, ranging from Eu to Ho and Y, exhibit multiple phases, including the orthorhombic and cubic, as well as the hexagonal phase with the $P6_3/mmc$ space group (z = 1.2). In the M.A. Petrova study, it was found that the polymorphic transformations in the Ln_2TiO_5 system resemble those in the Ln_2O_3 systems studied by Foex and Traverse and depend on the temperature and ionic radii of the rare-earth element [18–20]. The end members of the series (Ln = Er-Lu and Sc) exhibit the cubic phase. In this regard, to understand the polymorphism and structural stability of different polymorphs in these Ln_2TiO_5 compounds, *Shepelev and Petrova, 2008* gave a phase stability diagram [34] that represents almost all possible synthesized compositions in all temperature ranges corresponding to the ionic radius of the lanthanide element, as shown in **Figure 1.4**.

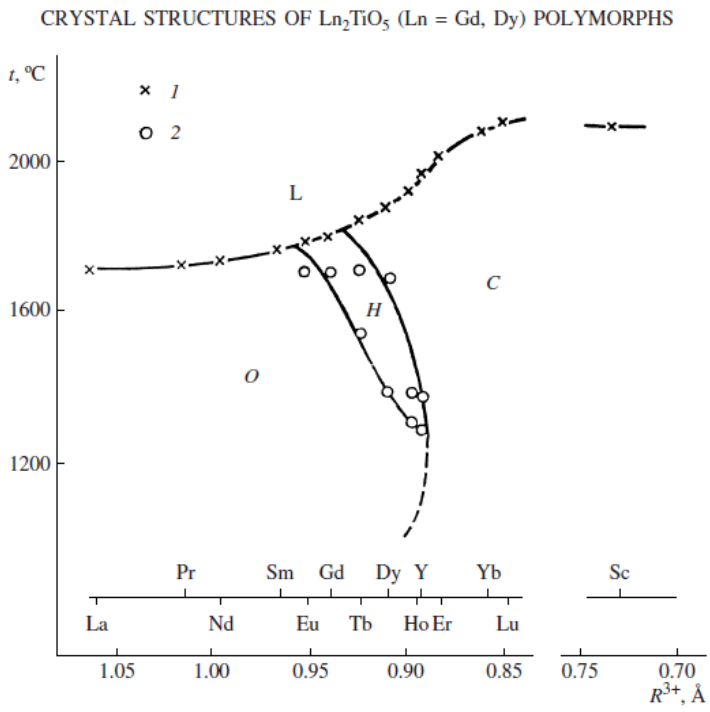

Figure 1.4 The schematic diagram represents the Stability diagram of Ln_2TiO_5 polymorphs, where O represents the orthorhombic, H hexagonal, and C cubic structures, and (1) represents the melting, and (2) the polymorphic transformation in the Ln_2TiO_5 family. The Schematic has been taken from *Shepelev and Petrova, 2008* study

1.4.2 Orthorhombic Phase (Large Size Rare-earth Titanates)

Rare-earth titanates, such as those from La-Sm, exist in an orthorhombic structure with the *Pnam* space group. Other examples of orthorhombic structure include the La_2TiO_5, Nd_2TiO_5, Eu_2TiO_5, and Y_2TiO_5. Here, we take the example of Gd_2TiO_5, which has been found to possess the orthorhombic phase, and Rietveld refinement analysis confirmed the *Pnam* space group of the crystal structure geometry. In our analysis, no impurity peak was observed in the XRD diffraction pattern of Gd_2TiO_5, which was analyzed using both the laboratory source X-ray diffractometer as well as using the synchrotron source. The crystal structure geometry extracted from the refinement results is illustrated in **Figure 1.5** and has been found to contain no mixed occupancy sites. In the orthorhombic crystal structure, the rare-earth cations were found to possess the seven-fold coordination number, which is generally found in coordination complexes. The Gd(1)-O(7)/ Gd(2)-O(7) polyhedron consists of a capped trigonal prismatic molecular geometry or monocapped trigonal prism, where all seven oxygen atoms are arranged around the Gd-atom and define the vertices of an augmented triangular prism. An augmented triangular prism is a triangular prism where one of the rectangular faces of the prism is augmented by a square pyramid. In other words, it can be described by a monocapped octahedron geometry (Octahedron with one face capped), which can be thought of as an octahedron with one extra atom (‘cap’) added on one triangular face or vertex of it.

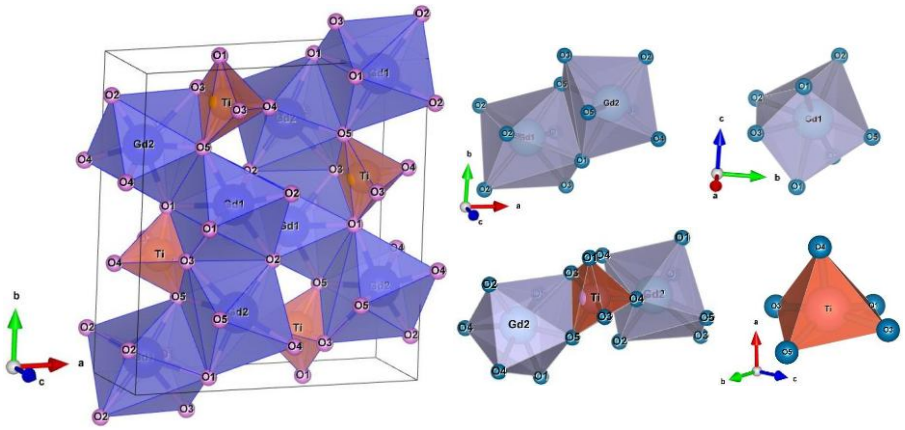

Figure 1.5 The orthorhombic crystal structure of Gd_2TiO_5 representing the square pyramid geometry of TiO_5 polyhedral and Gd atoms in seven-fold coordination number

1.4.3 Cubic Phase (Small Size Rare-earth Titanates)

Rare-earth Titanates (end members of the series) (Ln = Er-Lu and Sc) exhibit a cubic crystal structure. The crystal structure symmetry of the cubic phase can be understood by considering the example of Dy_2TiO_5, which was first reported by Tiedemann and Mueller-Buschbaum et al. in 1985 [70] with the space group symmetry of *F*4(3)*m*. Later, *Shepelev and Petrova, 2008* [20, 33] conducted a detailed structural analysis of the single crystal of Dy_2TiO_5 and found that the structural phase *F*d3*m* was the same as that of the $Dy_2Ti_2O_7$ pyrochlore structure. In the cubic crystal structure of Dy_2TiO_5, one of the dysprosium atoms is found in a mixed oxidation state with the Ti atom, at the M cation site, which possesses an octahedral coordination number. The other Dy atom is surrounded by eight oxygen atoms, leaving an oxygen atom in the tetrahedral coordination with the cation atoms. Besides the Cubic phase, a few single crystals of Dy_2TiO_5 were found to possess a monoclinic phase, the unit cell parameters of which can be derived from the cubic structure's parameters by the relation a=ac, b=0.25(bc+cc), and c=0.5(bc-cc). The XRD diffraction patterns of both phases were found to differ by a very small amount.

1.4.4 Intermediate Rare-earth Titanates, ranging from Eu to Ho and Y

These rare-earth titanates exhibit all three phases. At low temperatures, an orthogonal phase exists; subsequently, a more symmetric hexagonal phase is observed [19, 34]. At higher temperatures, the most stable cubic phase is observed. For example, Gd_2TiO_5 undergoes a reversible phase transformation from an orthogonal phase to a more symmetric hexagonal phase around 1700 °C and shows a melting point of 1790 °C. Similarly, Dy_2TiO_5 was found to exhibit two polymorphic transformations. It shows the first polymorphic transformation at 1370 °C, where the phase changes from orthorhombic to hexagonal, followed by another polymorphic transformation at 1680 °C, which transforms the phase to cubic. The hexagonal crystal structure can be understood in terms of the crystal structure geometry of $Gd_{1.8}Lu_{0.2}TiO_5$, which belongs to the P63/mmc space group and was studied in detail by Shepelev and Petrova. The structural phase of hexagonal Gd_2TiO_5 exhibits an ABABAB-type six-layer geometry with alternating octahedral and bipyramidal layers. The structural analysis showed that the structural geometry of the hexagonal polymorph of Ln_2TiO_5 is similar to $YAlO_3$ (*P*63/*mmc* space group), which is a member of the $LnAlO_3$ (Ln = lanthanide element) series.

1.5 Ion-Irradiation Response of Ln_2TiO_5 Materials

Rare-earth titanates of the $Ln_2Ti_2O_7$ composition, with the pyrochlore structure, have exhibited remarkable resistance to radiation damage from high-energy irradiating ions [24, 38, 70, 71]. This study led the researchers to investigate the related Ln_2TiO_5 compounds to evaluate their response under similar irradiation conditions. Subsequent studies have revealed that these materials also exhibit exceptional

radiation tolerance, which highlights their significant potential for applications in the nuclear industry [70, 72, 73].

1.5.1 Ion -Irradiation Mechanism

In ion irradiation, energetic particles or ions (He^{+}, Ar^{+}, Ni^{+}, Kr^{2+}, and Au ions) are generated and bombarded directly at the sample/target material. These ions penetrate the crystal and interact with the atoms and electrons of the target material, transferring energy and causing physical and chemical changes, such as atomic displacement, defect formation, and phase transformation, if the energy of the ions is high enough. The transfer of energy by the heavy-energy ions to the atoms of the target material can occur in two ways:

1. **Nuclear (Elastic Collisions):** This process leads to cascades of nuclear collisions, and atoms are knocked out directly from their lattice positions to create point defects and sometimes defect clusters.

2. **Electronic (Inelastic Collisions):** These collisions excite electrons and result in ionization, leading to migration of defects and annealing.

As these defects build up, they can change the material's structure, sometimes turning a crystal into an amorphous form or causing a phase shift, such as from an orthorhombic structure to a defect fluorite phase. Still, some titanates are surprisingly resilient and remain unchanged even when exposed to very high radiation doses.

1.5.2 Ion-Irradiation Studies

Numerous ion-irradiation studies have been conducted on the Ln_2TiO_5 composition series till now, where small-sized lanthanide elements have been found to exhibit better radiation tolerance. In a study by Zhang et al., Gd_2TiO_5, Dy_2TiO_5, and Y_2TiO_5 were found to be relatively highly radiation-resistant and possessing low critical

amorphization temperatures (T_c) due to their ability to form disordered structures easily, which is attributed to their smaller size. The simplicity of creating disordered structures correlates with their ability to develop high-temperature phases.

Tracy et al. (2012) studied the ion irradiation response of Gd_2TiO_5 and some of the other rare-earth titanates (La_2TiO_5, Nd_2TiO_5, and Sm_2TiO_5) by irradiating 1.47 GeV Xe ions [74]. From the study, the volume of the amorphous region was found to decrease systematically with decreasing lanthanide size in damaged ion tracks, indicating improved irradiation resistance within the series. In a study by *Aughterson et al. (2023)* a consistent flux of 1 MeV Kr^{2+} ions was irradiated in situ on the Gd_2TiO_5 crystal to observe the sample's response to accumulated ion irradiation, using the bright-field images and selected area electron diffraction pattern (SAED) [74–76]. It was noted from the SAED pattern of different grains that as the radiation dose increased, the relative intensity of Bragg peaks diminished and was replaced by diffuse rings, indicating an increase in short-range order and the emergence of an amorphous character in the crystal structure. From the in-situ room-temperature experiment, a linear trend was observed between the critical dose of amorphization and the lanthanide size, with deviations in the trend only observed in the cases of Eu_2TIO_5 and Dy_2TiO_5. At room temperature, as the lanthanide size decreases, the critical dose for amorphization, Dc, was found to increase. Their results were found to be in agreement with those of Tracy et al. In both results, the only difference was in the mechanism of energy loss due to ion irradiation. According to the study by *Tracy et al. (2012)*, the energy loss mechanism between the ion and the lattice was attributed to electronic losses (inelastic scattering). In contrast, Aughterson's study found that the energy was lost by the irradiating ions to the target material via nuclear collisions (elastic scattering). The unexpectedly lower value of D_c in the case of Eu_2TiO_5 indicates the instability of the orthorhombic phase at room temperature, while the higher value of D_c in the case of Dy_2TiO_5 signifies improved damage recovery from the irradiation

mechanism. In this work, the critical amorphization dose (D_c) was experimentally measured at multiple temperatures for a selected Ln_2TiO_5 composition. These D_c values were subsequently employed, using the equation below (**equation 1.5**), to estimate the critical amorphization temperature (T_c) for nearly the entire lanthanide series.

$$D_c = D_o / \left[1 - exp\left\{\left(\frac{E_a}{k_B}\right)\left(\frac{1}{T_c} - \frac{1}{T}\right)\right\}\right] \quad (1.5)$$

A comprehensive dataset was obtained by plotting Dc as a function of irradiation temperature and Tc as a function of the lanthanide ionic radius (Ln^{3+}). Notably, the calculated values showed strong agreement with the previously reported results, thereby validating the observed correlations.

1.6 Applications

1.6.1 High Dielectric Applications/ Biosensing Applications

Lanthanide titanates of the Ln_2TiO_5-type, especially Sm_2TiO_5, Gd_2TiO_5, and Pr_2TiO_5, are utilized in biosensing applications due to their unique properties, including a high dielectric constant, chemical and structural stability with temperature, and robust surface chemistry. Some Ln_2TiO_5 compounds have been utilized in urea biosensing applications [59, 77–81], where they act as high-dielectric sensing membranes in electrolyte-insulator-semiconductor (EIS) biosensors due to their exceptional pH sensitivity, compatible nature with enzyme immobilization, low hysteresis, and high selectivity for hydrogen ions over other common ions such as Na^+, K^+, and Ca^{2+}.

A typical biosensor consists of a high-k membrane with a Ln_2TiO_5 composition, which is coated with immobilized urease acting as a catalyst for breaking down urea. The breakdown of urea produces ions such as OH^-, NH^{4+}, and HCO^{3-}, which increases the pH in the local area. This change is then detected as a voltage shift and an electronic

signal by the pH-sensitive Ln_2TiO_5 membrane of the EIS-based biosensor. The high dielectric constant, thermal stability, and chemical stability, along with excellent pH sensitivity, of Ln_2TiO_5 materials are attributed to their rapid and reliable ion/pH concentration sensing capabilities and their capacity for integration in miniaturized chip devices. This makes them compatible for use as sensing membranes and is excellent compared to other conventional membranes, such as Si_3N_4, Al_2O_3, and Ta_2O_5. Based on the above properties, various studies have been conducted on the use of Ln_2TiO_5 materials in biosensing applications related to the industrial and medical fields.

1.6.2 Optical Applications/ Luminescence Applications

Rare-earth titanates of general composition Ln_2TiO_5 have been found to be of significant use in the field of photoluminescence and cathodoluminescence, where they are being used in optical sensors, display phosphors, and in solid-state lighting (LEDs) [82–89]. Their ability to emit light when excited by UV or laser sources, combined with tunable crystal structure properties that facilitate efficient light emission, and the unique nature of the rare-earth element, make them highly efficient luminescent materials. The increasing demand for visible and mid-infrared sources in IR spectroscopy, gas detection, and remote sensing has prompted researchers to explore new methods for generating mid-infrared radiation. The conventional methods used for generating IR sources include oxide glasses, optically pumped semiconductors, and quantum cascade lasers. However, rare-earth-doped chloride crystals with reduced phonon energies are also a viable alternative to conventional oxide and fluoride crystals. If we dope rare-earth ions into host crystals that are specifically sensitized for diode pumping with the rare-earth ion, they emit efficiently even with low-cost available diodes, due to their phonon-assisted cross-relaxation mechanism between the pumped state and the ground state. For instance, the cross-relaxation mechanism in singly doped Tm^{3+}: YAG results in lattice phonon

conversion into infrared emission by sensitizing the 2 μm sources for laser diode pumping. In crystals doped with Tm^{3+} and Pr^{3+}, cross-relaxation processes facilitate energy transfer mechanisms by lowering the energy levels of Pr^{3+}, resulting in optically pumped phosphor emission in the mid-infrared range (4-5.5 μm). Hence, by reducing the multi-phonon relaxation rates in rare-earth-ion-doped host crystals, diode pumping yields sensitized luminescence in the mid-IR range.

The doping of rare-earth ions in host crystal lattices and glasses has led to a significant enhancement in luminescence properties due to their unique characteristics, which have found numerous potential applications in the fields of optical sensors, optical laser devices, and optoelectronics. Due to the unusual electronic configuration and structure, rare-earth ions (Eu^{3+}, Tb^{3+}, Dy^{3+}, Sm^{3+}, Ce^{3+}, and Er^{3+}) [82, 89, 90] are very sensitive to UV or blue light absorption, which causes $4f^N$-$4f^N$ intraband transitions in their electronic structure. Generally, rare-earth ions exist in the +2 and +3 oxidation states and possess one or two electrons in their outermost orbital (4*f*). This results in their energy levels being abundant and characterized by distinct electronic configurations. The 4*f* electrons lie deeper and are therefore partially shielded by the outermost electrons of the 5*p* and 5*s* orbitals. This makes their spectral features very coherent and highly resolved, resulting in sharp absorption lines. Because of these qualities, when they are doped or added to a host crystal lattice, the mixing of *p* or *d* orbitals with the *f* orbital (even-parity and odd-parity) of dopant ions relaxes them from the constraints of the selection rules of electronic transitions, allowing the occurrence of disallowed transitions. These traits enhance the performance of phosphor materials by improving both the absorption efficiency and the emission spectra. In rare-earth phosphors, the rare-earth ions act as both activators (A) and sensitizers (S), making the energy transfer process easier. The sensitizer ions absorb the incoming excitation energy and then transfer it to the activator ions, which are the rare-earth elements themselves, making the light emission a very efficient process. The presence of phonon sidebands facilitates excitation transitions and

enables charge transfer processes. The interband 4*f*-4*f* electron transitions enable efficient energy absorption and transfer processes, resulting in sharp absorption peaks in the UV-blue region and intense, narrow bands that lead to subsequent red emission. These transitions are parity forbidden but become partially allowed due to the lattice site symmetry configuration, resulting in an improvement in quantum efficiency and a stronger emission intensity by reducing non-radiative losses.

1.7 Motivation and Origin of the Scientific Problem

The initial work carried out on the rare-earth titanates of Ln_2TiO_5 mainly consists of studies of phase diagrams for different rare-earth cations and transitions governed by temperature and pressure. A significant number of studies have been conducted in this respect by *Petrova and Grebenshchikov,* (*2008*) [19]. In recent years, *Aughterson et al.* (*2015*) [28] have conducted more rigorous work on crystal structure and its applications in the nuclear industry, discussing the ion-irradiation behaviour of nearly all the lanthanide titanate series. Although a lot of ion-irradiation studies have been carried out on the basis of the applications of these materials for nuclear immobilization and nuclear waste management, the optical, electronic and magnetic characteristics correlations still need to be studied, which can be of significant importance for the photocatalysis, solar energy conservation and luminescence behaviour, opening new doorways in the field of optoelectronics and photonics. These applications enforce the study of rare-earth tannates in other aspects of optical, thermal, and magnetic behaviour, and a correlation needs to be established among different properties. This will provide detailed insight into lattice dynamics and electron-phonon coupling, a crucial phenomenon for band gap engineering.

Gd_2TiO_5, belonging to the rare-earth titanate, forms an interesting and rare example of mixed seven- and five-fold geometry among rare-earth oxide materials, which are known for their high thermal stability, chemical resistance, and radiation robustness, leading to their extensive applications in the nuclear industry. The titanium atom, present in a distorted square pyramidal geometry, makes them stand out from other traditional titanium oxides, where a strong correlation exists between the structural, optical, and electrical properties, rendering them highly efficient multifunctional oxides. To investigate such a correlation among the rare-earth of A_2BO_5-type compositions, Gd_2TiO_5 have been chosen as it lies in the mid-way of the lanthanide series, having intermediate radii, making it a standard model for studying the rare-earth titanates family. As the titanium polyhedra possess a five-fold coordination geometry, which is very rarely seen in oxide materials, Gd_2TiO_5 is of specific interest due to its unique and distinct crystal field environment compared to conventional oxide systems having titanium atom. The crystal field splitting determines various optical transitions that take place in the material, affecting absorption edges and band gap, and relates to the bond strength, force constant, which leads to the modification in the bond length and other structural parameters of the material's crystal structure.

The emerging application of solar energy conversion, photocatalysis, and water splitting demands the band gap to be engineered according to the specific application. The rare-earth titanates allow easy tuning of their lanthanide radius by enabling the incorporation of other rare-earth ions, making them an ideal candidate for substitution. This results in their properties being conveniently tunable, which can modify their optical, electronic, and magnetic properties, affecting their band gap, luminescence, and dielectric behaviour, and leading to applications in optical sensors, LEDs, lasers, and phosphor materials. These applications require tuning of the band structure and electronic density of states, resulting in modifications to the band gap, Urbach energy (E_U), and electron-lattice interaction

strength, which play a crucial role in tailoring the material's functionalities for specific applications. There are numerous ways to tune the band structure and electronic density of states, including perturbations within the system, such as introducing structural disorder through doping or substitution, and external perturbations, such as temperature and pressure.

Keeping this in view, in the first two studies (Chapter 3 and Chapter 4), we have carried out the composition-dependent Gd_2TiO_5 studies where Eu and Fe were substituted at the Gd- and Ti-site, respectively, for establishing a correlation between structural, optical and electronic properties via using simple methodology of structural refinement and widely used Optical Absorption Spectroscopy. Keeping the centre of attention on the temperature dependence studies of the optical band gap, the next study (Chapter 5) deals with the scope of composition-dependent Optical Absorption Spectroscopy and Raman Spectroscopy techniques, which can open new avenues for investigating the structural-disorder-driven lattice dynamics and band gap tuning in multifunctional oxide systems, such as rare-earth titanates Ln_2TiO_5[42, 74]. Here, the structural disorder is considered analogous to thermal disorder, which can lead to changes in the electronic band structure and, consequently, variations in the band gap. These band gap variations, based on the same causing factor, can result from two competing phenomena: Lattice Dilation and Electron-phonon coupling (EPC). One of these leads to a decrease in the band gap, while the other causes an increase in the band gap trend. In this regard, various theoretical as well as experimental studies have been carried out by previous research, but most of them concern the temperature variation of the band gap. In this respect, this work, which attempts to determine the qualitative contribution of variation in the band gap due to structural disorders such as doping or substitution effects, emerges as of significant importance and can provide alternative methods for band gap tuning and a more rigorous insight into the band gap dynamics of the material.

1.8 Organization of the Thesis

Chapter 1: Introduction

This chapter begins with a brief introduction of the study carried out and subsequently outlines the motivation behind the work.

Chapter 2: Experimental Techniques

This chapter provides a detailed description of the experimental facilities and techniques used for the synthesis and characterization of the samples studied in this work. For synthesizing the samples, the well-established solid-state reaction route has been employed, which is a simple yet high-temperature treatment technique. X-ray diffraction has been employed for material characterization and is described in detail in this chapter. For further analysis of optical and vibrational properties, UV-vis optical absorption spectroscopy in the diffuse reflection mode and Raman spectroscopy have been used extensively, as they are the most common and effective tools for characterizing material properties and are therefore discussed thoroughly.

Chapter 3: Influence of Fe Substitution on the Structural and Optical Properties of Gd_2TiO_5 Ceramic

Thus, the structural geometry of the compound plays a significant role in determining the crystal field splitting in transition metal oxides, and hence affects the material's optical, electronic, and band structure. In the rare-earth titanates of composition Ln_2TiO_5 (Ln = La, Pr, Nd, Sm, Gd, and Dy), the Ti atom is surrounded by the five oxygen anion atoms, which is rarely observed in Ti-bonded compounds. Hence, due to the different behavior of the crystal field and thus splitting in this case, it is expected that the evolution of optical and band structure properties will differ from those of other conventional oxides, such as

perovskite materials. Keeping this in mind, the present study investigates the effect of Fe substitution at the Ti-site in parent Gd_2TiO_5 on the optical properties of these compounds. To further support the experimental results, ab initio calculations using Density Functional Theory have been discussed.

Chapter 4: Experimental and First-principles Investigation on the Optical Properties of Eu and Fe-substituted Gd_2TiO_5

This chapter provides a description of the comparative study of the optical and electronic properties of Eu-substituted and Fe-substituted Gd_2TiO_5 samples, which were studied using Optical absorption spectroscopy. To find out the contribution of Ti-3*d* and Gd-5*d* states near the Fermi level and at the band edges, Eu and Fe have been substituted in Gd_2TiO_5 at the Gd- and Ti-sites, respectively, using the solid-state route synthesis. For further analysis by first-principles calculations using the GGA + U methodology performed by the VASP software.

Chapter 5: Interplay of Electron-Phonon Coupling and Lattice Dilation in Band Gap Tuning of $Gd_2Ti_{1-x}Fe_xO_5$

The temperature dependence of the band gap E_g in semiconductors is governed mainly by two phenomena: electron-phonon coupling (EPC) and lattice dilation (LD) effects, which have been well established in the previous reports, and many researchers have tried to find the explicit contribution of the electron-phonon interaction using the theoretical calculations of the electron self-energy terms and Debye-Waller (DW) factors. Keeping thermal effects analogous to the chemical disorder induced by substitution in the host lattice, it can be assumed that the chemical disorder also perturbs the system in the same

way as temperature, and hence both EPC and LD effects contribute here. To explore the individual contributions to E_g variation under substitution, this work investigates the role of EPC and LD in shaping the band gap of Fe-substituted Gd_2TiO_5. For this, X-ray diffraction, Raman spectroscopy, and optical absorption measurements have been performed. This work provides insights into how chemical substitution mediates electronic and structural interactions in complex oxides, with implications for band gap engineering.

Chapter 6: Conclusion and Future Scopes

This chapter presents a summary of the results obtained in the present research work, followed by the concluding remarks. It also discusses the potential future scope of the study carried out in this work.

Bibliography

Chapter 2

Experimental Techniques

This chapter discusses the synthesis procedure and the experimental techniques employed to carry out the present research work. It provides the detailed description of the solid-state reaction method used for the material synthesis, followed by the description of the X-ray diffraction which is a versatile technique for determining the phase purity of the synthesized samples. Furthermore, detailed descriptions of optical absorption spectroscopy and Raman spectroscopy have been presented, which has been employed to study the band gap characteristics and lattice dynamics.

2.1 Solid-State Synthesis Route

Solid-state synthesis is a simple and straightforward method for synthesizing the materials, which produces solid compounds with the required structural and functional properties [91–94]. Due to its simplicity and versatility, this method has a wide range of applications across various sectors, which includes materials used for energy storage, electronic devices, catalysis, and advanced ceramics. In the field of materials science research, the solid-state synthesis method plays an essential role in designing materials with tailored functionalities and is used regularly due to its simplest methodology.

2.1.1 Fundamentals of Solid-State Synthesis

2.1.1.1 Thermodynamic and Kinetic Considerations

Reactions that take place in the solid state are primarily affected by thermodynamic feasibility and kinetic limitations [94–96].

Thermodynamics provides information of the conditions that allow a reaction to proceed under given circumstances. In this context, the Gibb's free energy change (ΔG) is used as a key parameter which gives the information of spontaneity. The negative value of ΔG indicates that the reaction is thermodynamically favourable under those particular conditions. The expression for Gibbs' free energy is given by

$$\Delta G = \Delta H - T\Delta S \quad (2.1)$$

Here, ΔH represents the enthalpy change, T is the absolute temperature, and ΔS gives the change in the entropy of the reaction. Thermodynamics provides the possibility of a reaction, and kinetics determines how fast the reaction will occur. Thermodynamics gives the idea whether a reaction will take place or not, while kinetics provides information about the rate at which it is going to take place. The rate of reaction further depends on many factors, including temperature and pressure conditions, the rate of the diffusion process, particle size, and the presence of external catalysts. To achieve the effective diffusion of reactant materials, the temperature of operation and heating time play a crucial role in determining the desired characteristics of the material formed.

2.1.1.2 Role and Interpretation of Phase Diagrams

The phase diagram provides important information about the synthesis conditions and optimizing the solid-state reaction process. It provides information of the stability of different phases of the material under varying temperature and pressure conditions for different compositions. The information of phase boundaries and invariant points can provide the identification of suitable conditions which require the formation of stable phases and regions of phase transformation while heating or cooling cycles. The understanding of these stability regions can provide the information of heating profiles and reactant ratios which need to be adjusted to obtain the required composition without the formation of impurity and secondary phases. Hence, phase diagrams act as a guiding tool for acquiring suitable temperature and pressure

conditions, controlling reaction kinetics and preventing impurity phases during the synthesis process.

2.1.1.3 Influence of Defects in Solid-State Materials

The material defects also play a crucial role during the material synthesis process. The presence of defects can enhance or degrade the material's properties and, hence, affect the material's synthesis conditions. There are various defects, including anion or cation vacancies, interstitial and substitutional defects, that can modify and govern the materials' thermal and electronic conductivity, transport phenomena, optical, and magnetic properties. Sometimes, these defects enhance the functional characteristics of materials, and in such cases, they are intentionally introduced to optimize and tune the materials' properties for use in desired conditions.

2.1.2 Synthesis Process

The solid-state synthesis route, also known as the ceramic route, is the most rigorous and versatile technique used for synthesizing a variety of solid materials that utilize precursors in solid form. In this method, chemical reactions occur between powdered precursors, resulting in a solid material with a specific composition and crystal structure. Based on the subsequent heating cycles and processing conditions, the method enables the formation of highly pure single crystals, polycrystalline materials, glasses, ceramics, and thin films. The versatility of this technique of producing a vast range of materials makes it an essential method of materials synthesis that can be used for various optical and energy applications.

During the synthesis process, the powdered precursors are weighed accurately, mixed thoroughly, and then ground in an agate mortar pestle continuously for a specific number of hours. To obtain the material in a compact and dense form, the ground powders are then converted into pellets by applying minimum pressure using pelletizer

machines. Then, these grounded powders or pellets are subjected to heat treatment under high-temperature conditions for a specified number of hours to achieve the desired composition and pure phase. Certain metal oxides, salts, or mixed compounds may require more extreme synthesis environments, such as very high temperatures, high pressures, or flux-assisted conditions, to enable the required reactions. Due to the straightforward and robust nature of solid-state synthesis, this technique is sometimes described as the "shake and bake" or the "heat and beat" chemistry, which reflects the mechanical mixing followed by the thermal activation of powder materials.

In this work, a series of polycrystalline Eu- and Fe-substituted Gd_2TiO_5 samples has been synthesized using the solid-state reaction route to obtain the respective series compositions of $Gd_{2-x}Eu_xTiO_5$ and $Gd_2Ti_{1-x}Fe_xO_5$, where x represents the concentration and takes values of 0.03, 0.05, 0.07, and 0.10. The Eu has been substituted at the Gd-site, and Fe has been substituted at the Ti-site, respectively. For the formation of the Gd_2TiO_5 composition, highly pure (99.99% purity) gadolinium oxide (Gd_2O_3) and titanium oxide (TiO_2) were used as the starting precursor materials. To form the respective series $Gd_{2-x}Eu_xTiO_5$ and $Gd_2Ti_{1-x}Fe_xO_5$, iron oxide (Fe_3O_4) and europium oxide (Eu_2O_3) were mixed in stoichiometric amounts along with the starting precursors and were finely ground in an agate mortar pestle for approximately six hours. During the grinding process, isopropanol was used as a mixing reagent (liquid). The grounded samples were then calcined at temperatures of 1000 °C, 1250 °C, and 1300 °C, with intermediate grindings for a minimum of 24 hours. A maximum heat treatment of 1350 °C was given for the formation of pure Gd_2TiO_5, while 1300 °C and 1250 °C were given for the formation of $Gd_{2-x}Eu_xTiO_5$ and $Gd_2Ti_{1-x}Fe_xO_5$ series, respectively. The reaction for the synthesis can be represented below:

$$Gd_2O_3 + TiO_2 \xrightarrow{1350\,^{\circ}C} Gd_2TiO_5 \qquad (2.2)$$

$$\left(1-\frac{x}{2}\right)Gd_2O_3+\frac{x}{2}Eu_2O_3+TiO_2 \xrightarrow{1300\,^{\circ}C} Gd_{2-x}Eu_xTiO_5 \qquad (2.3)$$

$$Gd_2O_3+\frac{x}{3}Fe_3O_4+(1-x)TiO_2 \xrightarrow{1250\,^{\circ}C} Gd_2Ti_{1-x}Fe_xO_5+\frac{x}{3}O_2\uparrow \qquad (2.4)$$

In addition to the traditional ceramic route, modern techniques have expanded the scope of solid-state synthesis. For example, Solid-state metathesis involves initiating reactions between the metal compounds using an external energy source, such as a flame or mechanical milling, after which the reaction often proceeds automatically due to the heat released during the compound formation. Solution-assisted methods are also used significantly for the preparation of solid materials. In the sol-gel process, a homogeneous sol gets transformed into gels, powders, coatings, or nanostructures through drying and heat treatment. Solvothermal and hydrothermal techniques, which use sealed, pressurized vessels to promote crystal growth at elevated temperatures, offer additional advantages over phase formation and particle morphology.

Other processes that yield solid materials, such as vapour-phase deposition, intercalation reactions, single-crystal growth, and nanomaterial fabrication, are also considered as a part of the broader solid-state synthesis toolbox.

2.2 X-Ray Diffraction Technique

X-ray diffraction is a non-destructive and highly impactful technique which is used for characterizing materials and provides information about the phase, crystal structure, lattice spacing, strain, and crystal defects [97–99]. X-ray diffraction is obtained from the constructive interference which is produced by the scattering of the X-ray beam by the lattice planes of the sample [100]. X-ray diffraction

gives a fingerprint of the atomic distribution and the lattice plane arrangement of the material [101, 10$\underline{2}$].

In the X-ray diffraction (XRD) experiment [99, 103, 104], X-rays are produced by the X-ray tube, where electrons are emitted from the heating of the filament and then are accelerated toward the metal target. Their interaction with the metal target generates characteristic X-rays, which are then filtered to obtain a predominantly monochromatic beam. This is followed by collimation, resulting in a well-defined beam. This beam is then incident on the sample surface, where it interacts with the lattice planes of the crystalline material, and a constructive interference occurs, which follows geometric conditions given by Bragg's law [105],

$$nl = 2d \sin\theta \tag{2.5}$$

where λ is the wavelength of the incident X-ray beam, n is the integer, and gives the order of reflection, d is the spacing between the crystal planes, and θ is the angle of diffraction. This has been illustrated in the schematic of **Figure 2.1**. Bragg's law gives the relationship between the wavelength of X-rays, the angle of diffraction, and the distance between crystallographic planes in a solid. The detector records the diffracted beams once the Bragg diffraction condition is satisfied. The signal is then processed and measured. During the powder XRD measurement, the sample is scanned across a set range of 2θ values. The equipment can capture all conceivable diffraction directions related to the lattice, as the crystallites in a powdered sample are randomly aligned. After that, the observed peak positions are then converted into the corresponding d-spacings, from which the phase information can be obtained. Every crystalline compound has its unique set of d-spacings, which are used to compare the material's crystal structure and phase purity with the standard reference patterns.

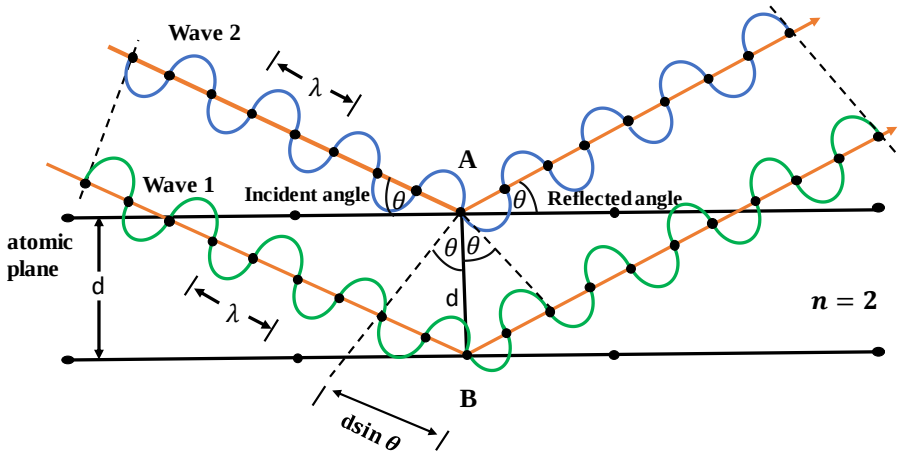

Figure 2.1 Schematic represents the X-ray diffraction from the crystal lattice planes having a periodic arrangement of basis atoms

A typical X-ray diffractometer mainly consists of three major components, which include the X-ray source, the sample stage, and the detection unit. The X-ray tube operates by heating a filament to release electrons, which are then accelerated toward the metal target under high voltage and strike the target material. When the incoming electrons possess sufficient energy to remove inner-shell electrons of the target atoms, characteristic X-ray lines, most notably the K_α and K_β emissions, are produced. These characteristic lines form the basis of the monochromatic radiation used for diffraction analysis.

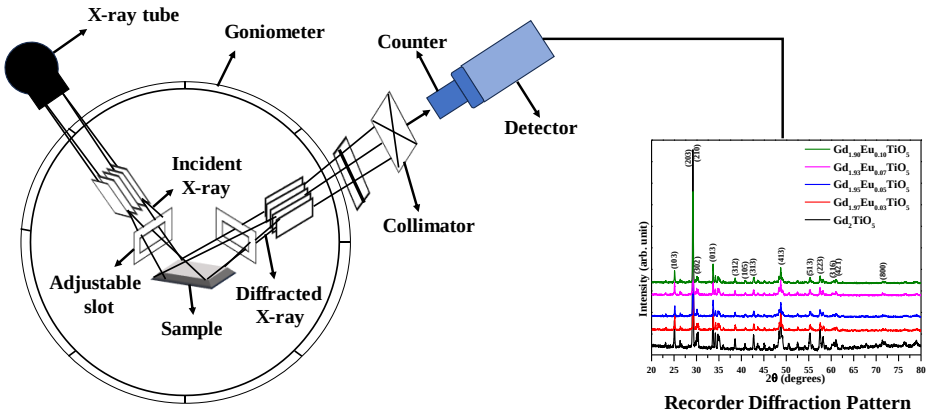

Figure 2.2 Schematic diagram of a typical recorded diffraction pattern

Copper is mostly used as the target material in X-ray tubes for single-crystal and powder diffraction experiments and produces the characteristic wavelength 1.5418 Å of Cu K_α radiation. These generated X-rays are then filtered, collimated and then made to incident on the specimen. While data is being collected, both the sample and the detector are rotated in a controlled manner, and the intensity of the diffracted beam is measured continuously. When the incident X-ray beam meets the geometric conditions of Bragg's law, constructive interference occurs, and a diffraction peak is observed. Then, this signal is detected by the detector after being converted into an electronic signal, and the information is sent to the acquisition system so it can be recognized and studied.

The diffractometer is set up so that the sample rotates through the path of the incoming collimated beam at an angle of θ. At the same time, the detector, which is positioned on an arm, moves through 2θ to follow the diffracted rays. The goniometer is the key mechanical component that maintains the right angle between the two parts, allowing for accurate diffraction measurements. It controls the exact alignment and movement. The schematic of a typical recorded diffraction pattern is shown in **Figure 2.2**. X-ray diffraction is a common technique for identifying the unknown crystalline phases, including minerals and many other inorganic compounds. Determining the composition of unknown substances is crucial in various fields, including geology, environmental science, materials science, engineering, and several branches of biology. XRD is useful for more than just identifying basic phases. It is especially useful for examining fine-grained materials, such as clays and mixed-layer clay minerals, which are typically difficult to distinguish with optical methods. The method also enables the determination of unit-cell parameters and provides insight into the overall purity of the sample.

Advanced analytical methods further enhance the utility of XRD. Rietveld refinement and other methods are used to examine the structure of a mixture closely and determine the number of different

crystal phases it contains. XRD can also be used to study thin films, determine the preferred orientation or texture in polycrystalline materials, and identify the prevalence of different mineral phases. These new applications make XRD a vital and valuable tool for modern research that requires knowledge of structure and composition.

2.3 UV-VIS-NIR Spectroscopy

Ultraviolet-Visible-Near-Infrared (UV-Vis-NIR) spectroscopy is a common and versatile analytical technique used to probe the optical and electronic properties of a broad range of technologically important materials. These materials commonly find applications in window coatings, protective layers, optical filters, and the pharmaceutical, food and beverage, and chemical industries. In general, this method involves measuring one or more parameters such as absorption, transmission, or reflection, over a selected portion of the electromagnetic spectrum to qualitatively assess the material's behaviour.

2.3.1 Absorbance Spectroscopy

Absorbance spectroscopy [102–106] [106-110], also known as spectrophotometry, is based on the principle that a sample absorbs ultraviolet or visible radiation at certain wavelengths. The resulting absorbance gives the idea of the composition and concentration of the chemical species present in the material. In the early stages of absorbance-based techniques, measurements relied on simple light sources, which used to be natural white light or artificial illumination, and the colour intensity of the sample was assessed directly by the human eye. As the method improved, visual observation was replaced by photometers and colourimeters, with the use of optical filters to restrict the measurements in specific spectral regions. Modern instruments have come a long way. Today, spectrophotometers are used to detect absorption. These instruments utilise monochromators or

wavelength selectors to separate and direct specific wavelengths of light to the sample.

2.3.1.1 Instrument Components for Absorption Measurements

Typically, an absorption measurement setup consists of five main components, which includes: (i) a radiant source that generates required intensity in the desired wavelength range; (ii) monochromator or wavelength selector, which selects a specific wavelength; (iii) sample holder; (iv) detector that measures the transmitted radiation; and (v) the display unit or the signal processor that converts the detected signal into the readable spectrum.

(i) Radiation Sources

For the UV region (180-350 nm), hydrogen or deuterium discharge lamps are generally used, which operate at low pressure. Between the anode and cathode, a mechanical aperture is used, which confines the discharge to a narrow path, ensuring the stable emission of the light. In the visible and NIR (Vis/NIR) regions, incandescent tungsten filament lamps are typically used. These consist of a tungsten coil sealed within a glass bulb under vacuum or filled with an inert gas, where radiation is produced as the filament is heated to incandescence. In the Mid-Infra-Red regions (MIR), globar and ceramic sources are used. The type of transition, whether molecular or electronic, will be determined by the source used for the spectroscopy measurements.

(ii) Wavelength Selector (Filters and Monochromators)

To select a specific wavelength region from the radiation source, wavelength selectors are used to create a narrow band of light. This specific wavelength region is isolated from the continuous spectral range using filters and monochromators, which are accompanied by dispersive devices, such as prisms or gratings.

(iii) Filters

A filter is made up of glass that has a particular colour and transmits the same colour of light that is incident on it, while absorbing the complementary colour of light. These types of filters are called absorption filters. Hence, the filter chosen is of the complementary colour of the colour that is transmitted by the sample itself. Hence, a filter that is of complementary colour is said to be best for the measurement. For example, for a blue-coloured solution, an orange-coloured filter, which is complementary to it in the VIBGYOR spectrum, must be used. In a transmittance versus wavelength plot, the response of the filter will be characterized by its Full Width at Half Maximum (FWHM) value, that is, the bandwidth of that spectrum. The narrower bandwidth (Dl) will make the filter better. For an extended range of the spectrum in the UV, visible, and infrared regions, interference filters are used, which have a wide range and an effective, narrower bandwidth, and offer better performance, possessing superior characteristics to absorption filters.

(iv) Monochromators

To obtain single-wavelength light (Monochromatic light) from white light, monochromators are used, which contain a dispersive element. A dispersive device breaks down light into its constituent wavelength components. Generally, prisms and diffraction gratings are used as the dispersive devices. The white light shining on the prism and the diffraction grating consists of light that gets reflected in VIBGYOR colours, as seen in rainbows. The desired colour or wavelength of light can be obtained by inserting a slit and rotating the prism or diffraction grating to a particular orientation. Diffraction Grating monochromators are used mostly in advanced spectrophotometers instead of prism monochromators. A monochromator mainly includes the entrance slit, a collimating mirror to form a parallel beam, a dispersive element (prism or grating) to disperse the light into the wavelength components, and a mirror camera to focus the dispersed light on the exit slit to extract the desired wavelength.

The smaller the wavelength band, the better the resolution. The resolution and bandwidth are defined as the peak width at half maximum (PWHM). The resolution of a monochromator is determined by the slit width. A larger slit width decreases the resolution, as more wavelengths than the desired ones enter the exit slit. Along with this, the diffraction grating has its own inherent resolution determined by the number of grooves per millimetre in that grating. Generally, in a spectrophotometer, the monochromator slit width is given by the resolution it has.

(v) Sample Compartment

In a single-beam spectrophotometer, after leaving the monochromator, the beam enters the sample compartment. In a dual-beam spectrophotometer, the beam is split into the two compartments. **Figure 2.3** shows the example of a dual-beam diffractometer.

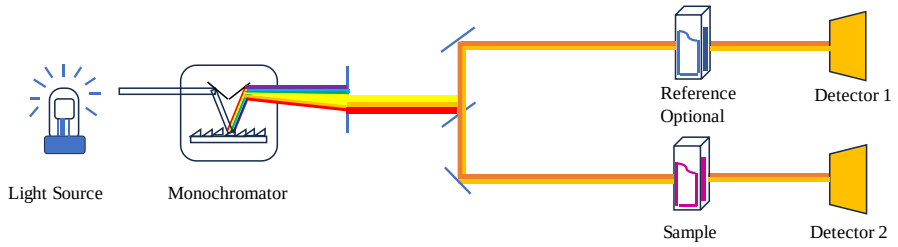

Figure. Schematic diagram of a double-beam optical system, with dual detectors.

Figure 2.3 Schematic diagram of a double-beam optical system, with dual detectors

(vi) Detectors

In most photometers, the output signal generated is linear with respect to transmission. This transmission signal is subsequently transformed into an equivalent absorbance value through either electrical or mechanical processing. In this setup, the detector functions as a transducer, converting one form of energy into another. At earlier stages, the photographic plate was used to detect the signal. Modern photoelectric detectors operate on the principle that incident photons are converted into electrical energy, generating a measurable flow of

electrons. This electron flow produces a current or voltage, which is then recorded as the analytical signal.

(a) Photoelectric Detectors

These detectors convert photon energy into an electric signal, encompassing both photovoltaic detectors and photoemissive devices.

(b) Photovoltaic Cell

These detectors are primarily used to detect the intensity of light in the visible region. The arrangement typically consists of a flat electrode, which is generally made of copper or iron, and acts as an anode. On top of this anode, a semiconducting layer made of selenium or cuprous oxide is deposited, which is then coated with a transparent film of gold, silver, or other materials, and protected by a transparent glass plate. A metal ring serves as the cathode material, positioned on the metallic film and connected to the galvanometer, with the other end connected to the anode. The current flows through the galvanometer when the photon intensity impinges on the cell and is directly proportional to the energy absorbed per unit time.

(c) Photoemissive Detectors

To detect very low-intensity signals and small variations in them, photomultiplier detectors are used in place of photovoltaic devices. In spectrophotometers, where the resolution of the detector is of prime concern, such detectors are used. The photoemissive detectors are of two main types:

(1) Vacuum Phototubes

A vacuum phototube is designed to contain two main electrodes, an anode and a photocathode. These are sealed inside an evacuated, clear, and transparent glass box. A photoemissive material is coated on the photocathode, which is based on alkali metals such as potassium or cesium and facilitates the efficient emission of electrons upon illumination. A phototube operates on the principle of the external photoelectric (photoemissive) effect, where photons strike a

photosensitive surface and eject electrons from it. Most of the time, these devices are completely evacuated; however, other versions may contain a low-pressure inert gas inside to enhance their performance characteristics.

The photocathode typically has a cylindrical shape and acts as the photosensitive element, while the anode collects the emitted electrons. The external voltage is applied during the operation such that the anode remains at a positive potential with respect to the cathode. The generated electric field between the electrodes accelerates the photoelectrons toward the electrode and results in a measurable amount of photocurrent. For vacuum tubes, the magnitude of this generated photocurrent shows a direct relation to the incident optical power and follows the relationship expressed below

$$I = S.P = \frac{\eta e}{h\nu}.P \tag{2.6}$$

where $h\nu$ is the photon energy, η represents the quantum efficiency, e is the electronic charge, and the quantity S is named as responsivity.

(2) Photomultiplier Tubes

Photomultiplier tubes, also known as photon multipliers, possess high sensitivity and a wider detection bandwidth in comparison to phototubes, due to the occurrence of the avalanche multiplication phenomenon. A photomultiplier tube (PMT) is made up of a series of functional elements that are enclosed in an evacuated glass envelope. When the incident photons strike the photocathode, where they are absorbed and release photoelectrons through the process of the photoelectric effect. These electrons are then accelerated by an applied high voltage, typically of the order of several hundred volts, towards the first dynode. These electrons, after striking, generate multiple secondary electrons that further strike other dynodes. This multiplication process continues sequentially across a cascade of dynodes, with the electron population increasing substantially at each stage. By the time the electrons reach the final dynode, the signal has undergone significant amplification, resulting in an enhanced photocurrent, which is ultimately

collected at the anode, positioned near the end of the dynode chain. **Figure 2.4a** and **b** show the cross-section and schematic of a photomultiplier tube, which can be understood as a combination of multiple phototubes arranged in a particular way.

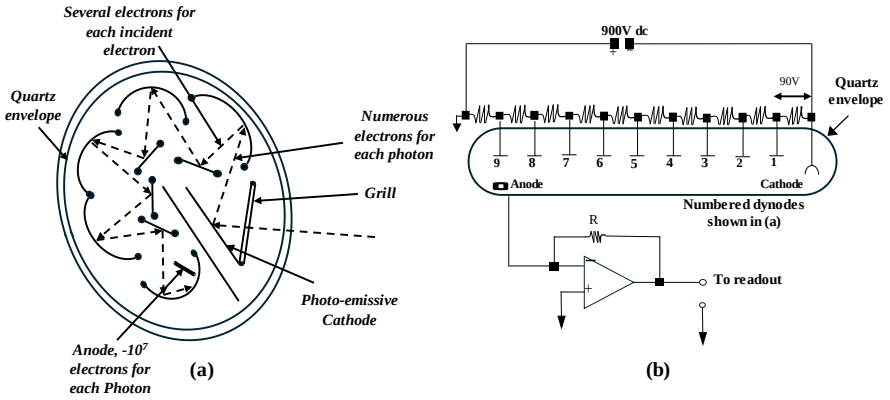

Figure 2.4a and **b** show the cross-section and schematic of a photomultiplier tube

In most molecules, electronic transitions from the ground state to vibrational levels of the first excited state occur within the UV-visible region. Lower-energy transitions between vibrational levels of the same electronic state results the infrared absorption. The internal energy of a molecule, in either its ground or excited electronic state, can be approximated as:

$$E_{\text{int}} = E_{\text{el}} + E_{\text{vib}} + E_{\text{rot}} \tag{2.7}$$

where the terms represent the electronic, vibrational, and rotational contributions, respectively. Absorption of a photon changes the electronic energy and simultaneously alters the vibrational and rotational states. Each vibronic transition therefore produces an absorption band; however, rotational structure remains usually unresolved in condensed phases due to extensive broadening.

Molecules absorbing in the 190-1000 nm range exhibit UV-Vis spectra. Quantitative absorption measurements follow the Beer-

Lambert-Bouguer law (Beer-Lambert Law), which measures the amount of light a sample absorbs at a specific wavelength and is given by

$$A = -\log_{10}(I_t/I_i) = \varepsilon\, c\, d \qquad (2.8)$$

Here, A gives the absorbance of the material. I_t and I_i are the transmitted and incident radiant powers, ε is the molar absorption coefficient, c is the concentration, and d is the optical path length.

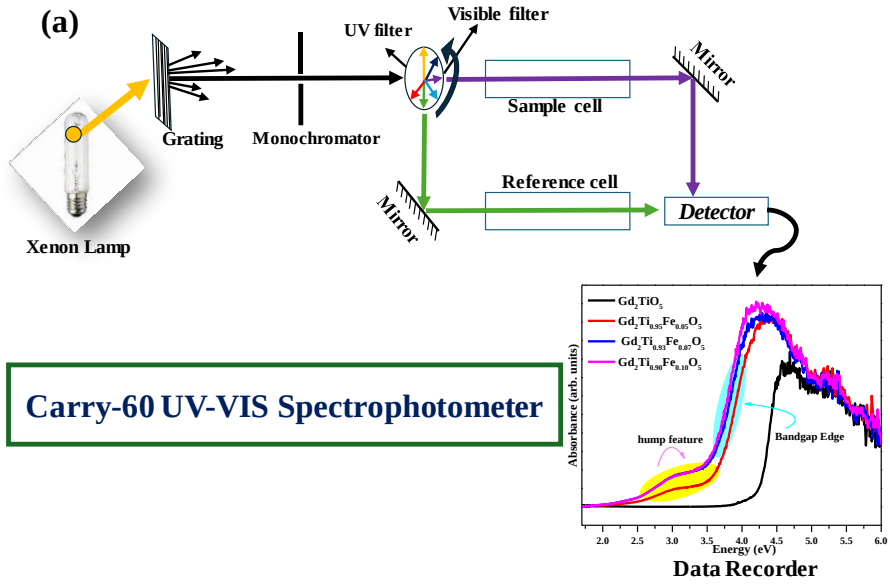

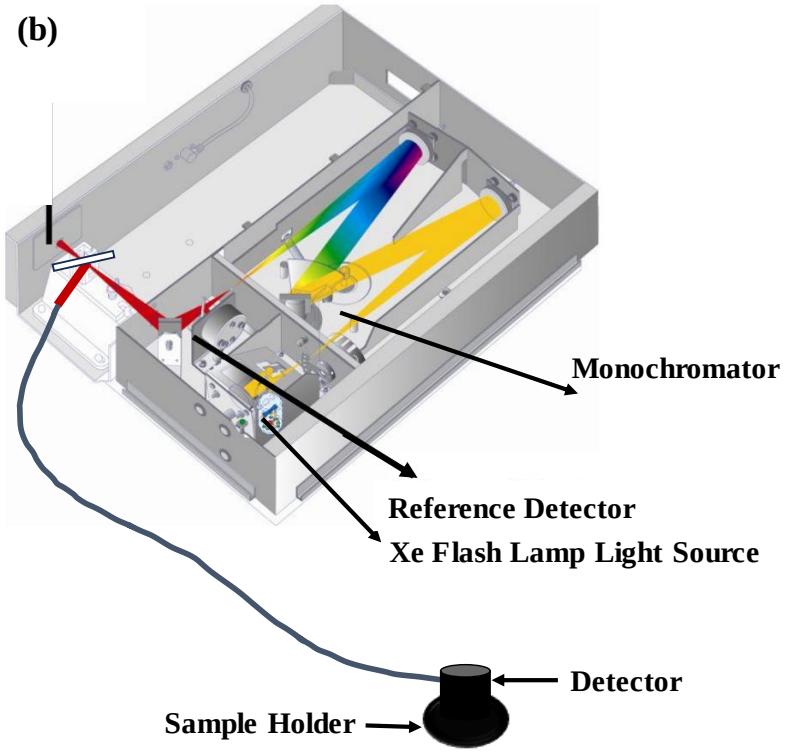

Figure 2.5a shows the schematic of a typical UV-VIS-NIR spectrophotometer, and **b** representative depiction of the internal assembly of the commercial UV-vis spectrophotometer used in the present research work

The schematic exhibiting the operation of a typical UV-VIS-NIR spectrophotometer is shown in **Figure 2.5a**. In the current research work, diffuse reflectance spectroscopic measurements have been performed using a commercial spectrophotometer, as shown in **Figure 2.5b**. The diffuse reflected spectra are collected using the diffuse reflectance assembly (DRA) with the help of the optical fibre cable.

2.3.2 Transmission Spectroscopy

Transmission spectroscopy is closely related to absorption spectroscopy and can be applied to a variety of samples in the solid, liquid, or gaseous form. In this technique, the intensity of light that passes through a sample is compared with the intensity of the incident

beam. The transmitted spectrum is influenced by several factors, including the optical path length, the material's absorption coefficient and reflectivity, the angle and polarization of the incoming radiation, and, when particulates are present, their size and orientation. In the Beer-Lambert law, the ratio I_t/I_i represents transmittance. The experimental configuration used for transmission measurements is therefore very similar to that used in the conventional absorption spectroscopy technique.

2.3.3 Reflectance Spectroscopy

Reflectance spectroscopy measures how light, across different wavelengths, is returned from the surface of a solid, liquid, or gas. When photons interact with a mineral or material surface, a portion of the incident light is immediately reflected, some penetrate the grains, and others are absorbed. Photons that are redirected either by surface reflection or by refraction within individual particles are collectively referred to as scattered light. These scattered photons may undergo further interactions with neighbouring grains or escape the surface, where they can be detected and analyzed accordingly.

2.3.3.1 External Reflectance Spectroscopy

This technique is a non-destructive method, where light reflected from a smooth surface (a Mirror-like surface) is noted and measured; accordingly, hence, this technique is also known as specular reflectance. This technique is primarily used for measuring film thickness and refractive indices, as well as investigating the spectra of thin films. The reflection spectra obtained in this technique differs from the transmission spectra in the sense that their spectral contrast doesn't depend on the sample thickness linearly, and bands get shifted a little to higher energies.

2.3.3.2 Internal Reflectance Spectroscopy

In the Internal Reflection Spectroscopy (IRS), light enters a prism at an angle greater than the critical angle, generating an evanescent field at the interface. When a sample is placed in contact with this surface, the evanescent wave interacts with it, allowing a spectrum to be obtained with minimal sample preparation. IRS is also a non-destructive method suitable for solids, liquids, and powders. Thin films typically produce spectra like those obtained from transmission measurements, while thicker films exhibit stronger absorption features at longer wavelengths. As the incident angle approaches the critical angle, absorption bands broaden toward lower wavenumbers and shift to longer wavelengths, with dispersion-like features that appear near or below the critical angle.

2.3.3.3 Diffuse Reflectance Spectroscopy

Diffuse reflectance spectroscopy is used to measure the absorbance of powder samples and rough surfaces by recording the scattered light from the sample's surface using suitable optical instrumentation. The spectra collected in the DR Spectroscopy provide information of transmission, internal, and external reflection. In diffuse reflection, a collimated light beam strikes a rough or matte surface, causing the light to be redistributed uniformly in all directions. This differs from specular reflection, which occurs on a polished surface. **Figure 2.6** depicts the phenomenon of specular and diffuse reflectance occurring on a sample surface. Techniques based on regular reflection, such as ATR and IRRAS, also rely on the reflected light, but they operate under different optical conditions.

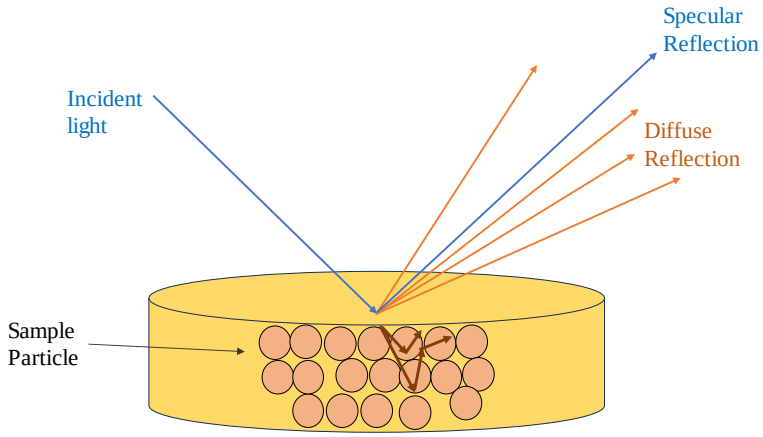

Figure. Schematic figure showing specular and diffuse reflectance occurring on the sample surface when a light beam shines over it.

Figure 2.6 Schematic figure shows the specular and diffuse reflectance occurring on the sample surface after the shining of an incident light beam

In DR measurements across the mid-infrared and UV/Vis/NIR regions, the reflected light is assumed to be isotropically scattered. This condition is satisfied when the sample consists of large, randomly oriented particles and when multiple reflections, refractions, and diffractions occur within the densely packed surface of the powder. For smaller particles also, where single-particle scattering would be anisotropic, compact fine powders produce near-isotropic diffuse scattering due to the repeated scattering events. For the sufficiently thick layers, no light is transmitted through it.

The absorption features of the material modify the spectrum of the diffusely reflected radiation. The diffuse reflectance, R, is defined as the ratio of the reflected flux J to the incident flux I. Recording R as a function of wavelength or wavenumber yields the reflectance spectrum. Like the transmission spectroscopy, it is common to plot $\log(1/R)$, referred to as the 'apparent absorbance,' to represent the absorption behaviour of the sample.

2.3.3.4 Kubelka-Munk Theory and Measurement of Absorption Spectra

According to Kubelka-Munk theory [108, 111–114], the measured diffuse reflectance, R, depends on the *ratio* of a material's absorption and scattering coefficients, and not on their absolute magnitudes. Hence, R itself is not directly proportional to the concentration of the absorbing species. Under specific measurement conditions, however, the Kubelka-Munk or 'remission' function, $F(R_\infty)$, enables these contributions to be separated:

$$\frac{K_\lambda}{S_\lambda} = \frac{(1-R_\infty)^2}{2R_\infty} \equiv F(R_\infty) \tag{2.9}$$

Here, R_∞ denotes the diffuse reflectance of an optically thick layer, K_λ is the absorption coefficient, and S_λ represents the scattering coefficient. Achieving the R_∞ condition depends on the material's optical properties, particle packing, and the wavelength of illumination. In diffuse reflectance spectroscopy, the reflectance of the sample, $R_{\infty,\text{sample}}$, is typically measured relative to a reference white standard using a double-beam spectrometer. The recorded value,

$$R'_\infty = \frac{R_{\infty,\text{sample}}}{R_{\infty,\text{standard}}}, \tag{2.10}$$

equals the absolute reflectance only when the standard behaves ideally ($R_{\infty,\text{standard}} = 1$). In practice, real standards deviate from this ideal because their scattering and absorption properties vary with wavelength.

A standard material reflects almost all the wavelengths of the region in which the absorption occurs. Some suitable standard materials include $BaSO_4$, Halon, and Teflon. For powdered and pellet samples, which possess a smaller grain size, it is assumed that the incident light diffuses uniformly in the sample; hence, the scattering is almost constant in this case. Thus, the K-M function becomes proportional to the absorption coefficient in such sample materials, and is written as

$$(R_\infty) \propto \acute{\alpha} \tag{2.11}$$

Here, $\acute{\alpha}$ is the energy of the absorption coefficient of the material. Hence, in the research work presented here, the evaluation of the absorption coefficient is noted with respect to the incident wavelength/energy, which has been studied in terms of the K-M function.

2.4 Raman Spectroscopy

2.4.1 Introduction

Raman spectroscopy is a versatile and non-destructive technique used to obtain descriptive information about the vibrational and bonding behaviour of a material, thereby providing detailed chemical information about the material's structure and composition. In Raman spectroscopy, the sample is illuminated with monochromatic light (usually laser light) in the visible and near-infrared regions [115–118]. During laser illumination, the maximum amount of light is scattered without any loss of energy, which does not provide detailed information about the material. This phenomenon is known as Rayleigh scattering. A small portion of the light scattered gains or loses some energy to molecular vibrations, which are reflected in the change of wavelength (colour) of these vibrations. The scattering effect that occurs is called Raman scattering and is also known as the Raman effect. Raman spectroscopy provides the chemical fingerprint of the molecule by generating information about the molecular vibrations, the material's composition and its structure. It is a highly sensitive spectroscopic technique that provides detailed, unique information about the sharp peaks observed in the Raman spectra, which correspond to a particular molecular vibration and can reveal information about the concentration, identity, phase, polymorphic properties, and morphological characteristics of the material.

2.4.2 Raman Scattering

In the Raman scattering process, the energy and the direction of the incident photon change after the scattering process. Whenever the light interacts with the matter, three main phenomena occur: absorption, transmission, and reflection. However, a portion of the light is scattered back, which includes the components of Rayleigh, Stokes, and Anti-Stokes Raman scattering lines. The scattering processes could be elastic or inelastic. In elastic processes, the energy (or the wavelength) of the scattered light remains the same, whereas in inelastic processes, the energy changes after scattering from the original one. Rayleigh scattering is elastic scattering, whereas Stokes and anti-Stokes Raman scattering come under the inelastic scattering processes. **Figure 2.7** illustrates the three Raman scattering processes. In Raman-Stokes scattering, the interaction of the photon with the material results in the excitation of the photon to a higher energy state, known as a virtual state. After this excitation, the material relaxes back to one of the higher vibrational energy states. Throughout the process, the material gains energy from the incident photon; hence, the scattered photon possesses lower energy. This scattering process is known as Stokes Raman scattering, resulting in longer-wavelength photons. On the other hand, Raman anti-Stokes scattering occurs when a molecule already exists in a higher vibrational energy state; it then interacts with the photon and transitions to a virtual state. After this, the molecule relaxes back to a level having low vibrational energy, and hence, the photon in this scattering process gains energy with decreased frequency or wavelength. **Figure 2.8** illustrates the transitions corresponding to Rayleigh, Stokes and anti-Stokes Raman scattering lines. In the Raman application, we generally observe the Stokes lines, as anti-Stokes lines are weaker, which depends on the population of the molecule being in the higher energy vibrational state. For a material to exhibit the Raman effect, it must be Raman active, meaning that its vibrational modes must follow certain selection rules. Even when this condition is satisfied, the number of Raman-scattered photons generated is extremely low, making their

detection challenging against the overwhelmingly larger population of incident photons and the strong elastic scattering background (Rayleigh scattering). Rayleigh-scattered photons retain the same wavelength as the excitation laser, where optical filters are used to selectively remove those photons. This prevents the suppression of the weaker Raman signals.

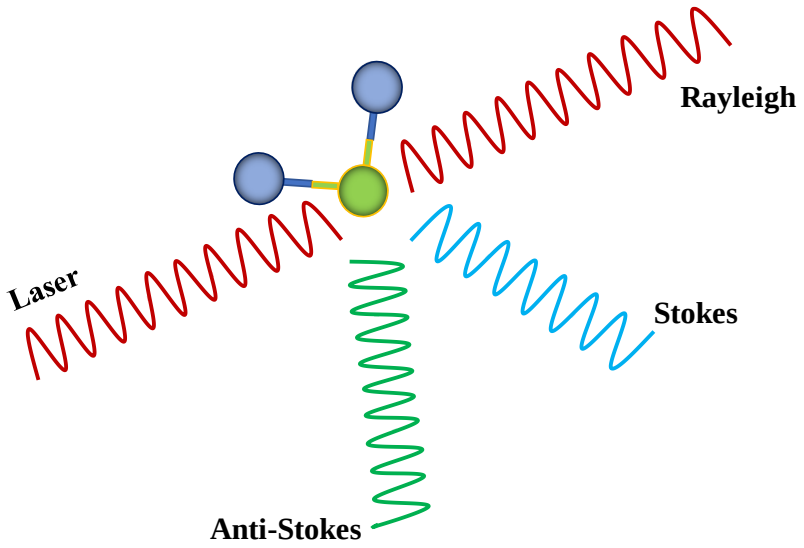

Figure 2.7 Raman scattering exhibiting three types of processes resulting from the interaction of the light with the molecule

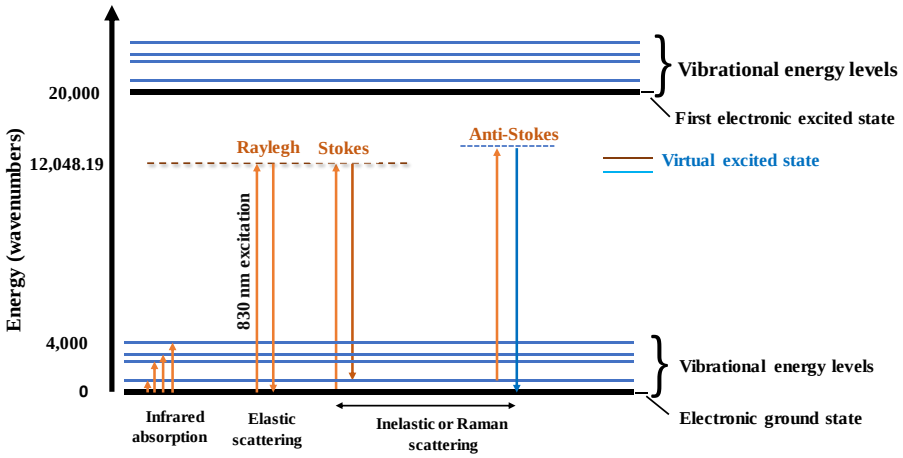

Figure 2.8 Schematic representation of the Raman scattering phenomenon

In contrast to infrared spectroscopy, where vibrational modes become active only if they involve a change in dipole moment. Whereas Raman spectroscopy requires a change in the molecule's polarizability, essentially a change in the distribution or distortion of its electron cloud during vibration. Vibrational modes that induce such variations in polarizability can undergo inelastic scattering, producing measurable Raman shifts. Each feature in a Raman spectrum corresponds to a distinct molecular vibrational mode, although the relative intensities of these peaks can vary widely. In general, vibrational modes that are associated with homonuclear bonds, such as C─C and C═C, tend to generate stronger Raman responses because they more readily modify polarizability. Conversely, vibrations involving more polar bonds like C─O or O─H often appear weaker in the Raman spectrum. However, molecular symmetry can significantly influence these trends, and in some cases, highly symmetric polar groups, such as phosphate units, can also produce intense Raman bands. In the present research work, a commercial high-resolution dispersive spectrometer has been used, which consists of excitation sources of two solid-state lasers having excitation wavelengths of 532 nm and 785nm, and a Helium-Neon gas laser of 633 nm excitation wavelength. A representative diagram of a typical Raman spectrophotometer [117, 118] is shown in **Figure 2.9**.

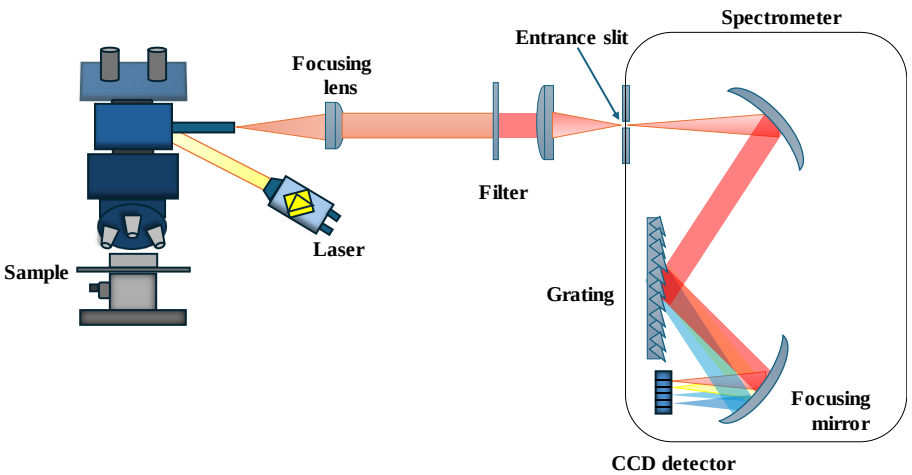

Figure 2.9 Schematic representation of a typical Raman Spectrometer

2.4.3 Classical Theory of Raman Scattering

In the classical picture, molecules are considered to be an ensemble of atoms exhibiting simple harmonic vibrations, without having quantization of energy levels. In the classical picture, the electromagnetic field changes the electric dipole moment of the molecule or the solid. Such an induced dipole moment possesses the frequency of the oscillation as that of the incident wave. The incoming incident light possesses a time-dependent oscillating electric field, which is given as

$$\vec{E} = \overrightarrow{E_0} \cos \omega_i t \qquad (2.12)$$

Where E_0 represents the amplitude, and ω_i gives the angular frequency of the incident oscillating electric field. This oscillating electric field induces a dipole moment, which is given by

$$\mu = \rho E \qquad 2.13$$

Here, ρ is the proportional quantity, represents the induced polarizability of the molecule, and represents a tensor quantity of second order rank given by the equation below

$$\begin{array}{llll} \mu_x = & \rho_{xx}E & \rho_{xy}E & \rho_{xz}E \\ \mu_y = & \rho_{yx}E & \rho_{yy}E & \rho_{yz}E \\ \mu_z = & \rho_{zx}E & \rho_{zy}E & \rho_{zz}E \end{array} \qquad (2.14)$$

From these relations, it becomes evident that the three cartesian components of the electromagnetic field interact with the nine independent components of the polarizability tensor, which gives rise to the three corresponding components of the induced dipole moment. However, in most cases, ρ is a symmetric tensor, hence there lefts only six independent elements of the polarizability tensor. Let's consider first that the incident light is polarized in the x-direction and induces a dipole moment only in the x-direction, then the above equation reduces to

$$\mu_x = \quad \rho_{xx}E \qquad (2.15)$$

In the simplest form, the above equation can be rewritten as

$$\vec{\mu} = \rho\vec{E} \tag{2.16}$$

Now, substituting the expression of the electric field from equation 1 in the above equation, we get

$$\mu = \rho E_0 \cos \omega_i t \tag{2.17}$$

Here, the electric field is assumed to oscillate along the x-axis, which induces a dipole moment in the same direction. Classical electrodynamics states that an oscillating dipole radiates at the same frequency as its own frequency of oscillation. Therefore, if the molecular polarizability ρ remains constant with time, the induced dipole will simply reradiate light at the incident angular frequency ω_i, which gives rise to the Rayleigh scattering.

If the polarizability ρ includes the components that vary with the vibrational motion of the molecule, these fluctuations introduce a change in the incident electromagnetic field. As a result of this time-dependent polarizability associated with molecular vibrations, additional frequency components, which are shifted relative to the excitation frequency, appear in the scattered light. For the mathematical representation of a specific vibrational mode or lattice oscillation, it is typically modelled as a harmonic oscillator of angular frequency ω_r, whose time-dependent amplitude is expressed by the relation,

$$Q = Q_0 \cos \omega_r t \tag{2.18}$$

For the small amplitude of vibration, expanding the polarizability in the Taylor series expansion around the equilibrium ($Q = 0$), then the polarizability can be written as

$$\rho = \rho\{Q\} = \rho_0 + \left\{\frac{\delta\rho}{\delta Q}\right\}_0 Q + \cdots ... \tag{2.19}$$

If we consider the terms only up to first order, and combine equations 6,7, and 8, then we get the equation 9 as

$$\mu = \left[\rho_0 + \left\{\frac{\delta\rho}{\delta Q}\right\}_0 Q_0 \cos\omega_r t\right] E_0 \cos\omega_i t \ldots\ldots \quad (2.20)$$

$$\mu = \rho_0 E_0 \cos\omega_i t + \left\{\frac{\delta\rho}{\delta Q}\right\}_0 Q_0 \cos\omega_r t * E_0 \cos\omega_i t \quad (2.21)$$

$$\mu = \rho_0 E_0 \cos\omega_i t + \frac{1}{2}\left\{\frac{\delta\rho}{\delta Q}\right\}_0 Q_0 E_0 \cos\{\omega_r - \omega_i\}t + \frac{1}{2}\left\{\frac{\delta\rho}{\delta Q}\right\}_0 Q_0 E_0 \cos\{\omega_r + \omega_i\}t \quad (2.22)$$

The above equation (equation 11) signifies that incident light will be scattered into its parts. The first term will contain the coherent Rayleigh Raman scattering, where there will not be any change in the phase, and the frequency of the scattered light, and the phenomenon will occur in all types of substances. There will be a change in the frequency and energy of the second and third term, which represents the Raman scattering term. The lower-frequency terms represent Stokes Raman scattering, giving rise to Raman Stokes lines, and the higher-frequency terms give rise to anti-Stokes Raman scattering, which will give the anti-Stokes Raman lines in the spectrum, as shown in **Figure 2.8**.

2.4.4 Quantum Theory of Raman Scattering

2.4.4.1 Vibrational Raman Spectra

In the quantum theory, Raman Scattering can be understood in terms of the collision between the incident light beam and the molecules of the sample material. After the collision, the energy of the molecules will get changed and new energy state will follow the law of conservation of energy, hence it can be written as

$$E_\alpha + \frac{1}{2}mv^2 + h\nu = E_{\alpha^\star} + \frac{1}{2}mv^{\star 2} + h\nu^\star \quad (2.23)$$

where, $E_\alpha, v, and\ \nu$ are the energy, velocity, and frequency of the molecule before the collision, and the $E_{\alpha^\star}, v^\star, and\ \nu^\star$ represents these

quantities after the collision, respectively. By neglecting the change in the velocity of the molecule, above equation can be written as

$$E_\alpha + h\nu = E_{\alpha^\star} + h\nu^\star \tag{2.24}$$

$$\upsilon^\star = \frac{\upsilon + (E_\alpha - E_{\alpha^\star})}{h} \tag{2.25}$$

$$\upsilon^\star = \upsilon + \Delta\upsilon \tag{2.26}$$

$$\upsilon^\star - \upsilon = \pm\, \upsilon_c \approx \Delta\upsilon \tag{2.27}$$

Now, from above equations, it can be concluded that

1) For $E_\alpha = E_{\alpha^\star}$, frequency difference is zero here (No Raman Shift), which means that the collision is elastic as there is no change in the kinetic energy. This case corresponds to the Rayleigh Raman scattering.

2) $E_\alpha > E_{\alpha^\star}$ ($\upsilon^\star > \upsilon$), which means the molecule already existed in the excited state and after collision the energy was lessen to the incident photon. Hence the photon energy increases after collision which corresponds to the Anti-Stokes Raman scattering.

3) $E_\alpha < E_{\alpha^\star}$ ($\upsilon^\star < \upsilon$), which means molecules gains some energy from the incident photon and hence the scattered photon will have less energy after the collision, hence corresponds to the Stokes Raman lines.

2.4.4.2 Pure Rotational Raman Spectra

A rigid rotator is considered to have the energy given by

$$E_r = \frac{h^2}{8\pi^2 I_c} I(I+1) \tag{2.28}$$

where I_c is the moment of inertia of the molecule. The following selection rule are followed in the rotational Raman spectrum,

$$\Delta I = 0, \mp 2$$

where, $\Delta I = 0$ will give rise to the scattered Raman radiation of the same energy (frequency) and hence will correspond to Rayleigh-Raman scattering.

$\Delta I = +2$, will correspond to the Stokes' Raman lines (lower frequency)

$\Delta I = -2$, corresponds to the anti-Stokes Raman lines (higher frequency)

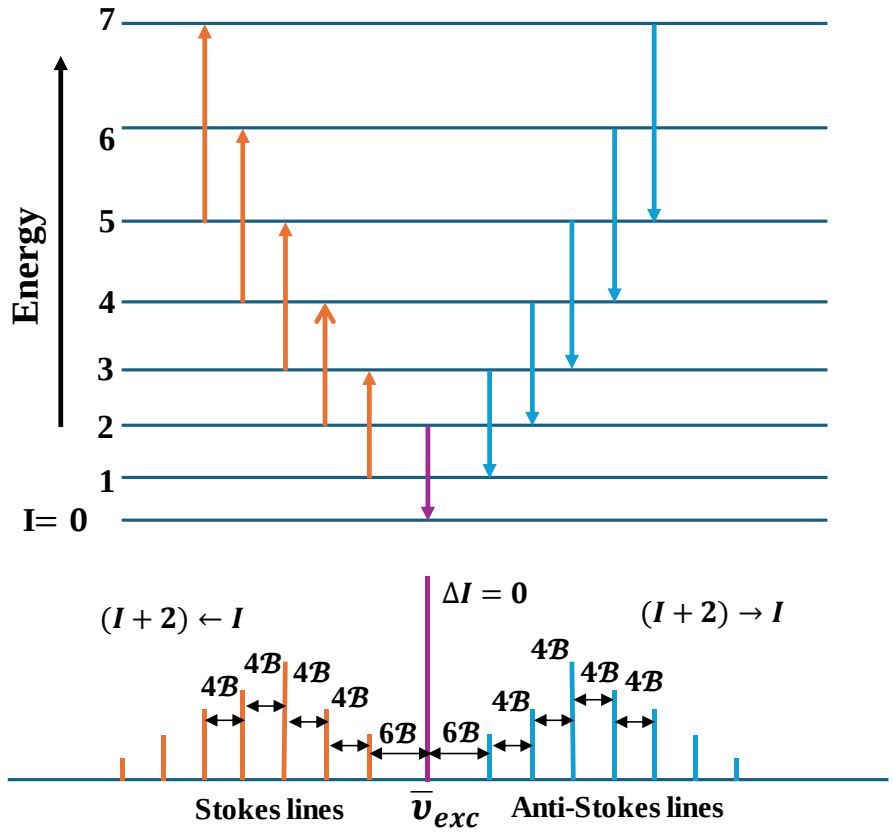

Figure 2.10 Schematic shows the representation of rotational Raman Spectra

The rotational Raman shift corresponding to the $\Delta I = +2$ will give Raman Anti-Stokes lines and is represented by

$$\Delta\bar{\nu} = \frac{h^2}{8\pi^2 I_c}[(I+2)(I+3) - (I+1)] \qquad (2.29)$$

$$\Delta\bar{\nu} = 2B(2I+3) \qquad (2.30)$$

Here,

$$\mathrm{B} = \frac{h^2}{8\pi^2 I_c} \tag{2.31}$$

The rotational Raman shift corresponding to the $\Delta I = -2$ gives Stokes Raman lines and is represented as

$$\Delta\bar{\nu} = 2B(2I + 3) \tag{2.32}$$

By combining both the above equations, Ramn Shift is reprinted by

$$\Delta\bar{\nu} = \mp 2B(2I + 3),\ I = 0,1,2,3, \ldots \tag{2.33}$$

Raman Shift in terms of wavenumber is given by

$$\Delta\bar{\nu} = \bar{\nu_s} - \overline{\nu_{as}} \tag{2.34}$$

Here, $\bar{\nu_s}$ represents the wavenumber of the exciting radiation, and $\overline{\nu_{as}}$ corresponds to the wavenumber of the scattered radiation. The corresponding obtained rotational Raman spectra is shown in the **Figure 2.10**. Hence, from the information of the Raman shifts, the lattice dynamics of the system can be understood, which provides fundamental insights into the structural dynamics of the system.

Chapter 3

Influence of Fe substitution on the structural and optical properties of Gd_2TiO_5 ceramic

Subtle variations in metal-oxygen bond lengths play a pivotal role in shaping the electronic band structure of oxide materials by regulating orbital interactions within the lattice. In the present study, this structure-property interplay is experimentally demonstrated for Gd_2TiO_5, an example of a mixed seven- and five-fold coordination lanthanide titanate system. Precise structural insights obtained from the Rietveld refinement, along with optical absorption measurements, reveal that changes in the local bonding geometry systematically influence the band gap through modifications in titanium (d)-oxygen(p) hybridization. These findings highlight the effectiveness of combining the structural refinement and optical absorption spectroscopy as accessible experimental tools for uncovering bond length-dependent electronic behavior and emphasize the potential of bond length control as a viable route for band gap engineering in complex oxide materials.

3.1 Introduction

Rare-earth titanates, specifically lanthanide titanates, which are part of the R_2O_3-TiO_2 (R is a rare-earth element) binary system with complex compositions, exhibit interesting physical, structural, and chemical properties [37, 119, 120]. Due to their ability to withstand high thermal and chemical resistance against radiation damage, caused by

high-energy particles, these complex oxide materials find wide applications in the nuclear, radiation industry [37, 68, 121–123] and are used for the geological disposal of high-level radioactive waste [124, 125], which includes high radioactive elements like Plutonium, Neptunium, and other minor actinides. Complex oxides in this category include perovskites ($RTiO_3$), pyrochlore structures ($R_2Ti_2O_7$) [6, 123, 126], δ-phase ($R_4Ti_3O_{12}$) compounds, lanthanide-rich titanates ($Ln_4Ti_9O_{24}$, $Ln_2Ti_3O_9$). In this category, perovskite and pyrochlore structures have been rigorously studied by researchers due to their enormous technological applications in the fields of optics and the nuclear industry [6, 127–129].

In this category, perovskites and pyrochlores ($Ln_2Ti_2O_7$) have been previously studied by researchers due to their numerous technological applications in the fields of optics and the nuclear industry. Additionally, in all of the above compositions, Ti exists in a sixfold coordination geometry and forms the corner-sharing octahedral network. In this ternary Ln-Ti-O phase system category, a unique crystal structure of A_2BO_5/R_2TiO_5 (where R is the lanthanide or Y, Sc; B = tetravalent or pentavalent transition metal or group 14 element) was found to emerge, as reported by Mumme et al. [41, 130], where Ti^{+4} was found to possess five-fold coordination with an off-centred square pyramid geometry, forming a TiO_5 polyhedron. The rare-earth cation R^{3+} or Ln^{3+} is coordinated with seven oxygen atoms and crystallizes into the RO_7 polyhedron, which is also a quite unusual coordination number as seen in conventional perovskite and other oxide structures containing a Titanium atom. Almost all the lanthanide elements, starting from lanthanum to Lutetium and including yttrium, crystallize into the same composition of R_2TiO_5 [28, 130]. Hence, the composition R_2TiO_5/Ln_2TiO_5 exhibits a unique structural chemistry, characterized by a rare combination of coordination numbers of five and seven, which are rarely observed in nature [131]. A notable point is that all these rare-earth titanates of Ln_2TiO_5 composition exhibit interesting polymorphic properties [19, 34, 75, 132], whereby they transform into different

phases corresponding to changes in temperature, pressure [42], and the size of the rare-earth cation atom [132]. For example, the orthorhombic structures of Ln_2TiO_5, where Ln is Sm, Tb, and Dy, transform to hexagonal polymorphs at temperatures above 1300 °C. Lanthanides titanates having an ionic radius less than of Ho transform to the cubic pyrochlore structure, which possesses antisite defects. In general, titanates having rare-earth A-site cations of larger size, i.e., lighter elements (Ln = La-Sm), exist in the orthorhombic phase at all temperature ranges. The rare-earth cations with a smaller A-site cation radius (Er-Lu, Sc) exhibit the cubic phase [19, 34, 133]. The Ln_2TiO_5 compounds, having intermediate lanthanide elements (Ln = Eu-Ho and Y), are found to exist in the orthorhombic phase [28, 34] at low temperatures, exhibit a symmetric hexagonal polymorph ($P6_3/mmc$ space group) at intermediate temperature ranges, and at higher temperatures, the cubic phase exists with partial cation disordering [121]. These thermally driven transformations occur around a particular temperature, described as an order-disorder transformation temperature [74]. For Gd_2TiO_5, the polymorphic transformation occurs from the orthorhombic phase to the hexagonal phase [74, 133, 134] around the temperature of 1700 °C, and then it melts around the temperature of 1790 °C. Similarly, Dy_2TiO_5 exhibits two reversible polymorphic transformations: from the Orthorhombic to the Hexagonal phase at 1370 °C, and then transforms to the Cubic Phase at 1680 °C. At room temperature, Gd_2TiO_5 was found to exist in the orthorhombic phase with the *Pnam* space group [26, 28], where the Gd-atom cation forms a monocapped octahedron, surrounded by seven oxygen atoms, and the resulting geometry is referred to as the capped trigonal prismatic molecular geometry. The Ti atom is coordinated with five oxygen atoms and forms a TiO_5 polyhedron, and hence forms a distorted square pyramidal geometry [74]. Now, most of the titanium-based binary rare-earth oxides and other conventional oxides having the titanium atom are found to exist mostly in the tetrahedral geometry or the octahedral geometry surrounded by six oxygen anions. As it is well known that in the case of transition metal oxides, the crystal field splitting results in

the lifting of the degeneracy of the 3*d* orbitals of the transition metal ion, which results in a threefold degenerate t_{2g} level at the lower energy state and a twofold degenerate e_g, energy level at a slightly higher state [135]. Now, this is true only in the case of an octahedral geometrical cage. In the case of the tetrahedral systems, the doubly degenerate e_g states, states occupy the lower energy as compared to the triply degenerate t_{2g} states. Thus, the structural geometry of the compound plays a very significant role in deciding the crystal field splitting in transition metal oxides. In materials such as Ln_2TiO_5 (Ln = La, Pr, Nd, Sm, Gd, and Dy), the Ti atom is surrounded by five oxygen anions in a square pyramidal geometry, a very rare case seen in Ti-bonded compounds [131, 136]. Hence, one may expect a different behavior of the crystal field and thus splitting in these rare-earth titanates, which are further expected to modify the electronic, optical, and other properties of the material. Keeping this in mind, the present study aims to investigate the effect of Fe substitution at the Ti-site in parent Gd_2TiO_5 on the optical properties of these compounds. To further explore and understand the observed results, ab initio calculations were carried out using Density Functional Theory.

3.2 Experimental Section

The polycrystalline powder samples of Gd_2TiO_5 have been synthesized using the conventional solid-state reaction method [91, 95]. The stoichiometric amounts of gadolinium oxide (Gd_2O_3) and titanium oxide (TiO_2), with a phase purity of 99.99%, were used as precursors. They were then mixed thoroughly and ground in an agate mortar pestle in isopropyl alcohol for at least four hours. For the synthesis of Fe-substituted Gd_2TiO_5 series, Iron oxide (Fe_3O_4), with 99.99% phase purity, was taken in the stoichiometric amount and ground along with the above precursor materials to form the composition of $Gd_2Fe_xTi_{1-x}O_5$. The powder samples with Fe percentages of x = 0.05, 0.07, and 0.10 were nomenclated as Fe5% GTO, Fe7% GTO, and Fe10% GTO,

respectively. The grounded powder samples were then calcined at 1300 °C for 24 h with intermediate grinding and heat treatments of 1000 °C and 1250 °C in the muffle furnace. The final sintering process was carried out at 1350 °C.

3.2.1 X-ray Diffraction Analysis

The X-ray diffraction (XRD) measurements [26] were performed on the sample series using the Bruker D8 diffractometer equipped with a Cu-target of Kα wavelength of 1.5405 Å. The operating voltage and the current of the diffractometer were set to be 40 kV and 40 mA, respectively. The XRD data were collected in the angular range of 2θ varied from 10° to 90° with a step size of 0.02°. For the crystallographic and structural parameter information, Rietveld refinement was performed on all the series samples using the FullProf Software [137–139]. Refinement was carried out considering the orthorhombic [25, 28, 140–142]and the *Pnam* space group of the samples. For fitting the peaks, the pseudo-Voigt function was used with the 6-polynomial background method. For further extraction of structural information, including lattice parameters, bond lengths, and bond angles, the VESTA (Visualization for Electronic and Structural Analysis) software has been utilized [143–145].

3.2.2 Optical Absorption Spectroscopy

The optical absorption spectra [146] of parent and Fe-substituted samples were taken at room temperature using the high-precision UV–Vis diffuse reflectance spectrophotometer [147–149]. Data was collected in the diffuse reflectance mode [106, 109, 150–152] in the wavelength range of 200-900 nm. The detailed analysis of diffuse reflectance spectroscopy (DRS) has been discussed in Chapter 2.

3.2.3 First-Principles (ab-initio) Calculations

The first-principles calculations were conducted using the Quantum Espresso (QE) software [153], specifically employing the plane-wave self-consistent field (PWscf) method [154]. Heyd–Scuseria–Ernzerhof (HSE06), a popular and trustworthy hybrid functional [155–157] was employed for all calculations with the mixing parameter (α') set at 25%, and its screening parameter was set at 0.2 $Å^{-1}$. The exchange-correlation energy is calculated as;

$$E_{XC}^{HSE} = a¢E_X^{HF,SR} + (1 - a¢)E_X^{PBE,SR} + E_X^{PBE,LR} + E_C^{PBE} \quad (3.1)$$

where, $a¢E_X^{HF,SR}$, $E_X^{PBE,SR}$ and $E_X^{PBE,LR}$ are short- and long-range HF and PBE exchange functionals, and E_C^{PBE} shows the PBE correlation energy. α'represents the HF mixing constant using the perturbation theory. A k-mesh with dimensions of 7 × 7 × 7 was used in the first Brillouin zone for both pristine and doped structures. Self-consistent calculations were used with an energy convergence value of 2×10^{-6} eV, and forces per atom were reduced to 0.05 eV [158999].

3.3 Results and Discussion

3.3.1 X-ray Diffraction and Rietveld Refinement Analysis

The X-ray diffraction measurements were carried out on the synthesized samples of Fe-substituted Gd_2TiO_5 ($Gd_2Ti_{1-x}Fe_xO_5$, x = 0.05, 0.07, and 0.10) to check the phase purity and structural characterization. The XRD pattern of all the prepared samples is shown in **Figure 3.1**. As can be seen from the diffraction pattern, no extra impurity peak has been observed in the analyzed 2θ range of 10-90 degrees. Hence, all the samples were found to be in a single phase. The results agreed with the previous literature results of Gd_2TiO_5 and Ln_2TiO_5 series and suggested that Gd_2TiO_5 exists in the orthorhombic phase with the *Pnam* [25] space group (number 62) at room temperature. From the inset of **Figure 3.1**, it can be seen that the 2θ values are shifting

to lower values, indicating an expansion of the system with Fe substitution. This is expected, as the substitution of larger ionic radii of Fe (0.585 Å) at the Ti site (the ionic radius of Ti^{+4} is 0.51 Å) will tend to increase the lattice parameters, resulting in the elongation of the unit cell.

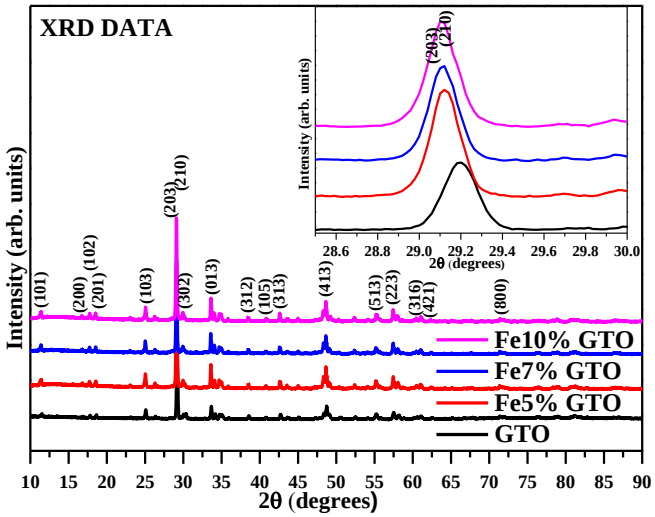

Figure 3.1 X-ray diffraction data of pure and Fe-substituted Gd_2TiO_5. The inset shows the peak shift in the direction of the decrease in the diffraction angle with Fe-substitution in the sample

For further extraction of crystallographic and structural information from the crystal structure, refinement was performed on all samples using the FullProf software package [137, 139, 159, 160]. A six-degree polynomial was used for fitting the background pattern, and a pseudo-Voigt function was used for fitting the peak profile, respectively. The scale factor, Zero-shift, lattice parameters, profile shape parameters, and Wyckoff positions were refined sequentially to achieve stability and convergence in the refinement pattern. The quality of the refinement fit was ensured by evaluating the values of standard reliability factors R_p and χ^2, which indicated a good agreement between the observed and calculated diffraction profiles. These refinement results confirmed the phase purity and structural reliability of the synthesized Fe-substituted Gd_2TiO_5 series. The refined patterns of pure Gd_2TiO_5 and 10% Fe-

substituted samples are shown in **Figure 3.2a and b**, respectively. The crystal structure was extracted from the CIF file, obtained from the refinement results using the VESTA (Visualization for Electronic and Structural Analysis) software.

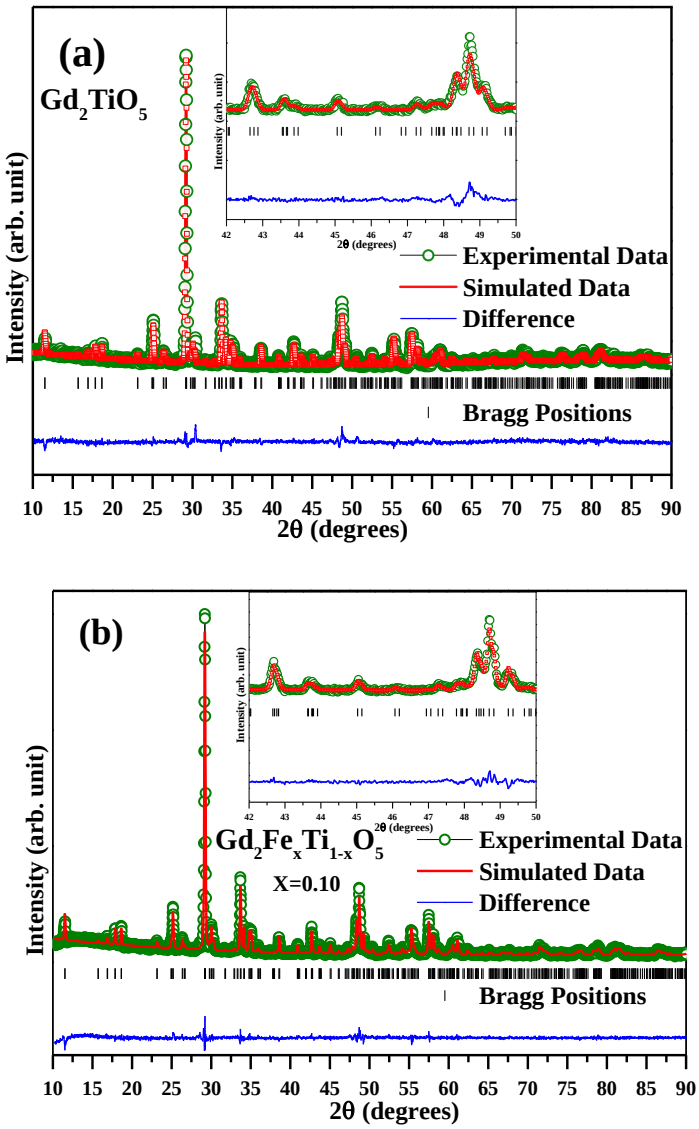

Figure 3.2 Rietveld refinement pattern of **a** parent and **b** 10% Fe-substituted Gd_2TiO_5 powder samples using the *Pnam* space group. The inset of the figure shows the magnified view of the refinement data, which confirms the quality of the refinement

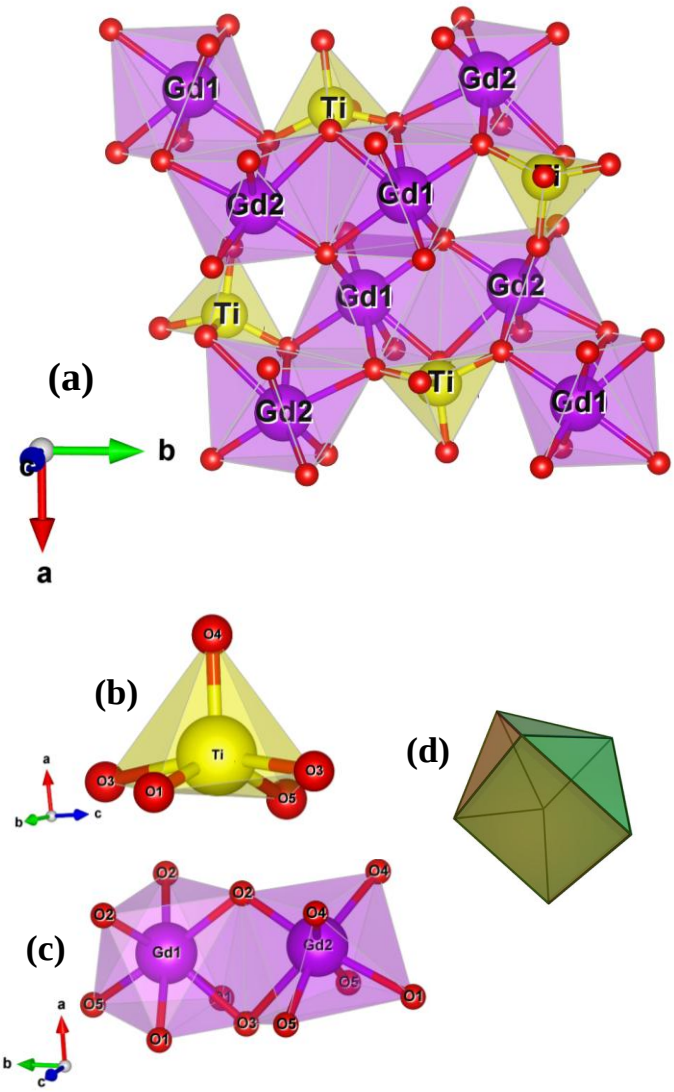

Figure 3.3 a Crystal structure of orthorhombic Gd_2TiO_5, **b** shows the GdO_7 polyhedra connected by a common edge. Lanthanide elements are seven-coordinated with oxygen and form a capped trigonal prismatic molecular geometry, **c** shows the TiO_5 polyhedron, where the Ti is five-coordinated with oxygen anions, **d** shows the schematic of an augmented triangular prism

The obtained crystal structure is shown in **Figure 3.3a,** along with the extracted titanium polyhedra (TiO_5) and one of the gadolinium polyhedra (GdO_7). As seen in the crystal structure of Gd_2TiO_5, the primitive unit cell contains four formula units of it. The titanium atom is surrounded by five oxygen atoms and forms the TiO_5 polyhedron. The geometry of the TiO_5 polyhedron is found to be square pyramidal, where four oxygen atoms form the square planar base and are bonded to the

Gd_1 and Gd_2 ions, as shown in **Figure 3.3b**. Out of these oxygens, two lie on the common edge, which connects the GdO_7 and TiO_5 polyhedra [28]. The 5th oxygen atom is bonded to another GdO_7 polyhedron and lies on the apex position of the square pyramid, forming the shortest Ti-O bond distance in the TiO_5. The titanium atom is displaced slightly from this square base towards the apex position in the polyhedron. Both the Gd atoms are coordinated to seven oxygen atoms and form a capped trigonal prismatic geometry as shown in **Figure 3.3c**. The capped trigonal prismatic geometry can be understood as a structure where seven atoms or groups of atoms or ligands are arranged around a central atom, forming the vertices of an augmented triangular prism, as shown in **Figure 3.3d.**

This interesting and unique combination of mixed seven- and five-fold coordination is structurally and geometrically rarely observed in materials science [41, 131]. This makes the square-pyramid geometry important from both structural and geometrical points of view. Most titanium-based transition metal oxides are found to have titanium atoms in the octahedral and tetrahedral cages. This makes the Gd_2TiO_5 materials interesting from the structural, optical, and electronic property aspects, and it will be interesting to study how these properties are affected in the case of different crystal fields and geometrically distinct behavior.

Table 3.1 Site occupancies and atomic position coordinates of the orthorhombic phase of Gd_2TiO_5 having the *Pnam* space group. The error in respective site occupancies is of the order of ~0.0003 Å

Atom	***Wyckoff***	***x***	***y***	***z***	***Occupancy***
Gd1	4c	0.1369(8)	0.0574(9)	1/4	1
Gd2	4c	0.3899(1)	0.2209(0)	3/4	1
Ti	4c	0.1786(5)	0.3758(5)	1/4	1
O1	4c	0.2046(4)	0.5238(4)	1/4	1
O2	4c	0.4920(3)	0.6214(0)	1/4	1
O3	4c	0.2957(2)	0.8886(0)	1/4	1
O4	4c	0.0224(7)	0.3556(5)	1/4	1
O5	4c	0.2525(2)	0.2397(5)	1/4	1

Table 3.2 Lattice parameter (a, b, c) results of Gd_2TiO_5 and Fe-substituted samples obtained from the refinement

Sample	***a* (Å)**	***b* (Å)**	***c* (Å)**
Gd_2TiO_5	10.487	11.309	3.7617
$Gd_2Fe_{0.05}Ti_{0.95}O_5$	10.4938	11.297	3.7604
$Gd_2Fe_{0.07}Ti_{0.93}O_5$	10.499	11.2932	3.7613
$Gd_2Fe_{0.10}Ti_{0.90}O_5$	10.5051	11.2728	3.7628

Table 3.3 The Ti-O(4) bond length and angles obtained from the refinement results of Gd_2TiO_5 and Fe-substituted samples

Sample	***Ti-O*(4) *Bond-length (Å)***	***Angle* (*O*(1)-*Ti*-*O*(5))**	***Angle* (*O*(3)-*Gd*(1)-*O*(5))**	***Angle* (*Gd*(1)-*O*(5)-*Ti*)**	***Angle* (*Ti*-*O*(1)-*Gd*(2))**
Gd_2TiO_5	1.66(4)	143.7(19)	108.3(13)	123(3)	146.5(18)
$Gd_2Fe_{0.05}Ti_{0.95}O_5$	1.68(3)	139.1(13)	110.6(10)	118.2(16)	142.2(12)
$Gd_2Fe_{0.07}Ti_{0.93}O_5$	1.71(3)	139.6(15)	111.6(11)	118.9(16)	143.5(18)
$Gd_2Fe_{0.10}Ti_{0.90}O_5$	1.74(3)	137.5(13)	115.1(9)	118.5(16)	141.1(12)

To further extend the analysis of how the substitution of an impurity atom at the Ti site affects the crystallographic structure and optical properties of the material, we aimed to study the Fe-substituted Gd_2TiO_5 system, where Fe was substituted for Ti. The structural information, including Wyckoff position and site occupancy, was obtained from the refinement results for the parent Gd_2TiO_5 and Fe-substituted samples and is presented in **Table 3.1**. The other information regarding the lattice parameters and bond lengths is noted in **Tables 3.2** and **3.3**. The lattice parameter '*a*' was found to increase systematically with increasing Fe-concentration. This is expected as the ionic radius of Fe [160, 161] (0.585 Å) is larger than the ionic radius of Ti (0.51 Å). Also, the Ti-O(4) bond length, which aligns almost in the '*a*' lattice parameter direction, is found to be increasing with Fe concentration in this direction. This is also confirmed by the shift in the peak position towards lower 2θ values in the XRD pattern, indicating the expansion of the unit cell. From this, it can be inferred that Fe substitution at the Ti

site results in the distortion of the Ti-O_5 polyhedron in the Gd_2TiO_5 crystal structure.

The distortion in the lattices of five-coordinate metal complexes was explained by Addison and co-workers [162], who defined a geometric parameter 'τ_5' called the "Index of the degree of trigonality" and focused on the five-coordinate copper (II) complexes. According to Addison's model, the geometry of mostly five-coordinate complexes lies on a continuum defined by two extreme geometries, square pyramidal and trigonal bipyramidal structure [131], where he identified the two largest angles in the corresponding geometries and gave an expression:

$$\boldsymbol{\tau_5 = \frac{(b_1 - a_1)}{60}} \qquad (3.2)$$

Here, 'α_1' and 'β_1' [131] represents the two largest angles in the respective geometries as shown in **Figure 3.4a**. For ideal square pyramidal geometry, $\alpha_1=\beta_1=180^o$, whereas for the perfectly trigonal bipyramidal structure, α_1 is 120^o *and* β_1 is 180^o. Hence, 'τ_5' comes to '0', [163] for a perfect square pyramidal structure and becomes '1' for the ideal trigonal bipyramidal structure as depicted in **Figure 3.4b**.

By estimating the value of this parameter, we can measure the distortion within the five-fold coordinated metal complexes. A variety of literature exists that is based on the application of the τ_5 parameter [164].

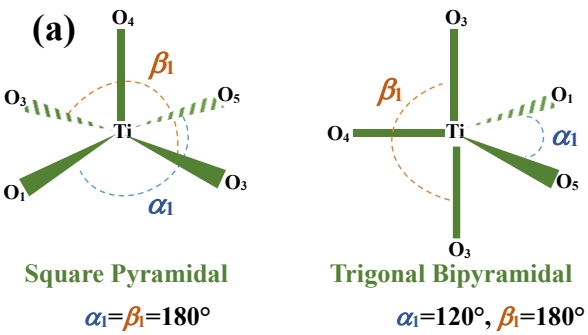

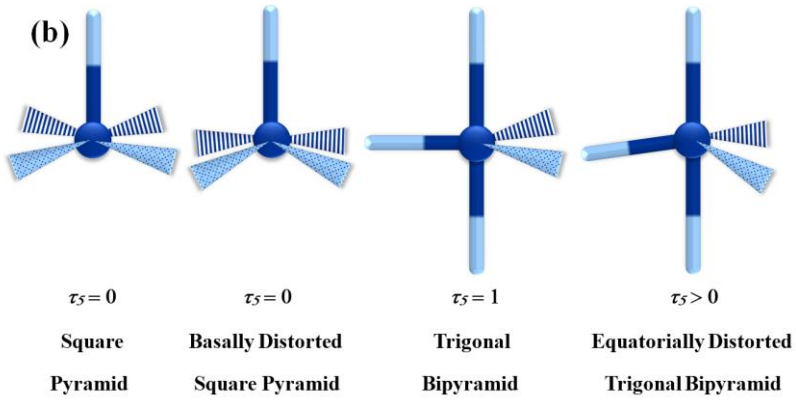

Figure 3.4 a and **b** The schematics of ideal square pyramidal (C_{4v}) and trigonal bipyramidal (D_{3h}) geometries [17, 23] exhibiting the transformation from square pyramid to distorted trigonal bipyramid geometry

Table 3.4 The observed geometrical parameters of the Ti-O_5 polyhedron in the case of pristine Gd_2TiO_5 and Fe-substituted samples

Sample	***O*(5)-*Ti*-*O*(1)=α_1 (°)**	***O*(3)-*Ti*-*O*(3)=β_1 (°)**	**$\tau_5 = (\beta_1-\alpha_1)/60$**
Gd_2TiO_5	143.7(19)	162(3)	0.305
$Gd_2Ti_{0.95}Fe_{0.05}O_5$	139.1(13)	147.5(13)	0.14
$Gd_2Ti_{0.93}Fe_{0.07}O_5$	139.6(15)	148.4(19)	0.14667
$Gd_2Ti_{0.90}Fe_{0.10}O_5$	137.5(13)	142(13)	0.075

Therefore, in this study, we attempted to measure the lattice distortion in terms of the degree of the trigonality parameter 'τ_5' for $Gd_2Ti_{1-x}Fe_xO_5$ (x = 0.05, 0.07, and 0.10) samples with an increase in the Fe substitution. The results are represented in **Table 3.4**. Surprisingly, in the present case, even though the value of parameter 'τ_5' is approaching zero, the angles α_1 and β_1 are both deviating from 180°, suggesting the complexity of the $Gd_2Ti_{1-x}Fe_xO_5$ system. However, the ~0.30 value of 'τ_5' lying close to zero suggests the distorted square pyramidal geometry of Gd_2TiO_5. And as the Fe content increases in the system, the geometry seems to be approaching more closely to ideal square pyramid geometry.

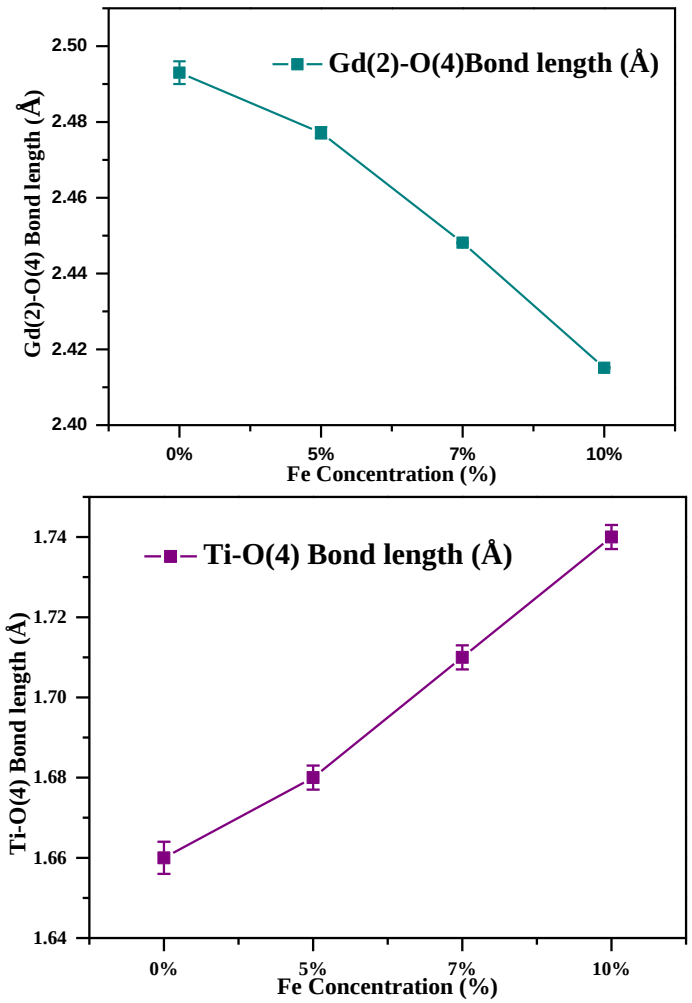

Figure 3.5a and **b** show the systematic variation of Gd(2)–O(4) and Ti–O(4) bond lengths with the increased amount of Fe in Gd_2TiO_5. The bond lengths were showing the opposite trend with Fe-substitution

For other structural information, variations in the Ti/Fe–O and Gd–O bond lengths were observed in proportion to the amount of Fe content. One of the Gd–O and Ti/Fe–O bond lengths was found to vary systematically with increased Fe concentration. The variation in the Gd(2)–O(4) and Ti/Fe–O(4) bond lengths is shown in **Figure 3.5a, b**, respectively, where both the bond lengths show the opposite trend with increasing Fe concentration.

3.3.2 Optical Absorption Spectroscopy and Band Gap

For further investigation of the optical properties and their correlation with the structural results, as well as their evolution with Fe-substitution, optical absorption measurements were performed on the prepared samples. The optical absorption spectra were recorded in the wavelength range of 200-900 nm, using diffuse reflectance mode [165]. The diffuse reflectance was then converted into absorption spectra using the Kubelka-Munk function $F(R)$ [108, 114, 151, 165]. In the optical absorption spectra [166–168], the absorption coefficient α [69-71], is proportional to Reflectance R by the Kubelka-Munk equation [169–171] as shown in the following relation:

$$\boldsymbol{F(R_\infty) \approx \alpha \approx \frac{K}{S} \approx \frac{(1-R_\infty)^2}{2R_\infty}} \quad (3.3)$$

here, $F(R_\infty)$ is the Kubelka-Munk function (K–M), α is the linear absorption coefficient of the material, and K and S are the K-M absorption and scattering coefficients, respectively. The above equation is only valid for infinitely thick samples.

$$\boldsymbol{R_\infty = R_{sample}/R_{standard}} \quad (3.3)$$

R_{sample} is the diffuse reflectance [172, 173] of the given sample, and $R_{standard}$ is that of a standard specimen. The absorption coefficient α is related to the band gap E_g of the material by the Tauc equation, which is given as

$$(\alpha h\nu)^n = A(h\nu - E_g) \quad (3.4)$$

where hν is the photon energy, and A is the proportionality constant. For direct band gap transitions, '*n'* has the value 2, and for indirect transitions, '*n*' has the value 1/2. In our case, we have used '*n'* as equal to 2 for considering indirect band transitions [54].

The optical absorption spectra of parent Gd_2TiO_5 and doped samples are shown in **Figure 3.6**. To determine the optical band gap, a graph was plotted between $(F(R) \times h\nu)^{0.5}$ and photon energy (hν) for

the diffuse reflectance spectra of Fe-substituted samples (**Figure 3.7**). The linear region in the diffuse reflectance spectra was fitted with a straight line to determine the band gap value of the prepared samples. The band gap of the parent Gd_2TiO_5 sample is found to be 4.12 eV, which agrees well with the previous literature [54], and it decreased to 3.11 eV for the maximum Fe-substituted ($Gd_2Ti_{1-x}Fe_xO_5$, x ~ 0.10) sample. The numerical values of the band gap of all Fe-substituted samples have been provided in **Figure 3.8**, where the variation in the band gap has been plotted as a function of Fe-substituted concentrations. It is observed that the band gap exhibits a systematic decrease as the Fe amount increases at the Ti site in Gd_2TiO_5.

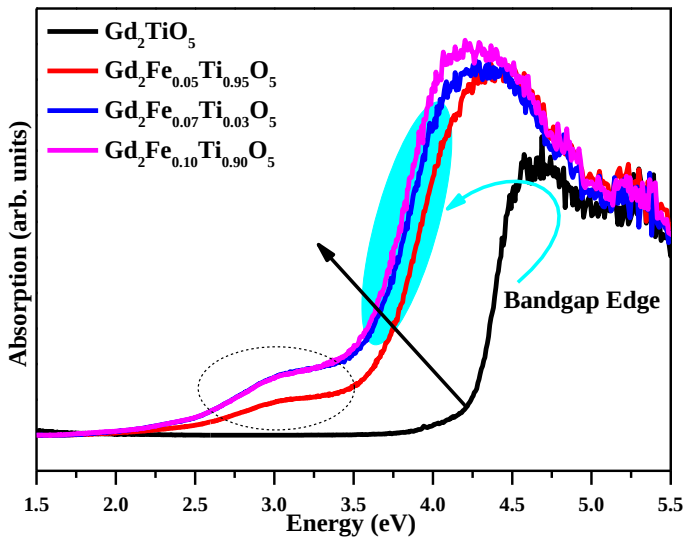

Figure 3.6 Optical absorption spectra of parent Gd_2TiO_5 and Fe-substituted samples, which have been taken in DR (diffuse reflectance) mode

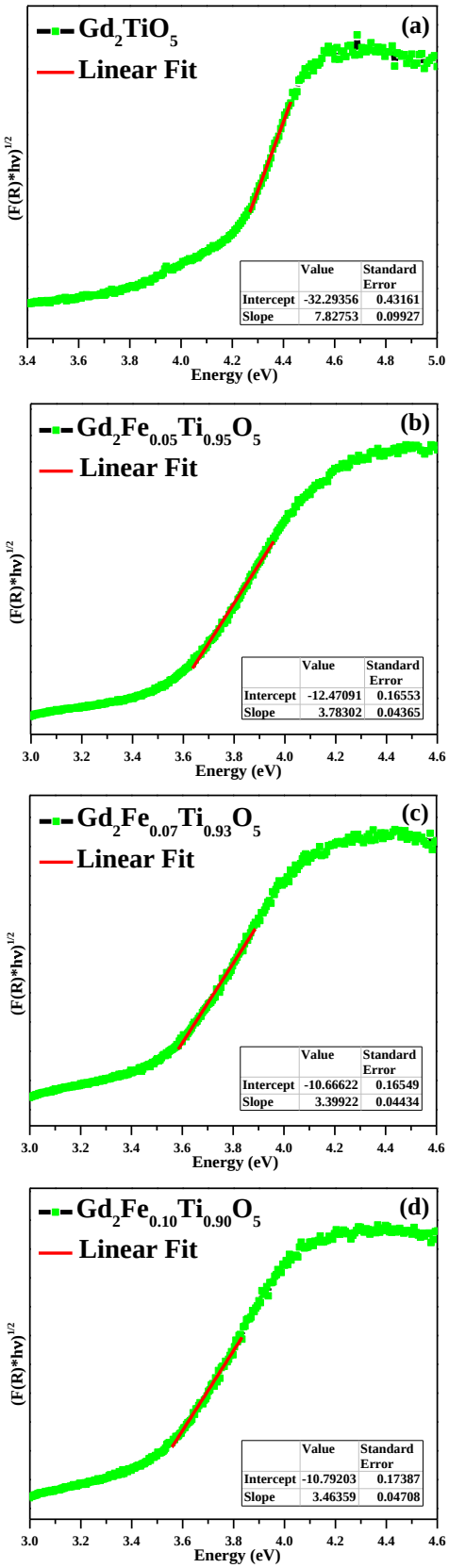

Figure 3.7 Tauc's plot showing the linear fit of the optical absorption spectra in the case of **a** parent Gd_2TiO_5 and **b-d** Fe-substituted $Gd_2Ti_{1-x}Fe_xO_5$ (x=0.05, 0.07, and 0.10) samples, respectively

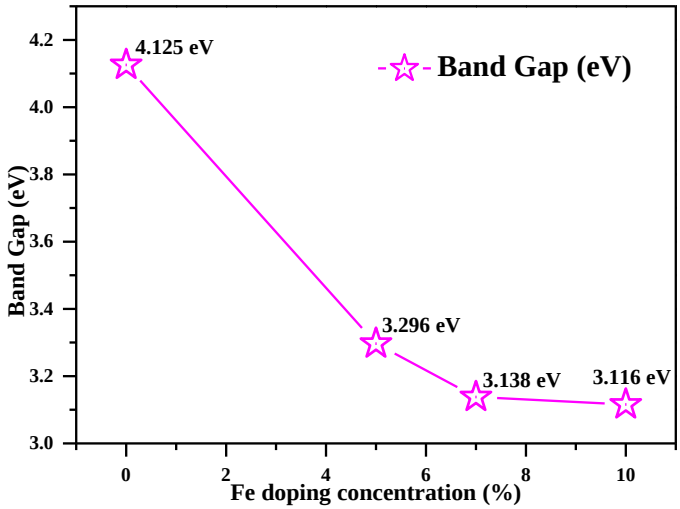

Figure 3.8 Variation of optical band gap (E_g) with Fe substitution in Gd_2TiO_5, obtained from the diffuse reflectance measurements

To account for this behavior of the change of band gap in Fe-substituted samples, it is necessary to further analyze the band structure and density of states of the prepared samples. It is important here to note that with Fe-substitution, a broad hump-like feature appears in the optical absorption spectra around ~ 3.0 eV. This may be due to the new states appearing below the conduction band due to the Fe substitution in Gd_2TiO_5 (See **Figure 3.13b**) as referred to in the subsequent section of the manuscript [174]. More extensive theoretical investigations will be necessary in this regard, which could be a separate topic for discussion. Some analysis part has been included in the last section of this study.

3.3.3 Density Functional Theory Calculation

To understand the experimentally observed trend of the optical band gap with increasing Fe concentration in Gd_2TiO_5 and how it is related to the electronic band structure of Gd_2TiO_5, the first-principles calculations were carried out using the density functional theory [175–177]. **Figure 3.9a, b** shows the calculated band structure, along with the total and partial density of states plots for the pristine Gd_2TiO_5. From these results, the computed value of the band gap was found to be ~4.0

eV, which is comparable to the experimentally observed value of ~4.12 eV. It is observed that the conduction band minimum was dominated by O-2*p* and Ti-3*d* orbitals, and the valence band maximum is also mainly composed of Ti-3*d* and O-2*p* states, near the Fermi level (E_F), which agrees well with the earlier studies carried out on the La_2TiO_5 and Dy_2TiO_5 by Niu et al. [178, 179]. **Figure 3.10a, b** shows the calculated band structure and the total and partial density of states for 10% Fe-substituted Gd_2TiO_5, respectively, which was also found to possess an indirect band gap, and the value of the band gap decreases to ~3.05 eV, which is close to the experimentally obtained value of ~3.11 eV. Here also, the conduction band minimum is mainly composed of O-2*p* orbitals, along with some contributions from the Fe-3*d* and Gd-5*d*, and the valence band maximum is dominated by Ti-3*d* and Fe-3*d* orbitals near the Fermi level. Therefore, from the results, it is natural to expect that orbital overlap between Ti-3*d* and O-2*p* orbitals (*p*-*d* hybridization) can affect the structural and optical properties of pure Gd_2TiO_5 and Fe-substituted samples. Hence, from the theoretical band structure calculations [180], it is clear that the band structure in these materials is governed by the Ti-3*d* and O-2*p* orbitals, and changes in orbital overlap (hybridization) between these orbitals can be a major contributing factor in altering the band gap properties.

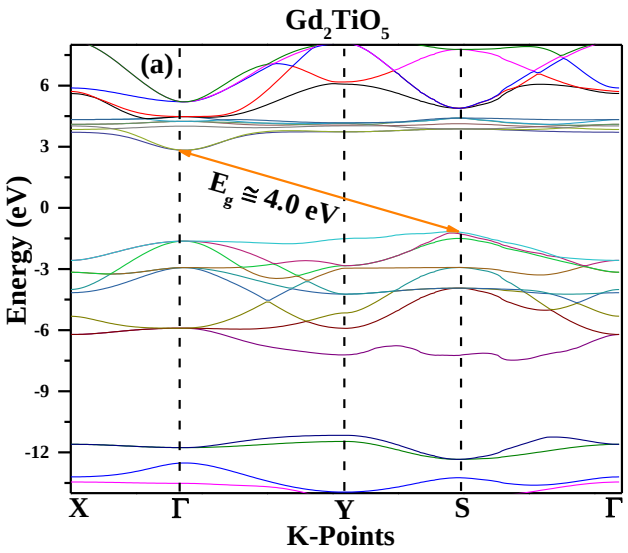

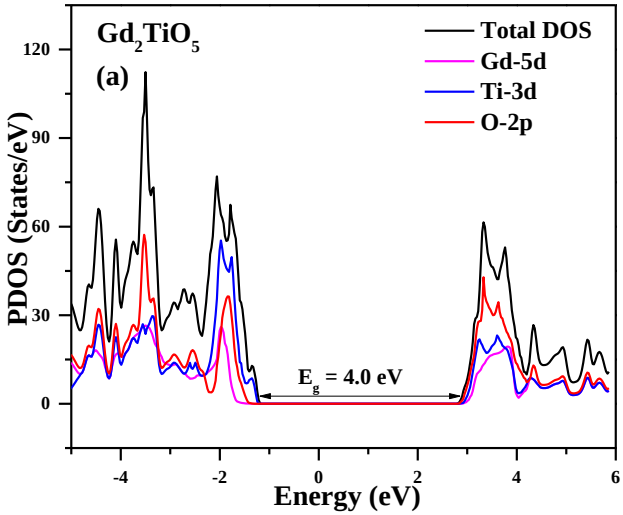

Figure 3.9 Simulated **a** band structure and **b** partial density of states (PDOS) of pristine Gd_2TiO_5

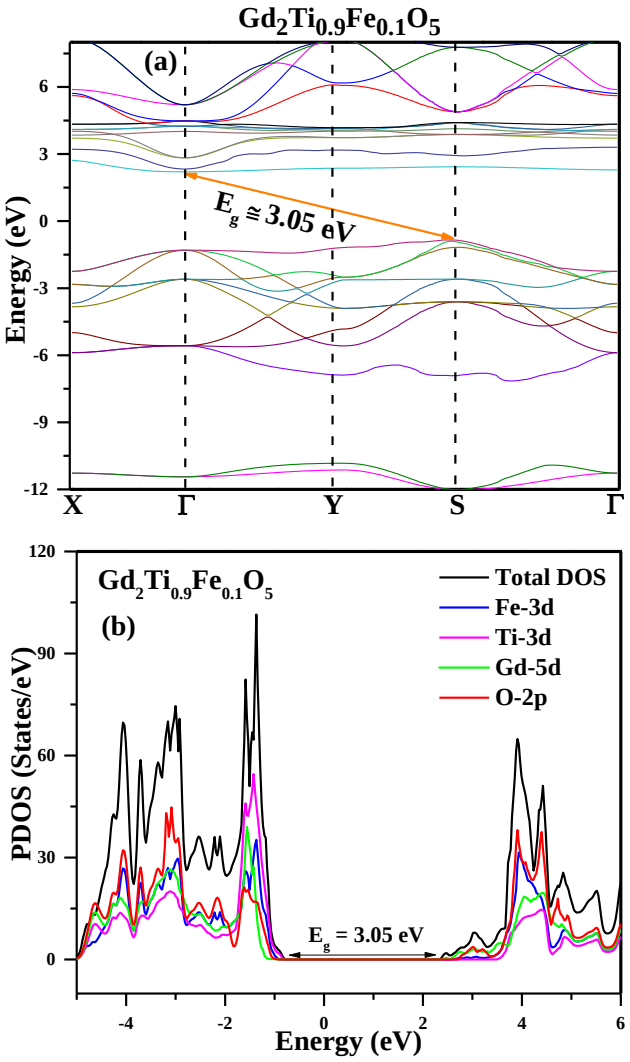

Figure 3.10 Simulated **a** band structure and **b** partial density of states of 10% Fe-substituted Gd_2TiO_5 substituted samples

3.3.4 Correlation between Band Gap and Bond Length

From the first principle investigation, it is clear that the conduction band minima and the valence band maxima are dominated by the O-2*p* and Ti-3*d* orbitals. Hence, any variation in the Ti–O bond length and hybridization between Ti-3*d* and O-*2p* orbitals is expected to affect the electronic band structure and, hence, the variation of the band gap. To understand this, the variation in Ti/Fe-O bond length and the value of the band gap in pure and Fe-substituted Gd_2TiO_5 have been carefully investigated. As we revisit the refinement results, where one of the Gd-O and Ti/Fe-O bond lengths was varying systematically (**Figure 3.5a and b**) with increasing Fe concentration, it was speculated that the variation in these bond lengths could be related to the systematic variation in the band gap. As both bond lengths showed an opposite trend with increasing Fe concentration, it is inferred that one of the bond lengths plays a key role and a deciding factor in the systematic variation of the band gap.

Now, from the theoretical band structure calculations, it is clear that the band structure in these materials is mainly governed by the hybridization between Ti-3*d* and O-2*p* orbitals, and hence the change in the orbital overlap between these orbitals, originating from the change in the bond length, can be a major contributing factor in altering the band edge properties. From **Figure 3.5**, it can be inferred that as the Ti-O bond length increases with Fe substitution, a decrease is expected in the corresponding orbital overlap between O-2*p* and Ti-3*d* orbitals, resulting in the decrease in the band gap. In such cases, it is believed that more orbital overlap results in tighter bonding of electrons, leading to the higher value of the band gap.

However, in general, it is also observed that more orbital overlap leads to an increase in the width of the conduction band and valence band [181], which may cause a decrease in the band gap. Here, it is important to note that the relative position of the valence band maxima

and conduction band minima on the energy scale is also equally important for the observed trend in the band gap.

The DFT calculations presented in **Figure 3.10** clearly indicate a significant shift in the position of the conduction band minima to lower energy values and the valence band maxima to higher energy values with Fe-substitution, which, in the present case, may be responsible for the observed decrease in the band gap value. A similar kind of work has been reported in several studies [168, 182].

3.3.5 The Optical Absorption 'Hump' Analysis

To investigate the optical properties of the Fe-substituted samples, Diffuse Reflectance Spectroscopy (DRS) has been performed on all the prepared samples, as discussed in the previous section. Gd_2TiO_5. The band gap of the pristine sample was found to be ~4.12 eV, which decreases to ~3.11eV for the 10% Fe-substituted sample. The Fe-substituted samples were found to exhibit an interesting feature of a broad hump around ~3 eV, which is absent in the pure sample, as shown in **Figure 3.11.** This indicates there seems to be an emergence of some defect states with the Fe-substitution at the Ti-site. The intensity of the broad hump increases as the Fe amount in the sample increases, indicating an increase in defects in the system with Fe substitution.

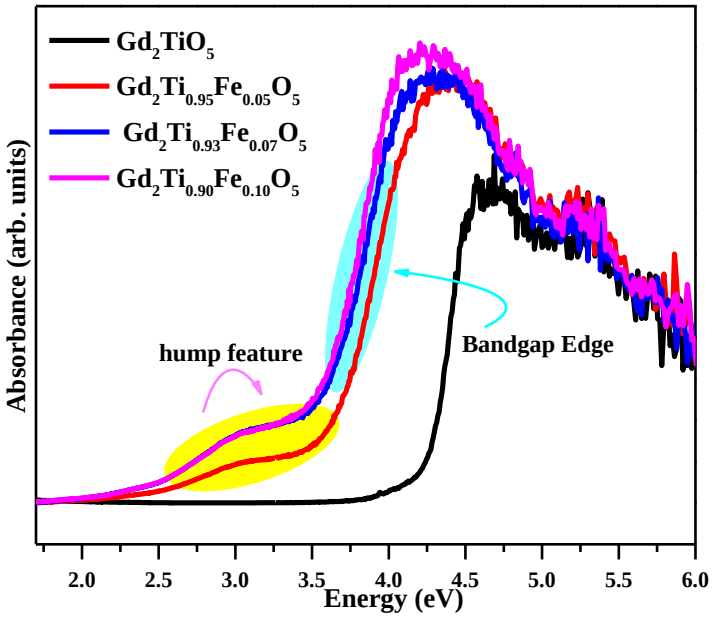

Figure 3.11 Optical absorption spectra of Fe-substituted Gd_2TiO_5 series samples. The yellow-highlighted region shows the broad hump feature observed with Fe substitution in Gd_2TiO_5

For further analysis of these results, theoretical calculations were performed with density functional theory using the Quantum Espresso software to simulate the optical absorption spectra of pure and maximum Fe-substituted Gd_2TiO_5, as shown in **Figure 3.12a**. The results agreed well with the experimental results and showed the emergence of hump features in the 10% Fe-substituted GTO sample. However, in the simulated spectra, we got two hump features instead of one broad hump. It appears that these two humps in the simulated optical spectra have been merged in the experimental data obtained from the DRS measurements. For the better understanding of these hump features, we have deconvoluted the simulated optical absorption spectra using the origin software. The peak positions of the two humps were found to be at 2.743 eV and 3.19 eV, which is shown in **Figure 3.12b**. Here, we also applied the Kubelka-Munk theory to calculate the band edges of these humps using the Tauc equation, and the band edges were found to be 2.42 eV and 2.2 eV for humps 1 and 2, respectively. The linear fit of the band edges of the humps is shown in **Figure 3.12c.**

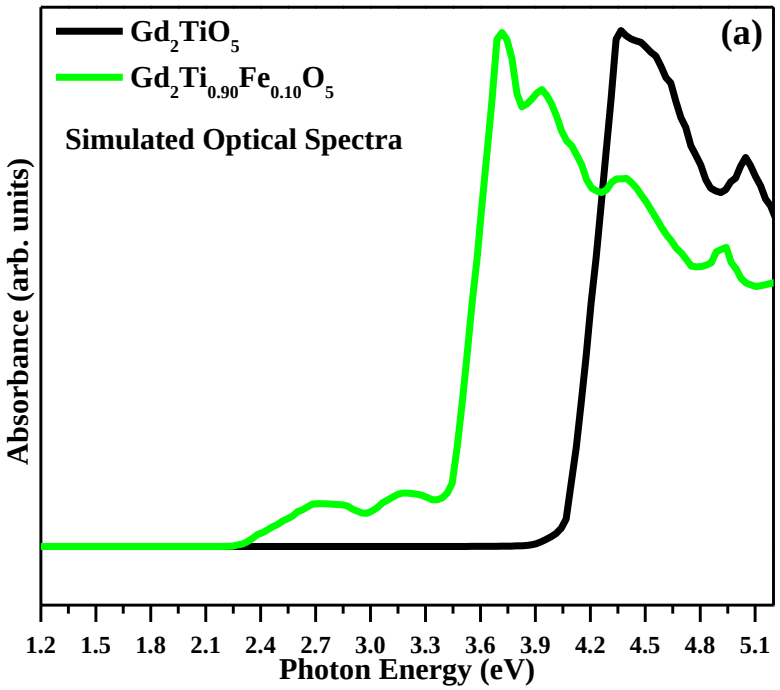

Figure 3.12a Simulated optical absorption spectra of pristine and 10% Fe-substituted Gd_2TiO_5

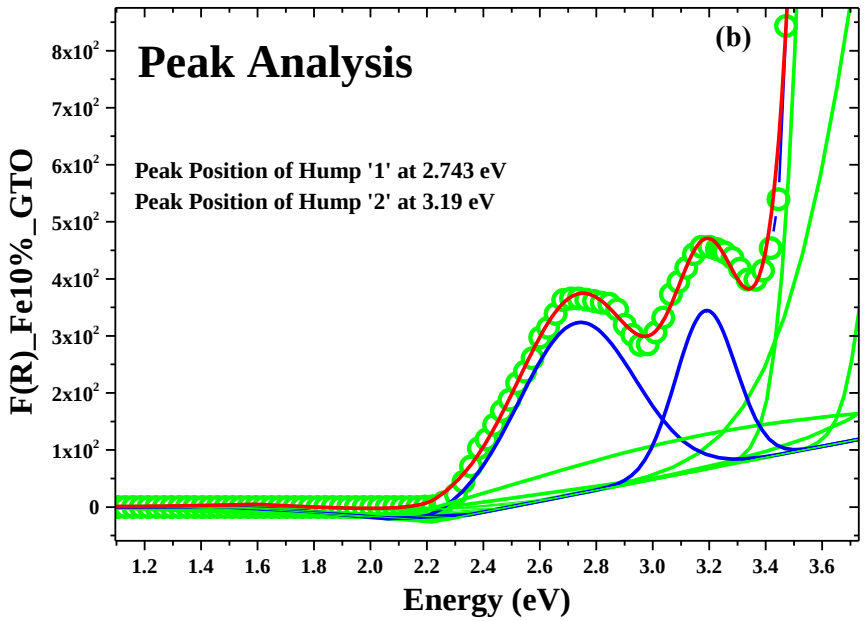

Figure 3.12b shows the deconvoluted peaks obtained from the simulated optical absorption spectra

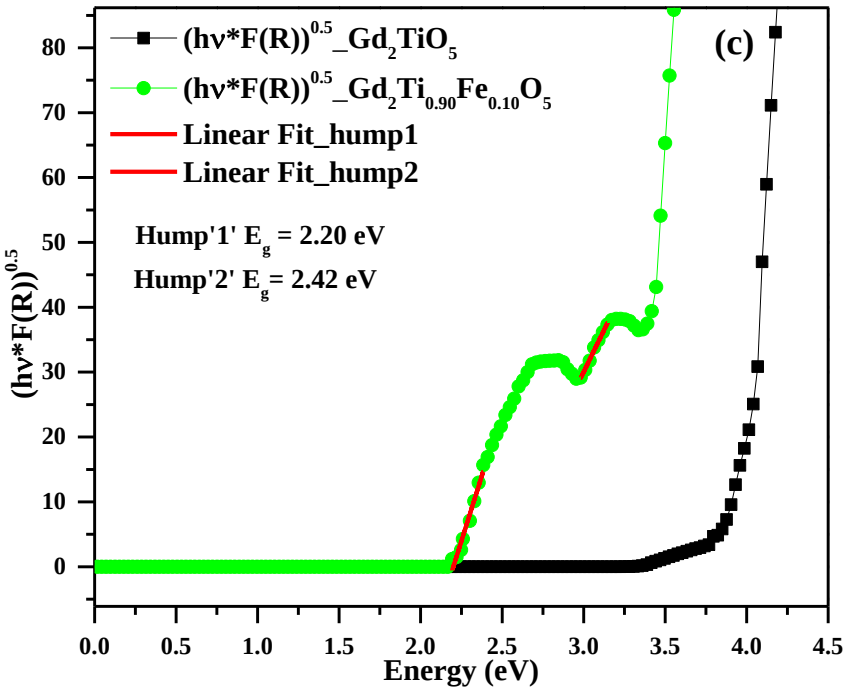

Figure 3.12c shows the band-edge values obtained from the Tauc plot fitting for band gap calculations

For further analysis of the results obtained from the experimental and theoretically simulated optical absorption spectra, the band structure calculation results were thoroughly analyzed. The band structure of the 10% Fe-substituted sample is shown in **Figure 3.13a.** If we compare the band structure of the Fe10%_GTO sample with that of the pristine one (**Figure 3.9a**), an extra state appears to be present in the band structure, as marked 'a' in the enlarged view of the band structure near the conduction band, shown in **Figure 3.13b**. If we calculate the transition energy from the maximum of the state 'a' to the minimum of the state 'j', the energy difference comes out to be 2.168 eV, which suggests this transition corresponds to the hump '2' coming in the Fe10%_GTO ($Gd_2Ti_{0.9}Fe_{0.1}O_5$) sample. Similarly, the transition from the maxima of state 'a' to the minima of state 'k' or state 'l', which coincides with the same minimum energy, may be responsible for the appearance of hump '1' in the Fe-substituted samples [174]. These transitions are shown by marked arrows in **Figure 3.13b**.

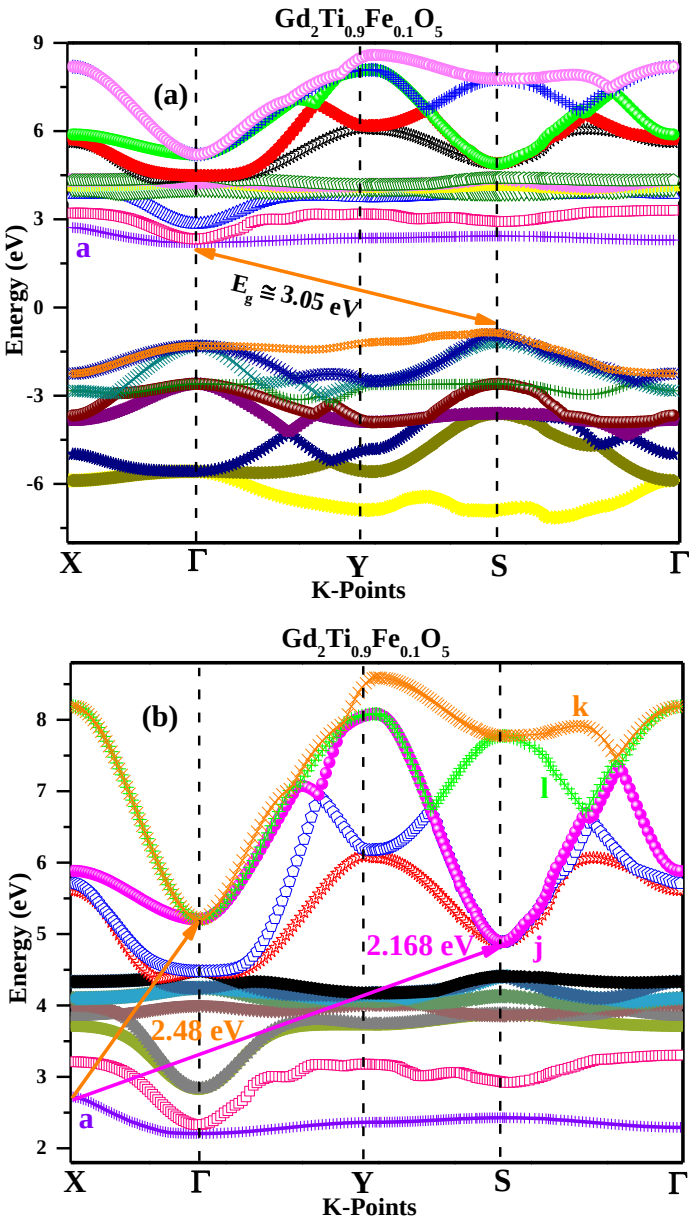

Figure 3.13a Simulated band structure of 10% Fe-substituted Gd_2TiO_5 substituted sample, **b** enlarged view of the band structure, showing the appearance of extra new state 'a' below the conduction band

Hence, from the above experimental and theoretical absorption spectroscopy results, it is inferred that a hump starts to appear near the band edge as the Fe concentration increases in the Gd_2TiO_5 samples. The appearance of this broad hump may be due to the occurrence of intraband transitions resulting from an extra state appearing below the conduction band, and is hence speculated to be the defect state [183, 184]. As the Fe-substitution increases in Gd_2TiO_5, the intensity of the

defect states increases, the signature of which is reflected in the form of two broad peaks in the simulated optical absorbance spectra, merging into a broad hump in the experimental spectra. Therefore, it is speculated that the appearance of these defects state, below the conduction band, leads to a reduction in the band gap as the Fe substitution increases at the Ti site in Gd_2TiO_5.

3.4 The Conclusion and Summary of the Results

The Polycrystalline samples of pure and Fe-substituted Gd_2TiO_5 were prepared using the solid-state synthesis method to investigate the structural and optical properties of the rarely observed square pyramidal geometry of the Titanium atom in Gd_2TiO_5. The X-ray diffraction techniques and Rietveld refinement were used to check the phase purity of the single-phase prepared samples, which revealed an orthorhombic structure and the Pnam space group of the synthesized samples. The variation in the lattice parameters and bond lengths was obtained from the refinement results, where the Ti–O and Gd–O bond lengths were found to exhibit the systematic variation with increasing Fe substitution. Further to investigate the optical properties, Diffuse Reflectance spectroscopy (DRS) measurements were used, and the optical band gap (*Eg*) was found to decrease systematically with Fe concentration indicating that the band gap of these materials is majorly controlled by the orbital overlap of Ti-3*d* and O-2*p* orbitals (*p*-*d* hybridization) and hence by altering the orbital overlap we can modify the band gap in these materials. Furthermore, these results were confirmed by density functional theory (DFT) calculations, which indicated that the states near the Fermi level are dominated by Ti-3*d* and O-2*p* orbitals, and thus play a crucial role in governing the band gap properties.

Chapter 4

Experimental and First-principles Investigation on the Optical Properties of Eu- and Fe-substituted Gd_2TiO_5

Optical absorption spectroscopy serves as an essential experimental tool for analysing the effects of substitution/doping on materials' optical and electronic properties by measuring their response in terms of wavelength-dependent absorption, reflectance, and transmission. This further provides information of bandgap coefficient, the shifting of band edges, dopant-induced states, and allowed sub-bandgap transitions, which directly gives the fingerprint of optical density of states and electronic transitions impacting light-matter interactions caused by substitution and doping effects. In this context, Eu and Fe have been systematically substituted for Gd- and Ti-site, respectively, in Gd_2TiO_5. For experimental support, Density Functional Theory (DFT) calculations have been performed, demonstrating the effectiveness of this approach in providing the computed band structure of altered electronic structure, electronic and phononic density of states (DOS), and charge distribution, thereby offering a comparison between the pristine and substituted crystal structures. By combining the mutually reinforcing applications of optical absorption spectroscopy and density of states theory, the controlled substitution effects can be observed in the materials' optical and electronic properties, which can establish significant paradigms for designing novel rare-earth titanate complexes with tailored optical properties applicable in fields of optoelectronics and photonics.

4.1 Introduction

Rare-earth titanates exhibit unique structural, physical, and optical properties, making them highly suitable for applications in the nuclear and radiation industries [22, 28, 53, 127, 185–188]. These materials are known for their high mechanical strength, as well as their excellent chemical and temperature resistance, which makes them effective in environments with high radiation flux, such as energy and nuclear settings [6, 25, 35, 37, 122]. This group of materials includes lanthanide perovskites ($LnTiO_3$), pyrochlore-related structures ($Ln_2Ti_2O_7$), and $Ln_4Ti_9O_{24}$ compositions (where Ln is a lanthanide element from La to Lu) [121, 189, 190]. A particularly interesting member of this class is Ln_2TiO_5, in which the Ti atom adopts a rare five-fold coordination geometry, a feature much less commonly observed and explored compared to other titanate systems. In this article, we focus on the Gd_2TiO_5, a compound from this category, which exhibits remarkable chemical and optical properties.

These multicomponent transition metal oxides based on rare-earth elements typically exhibit higher relative permittivity, enhanced thermal stability, and a high conduction band offset, making them an important class of materials for gate dielectrics [59]. Additionally, these oxides are highly valuable in the development of pH-ion-sensitive field-effect transistor (ISFET)-based biosensors, owing to their remarkably high dielectric strength [77, 191]. For instance, a thin layer of Nd_2TiO_5 is used in ISFET-based sensing devices [59] for deposition on the silicon substrates. ISFETs are solid-state electronic devices employed in microsensors to detect chemical ion concentrations in solutions. Gd_2TiO_5, with its unique electrochemical properties, emerges as a promising novel material for use as an anode in lithium and sodium-ion batteries, owing to its efficiency in ion transport and battery performance [192].

These rare-earth titanates exhibit an interesting phenomenon of polymorphism, where they can exist in multiple structural phases

depending on the temperature, pressure, and size of the lanthanide atom [69]. Specifically, Gd_2TiO_5 exists in two polymorphs: Orthorhombic and hexagonal [130, 193]. At ambient conditions, Ln_2TiO_5 compounds adopt the orthorhombic phase when the lanthanide element (Ln) is larger than Holmium (Ho). For lanthanide elements smaller than or equal to Yttrium (Y) (Dy-Lu, Sc, and Y), these compounds exhibit a cubic structure. In some cases, the cubic phase takes the form of a pyrochlore-type structure having the *Fd3-m* space group, isostructural with $Ln_2Ti_2O_7$. In other instances, a defect fluorite phase with *Fm3-m* symmetry is observed, where both A and B cations are disordered over a single site, with randomly arranged vacancies in the anion sublattice to maintain charge balance. A hexagonal polymorph (*P63*/*mmc*) occurs at higher temperatures (> 1350 °C) and under ambient atmospheric conditions for lanthanide elements from Europium (Eu) to Holmium (Ho). In the orthorhombic phase, the lanthanide element is coordinated in a seven-fold geometry, forming a monocapped octahedron [133]. The titanium atom adopts a five-fold coordination and exists in an off-centre square pyramidal geometry. No mixed-occupancy sites are found within this structural framework.

The composition Ln_2TiO_5 is one of the least explored members of the rare-earth titanates, and features titanium polyhedra in a square pyramidal configuration, a geometry rarely observed in most titanium-based transition metal oxides [41, 44]. Most titanium-based oxides are found to exist in four-fold or six-fold coordination, possessing tetrahedral and octahedral geometries. A significant amount of work has been done in this regard on perovskite ($LnTiO_3$) and pyrochlore ($Ln_2Ti_2O_7$) type structures. As discussed above, the existence of a Ti atom in a square pyramidal configuration is rarely observed; hence, it will be interesting to investigate the optical properties of such compounds. Additionally, the optical, electronic, and magnetic properties of Gd_2TiO_5 have not been explored yet experimentally as well as theoretically, except for a few works by *Jafar and Balhara et al.* [54] on the optical properties of Eu-doped Gd_2TiO_5 and the theoretical

studies of La_2TiO_5 and Dy_2TiO_5 by Hui Niu et al. [180]. The crystal geometry around a transition metal ion determines the crystal field splitting in an oxide material [64]. For instance, large splitting occurs in octahedral complexes as compared to the tetrahedral complexes [194]. The distortion and change in geometry lead to alterations in the spatial arrangement and interaction of atomic orbitals, which in turn modify the orbital overlap and hybridization, resulting in changes in the material's optical absorption and electronic band structure. Hence, crystal geometry can be used to tailor the electronic and optical characteristics for specific application [127, 130, 187]. The unique square pyramidal geometry of the TiO_4 polyhedra in Gd_2TiO_5 makes the material interesting, particularly from a structural standpoint, and it raises the question of how this geometry influences the optical and electronic properties of the material.

Being a wide-bandgap material, Gd_2TiO_5 absorbs most of the light in the UV range, which limits its applicability in light-emission processes. Hence, reducing its bandgap with doping or other means can be useful in light-emitting devices, photocatalytic, and solar cell applications. The tuning of the bandgap can be achieved by doping or substituting a suitable element, which alters the composition and structure, thereby modifying the orbital overlap and, consequently, the electronic bandgap structure of the material. A significant amount of research has been carried out in this area by tuning the bandgap of materials for optoelectronics applications through the substitution of suitable transition metal elements, such as Mn, Fe, Co, and Ni, or rare-earth elements, including La, Sm, Eu, and Tb. In this regard, Y. Zhang and X. Xu have applied statistical analysis to the bandgap data of doped ZnO and doped TiO_2, varying the synthesis methods and incorporating various dopant elements into the crystal structure of ZnO. A strong correlation was established among the lattice parameters, grain size, and bandgap of ZnO using the Gaussian process regression (GPR) model, which can serve as a guideline for selecting a material with a suitable bandgap [195, 196]. This will enable flexibility in selecting a material

with a specific bandgap, suitable for advanced applications in the fields of photonics and optoelectronics.

The structural, optical, and electronic properties of oxide materials can be tailored through various methods, including compositional tuning, defect and stoichiometry engineering, strain control, and phase transformations driven by controlling temperature and atmospheric conditions. The most common way to tune the optical and electronic properties of a complex material is through compositional tuning, defect chemistry, and stoichiometry engineering, where aliovalent or isovalent doping can modify the lattice parameters, bond lengths, carrier concentration, and band structure by inducing defect states and altering crystal chemistry [197–202]. This gives precise control over the local symmetry of the material's structure and bandgap properties. Keeping this in context, the strategic substitution of Eu^{+3} at the gadolinium Gd-site and Fe^{+3} at the Ti-site has been carried out in the Gd_2TiO_5, which belongs to the $Ln_2Ti_2O_5$ family, which emerges as the least explored members of the rare-earth titanate complexes, and possess titanium polyhedra in a square pyramidal configuration, a geometry which has been rarely observed in most titanium-based transition metal oxides. A significant amount of work has been carried out on perovskite ($LnTiO_3$) and pyrochlore ($Ln_2Ti_2O_7$) and other structures featuring Ti in four-fold or six-fold coordination geometry, where the effect of geometry on the structural and optical properties has been rigorously studied. As discussed above, the existence of a Ti atom in a square pyramidal configuration is rarely observed; hence, it will be interesting to investigate the structural and optical properties of such compounds. Additionally, the optical, electronic, and magnetic properties of complex oxide Gd_2TiO_5 have not been explored experimentally as well as theoretically, except for a few works carried out by M. Jafar and A. Balhara [203] on the optical properties of Eu-doped Gd_2TiO_5 and the theoretical studies of La_2TiO_5 and Dy_2TiO_5 by Hui Niu et al. [178]. In this respect, it will be of considerable interest to study Gd_2TiO_5, which lies at the midpoint of the rare-earth titanate series and serves as a

standard material for analyzing the structural and optical properties of the Ln_2TiO_5 series of rare-earth oxide materials. By controlling the substitution of Eu at the Gd site, perturbation can be induced in the cation radius, electronic configuration, crystal field environment [194, 204], and in the defect states, which can affect f-electron interactions, influencing magnetic ordering, and can be further applied in the systematic tuning of luminescence behavior and charge compensation mechanisms. Similarly, the substitution of Fe^{3+} at the Ti^{4+} site changes the local bonding environments and modifies the octahedral distortion and introduces the mid-gap defect states. This further modifies the optical absorption edges and carrier dynamics, thereby impacting the conductivity, photocatalytic activity, and electronic transport behavior in advanced multifunctional oxides, such as Ln_2TiO_5 materials [205–208].

Based on this, in this work, Eu and Fe have been substituted at the Gd-site and the Ti-site in the Gd_2TiO_5 to investigate the impact of substitution on the material's structural and optical properties [204]. A detailed discussion of the work related to Fe-substituted Gd_2TiO_5 has been carried out in the previous work [209]. The previous work includes structural refinement results, where a systematic variation was observed in one of the Gd-polyhedral and Ti-polyhedral bond lengths, suggesting that a significant and dominant contribution can come from either Gd-5*d* or Ti-3*d* orbitals at the band edges in these materials. To further explore these results, UV-visible spectroscopy was performed, revealing a consistent trend in the bandgap corresponding to the Fe substitution, which correlates with the observed trend in Ti–O bond length. These findings were confirmed by first-principles calculations using Density Functional Theory (DFT) with the Quantum-Espresso software. The total and partial density of states (TDOS and PDOS) plots revealed that the dominant contribution at the valence band edge and conduction band edge comes from the Ti-3*d* and O-2*p* orbitals, respectively. These results agree well with the previous work on these materials [180]. This suggests that the Ti–O bond length plays a critical role in determining the bandgap properties of these compositions. From

this, we inferred that substitution at the B-site (Ti-site) has a more significant impact on the optical properties than substitution at the A-site in A_2BO_5-type compositions. To further investigate this idea, the present work extends our study to examine the optical properties of A-site-substituted Gd_2TiO_5, where Eu is substituted at the Gd site, and compares the optical spectroscopy results for both Eu substitution at the A site and Fe substitution at the B site. To validate the results, theoretical calculations were performed with DFT using VASP software.

4.2 Experimental Section

4.2.1 Sample Synthesis

The polycrystalline samples of Eu- and Fe-substituted Gd_2TiO_5, including the pristine one, have been synthesized by the solid-state reaction route [92, 209, 210]. For the synthesis process, the gadolinium oxide (Gd_2O_3), titanium oxide (TiO_2), europium oxide (Eu_2O_3), and iron oxide (Fe_3O_4), all with a purity of 99.99% were taken in stoichiometric amounts to obtain the respective compositions of $Gd_{2-x}Eu_xTiO_5$ and $Gd_2Ti_{1-x}Fe_xO_5$, where x = 0.03, 0.05, 0.07, and 0.10. The stoichiometric amounts of the powders mentioned above were mixed thoroughly in an isopropyl alcohol medium and ground in an agate mortar pestle. The grounded samples were then subjected to heat treatments at 1000 °C, 1250 °C, and 1300 °C, with intermediate grindings. The final sintering was done at 1350 °C for 24 h.

4.2.2 X-ray Diffraction Analysis

The phase purity of the synthesized samples was characterized using a Bruker D8 diffractometer equipped with a Cu target and Kα wavelength of 1.5405 Å [103, 104, 211, 212]. The XRD pattern was taken in an angular range of 20-80° with a step size of 0.02°. To extract the structural information, Rietveld refinement was performed on all samples using the FullProf software, considering the *Pnam* space group

of the synthesized samples [92, 130, 138, 139, 213]. A pseudo-Voigt function with a six-polynomial fit was used to refine the data. For extracting crystallographic information about the crystal structure geometry and lattice parameters, VESTA (Visualization for Electronic Structural Analysis) software was used [143].

4.2.3 Optical Absorption Spectroscopy (OAS) Measurements

UV–visible absorption spectroscopy was used to carry out optical absorption measurements on both series of Eu- and Fe-substituted Gd_2TiO_5 samples [147, 166, 214, 215]. The optical absorption spectra were recorded using a UV-Vis-NIR spectrophotometer in the wavelength range of 200-900 nm at a scan rate of 60 nm/min [108]. $BaSO_4$ (barium sulphate) was chosen as a reference material for the baseline due to its high reflectance properties, reproducible baseline, and low cost. The detailed procedure for optical absorption spectroscopy is presented in Chapter 2.

4.2.4 Density Functional Theory Calculations

Density functional theory (DFT) calculations for the density of states (DOS) of pure and Eu- and Fe-substituted Gd_2TiO_5 have been performed using the Vienna Ab initio Simulation Package (VASP) [216, 217]. Charge densities were estimated through self-consistent field (SCF) calculations on 2 × 2 × 2 supercells. For Brillouin zone sampling, 10 × 10 × 10 and 20 × 20 × 20 k-point grids were used in the Monkhorst-Pack scheme for SCF and DOS calculations, respectively. The Perdew-Burke-Ernzerhof (PBE) functional [156], which is based on the generalized gradient approximation (GGA), was employed for the exchange-correlation potential of electrons. Since the GGA alone is insufficient for accurately describing the strongly correlated d-electrons in these systems, we applied the GGA + U method, following the

Dudarev approach as implemented in the VASP software. To model ion-electron interactions, we used projector-augmented wave (PAW) method-based potentials. A plane-wave energy cutoff of 500 eV and an energy convergence criterion of 10^{-4} eV were used in these calculations.

4.3 Results and Discussion

4.3.1 Material Characterization

The rare-earth titanate Gd_2TiO_5, belonging to the Ln_2TiO_5 composition, where Ln is the rare-earth element, was synthesized using the conventional solid-state synthesis method. Eu and Fe were substituted at the Gd- and Ti-sites, respectively, to form the respective compositions of $Gd_{2-x}Eu_xTiO_5$ and $Gd_2Ti_{1-x}Fe_xO_5$, where x = 0.03, 0.05, 0.07, and 0.10. **Figure 4.1** represents the X-ray diffraction data for pure, Eu-substituted, and Fe-substituted samples. No additional peak was found to be present in the X-ray diffraction patterns of both the Eu- and Fe-substituted samples, confirming the structural phase purity of the synthesized materials, which exhibit an orthorhombic phase and *Pnam* (62) space group [11, 133, 143, 218]. For the analysis of structural parameters, Rietveld refinement was performed on all the samples using the FullProf software [138, 213, 219, 220]. The pseudo-Voigt function was used to fit the peak shapes of the X-ray diffraction pattern. The refined patterns of the 10% Eu- and Fe-substituted samples, along with the pristine one, are shown in **Figure 4.1a-c**, respectively. For the visualization of the structure of the prepared samples, VESTA (Visualization for Electronic and Structural Analysis) software was used to extract the crystal structure geometry of the prepared samples [221].

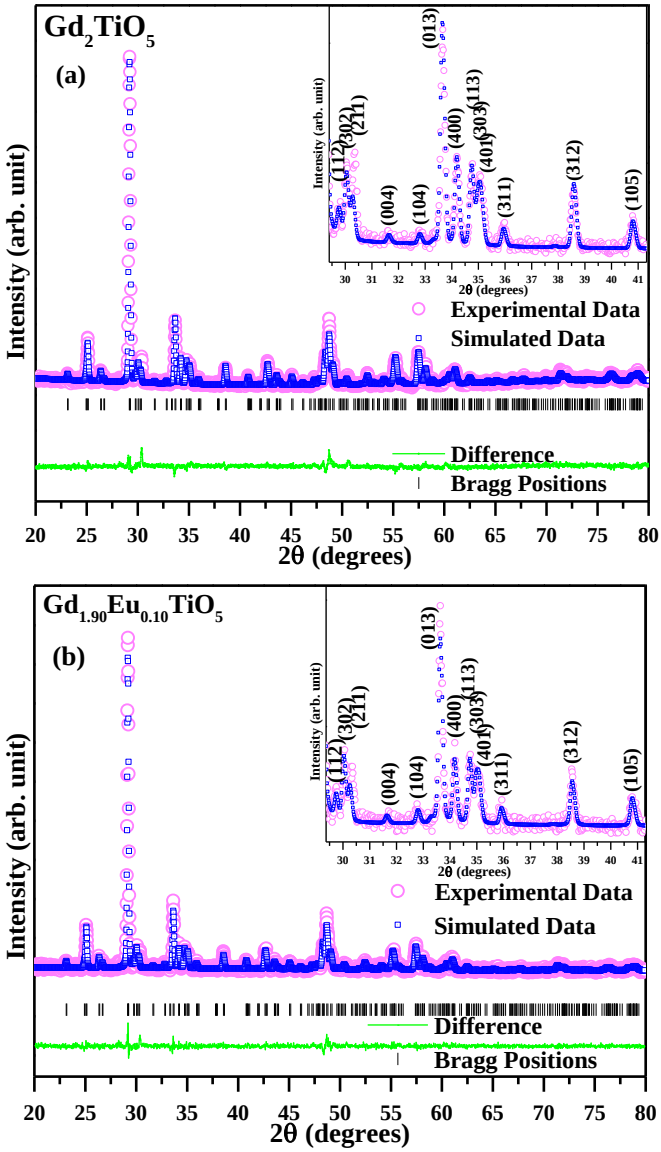
Gd2TiO5
(a)
Intensity (arb. unit)
2θ (degrees)
(112)
(302)
(211)
(004)
(104)
(013)
(400)
(113)
(303)
(401)
(311)
(312)
(105)
Experimental Data
Simulated Data
Difference
Bragg Positions
Gd1.90Eu0.10TiO5
(b)

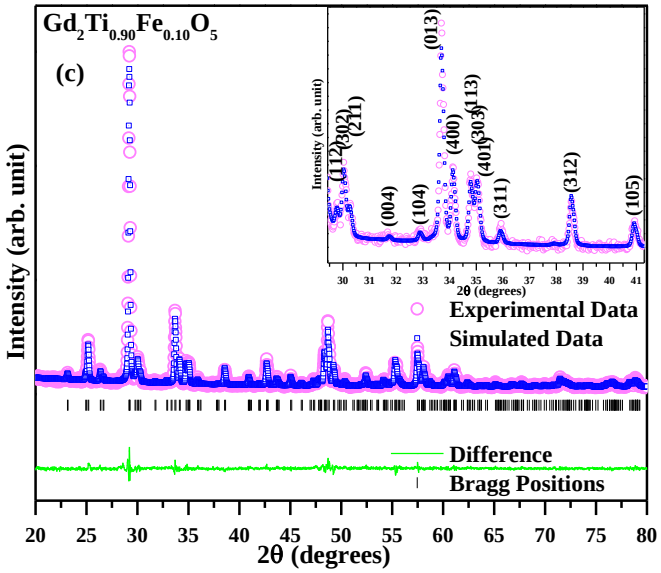

Figure 4.1a, b, and **c** show the representative Rietveld refined diffraction pattern for the pristine, Eu- and Fe- substituted samples ($Gd_{2-x}Eu_xTiO_5$) and $Gd_2Ti_{1-x}Fe_xO_5$, x = 0.10), carried out using the FullProf software. The inset figures show the goodness of the fitted data and the phase purity of the respective samples

Figure 4.2 shows the crystal structure of the primitive unit cell of Gd_2TiO_5, consisting of its four formula units, in which two Gd polyhedra (Gd_1O_7 and Gd_2O_7) are connected through a common edge. Each Gd atom is coordinated with seven oxygen atoms and forms the capped trigonal prismatic geometry. The Ti atom is coordinated with five oxygen atoms, O1, O3, O3', O4, and O5, and forms a distorted square pyramidal configuration. The Ti-O_5 polyhedron shares two common edges formed by O1, O3, and O3, O5 atoms, and a corner (formed by the O4 atom) with neighbouring Gd-O7 polyhedra, as shown in **Figure 4.2**. The five-fold coordination number and the square pyramidal geometry formed by the Ti-O_5 polyhedron are rarely observed in nature, which makes the Gd_2TiO_5 material interesting to study from the structural point of view [41, 131].

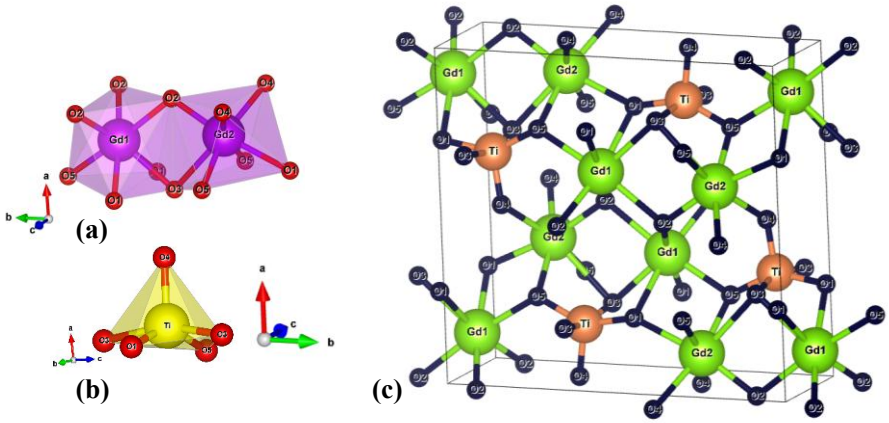

Figure 4.2a Both Gd atoms exist in seven-fold coordination with oxygen and form a capped trigonal prismatic geometry. **b** The Ti-O_5 polyhedron exists in the rarely observed distorted square pyramidal geometry. **c** The crystal structure of pristine Gd_2TiO_5 extracted from the VESTA software

4.3.2 Optical Absorption Spectroscopy (OAS)

The tailoring of the optical and electronic properties of a particular material by tuning its bandgap has enormous applications in the electrochemistry and optoelectronics industries. In contrast, diffuse reflectance spectroscopy (DRS) is an important tool for characterizing the optical properties of solid powder samples [214, 222, 223]. To investigate the optical properties of the Eu- and Fe-substituted samples, diffuse reflectance spectroscopy measurements were carried out on all the synthesized samples in the diffuse reflectance mode (DR). The optical spectroscopy data of the prepared samples have been analyzed by converting the obtained diffuse reflectance data into the Kubelka-Munk function *F*(R) [114, 224, 225] using the following relation,

$$F(\mathrm{R}_\infty) \approx a \approx \frac{K}{S} \approx \frac{(1-R_\infty)^2}{2R_\infty} \qquad (4.1)$$

where, $R_\infty = \frac{R_{\mathrm{Sample}}}{R_{\mathrm{Standard}}}$

Here, $F(\mathrm{R}_\infty)$ is the Kubelka-Munk function, which is related to reflectance *R* by the Kubelka-Munk equation [112, 203, 226]. Here, *S* and *K* represent the scattering and absorption coefficients, respectively.

R_{sample} and $R_{standard}$ represent the diffuse reflectance of the measured sample and standard sample, respectively. For the bandgap calculations, we followed the Tauc equation [167, 227], which relates the bandgap (E_g) of the material to the absorption coefficient (α) of the material through the Kubelka-Munk function and is given as

$$F(\mathrm{R}) \propto a \propto \frac{(h\nu - E_g)^{\frac{1}{n}}}{h\nu} \tag{4.2}$$

Here, 'n' gives the nature of the transition that takes place from the valence band to the conduction band. Here, 'n' is equal to 2, represents the direct bandgap transitions, and 'n' is equal to ½, corresponds to the indirect bandgap transitions [228, 229]. We have considered Gd_2TiO_5 as an indirect bandgap material in our calculation based on the theoretical calculation reported earlier [203]. The optical absorption spectra for both the Eu- and Fe-substituted Gd_2TiO_5 samples are shown in **Figure 4.3a, b,** respectively, where Eu substitution shows very small changes in the optical absorption spectra with increasing Eu content. In contrast, relatively greater changes are observed in the absorption spectra with the Fe amount. For the bandgap calculation, the absorption spectra of all the samples are fitted with Tauc's equation, which is given by **equation 2.** In the Tauc model, the optical absorption coefficient (here the $F(\mathrm{R}) \sim \alpha$) times the photon energy to the power 'n' is plotted against the photon energy (hν). The region of the Tauc plot, where a sharp linear drop in $(F(\mathrm{R}) \times h\nu)^{0.5}$ is observed, as shown in **Figure 4.4**, has been fitted with the linear equation to estimate the bandgap. The linear fits of the 10% Eu- and Fe-substituted samples, along with the pure sample, are shown in **Figure 4a** and **b**, respectively. In the case of pure Gd_2TiO_5, the bandgap was found to be 4.12 eV, which agrees well with the previous literature on this material [203]. For both cases of substitution, the bandgap was found to decrease systematically as the Eu/Fe substitution increases at the Gd and Ti sites, respectively. The bandgap decreases from 4.12 eV to 3.98 eV for the maximum amount of Eu substitution ($Gd_{2-x}Eu_xTiO_5$, x = 0.10) at the Gd-site, whereas for the Fe substitution ($Gd_2Ti_{1-x}Fe_xO_5$, x = 0.10), it was found to decrease from 4.12 eV to 3.12

eV. A detailed description of the bandgap calculation for the Fe-substituted Gd_2TiO_5 is provided in our previously published work [209]. The comparative bandgap data for both series samples are plotted in **Figure 4.5**.

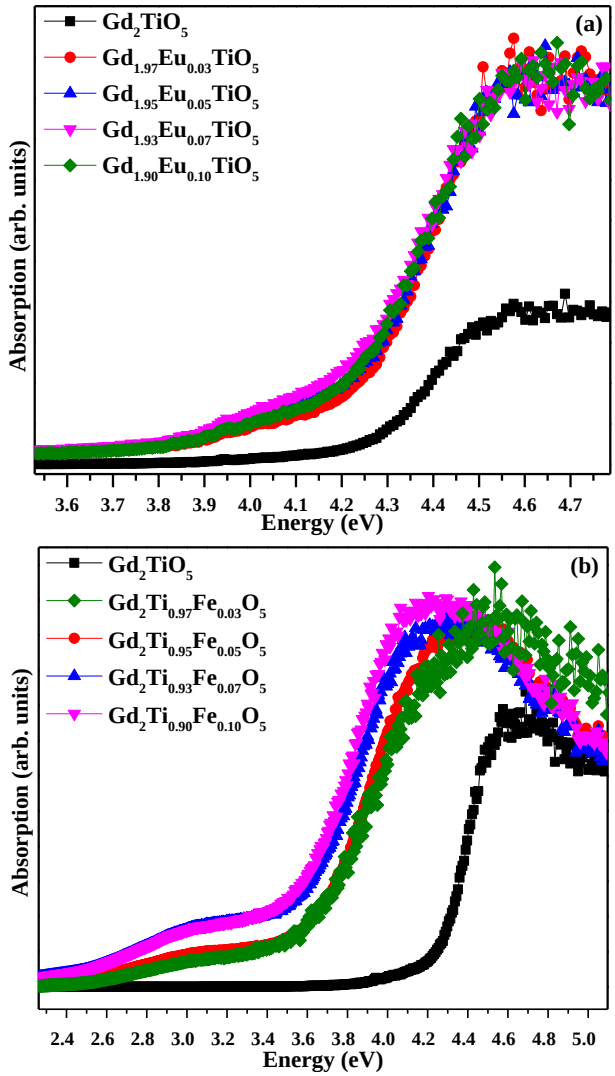

Figure 4.3 The optical absorption spectra of **a** Eu- and **b** Fe-substituted series samples ($Gd_{2-x}Eu_xTiO_5$, and $Gd_2Ti_{1-x}Fe_xO_5$, x = 0, 0.03, 0.05, 0.07, and 0.10) along with the pristine Gd_2TiO_5, carried out in the diffuse reflectance (DR) mode. The major changes in the absorption spectra compared to the parent one occurs in the case of Fe substitution

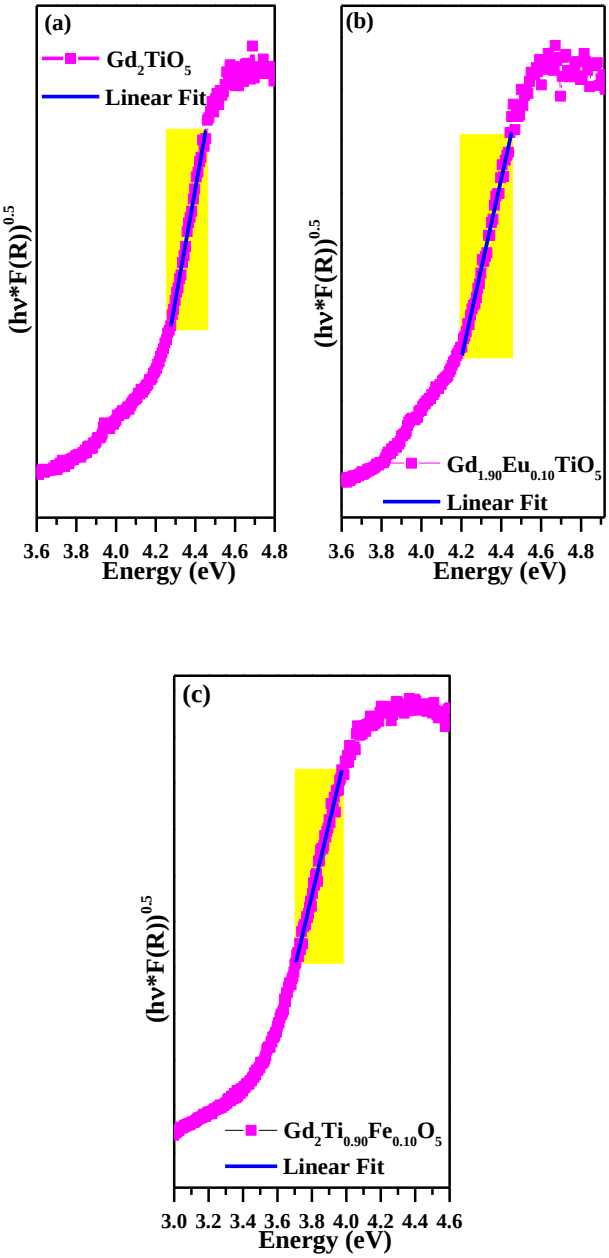

Figure 4.4a, b, and **c** show the respective linear fits of optical absorption spectra of the pristine Gd_2TiO_5, Eu- and Fe-substituted samples ($Gd_{2-x}Eu_xTiO_5$, and $Gd_2Ti_{1-x}Fe_xO_5$, x = 0.10), which are fitted using Tauc's equation for the estimation of the optical band gap

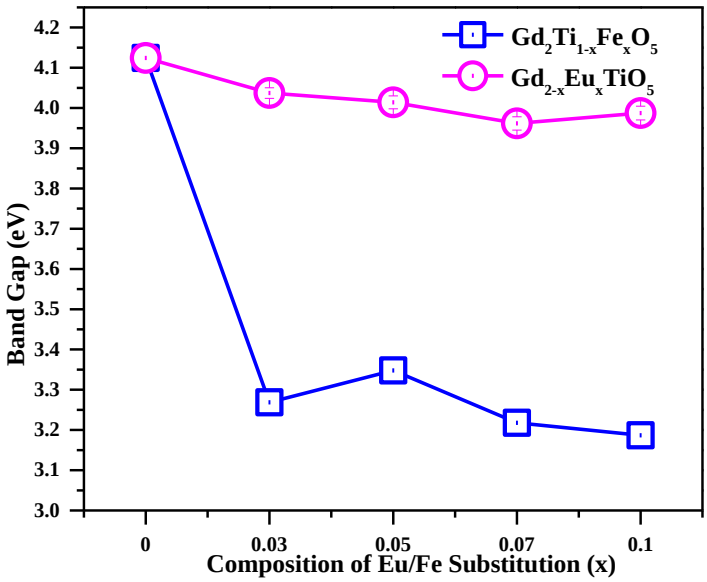

Figure 4.5 The band-gap variation observed in Eu- and Fe-substituted samples ($Gd_{2-x}Eu_xTiO_5$ and $Gd_2Ti_{1-x}Fe_xO_5$, x = 0, 0.03, 0.05, 0.07, and 0.10). The Fe-substituted Gd_2TiO_5 samples show a drastic change in the band gap with Fe concentration, whereas very little change is observed in the case of Eu substitution. The error is the order of error ~ 0.003 eV in the band gap in the case of Fe-substituted Gd_2TiO_5 samples

As clearly visible from **Figure 4.5**, both the series samples show a decrease in the value of the bandgap with Eu/Fe substitution, but the changes in the bandgap values are more for the Fe-substituted samples as compared to the Eu-substituted samples. The reduction in the bandgap, for the Fe-substituted samples, is of almost ~ 1 eV, whereas, in the case of Eu substitution, it is just of the order of ~ 0.14 eV, which is a very minor change in comparison with the parent sample. These results indicate that the substitution of any dopant at the Ti-site makes a significant contribution to the band structure formation and hence plays a crucial role in determining the bandgap properties, as compared to the Eu-substituted samples, which may have a lesser impact on the bandgap of Gd_2TiO_5. This hints that Ti-3*d* orbitals may be contributing more at the band edges and Fermi level as compared to the Gd-5*d* orbitals, and hence, the substitution of any dopant element at the Ti-site will affect the bandgap properties more significantly than making a substitution at the Gd-site. These results propose that the Ti-site, rather than the Gd-site in the case of Gd_2TiO_5, plays the dominant role in determining the band

edge and band structure properties in these rare-earth oxide systems. These results are important for understanding the band structure of these rare-earth titanates and will be applicable in enhancing their electronic and optical properties. To verify the above results, first-principles calculations were performed for both Eu and Fe substitution cases using Density Functional Theory, as explained in detail in the section below.

4.3.3 First-principles Calculations (ab initio calculations)

First-principles calculations were performed on the pure Gd_2TiO_5 sample using a 2×2×2 supercell containing 8, 4, and 20 atoms of Gd, Ti, and O, respectively. To investigate the effects of doping, we have maintained a constant doping percentage of 25%, i.e., two Gd atoms were substituted with Eu atoms to model $Gd_{1.50}Eu_{0.50}TiO_5$, and one Ti atom was replaced by a Fe atom to simulate $Gd_2Ti_{0.75}Fe_{0.25}O_5$. The density of states (DOS) results from our GGA + U calculations are shown in **Figure 4.6**. With U values of 5 eV for both Gd and Ti, we obtained a bandgap of 2.97 eV for pure Gd_2TiO_5, as depicted in **Figure 4.6a**. This theoretical bandgap is smaller than the experimentally observed value; however, we found that it is dependent on the U value used in the calculations. When the U value was increased to 8 eV, the theoretical bandgap increased to 3.2 eV in our GGA + U calculations.

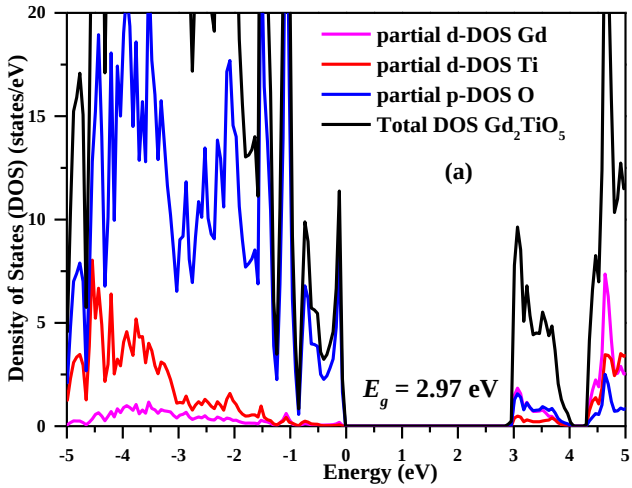

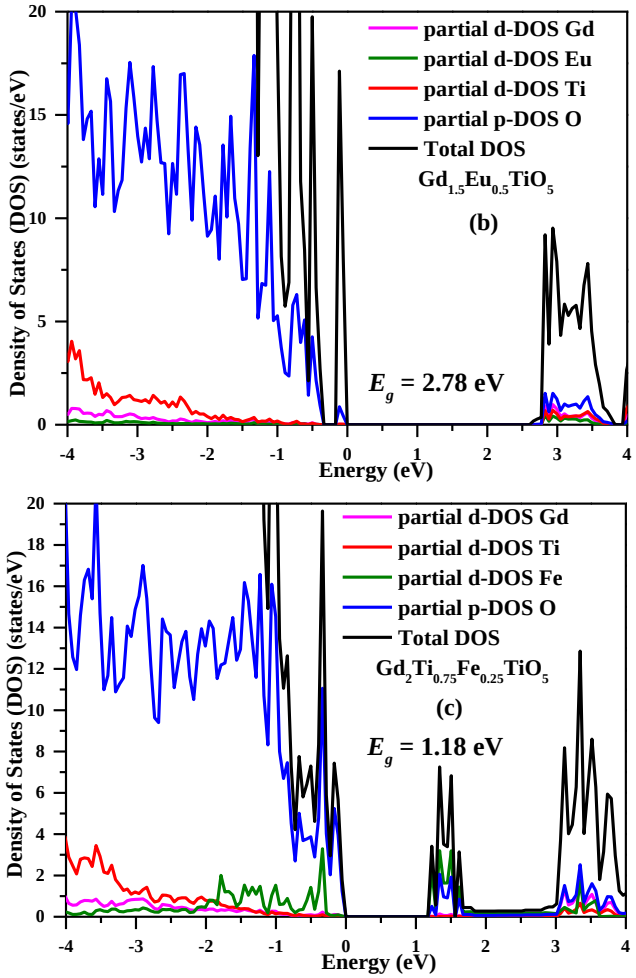

Figure 4.6 Density of states results obtained from the VASP calculations. **Figures a, b,** and **c** show the Total and partial density of states of pure Gd_2TiO_5, $Gd_{1.50}Eu_{0.50}TiO_5$, and $Gd_2Ti_{0.75}Fe_{0.25}O_5$ samples, respectively. As seen from the figures, Fe substitution causes drastic changes in the conduction band minimum as compared to the Eu substitution case, and new *p-d* hybridized states have evolved, which causes the band gap to decrease abruptly

The valence band maximum is primarily composed of O *p*-states, with minor contributions from the *d*-states of Gd and Ti. The conduction band minimum is formed by a mixture of Gd and Ti *d*-states and O *p*-states, all of which contribute significantly. In the case of $Gd_{1.50}Eu_{0.5}TiO_5$, the Eu *d*-states also contribute to both the valence band maximum and conduction band minimum. However, the introduction of Eu causes only a slight decrease in the bandgap (~ 2.78 eV), as shown in **Figure 4.6b**. In contrast, for $Gd_2Ti_{0.75}Fe_{0.25}O_5$, we observe a significant reduction in the bandgap (~ 1.18 eV) due to the appearance

of new *p-d* hybridized states, as shown in **Figure 4.6c**. Combined with the experimental results, these results conclude that Fe substitution at the Ti-site affects the bandgap properties more significantly than the Eu substitution at the Gd-site. Therefore, the bandgap structure of these rare-earth titanates can be modified accordingly by making the substitution of a suitable element at the Ti-site in comparison with the Gd-site. The above results will be helpful in exploring the band structure and altering the bandgap properties in the rare-earth titanates of the Ln_2TiO_5 system, which can further be useful for optical applications of these materials in the nuclear and radiation industries.

4.4 Summary and Conclusion

To explore the predominant contribution of 3*d* and 5*d* orbitals at the Fermi level and in the band structure of the rare-earth complex oxides of composition Ln_2TiO_5 (Ln = lanthanide element), Gd_2TiO_5 was synthesized using the conventional solid-state route, resulting in the orthorhombic phase under ambient temperature conditions. This composition features a unique fivefold coordination geometry of the titanium polyhedron, which is rarely observed in nature. To investigate the contributions of Ti-3*d* and Gd-5*d* orbitals at the Fermi edges of this rare-earth titanate, Eu and Fe were substituted at the Gd- and Ti-sites, respectively, at compositions of x values of 0.03, 0.05, 0.07, and 0.10. The phase purity of the synthesized samples was confirmed through the X-ray diffraction (XRD) measurements, and Rietveld refinement using the FullProf software was performed to extract the crystallographic information. UV-visible absorption spectroscopy, conducted in diffuse reflectance mode, was employed to study the optical absorption spectra and bandgap properties. A gradual decrease in the optical bandgap was observed with increasing amounts of both Eu and Fe substitution. However, the decrease was more significant in the case of Fe, Ti-3*d*/Fe-3*d* orbitals play a more significant role at the band edges and Fermi level compared to the Gd-5*d* orbitals. The findings were further supported by

Density Functional Theory (DFT) calculations using the VASP software, which revealed a significant alteration in the conduction bandgap upon substitution, with a change of ~1 eV. These results suggest that the case of Fe substitution, as compared to Eu substitution, and hence substitution at the Ti-site, has a more substantial impact on the band structure of these rare-earth oxides. This suggests that in the case of A_2BO_5-type complexes, the B-site, rather than the A-site, plays a crucial role in determining the band structure and bandgap properties of these materials, and consequently, their optical properties can be altered.

The above study will be useful in selecting materials with suitable optical and electronic properties for future applications in the field of photo-sensitive devices and optoelectronics. A detailed discussion on the features visible below the band edge in Fe-substituted samples, as well as their dielectric and magnetic properties, is still lacking in the present study. Additionally, there is a lack of experimental work on the vibrational study of these materials and the correlation between vibrational properties and optical and electronic characteristics [230]. The elaborative work on the vibrational and their correlation with other properties will hopefully be discussed in our future work.

Chapter 5

Interplay of Electron–Phonon Coupling and Lattice Dilation in Band Gap Tuning of $Gd_2Ti_{1-x}Fe_xO_5$

The temperature dependence of the optical band gap in oxide materials is generally governed by two phenomena: the Lattice Dilation effect and Electron-phonon coupling. The lattice dilation causes changes in bond lengths and orbital hybridisation, resulting in the shifting and renormalisation of band edges with temperature. The electron-phonon coupling allows charge carriers to interact with lattice vibrations, which produces phonon-assisted band gap reduction with temperature rise. Considering the structural disorder analogous to thermal disorder, the interplay between these structural vibrations and electronic states in has been studied in the complex oxide system of Fe-substituted Gd_2TiO_5, which exhibits competing behaviour between these two phenomena, resulting in nonlinear band gap variation with temperature. Such structural disorder-driven band gap variations will assist in determining the thermal reliability and tailoring the optical and electronic properties of Ln_2TiO_5-complex oxide materials. The additional support for the evolution of electron-phonon interactions in the system with structural disorder has been provided by the composition-dependent Raman Spectroscopy, using the well-established Fano model.

5.1 Introduction

Tuning the band gap for various applications is crucial in determining the optical characteristics of materials and their impact on device performance [231–233]. Applications in optoelectronics, such as photocatalysis, photovoltaics, light-emitting diodes (LEDs), laser diodes, and UV detectors, require optimal band gap materials that can be engineered via methods such as doping, annealing, and controlling their morphology for improved efficiency and performance. Numerous rare-earth oxides, characterized by their large band gap properties and their roles in metal-oxide-semiconductor (MOS) devices that necessitate a high dielectric constant (*k* value), require adjustments through methods such as doping, nitriding, and multilayer compositing to ensure their long-term stability in MOS applications [53, 203, 234]. As a result, band gap engineering has become a widely investigated area within the scientific community, which also requires further in-depth study of novel materials and techniques that can be easily adjusted through controllable external parameters, viz., doping, temperature variations, pressure, and structural modifications.

As we delve into the history of the problem, the fundamental absorption edge in many semiconductors was found to exhibit a red or blue shift, depending on the material and external stimuli such as temperature, pressure, and disorder in the system [235, 236]. To account for the shift of the long-wave absorption edge in semiconductors and explain their temperature dependence [237], Mőglich and Rompe [238, 239] were the first to take the initiative in explaining the behaviour of the band gap with temperature based on the lattice expansion and lattice vibration (e-ph interaction) effect with their two works of qualitative assumption. In their first work [238], they calculated the probability of an electron transitioning from the lowest band (Valence band) to the conduction band using the Debye model, where the electron gains energy through multiple interactions with lattice waves (the effect of lattice vibrations). By applying this technique, Möglich, Rompe, and

Riehl (1940) observed a minimal shift in the long-wave absorption edge, consistent with their experimental results. The effect was too small to be observable. In the second study by Möglich and Rompe [239], they investigated the contribution of lattice expansion to the red shift of the absorption edge using the one-dimensional Kronig and Penny model (1931). However, the effect appeared to be insufficient to explain the overall shift, as later experimental studies confirmed [240]. Also, Mög̈lich, Riehl, and Rompe [238, 239, 241] considered the contribution of lattice vibrations (electron-phonon interaction) to cause the broadening of energy levels and cause a shift of the whole absorption region and therefore account for the alteration of the energy band gap. However, the results fell short of the actual observed facts [242]. Then, Radkowsky [243] followed the same approach on the crystals with a broad absorption region because the absorption occurs in these crystals from the full band to the conduction band. The shift in the absorption limit with increasing temperature was found to be nearly the same in all cases. Overall, in Radkowsky's study, the presented theoretical description agreed well with the experimental data for polar crystals. Afterwards, to see the effect of lattice expansion on the band gap variation for nonpolar crystals, Bardeen and Shockley re-examined the results for Ge [244]. Then, Fan's description [241] came, which was the first significant theory of the temperature dependence of the energy band gap based on electron–phonon interactions. In their study, the authors reinvestigated the effect of lattice vibrations on the band gap of Ge and Si using the self-energy theory, concluding that the thermal expansion effect alone is insufficient for shifting the absorption edge in the cases of Ge and Si. Hence, other factors would also be necessary to provide a complete explanation of the results. Hence, it was considered that the lattice vibrations caused the shift in energy levels rather than the broadening of energy levels. Further, it was assumed that a crystal in the stationary state would have a different contribution to the electron–lattice interaction energy than a vibrating crystal that is perturbed by external stimuli. Their study concluded that the temperature dependence of the energy band gap is affected by lattice vibrations more in the case

of nonpolar crystals, whereas for polar crystals, the analysis was the same as that obtained by Radkowsky [243], where lattice expansion was sufficient to explain the experimental results for Si, but the results were not in much agreement for Ge. Based on Fan's formalism, Cohen [245, 246] later used more sophisticated phonon dispersion relations to obtain satisfactory results for Ge. Fan's theory was quite successful in explaining most of the results, explaining the decrement in the fundamental band gap with temperature; however, it was not able to explain the blue shift in the absorption edge with increasing temperature in some of the materials, like PbS, PbSe, and PbTe [247–251].

The most successful and widely accepted theory following Fan's calculations was based on the Brooks–Yu treatment, which was an unpublished work [252]. Based on Brooks and Yu's treatment, many researchers have presented their work, considering the temperature dependence of pseudopotentials with modified Debye–Waller factors [253–255]. Using the same approach, Keffer, Hayes, and Bienenstock (*Keffer et al.*, *1970*) employed several pseudopotentials for calculations in the case of PbTe, yielding a good agreement between the theoretical and experimental results, which further supported the Brooks–Yu theory [250]. After that, Tsang and Cohen *(Tsang and Cohen et al., 1971)* used their own value of pseudopotentials to match the theoretical calculations with experimental ones [246]. However, in Mostoller's study [24], it was examined that Fan and Brook's results have the same order of magnitude and are additive. Following this, one of Guenzer's reports [24] on the temperature dependence of the HgTe band gap was published, which concluded that the temperature dependence of the band gap still requires a more rigorous discussion and extensive calculations to reconcile the theoretical calculations with experimental results [256]. From the above-mentioned works, it was concluded that using suitable zero-temperature pseudopotential form factors and Debye–Waller factors [242, 243, 257] yields a good agreement between theoretical values and experimental results.

To date, numerous rigorous studies have been conducted to investigate the role of electron-phonon interactions and lattice dilation (Volume effect) in semiconductors and oxide materials, such as perovskites. In the late 1980s, a study by *Gopalan et al. (1987)* [258] calculated the contribution of e-ph interaction in the case of GaAs by considering the Debye-Waller and self-energy terms using a previously developed rigid-ion pseudopotential model for Ge and Si. In another theoretical study of the temperature dependence of band gaps in semiconductors, *Bhosale et al.* investigated the electron–phonon interaction for a series of chalcopyrite structures containing d-electron atoms [256].

Electron–phonon coupling (EPC) and lattice dilation are crucial in understanding material properties, particularly at higher temperatures, as they significantly influence phenomena such as negative thermal expansion [256, 259, 260]. Although there is enough literature available [245, 246, 256, 257, 261, 262] on calculating the strength of electron–phonon interaction theoretically as well as experimentally for finding the contribution to the temperature dependence of the band gap and the material's phononic properties, there is still very little work carried out on finding the explicit contribution of the lattice dilation effect in complex oxide materials [254, 255, 263, 264]. Additionally, this phenomenon has been studied by taking into account the disorder introduced into the system due to temperature and other thermal effects. Nevertheless, it is important to note that several material properties (including band gap) can be tuned by chemical substitution as well; in that view, a deeper insight into the cumulative effect of charge–lattice coupling and lattice dilation as a result of chemical substitution can be significant; however, it is not explored as vastly as temperature or pressure effects. Keeping this in consideration, in our study, we have attempted to find the cause of the variance of the band gap with respect to the general disorder coming from doping or other substitutional effects, which is analogous to temperature, causing the perturbation in

the electronic levels of the solid, and giving rise to disorder in the system.

In the mid-20th century, the awareness of managing nuclear waste took a great turn after acknowledging the fact that some waste, such as plutonium, remains radioactive for thousands of years [188, 265]. Therefore, this waste needed to be immobilised in either glass or ceramic materials that have resistance against high levels of radiation, chemical durability, impermeability to liquids, and long-term stability against degradation. In this regard, relevant materials, such as rare-earth titanates, particularly those with zirconolite or pyrochlore structures, have been found to be promising for handling and immobilising high-level nuclear waste (HLW). Focusing on these materials, the Ln_2TiO_5 (Ln = La, Sm, Gd, Tb, Dy, Ho, Er, and Yb) series is primarily suitable for incorporating the actinides (e.g., U, Pu, Am, Np) in their orthorhombic host lattice, exhibiting controlled amorphization under irradiation, and after annealing, it returns to the original structure [37, 69, 121]. Additionally, these materials have numerous applications in the optoelectronic industry due to their remarkable optical properties. As in our previous report, Gd_2TiO_5 was found to be an efficient diffusion-dominated electroactive dopant, which enhances the diffusion-controlled mechanism in electrochromic devices due to its high thermal and dielectric properties. The most researched electrochromic material, poly(3-hexylthiophene) (P3HT), has limited redox activity; however, when doped with Gd_2TiO_5, it was found to facilitate the diffusion mechanism and increase the device's overall efficiency and performance [187].

Concentrating on all these facts, Gd_2TiO_5 with Fe as a substituent at the Ti site ($Gd_2Ti_{1-x}Fe_xO_5$; x = 0.03, 0.05, 0.07, 0.10) was chosen due to its enhancing magnetic characteristics, catalytic action, and structural compatibility, having a similar radius to the Ti ion [130, 209]. The Ti site plays an important role in governing the electronic and optical properties of these materials due to the dominance of Ti-3d orbitals at the

conduction band edges in the density of states of Ln_2TiO_5-type titanates, as reported in our previous work [180, 203, 266], which makes Ti a suitable substitutional site, and Fe is the best dopant material.

Gadolinium (Gd^{3+}) exhibits a superior neutron absorption cross-section, rendering Gd_2TiO_5 suitable for controlling nuclear reactions [122, 267]. It serves as the best candidate for the long-term disposal of hazardous waste in geological repositories [3, 27, 68] due to its higher stability and low dissolution rate under groundwater-like conditions. As evidenced by recent work, Gd_2TiO_5 (gadolinium titanate) can be used as a single-component white-emitting phosphor when doped with specific rare-earth ions, such as Dy^{3+} (dysprosium) and Eu^{3+} (europium). Gd_2TiO_5 can be utilized for enhancing the photocatalytic degradation of dyes for wastewater treatment by using suitable metal dopants (such as iron (Fe) or europium (Eu)), which can enhance light absorption and charge separation. Fe doping can significantly reduce the band gap of Gd_2TiO_5, favouring the formation of oxygen vacancies that act as electron traps and hinder recombination with photogenerated holes, thereby improving the photocatalytic efficiency [187, 268, 269]. Now, what makes the Gd_2TiO_5 structure unique is the 5-fold coordination number of the Ti atom [131], which is exceptionally rare in most of the titanium-containing oxides. Gd_2TiO_5 exists in the orthorhombic phase [8, 27] with the *Pnam* space group at room temperature and exists in a 3-dimensional crystal structure, where the GdO_7 polyhedron shares corners and edges with other GdO_7 and TiO_5 polyhedra. The TiO_5 polyhedron forms a distorted square pyramidal geometry, which is usually not seen in most oxides [20, 69]. This makes the Gd_2TiO_5 an interesting material from the structural point of view, as most of the electrical and optical properties have been studied in the correlated oxides, where the titanium atom is found to exist in a tetrahedral or an octahedral cage [222, 270]. Hence, it will be interesting to correlate the structural, optical, and vibrational properties in these rare-earth titanates and to observe to what extent the geometry and structural modifications

affect these properties. Also, these rare-earth titanates (Ln_2TiO_5, Ln = lanthanide), when doped with transition metal ions like Mn^{2+}, Fe^{3+}, Co^{2+}, Ni^{2+}, or Cr^{3+} (which have d1–d9 configuration), can be expected to exhibit d–d transitions [271–273]. Speculating that the defect/structural disorder and line broadening originate from d–d transitions can provide information about the electron–phonon coupling (EPC) prevailing in the system, which can be further characterized using Vibrational Raman spectroscopy [274].

To investigate the correlation between optical, structural, and vibrational properties, optical absorption spectroscopy (OAS) and composition-dependent Raman spectroscopic measurements have been performed on Fe-doped Gd_2TiO_5 samples. Band gap analysis reveals systematic variations with Fe substitution, consistent with Raman analysis, which indicates an increase in structural disorder and electron–phonon coupling within the system.

5.2 Experimental Details

5.2.1 Synthesis Techniques

To investigate how the lattice vibrations and lattice expansion play a role in the band gap variation, the bulk sample of Gd_2TiO_5 [8, 15] belonging to the rare-earth titanate system [14, 18, 185, 275] has been chosen. To further explore the trend, Fe has been substituted at the Ti site, respectively, with the amount x having values of 0.00, 0.03, 0.05, 0.07, and 0.10, forming the respective compositions $Gd_2Ti_{1-x}Fe_xO_5$ (GTFO). The sample series, including the parent one, was synthesized using the conventional solid-state method [91, 94, 96, 266, 276]. The detailed procedure for the method has been described in Chapter 2.

5.2.2 X-ray Diffraction and Rietveld Refinement

The phase purity of the synthesised samples of Fe-substituted GTO series ($Gd_2Ti_{1-x}Fe_xO_5$; x = 0.03, 0.05, 0.07, 0.10) were checked by

the X-ray diffraction technique [68, 116], where no impurity peak was found in the XRD pattern, indicating the pure phase of the prepared samples. The samples were found to be exhibiting an orthorhombic phase [68] with the *Pnam* space group [37, 121]. For the structural phase and crystal parameter information, Rietveld refinement [139, 218, 277–279] was performed on all samples using the FullProf software, which confirmed the phase purity of the synthesised samples. A detailed description of the X-ray diffraction technique is summarised in Chapter 2.

5.2.3 Optical Absorption Spectroscopy

For determining the optical characteristics of the synthesized samples, the UV–vis spectroscopy [147, 280] measurements were performed on all the samples using the Diffuse reflectance method, where the diffuse reflectance [106, 151, 281] was converted into the absorption spectrum using the Kubelka–Munk function, which is further related to the absorption coefficient through the Kubelka–Munk equation, as explained in detail in Chapter 2. The absorption spectrum was collected with a scan rate of 60 nm/min, within the range of 200 to 600 nm. The baseline was carried out with a reference sample [282] of $BaSO_4$, which provides an accurate and stable baseline in the visible and near-infrared regions.

5.2.4 Raman Spectroscopy

The LABRAM HR dispersive spectrometer [115, 117, 118], equipped with a CCD detector in backscattered mode, was used to perform Raman spectroscopic [118, 283, 284] measurements on Fe-substituted Gd_2TiO_5 powder series samples. An excitation laser source with a 633 nm wavelength was used to collect the data, along with a grating having 600 grooves per millimetre. A compensating microscope objective with a magnification of 50× was used to achieve better spatial

resolution and signal strength. The laser beam power was adjusted to be approximately 2 mW.

5.3 Results and Discussion

The fundamental edge in the optical absorption spectra of most semiconductors was found to exhibit a red shift with increasing temperature (thermal disorder) [235]. Nevertheless, blue shifts are also observed due to lattice disorder resulting from thermal, chemical, and structural perturbations in the electronic states of the system [285]. For the case of temperature-induced variations, this disorder in the system leads to thermal expansion or contraction, depending on the material's properties [286–288], and an increase in electron–phonon interactions within the system, which together are responsible for the disorder-dependent variation of the band gap in semiconductors. That is, if we take temperature as a specific case of disorder present in the system, then this will generally have contributions from the two effects: thermal expansion and electron–phonon interactions within the system. The well-known equation of temperature dependence [237, 289, 290] of the energy band gap with temperature is given by **equation (5.1)** as

$$\left(\frac{\partial E_g}{\partial T}\right)_P = \left(\frac{\partial E_g}{\partial T}\right)_V + \left(\frac{\partial E_g}{\partial lnV}\right)_T \left(\frac{\partial lnV}{\partial T}\right)_P \tag{5.1}$$

where the $\left(\frac{\partial E_g}{\partial T}\right)$ gives the temperature coefficient of the energy band gap at constant pressure. The term $\left(\frac{\partial E_g}{\partial lnV}\right)$ represents the band-gap expansion coefficient and the term $\left(\frac{\partial lnV}{\partial T}\right)$ gives the temperature coefficient of lattice dilation (Volume-thermal expansion coefficient).

The first term in the above expression gives the contribution of the electron–phonon interactions, and based on the well-known theories given by Fan and Brooks [241, 252, 291], many researchers have tried to find the explicit contribution of the electron–phonon interaction using the calculation of electron self-energy terms and Debye-Waller (DW)

factors. The second term on the right-hand side, as a whole, represents the contribution of thermal expansion (lattice dilation) and can be determined both theoretically and experimentally through band structure calculations and the pressure dependence of the band gap, respectively [251, 285, 289]. While it is common to expect the lattice to expand with temperature, however, there exist physical systems where the lattice contracts with an increase in temperature [286–288]. In the case of Fe-substituted Gd_2TiO_5, XRD and refinement results indicated an expansion in the system. In one of the works done by *Olguín and Cardona et al. (2002)* [261], they have described **equation (5.1)** with a thermal expansion term given by the following equation, **equation (5.2)**

$$\left(\frac{\partial E_g}{\partial T}\right)_{TE} = \left(\frac{\partial E_g}{\partial p}\right)_T \left(\frac{\partial p}{\partial\, lnV}\right)_T \left(\frac{\partial\, lnV}{\partial T}\right)_P = -3ab\left(\frac{\partial E_g}{\partial p}\right)_T \qquad (5.2)$$

Here, $a = L^{-1}\left(\frac{\partial L}{\partial T}\right)$ is the linear expansion coefficient, and $B = -V\left(\frac{\partial p}{\partial V}\right)_T$ gives the isothermal bulk modulus. In their study, they calculated the contribution of self-energy terms and Debye–Waller factors using the tight-binding (linear combination of atomic orbitals) approach. It is known from previous scientific efforts that electron–phonon interactions give rise to a decrease in the band gap, and the dominance of lattice dilation (second term) makes the band gap responsible for the increase in the band gap with temperature. In a recent study by *Saxena et al.*, the contribution of electron–phonon interaction was quantified using the Frohlich theory in the case of Hybrid halide perovskites ($CH_3NH_3PBX_3$, X = I, Br, and Cl) [235]. They proved that enhancement in the band gap (E_g) in the case of $MAPbX_3$ (X = Br, I) is caused by the lattice dilation effect. However, the band gap was found to decrease in the case of $MAPbCl_3$, where the interaction of the LO phonon mode (Longitudinal Optical phonon mode) with the charge carriers via Frohlich interaction dominated, which is one of the most prominent mechanisms of electron-phonon interactions occurring in

materials. It should be noted that temperature variation introduces modifications in the lattice via unit cell expansion (also contraction in some cases) [288] and affects the electron–vibration interaction strength. Consequently, the electronic levels themselves and the Fermi level can change significantly, resulting in a variation in the material's band gap. Interestingly, the underlying chemical potential that is altered in such a process may also be affected by other physical conditions, viz., chemical substitution in the host lattice [292–294]. While temperature appears as a standard thermodynamic variable that defines the state of the system, chemical substitution can also affect the thermodynamic behaviour under given conditions, such as the variation of the band gap. This is because of the obvious effects on the lattice volume (dilation) and the Fermi level shifts due to modified orbital hybridizations (electron–phonon coupling). Therefore, the chemical substitution content in a solid host lattice can be viewed as an unconventional parameter that alters the optical band gap through the emerging lattice dilation and EPC effects, yet it remains underexplored. This is scientifically significant in view of tuning the optical properties for room-temperature applications. Thus, an explicit understanding of the LD and EPC effects is of importance.

In our work, we have considered that thermal and structural disorder are analogues to soften the phonon modes and/or to cause the lattice volume changes, eventually affecting the optical band gap (but to different extents). Hence, if we rewrite **equation (5.1)** of the temperature dependence of the band gap by considering only the substitution-induced structural disorder present in the system, we can write **equation (5.3)** as

$$\left(\frac{\partial E_g}{\partial c}\right)_P = \left(\frac{\partial E_g}{\partial c}\right)_V + \left(\frac{\partial E_g}{\partial \ln V}\right)_c \left(\frac{\partial \ln V}{\partial c}\right)_P \tag{5.3}$$

Here, c represents the concentration of the Fe content in Gd_2TiO_5, and dc gives the change in the consecutive values of the Fe concentration.

One can directly observe the variation of E_g with Fe content at ambient pressure, which would give the term on the LHS in **equation (5.3)**, i.e., the rate of variation of band gap with change in the Fe concentration. Furthermore, the contribution of the second term (lattice dilation term) can be experimentally accessed via the parallel analysis of the unit cell and electronic band structures, using X-ray diffraction and UV–vis spectroscopy measurements, respectively, as pursued in the current study. Although the explicit calculation has not been done for the first term (e–ph interaction contribution), it can be derived if the other two terms are known. Thus, we are able to resolve the effects of lattice dilation and electron–phonon coupling in these systems. The Raman Spectroscopy experiment was also performed to observe the impact on vibrational modes. The results of optical absorption spectroscopy and Raman spectroscopy are discussed in the following sections.

5.3.1 Material Characterization

For the phase-purity characterization of the Fe-substituted Gd_2TiO_5 samples, X-ray diffraction was taken, which confirmed the orthorhombic phase of all the synthesized samples with the *Pnam* space group [28, 133, 295]. All of the substituted samples were found to be in the pure phase, as observed from the X-ray diffraction pattern of the pure and Fe-substituted samples. The structural parameter information on the lattice parameters was calculated from the Rietveld refinement [46, 138, 139, 220, 278] using the VESTA software, which shows a systematic variation with Fe content. The refinement pattern for the 10% Fe-substituted sample is shown in **Figure 5.1**, the goodness of the fit indicates satisfactory results between the observed and calculated patterns. **Figure 5.2** shows the variation in the lattice volume with Fe concentration extracted from the refinement results. The volume of the overall unit cell was found to increase with the Fe content, exhibiting an expansion in the Gd_2TiO_5 (GTO) system as the Fe concentration increased.

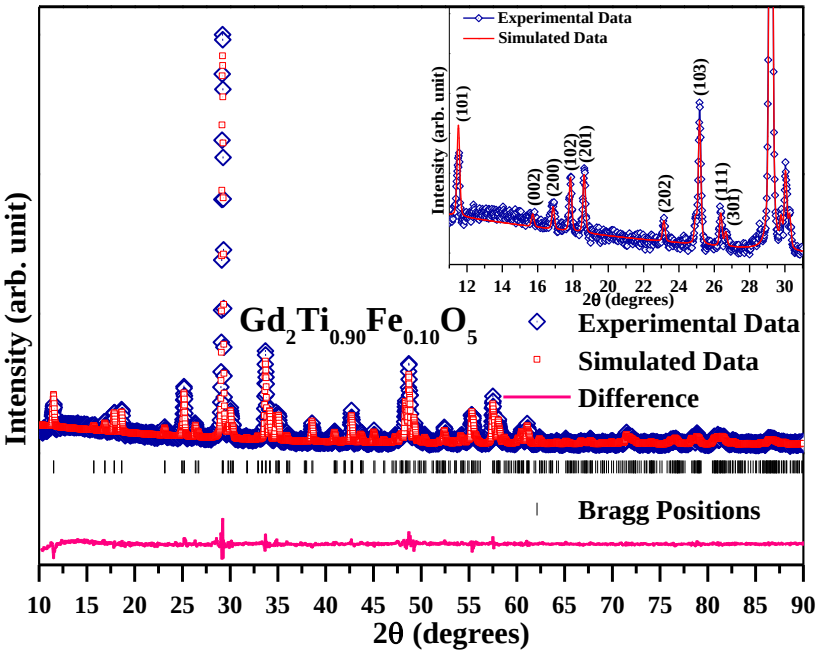

Figure 5.1 The figure shows the refinement pattern for the 10% Fe-substituted Gd_2TiO_5 sample. The inset figure shows the goodness of the fit of the refinement pattern, indicating the orthorhombic phase of Gd_2TiO_5 with the *Pnam* space group

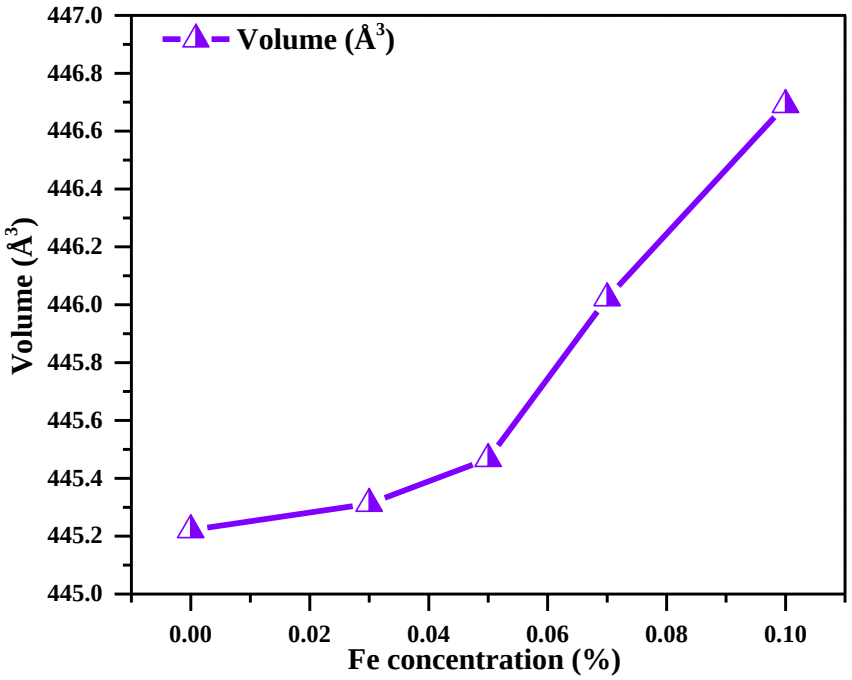

Figure 5.2 The overall volume of the unit cell extracted from refinement results shows the systematic increment with increasing Fe content, exhibiting expansion in the Fe-substituted Gd_2TiO_5 (GTO) system

5.3.2 Optical Absorption Spectroscopy and Band Gap Analysis

To study the effect of structural disorder on the electronic, structural, and optical properties of these rare-earth titanates, optical absorption spectroscopy was performed on the Fe-substituted samples [189, 215]. Optical absorption spectroscopy [166, 296, 297] is a useful and simplified technique that can be used to obtain band gap properties and band structure information of any material [48]. In this method, electrons of known energy are excited to higher energy levels, and in return, information about the optically allowed transitions at these levels can be obtained. In this work, diffuse reflectance spectroscopy (DRS) [298, 299] was used to calculate the optical absorption spectra of Fe-substituted Gd_2TiO_5 samples, a non-destructive technique applicable to a variety of samples. In this technique, diffuse reflection data are collected from the sample, providing information about the material's optical absorption. The diffuse reflectance data obtained is then converted into the absorption data by the well-known Kubelka−Munk theory [150, 300], where the reflectance R is related to the scattering (S) and absorption (K) coefficients and given by the following equation, **equation (5.4)**

$$R_\infty = \lim_{n\to\infty} R_\infty = a - b = 1 + \frac{K}{S}\sqrt{\frac{K^2}{S^2} + 2\frac{K}{S}} \tag{5.4}$$

Here, $R_\infty = \frac{R_{\text{Sample}}}{R_{\text{Standard}}}$, and $a = \frac{S+K}{S}$, $\quad b = \sqrt{a^2 - 1}$

The above equation holds for the infinitely thick samples, where R_{Sample} and R_{Standard} represent the diffuse reflectance of the measuring sample and the standard sample, respectively. In the present case, $BaSO_4$ was chosen as the standard sample. $F(R)$ represents the Kubelka–Munk function, which relates to reflectance R and the absorption coefficient α of the material by the Kubelka–Munk equation (K–M equation). In the

limiting case of infinitely thick samples, the K–M equation can be written as **equation (5.5)**

$$F(R) \text{ or } a \approx \frac{K}{S} \approx \frac{(1-R_\infty)^2}{2R_\infty} \quad (5.5)$$

For the band gap calculation, we followed the Tauc equation [301, 302], which relates the band gap to the absorption coefficient (α) [107] of the material through the Kubelka–Munk function and is given by **equation 5.6** as

$$F(R) \propto a \propto \frac{(h\nu - E_g)^{1/n}}{h\nu} \quad (5.6)$$

Here, "*n*" gives the nature of the transition that takes place from the valence band to the conduction band, where "*n*" is equal to 2, representing the direct band gap transition, and "*n*" is equal to 1/2, representing the indirect band gap transition.

The optical absorption spectra of the pure and 10% Fe-substituted Gd_2TiO_5 sample are shown in **Figure 5.3**. The band gap values were calculated and found to show a systematic decrement with Fe substitution, as shown in **Table 5.1**; the detailed characterization is described elsewhere [209]. It is noted that in the optical absorption spectra of Fe-substituted samples, a broad hump emerges near ~3.0 eV, which becomes more pronounced with the increasing Fe concentration, as seen in the optical absorption spectra of the 10% Fe-substituted sample (**Figure 5.3**). This feature may arise from two possible origins: (i) the formation of oxygen vacancies induced by Fe substitution [166] or (ii) the presence of additional states that appear near the conduction band minimum (likely Fe-related states), as suggested by the band structure of the 10% Fe-substituted Gd_2TiO_5 sample, as hinted in our earlier study [209]. This feature needs further investigation via advanced techniques [303]. Hence, the decrease in the band gap could be attributed

to these additional states observed in the band structure of the Fe-substituted Gd_2TiO_5 samples. Additionally, structural disorder arises in the system as the Fe substitution increases, which includes contributions from the lattice dilation effect and increased electron–phonon interactions within the system. To find the individual contribution of lattice dilation and the role of electron–phonon interactions in the observed behaviour of the band gap with Fe amount, we calculated the contribution of the second term on the right side of **equation (5.3)** by using the simple mathematics of derivatives. Since the consideration of derivatives mathematically requires continuous functions, however, we are limited to a finite, discrete data set while dealing with chemical substitution. This problem can be overcome by considering a suitable Fe-content-dependent model function that describes the observed trend and is continuous within the considered range of Fe concentrations. Thus, the derivative of the same can be dealt with, and the necessary information can be obtained. We have followed the same approach for each of the required cases, specifically for the Fe content-dependent band gap, volume, and interdependence of band gap and volume. This, in a way, also provides a perspective for interpreting the underlying correlation between the physical quantities related to the band structure and the lattice dimensions.

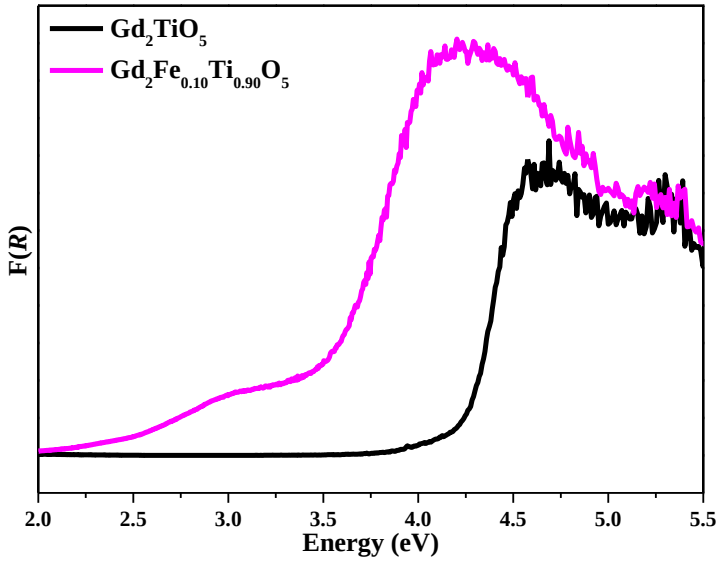

Figure 5.3 The optical absorption spectra of the pure and 10% Fe-substituted sample exhibiting significant shift in the band edge toward higher wavelength with Fe substitution

Table 5.1 The band gap values were calculated from the optical absorption spectra using the Tauc equation. The error in the second column represents the statistical error. The instrumental error for optical absorption measurements is of the order of 5 meV, and the statistical error is of the order of 3 meV

Fe concentration in Gd_2TiO_5	**Band Gap (eV)**
0	**4.125**
0.03	**3.309**
0.05	**3.296**
0.07	**3.138**
0.10	**3.116**

The experimental results of the overall band gap values were plotted as a function of Fe concentration, which shows the exponential decrement as shown in **Figure 5.4a** and is fitted with an exponential equation to interpolate the large number of data points in order to realize the derivative (coefficient of energy band gap, $(\partial E_g/\partial c)_P$ more consistently in reference to **equation (5.3)**. The respective derivative curves are shown in **Figure 5.4b**. In the second step, we plotted the

variation of logarithmic volume with Fe concentration and fitted the equation again with the exponential function, followed by the derivative of the curve (coefficient of lattice dilation ($(\partial \ln V/\partial c)_P$), which gave the contribution of the temperature coefficient of the lattice dilation term. The respective plots are shown in **Figures 5.4c** and **5.4d**. Similarly, for further calculation of the lattice dilation contribution (LD term), the band gap is plotted as a function of the natural logarithm of the volume and fitted with an exponential decay function, as shown in **Figure 5.4e**. The derivative of the curve $(\partial E_g/\partial \ln V)_c$ is illustrated in **Figure 5.4f**. Now, the calculated derivative product $(\partial E_g/\partial \ln V)\cdot(\partial \ln V/\partial c)$ represents the LD effect and accounts for the variation in the band gap resulting from volume change. The e–ph contribution $(\partial E_g/\partial c)_c$ was obtained after subtracting the lattice dilation term from the total contribution of the variation of the band gap with Fe substitution $(\partial E_g/\partial c)_P$. After that, individual contributions of the first (~EPC) and second term (~lattice dilation) are plotted in **Figure 5.5a** along with the total contribution of band gap variation with Fe concentration, and **Figure 5.5b** shows the plot of all the terms on a single axis. The derived variations, which are expected to distinctly represent the band gap variation due to volume– and electron–phonon coupling effects, likely represent the contribution of the respective interaction to cause the observed band gap variation.

From the plots (**Figure 5.5a** and **5.5b**), it is inferred that the concentration derivative of the band gap is negative for Fe content ≤10%; however, it becomes less negative (tends to 0) with increasing Fe content. This is because the band gap reduces exponentially with the Fe concentration and attains an asymptotic behaviour, as observed from the experimental data (**Figure 5.4a**). The band gap variation due to the volume effect is greater at low Fe concentrations, as the Gd_2TiO_5 host lattice undergoes significant local modifications in the unit cell dimensions. However, as the Fe content increases, more Fe substitutions occur at the Ti site, leading to a global equilibrium in the unit cell volume that shifts away from the host lattice value. It should be noted that the

volume is found to systematically expand with increasing Fe concentration, as indicated by the values from the Rietveld refinement output (**Figure 5.2**). The obtained plot for the LD effects can be understood to represent the part of the band gap variation as the cell volume changes, which is stronger only at lower concentrations, and for Fe% >1%, this contribution seems to decrease significantly and asymptotically approaches zero (**Figure 5.5a** and **Figure 5.5b** lattice dilation curve). Similarly, the plot of the EPC versus Fe concentration (**Figures 5.5a** and **5.5b**, e–ph curve**)** represents the contribution of charge lattice interaction to the variation in band gap as the Fe content changes. The curve initially is positive and traces a sharp drop to negative values within 1% Fe variation. Nevertheless, it then increases and asymptotically tends to zero. This means that the band gap slightly opens at low Fe doping; however, this is not realized due to the parallel compensation by the volume expansion effect, as we sample the simultaneous effects in a regular absorption experiment. However, at higher Fe content, the EPC interaction appears to contribute to the band gap shrinkage and ultimately achieves saturation, as evidenced by the asymptotic value of zero. From temperature-dependent band gap studies on semiconductors, it is known that the gap decreases with increasing temperature due to enhanced electron–phonon interactions. However, it should be noted that the stimulus here is of chemical origin rather than the temperature.

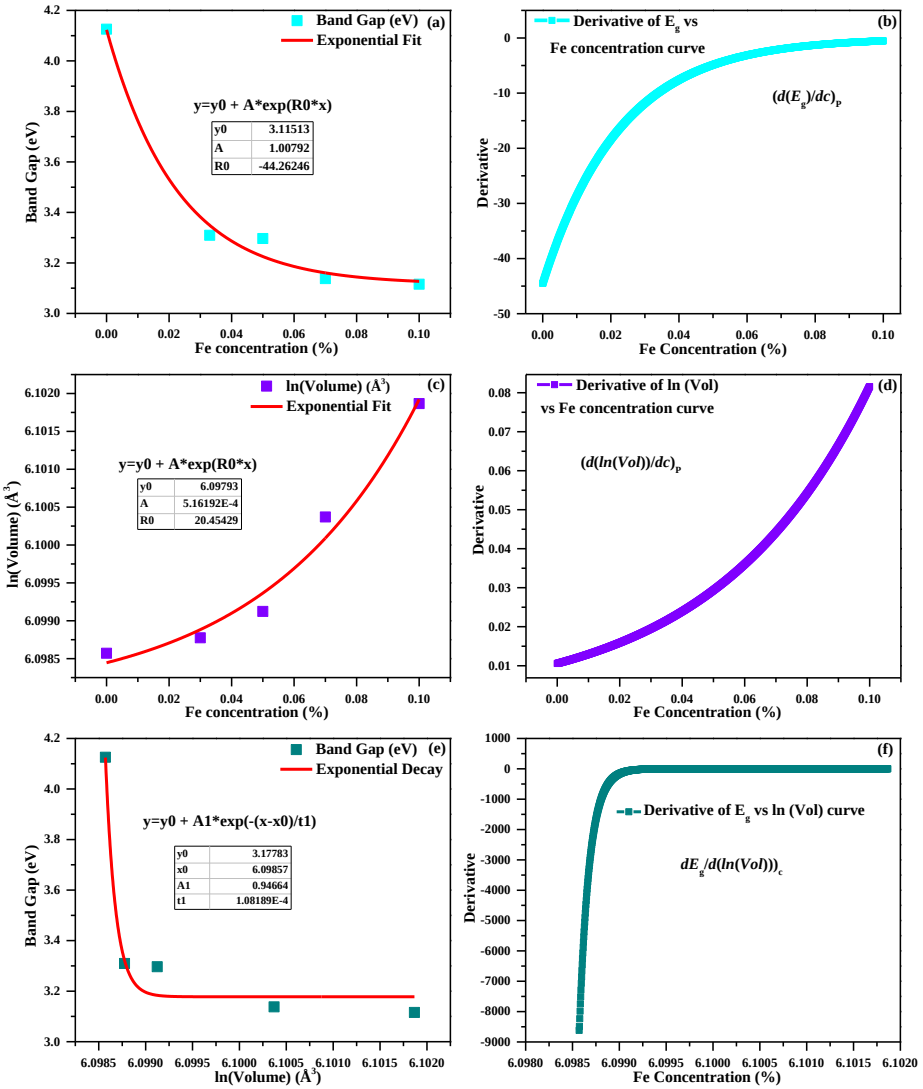

Figure 5.4a The optical band gap shows a systematic decrement with the increasing Fe amount and shows a good agreement for the exponential equation fit. **Figure b** shows the derivative of the curve of band gap (E_g) vs Fe concentration at constant pressure ($(\partial E_g/\partial c)_P$). **Figure c** shows the natural logarithm of the volume as a function of Fe concentration, fitted with the exponential function. **Figure d** shows the derivative curve of the ln (Volume) vs Fe concentration curve at constant pressure ($(\partial \ln V/\partial c)_P$). **Figure e** shows the variation of the band gap data as a function of the logarithmic volume plot, fitted using the exponential decay function. **Figure f** represents the derivative of the band gap vs ln (Volume) curve representing the contribution as $((\partial E_g/\partial \ln V)_c)$

The temperature-induced band shifting of electronic levels in semiconductors is quite trivial, which cannot be the case for chemical substitution, as it is often strongly dependent on how hybridization is affected. Furthermore, Fe^{3+} is more stable in octahedral coordination, so the aliovalent substitution at the Ti^{4+} site can introduce additional states within the forbidden gap region (evident from the optical absorption spectra of GTFO samples as discussed in Chapter 3) [209], which can also couple with the lattice phonons in a nontrivial manner. This may also include nonsymmetric shifting of valence and conduction bands arising from the EPC due to the Fe substitution. Once the Fe concentration is enough that the (conduction) bands are potentially dominated by their *d*-character and the resulting defect states can form into a band rather than a state in the forbidden region, the trivial contribution for EPC can be realized as the negative derivative term at later Fe content values. This contribution also saturates as the calculated term can be seen to reach zero; however, it does so quite slowly compare to LD effects. Though the contribution to band gap variation due to the LD effects rapidly approaches zero, the nonzero values of the same for the derived EPC contribution suggest EPC-dominated variation of the overall band gap as a result of Fe substitution in the GTFO system. Thus, our work aims to understand the variation in band gaps induced by chemical perturbations in the Gd_2TiO_5 system.

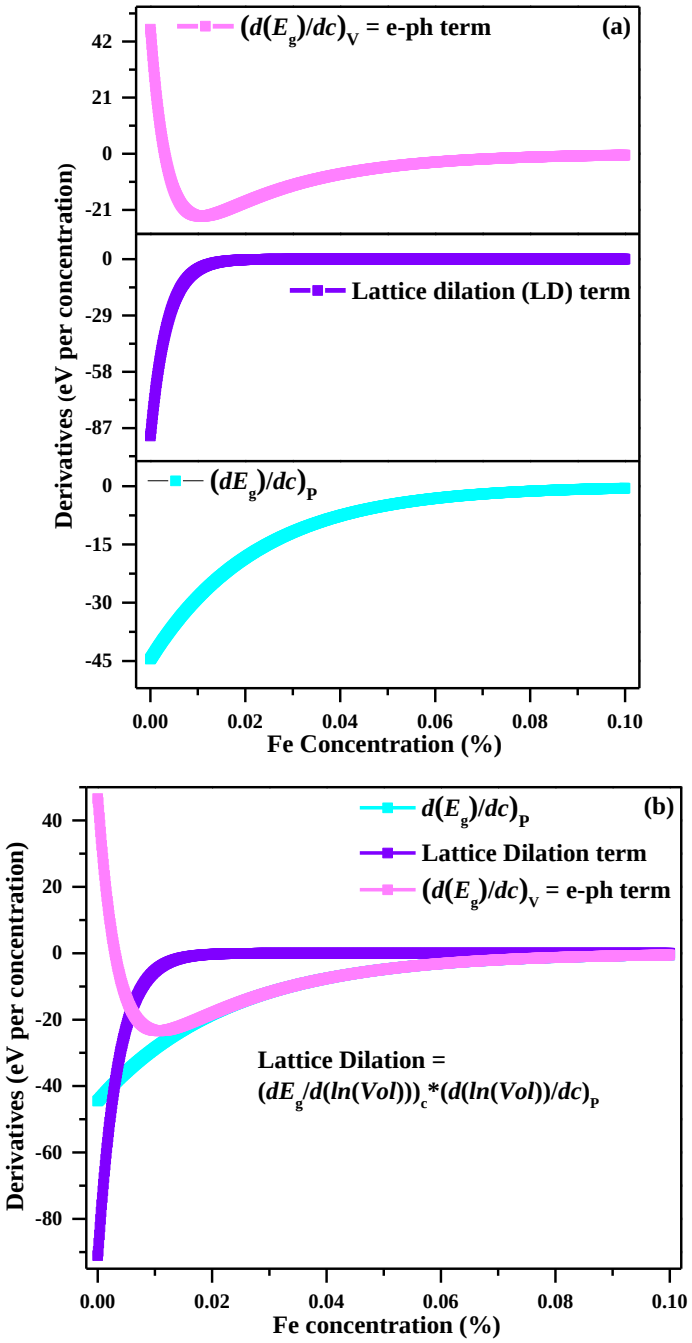

Figure 5.5a and **b** The total contribution to the band gap variation with Fe concentration is represented by the sky-blue dotted curve ($(\partial E_g/\partial c)_P$). The magenta and purple-coloured curves define the contribution of electron-phonon interactions ($(\partial E_g/\partial c)_V$) and lattice dilation terms, respectively, in the band gap variation

Hence, it is concluded that in the rare-earth materials of the Ln_2TiO_5-type (Ln is a lanthanide element), the overall contribution from the substitution disorder in band gap variation comes mainly from the e–ph coupling term, and lattice dilation effect (volume effect)

contributes significantly at lower concentrations, after that its effect fades away.

5.3.3. Raman Spectroscopy Results

Raman spectroscopy is a non-destructive and powerful technique for analyzing the lattice dynamics of the crystal structure by detecting lattice phonons and their vibrations. This is a sensitive technique that can be used to explore phonon dynamics and structural disorder (due to temperature, pressure, and composition), as well as electron–phonon interactions (EPC) prevailing in the system, which influence the thermal and electronic transport behaviour and other optical properties in the system [304]. It provides structural and vibrational information about the molecule, along with information about defect states, phases, and chemical composition. The Gd_2TiO_5 belongs to the category of Ln_2TiO_5 (Ln is a lanthanide element, Ln = La, Sm, Gd, Tb, Dy, Ho, Er, and Yb) compounds, all of which show similar Raman spectra. These compounds are predicted to exhibit 48 Raman active modes, out of which only a few are visible in the Raman spectra [230]. The Raman spectra of all the Fe-substituted Gd_2TiO_5 samples were taken with an excitation laser source of 633 nm wavelength and at a power of ~2 mW. The Raman spectrum of the Gd_2TiO_5 powder and the doped sample is shown in **Figure 5.6**. In the previous theoretical study carried out by Paques-Ledent [230], which was based on the isotopic vibrational data and the geometrical description of the normal modes, we infer that the low-frequency vibrational modes below 350 cm^{-1} correspond to the translational motion of the Ln cation, being sensitive to the mass of the Ln atom. The region above 500 cm^{-1} represents the stretching vibrations of the square pyramid TiO_5 frame. A very intense Raman mode is observed around 593 cm^{-1} (555 cm^{-1} reported in the literature [230]), which represents the symmetric stretching vibrations of the Ti−O bond with Ag symmetry. Another mode visualized at 660 cm^{-1} (648 cm^{-1}) corresponds to the antisymmetric

stretching vibrations of the Ti–O bond. The symmetric mode represents the stretching vibrations of the TiO_5 polyhedron.

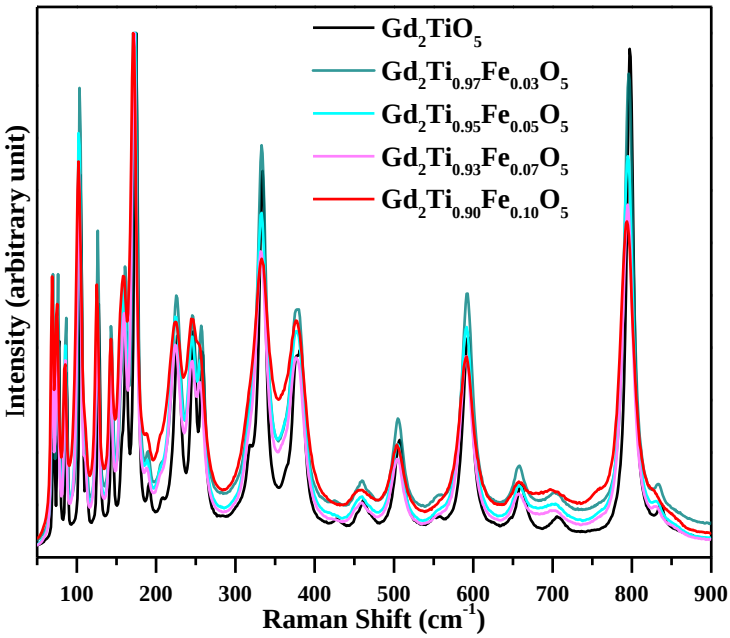

Figure 5.6 The composition-dependent Raman Spectra of Fe-substituted samples ($Gd_2Ti_{1-x}Fe_xO_5$; x = 0.03, 0.05, 0.07, 0.10)

In this report, we have selected the vibrational modes corresponding to the frequencies at 227 cm^{-1}, 247 cm^{-1}, 507 cm^{-1}, and 660 cm^{-1}, which were found to exhibit visible asymmetricity in their peak shapes. Asymmetricity here refers to the deviation of the peak shape from its perfect Lorentzian shape, which is found in the case of crystalline materials. For the measurement of asymmetricity, a parameter was defined by Fano [305] called the asymmetricity parameter (q), which measures the amount of asymmetricity in the Raman peak shape. Asymmetry can occur on the left side or the right side of the maximum of the peak, as shown in **Figure 5.7a**, where the left side asymmetry will give a negative q value and the right-side asymmetry has a positive sign of q. It is defined by the Fano function, where the Intensity ($I(\omega)$) of the observed Raman mode is given by the expression represented in **equation 5.7**

$$I(\omega) = I_0(\omega)\frac{(I+\epsilon)^2}{(1+\epsilon^2)} \qquad (5.7)$$

Here, I_0 is the scaling factor, and ϵ represents the reduced energy variable, which is given as, $\epsilon = \frac{(\omega-\omega_0)}{\Gamma}$; ω is the independent variable representing the incident phonon wavenumber (frequency), and ω_0 gives the experimentally observed phonon wavenumber (frequency). Γ gives the experimentally observed line width (FWHM) of the respective Raman mode. The term $1/q$ represents the strength of the electron−phonon coupling. The stronger interaction between the continuum electronic states and discrete phonon states will give a smaller value of q, as exhibited in **Figure 5.7b**.

Hence, for evaluating the strength of electron–phonon interactions occurring in the Fe-substituted samples, the composition-dependent Raman data were fitted with the Fano model, which showed that the asymmetry was increasing (decreasing mod (q)) with the increasing Fe concentration in the Gd_2TiO_5 sample, which can be visualized in respective **Figures 5.8a–5.11a**. All of the respective modes exhibited a red shift and broadening (FWHM) of their peaks, indicating an increase in structural disorder in the system with Fe substitution, as can be seen in the **b** and **c** parts of **Figures 5.8–5.11**. The increase in the FWHM indicates the increment in the disorder in phononic energy due to the Fe substitution that leads to broadening of the phonon states and favours the electron–phonon interactions in the substituted systems, the signature of which appears as the asymmetric line shape of the Raman mode [306, 307]. In this regard, the quantitative expression of the correlation between the disorder and the electron−phonon interactions was established by *Rambadey et al.*, given in the form $1/q^2 \propto E_U \mp \lambda$ which phenomenologically discusses the correlation between the disorder ($\sim E_U$) and the electron–phonon interactions ($\sim 1/q$) [260]. From the Raman results, it was inferred that Fe substitution leads to an increase in the disorder in all four Raman modes, indicated by the systematic increment in the FWHM as a function of Fe concentration, as shown in **Figures 5.8c–5.11c** for different Raman modes. The strength of the electron–phonon coupling ($\sim 1/q$) was found to increase

with Fe substitution, as shown in **Figures 5.8d-5.11d** and visualised from the asymmetric line shape of the Raman modes.

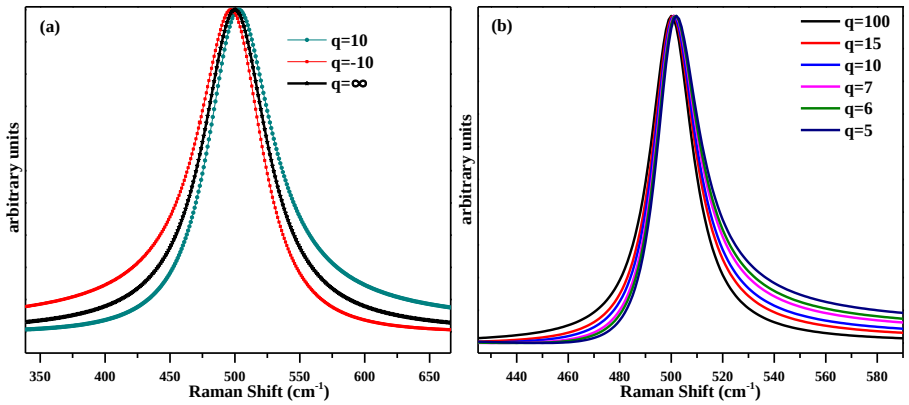

Figure 5.7a The schematic depicts the simulation performed to show asymmetricity on the right side and left side for the positive and negative q values, respectively, with respect to the Lorentzian Raman peak profile. **Figure b** depicts the increase in the asymmetricity with decreasing value of q

From the results obtained so far, it is inferred that the disorder increases in the system with Fe substitution, which favours the electron–phonon interactions in the substituted samples, as reflected in the asymmetric line shape of the Raman modes, which was quantified using the Fano model [305]. Now, it must be noted that while the asymmetric Raman lines can represent the signature of electron–phonon interactions in terms of the resonant Fano interference, the presence of electron–phonon coupling in symmetric phonon lines can also be inevitable. This may appear as enhanced scattering mechanisms and reduced phonon lifetime [253, 308, 309], where the electrons can participate in the exchange process; hence, the phonon line width can be understood to contain the information on EPC even for symmetric modes. Additionally, the Raman line shifts would reflect variations in bond length and hence be representative of lattice dilation effects. Thus, examining vibrational behaviour can provide insight into the interplay between the LD and EPC effects on different vibration modes under the influence of a given substitution concentration in the present case. In that view, the relative change (in %) in the peak position (~LD effects)

and that in line widths (~EPC effects) were checked between the end compositions (pure GTO and 10% Fe-substituted GTO) in the respective Raman modes, and the results obtained are plotted in **Figure 5.12**. The respective modes are mentioned near the marker points and are colour-mapped according to their line widths at the 0% Fe state, and the side colour bar provides the mapped width values. By examining the guiding line, it appears that the values extracted for different modes under the substitution-induced chemical perturbation exhibit a discernible trend, with only two data points being outliers. This plot basically reveals the phonon-specific sensitivity toward the interplay of EPC and LD effects. It can be concluded that for the vibrational modes of this sample, the sensitivity to EPC and LD follows a monotonic correlation, such that a stronger dependence on LD (here, lattice expansion) enhances the EPC sensitivity, thereby revealing a phonon-specific correlation between the sensitivity of vibration modes to the two effects. The 462 cm^{-1} mode (yellow colour) exhibits the highest line width and also deviates from the trend, suggesting that it crosses a threshold that allows it to break the dependence/correlation between EPC and LD, whereas the data point for 797 cm^{-1} remains closer to the global trend.

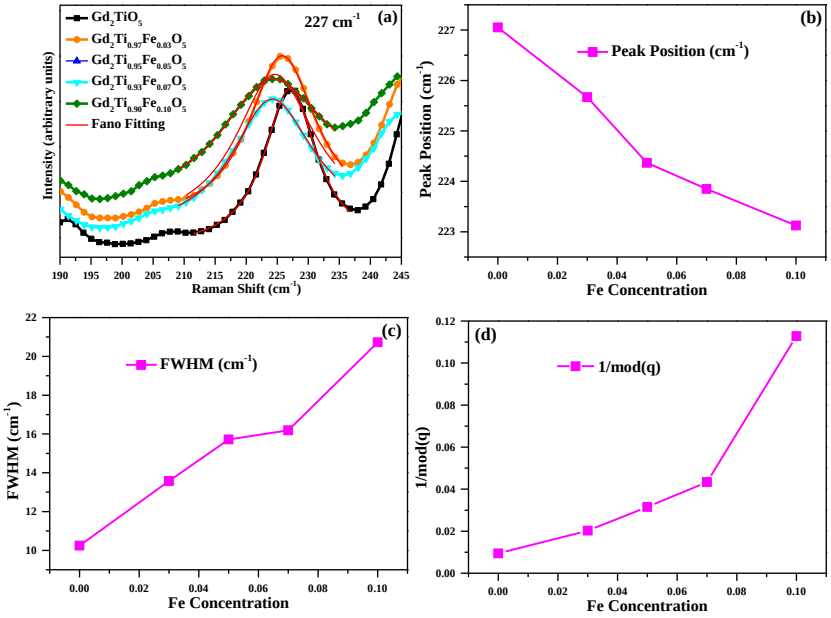

Figure 5.8a The Raman mode having the vibrational frequency 227 cm^{-1} was fitted with the Fano model, **b** shows the Peak position, **c** shows the FWHM, and **d** shows the strength of the e-ph coupling parameter (~1/*q*) which exhibits the systematic variation with Fe concentration, indicating the increased disorder in the system, and leading to the increased e-ph interaction (EPC)

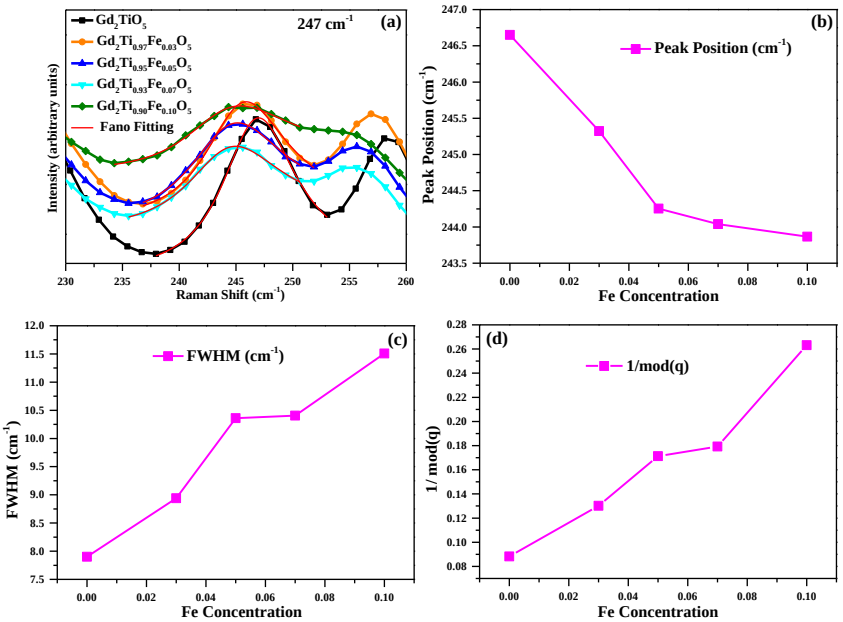

Figure 5.9a The Raman mode having a vibrational frequency of 247 cm^{-1} was fitted with the Fano model, **b** shows the systematic variation of peak position, **c** shows the FWHM, and **d** exhibits the strength of the e-ph coupling parameter (~1/*q*)

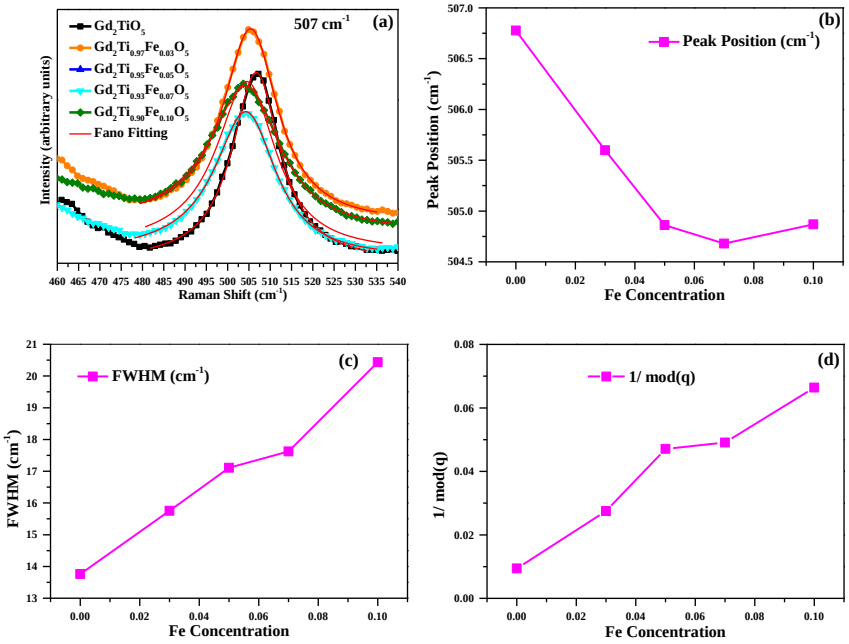

Figure 5.10a The Raman mode having vibrational frequency of 507 cm^{-1} was fitted with the Fano model, **b** shows the systematic variation of Peak Position, **c** shows the FWHM, and **d** exhibits the e-ph coupling parameter (~1/*q*)

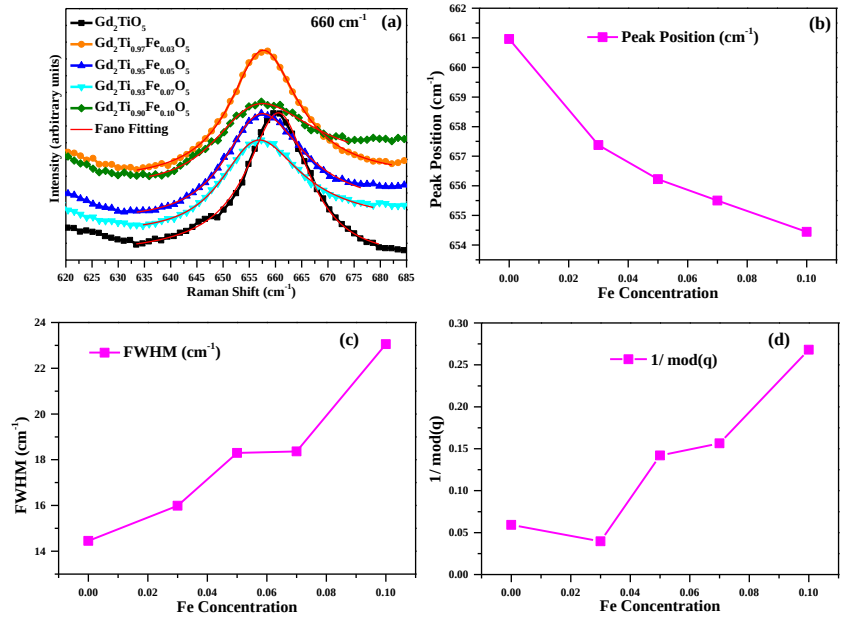

Figure 5.11a The Raman mode corresponding to the vibrational frequency 660 cm^{-1}, fitted with the Fano model, **b** shows the systematic variation of Peak Position, **c** shows the FWHM, and **d** exhibits the e-ph coupling parameter (~1/*q*) with Fe concentration

From the above discussion, it can be concluded that electron–phonon interactions play a significant role in these systems. As the Fe substitution increases, the magnitude of e–ph interactions increases (% change in widths of modes), along with the lattice dilation effect (% change in peak shifts). The interplay of both phenomena causes the abrupt decreasing behavior of the band gap at lower Fe concentration. Hence, the variation in the band gap comprises a strong competition between the EPC and LD effects at lower Fe content (~3% Fe), whereas the e–ph interaction (EPC) remains the contributing factor at a higher concentration of Fe, dominating the band gap variation, as evident from the decrement of the band gap in these systems. The systematic, perceivable trend observed for this interplay across different phonon modes (**Figure 5.12**) supports this interpretation.

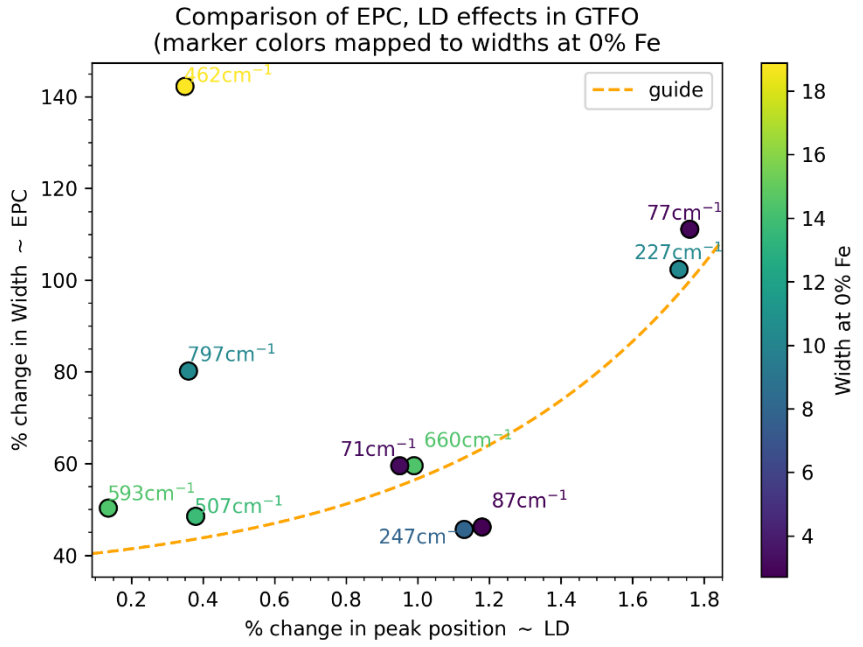

Figure 5.12 The relative change (% change) in linewidths (~ EPC effects) vs the peak positions in the respective Raman modes between the end compositions (0% and 10% Fe) shows competitive behaviour in EPC and LD effects

5.4 Conclusion

The shift in the optical absorption edge of various semiconductors with temperature has been known to emerge from the collective phenomena of e–ph interaction (EPC) and the lattice expansion (LD) effect. Following the same analogy as chemical substitution, this work investigates the role of resulting structural disorder in band gap variation at constant temperature using a modified approach that analyzes the lattice dilation contribution and the e–ph interaction from diffuse reflectance spectroscopy (DRS) and X-ray diffraction experiments. For this purpose, $Gd_2Ti(Fe)O_5$ samples were prepared by the solid-state synthesis method with a maximum Fe percentage of 10. At lower concentrations of Fe, both EPC and lattice dilation effects (LD) were found to dominate the decrement of the band gap, which was followed by the dominating electron–lattice interaction (EPC phenomenon), causing the slow decrement in the band gap with Fe substitution. The Raman spectroscopy measurements revealed a one-to-one correlation between e–ph and lattice dilation effects, as extracted from the vibration modes. This opens up further dimensions to be explored for structural and vibrational correlations in view of band gap engineering, which is useful for understanding and altering the functionalities of finite band gap materials. This work also emphasizes that the utility of DRS and Raman spectroscopy can be an important tool for visualizing the dominance effects of e–ph interaction and lattice expansion phenomena in semiconductors and can be applied to complex systems, such as rare-earth titanates (Ln_2TiO_5) and others.

Chapter 6

Thesis Conclusion and Future Scope

This chapter presents the summary and concluding remarks of the results obtained in this study, providing insight into future work that can be conducted within the context of the present work.

6.1 Overall Thesis Conclusion

This study outlines the scope of Optical Absorption Spectroscopy and Raman Spectroscopy in examining the structural, optical, and electronic properties of the less-explored rare-earth titanate Gd_2TiO_5, which forms a complex oxide within the Ln_2TiO_5 family. Gd_2TiO_5, lying in between the rare earth titanates series, serves as a centred titanate and forms an example of rarely observed mixed seven-fivefold coordination geometry. The first chapter of this study establishes an analytical correlation between the bond length and band gap in the Fe-substituted Gd_2TiO_5 series through structural refinement and UV-vis Optical Absorption Spectroscopy results. The first chapter establishes an analytical correlation between the bond length and the band gap of Fe-substituted Gd_2TiO_5 series by using the simple methodologies of structural refinement and well-known UV-vis Optical Absorption Spectroscopy, which indicates that one of the Ti-O bond lengths is primarily driving the optical band gap trend in these materials, asserting that the orbital overlap between the Ti-3*d* and O-2*p* orbitals mainly governs the band gap structure and band gap properties in these materials. The experimental results have been supported by density functional theory calculations conducted using the Quantum Espresso (QE), which demonstrate a substantial contribution from Ti-3*d* and O-

2*p* orbitals at the band edges, highlighting the predominant role of these orbitals in shaping the band structure. In an additional study of the 'hump analysis', the emergence of a broad hump with increasing Fe substitution in the optical absorption data obtained by diffuse reflectance spectroscopy has been elucidated. The results obtained from the theoretical band structure and optical absorbance data indicate the occurrence of intra-band transitions from the additional defect state (located below the conduction band) into the conduction band, which corresponds to the two broad peaks in the simulated optical absorbance spectra. The energy of these transitions was found to be comparable to the energy of the broad peaks. This suggests that the Ti-site predominantly influences the band gap properties, rather than the Gd-site. The results were corroborated by Density Functional Theory calculations conducted with VASP, revealing significant alterations in the Density of States (DOS) plots for 25% Fe-substituted Gd_2TiO_5 compared to the Eu-substituted variant and the pristine Gd_2TiO_5. These results indicate that the optical properties and band structure of the se complex rare-earth titanates of A_2BO_5 can be modified and altered by making suitable substitutions or doping at the B-site, in contrast to the A-site, which contributes less to the band formation. These studies will assist in designing novel rare-earth titanate complexes with tailored optical and electronic band structure functionalities appropriate for optoelectronic and energy-related applications.

The third chapter discussed the variation in the composition-dependent band gap, treating structural disorder analogously to thermal disorder in the Fe-substituted Gd_2TiO_5 series. The temperature dependence of the optical band gap has been attributed to arise from two factors: the Lattice Dilation effect, which leads to an increase in the band gap with rising temperature, and the Electron-phonon coupling (EPC), causing band gap renormalization by decreasing the band gap with increasing temperature. In this respect, numerous studies and theoretical models have been applied to investigate the contribution of both effects in various samples; however, fewer studies provide insight into the

quantitative contribution of these two phenomena in governing the band gap trend as a function of structural disorder. In this context, in our work, we have used the simple methodologies of structural refinement and composition-dependent optical absorption spectroscopy quantitatively to elucidate the quantitative contribution of lattice dilation effect and electro-phonon interactions (EPC) in the composition-dependent variation of band gap in Fe-substituted Gd_2TiO_5 series, which states the interplay of these effects in governing the band gap properties with structural disorder introduced in the system via substitution or doping effects. This study demonstrates the capacity of simple techniques, such as structural refinement and optical absorption spectroscopy, in investigating the correlation between lattice dynamics and structural variations, including bond lengths and bond angles, which leads to alterations in the optical and electronic properties of complex oxide systems, like Gd_2TiO_5.

6.2 Future Scope of Study

The present work provides insight into the various aspects of the rare-earth titanates of the Ln_2TiO_5 series to be studied for future pathways:

- The experimental Optical absorption spectra of Fe-substituted Gd_2TiO_5 samples include a feature around 3 eV as the Fe concentration increases in the pristine sample. Although we have attempted to address the cause of the broad hump observed in the experimental spectra by providing support from density functional theory through band structure calculations, further detailed study is needed in this regard. By providing the contribution of each individual orbital in the band structure and knowing which orbital contribution the additional defect state corresponds to, a clear insight into the transitions which correspond to these humps (in the simulated optical absorption spectra) can be obtained by applying appropriate selection rules.

Further theoretical band structure calculations providing insight into individual orbital contributions will be impactful in this regard.

- In the third chapter, the structural disorder has been treated analogously to the thermal disorder by applying the same approach, which has been applied for treating the temperature dependence of the band gap [290, 310, 311]. For treating structural disorders, more appropriate and alternative approaches can be considered, the results of which can be verified using well-studied and well-known oxide materials, such as TiO_2, ZnO, and $BaTiO_3$, to assess the suitability and accuracy of the methodology. Additionally, the individual contributions of e-ph (EPC) and Lattice Dilation needed to be evaluated for the temperature dependence of the band gap in Gd_2TiO_5 and Eu-substituted Gd_2TiO_5 series by applying the approach carried out in this study (Chapter 3), as well as other previously applied methodologies for providing a detailed and solid pathway for future studies.

- To gain insight into the vibrational properties and lattice dynamics of these materials, this study provides a few glimpses of the composition-dependent Raman spectroscopy studies. However, rigorous and elaborate studies are needed to investigate the emergence and softening of certain modes with increasing Fe content in Gd_2TiO_5, as well as in the Eu-substituted series, to compare the lattice dynamics and information on the vibrations of phonon modes [304, 312]. As these properties are rarely studied, theoretical calculations of simulated Raman spectra can provide great evidence and support in this regard. On the same note, to analyse the lattice dynamics and vibration of phonon modes with thermal fluctuations, the temperature-dependent Raman spectroscopy can be of significant relevance,

and a comparative analysis can be made for Fe and Eu-substituted Gd_2TiO_5 series.

- For analysing other aspects and properties of visualising thermal, dielectric, magnetic, and temperature-dependent dielectric measurement using the impedance spectroscopy and temperature evaluation of magnetic susceptibility using sophisticated instrumentation (SQUID) [313, 314], further evaluation is needed in the Fe- and Eu-substituted Gd_2TiO_5 sample series [315–317]. This will help in developing a structural correlation between optical, electronic, and magnetic properties of these rare-earth titanates.

- The above-mentioned methods and techniques can be applied to the other members of the rare-earth series of Ln_2TiO_5 for a systematic and comparative correlation of thermal, optical and electronic properties.

REFERENCES

1. Lian J, Chen J, Wang LM, Ewing RC, Farmer JM, Boatner LA, Helean KB (2003) Radiation-induced amorphization of rare-earth titanate pyrochlores. Phys Rev B 68:134107. https://doi.org/10.1103/PhysRevB.68.134107

2. Shcherbakova LG, Mamsurova LG, Sukhanova GE (1979) Lanthanide Titanates. Russ Chem Rev 48:228–242. https://doi.org/10.1070/RC1979v048n03ABEH002319

3. Aughterson R (2023) The in situ 1 MeV Kr - irradiation study of amorphisation resistance for the Ln2TiO5 (Ln = Lanthanides and Yttrium) Series. A review. Nuclear Instruments and Methods in Physics Research Section B: Beam Interactions with Materials and Atoms 538:144–156. https://doi.org/10.1016/j.nimb.2023.02.026

4. (2024) Phase Relations in the Pseudobinary Systems La2TiO5–Lu2TiO5and Gd2TiO5–Tb2TiO5 | Inorganic Materials. https://link.springer.com/article/10.1023/A:1023628812895. Accessed 16 Sep 2024

5. Porat O, Heremans C, Tuller HL (1997) Phase Stability and Electrical Conductivity in $Gd_2Ti_2O_7$-$Gd_2Mo_2O_7$ Solid Solutions. Journal of the American Ceramic Society 80:2278–2284. https://doi.org/10.1111/j.1151-2916.1997.tb03118.x

6. Xu J, Xi R, Xu X, Zhang Y, Feng X, Fang X, Wang X (2020) A2B2O7 pyrochlore compounds: A category of potential materials for clean energy and environment protection catalysis. Journal of Rare Earths 38:840–849. https://doi.org/10.1016/j.jre.2020.01.002

7. Shepelev YuF, Petrova MA (2008) Crystal structures of Ln2TiO5 (Ln = Gd, Dy) polymorphs. Inorganic Materials 44:1354–1361. https://doi.org/10.1134/S0020168508120170

8. Newman R, Aughterson RD, Lumpkin GR (2018) Synthesis and Structure of Novel A2BO5 Compounds Containing A = Y, Yb, Gd, Sm, and La and B = Zr, Ti, and Sn. MRS Advances 3:1117–1122. https://doi.org/10.1557/adv.2018.210

9. Aughterson RD, Lumpkin GR, Ionescu M, Reyes MDL, Gault B, Whittle KR, Smith KL, Cairney JM (2015) Ion-irradiation resistance of the orthorhombic Ln2TiO5 (Ln = La, Pr, Nd, Sm, Eu, Gd, Tb and Dy) series. Journal of Nuclear Materials 467:683–691. https://doi.org/10.1016/j.jnucmat.2015.10.028

10. Collongues MR, Queyroux F, Perez M, Jorba Y, Gilles J-C (1965) STRUCTURES AND PROPERTIES OF COMPOUNDS FORMED

BY THE RARE EARTH OXIDES WITH THE OXIDES OF THE IV-A ELEMENTS (Journal Article) | OSTI.GOV

11. Mumme WG, Wadsley AD (1968) The structure of orthorhombic Y2TiO5, an example of mixed seven- and fivefold coordination. Acta Crystallogr B Struct Crystallogr Cryst Chem 24:1327–1333. https://doi.org/10.1107/S0567740868004243

12. Ault JD, Welch AJE (1966) The yttrium oxide-titanium system. Acta Cryst 20:410–412. https://doi.org/10.1107/S0365110X6600094X

13. Waring JL, Schneider SJ (1965) Phase equilibrium relationships in the system Gd2O3-TiO2. J RES NATL BUR STAN SECT A 69A:255. https://doi.org/10.6028/jres.069A.025

14. McCarthy GJ, White WB, Roy R (1969) Samarium titanates, strontium samarium titanates, and the question of the existence of divalent samarium in oxides. Inorg Chem 8:1236–1239. https://doi.org/10.1021/ic50076a007

15. Queyroux F (1963) Sur l'existence d'un composé nouveau Gd2TiO5 et sur le diagramme d'équilibre du système TiO2-Gd2O3. bulmi 86:295–296. https://doi.org/10.3406/bulmi.1963.5651

16. Müller-Buschbaum Hk, Werner J-P (1994) Zur Kenntnis von Eu2TiO5. Journal of Alloys and Compounds 206: L11–L13. https://doi.org/10.1016/0925-8388(94)90024-8

17. Müller-Buschbaum Hk, Scheunemann K (1973) Zur kenntnis von Nd2TiO5. Journal of Inorganic and Nuclear Chemistry 35:1091–1098. https://doi.org/10.1016/0022-1902(73)80181-2

18. Petrova MA, Novikova AS, Romanov DP, Grebenshchikov RG Solid solutions in Ln2TiO5-Lu2TiO5 (Ln - Gd, Tb, Er) systems

19. Petrova MA, Grebenshchikov RG (2008) Specific features of the phase formation in the titanate systems Ln 2TiO5-Ln′2TiO5 (Ln = La, Gd, Tb, Er; Ln′ = Tb, Lu). Glass Phys Chem 34:603–607. https://doi.org/10.1134/S1087659608050118

20. Shepelev YuF, Petrova MA (2006) Structures of two high-temperature Dy2TiO5 modifications. Russ J Inorg Chem 51:1636–1640. https://doi.org/10.1134/S0036023606100196

21. Guillen M, Bertaut EF (1966) DETERMINATION OF THE STRUCTURE OF La$sub 2$TiO$sub 5$ WITH X RAYS AND NEUTRONS (Journal Article) | OSTI.GOV

22. Sinha A, Sharma BP (2005) Development of Dysprosium Titanate Based Ceramics. Journal of the American Ceramic Society 88:1064–1066. https://doi.org/10.1111/j.1551-2916.2005.00211.x

23. Whittle KR, Lumpkin GR, Blackford MG, Aughterson RD, Smith KL, Zaluzec NJ (2010) Ion-beam irradiation of lanthanum compounds in the systems La2O3–Al2O3 and La2O3–TiO2. Journal of Solid State Chemistry 183:2416–2420. https://doi.org/10.1016/j.jssc.2010.07.033

24. Whittle KR, Blackford MG, Aughterson RD, Lumpkin GR, Zaluzec NJ (2011) Ion irradiation of novel yttrium/ytterbium-based pyrochlores: The effect of disorder. Acta Materialia 59:7530–7537. https://doi.org/10.1016/j.actamat.2011.09.021

25. Aughterson RD, Lumpkin GR, Reyes MDL, Sharma N, Ling CD, Gault B, Smith KL, Avdeev M, Cairney JM (2014) Crystal structures of orthorhombic, hexagonal, and cubic compounds of the Sm(x)Yb(2−x) TiO5 series. Journal of Solid State Chemistry 213:182–192. https://doi.org/10.1016/j.jssc.2014.02.029

26. Aughterson RD, Lumpkin GR, Smith KL, Thorogood GJ, Whittle KR (2008) Synthesis and Characterisation of Ln_2 TiO_5 Compounds. MRS Proc 1107:365. https://doi.org/10.1557/PROC-1107-365

27. Aughterson RD, Lumpkin GR, De Los Reyes M, Gault B, Baldo P, Ryan E, Whittle KR, Smith KL, Cairney JM (2016) The influence of crystal structure on ion-irradiation tolerance in the Sm(x)Yb(2-x)TiO5 series. Journal of Nuclear Materials 471:17–24. https://doi.org/10.1016/j.jnucmat.2015.12.036

28. Aughterson RD, Lumpkin GR, Thorogood GJ, Zhang Z, Gault B, Cairney JM (2015) Crystal chemistry of the orthorhombic Ln2TiO5 compounds with Ln=La, Pr, Nd, Sm, Gd, Tb and Dy. Journal of Solid State Chemistry 227:60–67. https://doi.org/10.1016/j.jssc.2015.03.003

29. Panneerselvam G, Venkata Krishnan R, Antony MP, Nagarajan K, Vasudevan T, Vasudeva Rao PR (2004) Thermophysical measurements on dysprosium and gadolinium titanates. Journal of Nuclear Materials 327:220–225. https://doi.org/10.1016/j.jnucmat.2004.02.009

30. Zhang W, Govorov AO, Bryant GW (2006) Semiconductor-Metal Nanoparticle Molecules: Hybrid Excitons and the Nonlinear Fano Effect. Phys Rev Lett 97:146804. https://doi.org/10.1103/PhysRevLett.97.146804

31. Hayun S, Navrotsky A (2012) Formation enthalpies and heat capacities of rear earth titanates: RE2TiO5 (RE=La, Nd and Gd). Journal of Solid State Chemistry 187:70–74. https://doi.org/10.1016/j.jssc.2011.12.033

32. Shepelev YuF, Petrova MA, Novikova AS (2004) Crystal Structure of the Hexagonal Modification of Lutetium-Stabilized Gadolinium

Titanate $Gd_{1.8}Lu_{0.2}TiO_5$. Glass Physics and Chemistry 30:342–344. https://doi.org/10.1023/B:GPAC.0000038707.79995.d9

33. Shepelev YuF, Petrova MA (2008) Crystal structures of Ln2TiO5 (Ln = Gd, Dy) polymorphs. Inorganic Materials 44:1354–1361. https://doi.org/10.1134/S0020168508120170

34. Shepelev YuF, Petrova MA (2008) Crystal structures of Ln2TiO5 (Ln = Gd, Dy) polymorphs. Inorganic Materials 44:1354–1361. https://doi.org/10.1134/S0020168508120170

35. Aughterson RD, Lumpkin GR, Ionescu M, Reyes MDL, Gault B, Whittle KR, Smith KL, Cairney JM (2015) Ion-irradiation resistance of the orthorhombic Ln2TiO5 (Ln = La, Pr, Nd, Sm, Eu, Gd, Tb and Dy) series. Journal of Nuclear Materials 467:683–691. https://doi.org/10.1016/j.jnucmat.2015.10.028

36. Zhang FX, Wang JW, Lian J, Lang MK, Becker U, Ewing RC (2008) Phase Stability and Pressure Dependence of Defect Formation in Gd 2 Ti 2 O 7 and Gd 2 Zr 2 O 7 Pyrochlores. Phys Rev Lett 100:045503. https://doi.org/10.1103/PhysRevLett.100.045503

37. Liu X, Yang D, Liu C, Liu H, Ji S, Mu P, Wu Y, Li Y (2017) Insights into the radiation behavior of Ln2TiO5 (Ln=La-Y) from defect energetics. Computational Materials Science 139:295–300. https://doi.org/10.1016/j.commatsci.2017.08.006

38. Lumpkin GR, Smith KL, Blackford MG, Whittle KR, Harvey EJ, Redfern SAT, Zaluzec NJ (2009) Ion Irradiation of Ternary Pyrochlore Oxides. Chem Mater 21:2746–2754. https://doi.org/10.1021/cm9003917

39. Lang M, Zhang FX, Ewing RC, Lian J, Trautmann C, Wang Z (2009) Structural modifications of $Gd_2Zr_{2-x}Ti_xO_7$ pyrochlore induced by swift heavy ions: Disordering and amorphization. J Mater Res 24:1322–1334. https://doi.org/10.1557/jmr.2009.0151

40. Abramov YuA, Tsirelson VG, Zavodnik VE, Ivanov SA, Brown I. D. (1995) The chemical bond and atomic displacements in $SrTiO_3$ from X-ray diffraction analysis. Acta Crystallogr B Struct Sci 51:942–951. https://doi.org/10.1107/S0108768195003752

41. Mumme WG, Wadsley AD (1968) The structure of orthorhombic Y2TiO5, an example of mixed seven- and fivefold coordination. Acta Crystallogr B Struct Crystallogr Cryst Chem 24:1327–1333. https://doi.org/10.1107/S0567740868004243

42. Zhang FX, Wang JW, Lang M, Zhang JM, Ewing RC (2010) Pressure-induced structural transformations in lanthanide titanates: La2TiO5 and Nd2TiO5. Journal of Solid State Chemistry 183:2636–2643. https://doi.org/10.1016/j.jssc.2010.09.014

43. Hoffmann Roald, Beier BF, Muetterties EL, Rossi AR (1977) Seven-coordination. A molecular orbital exploration of structure, stereochemistry, and reaction dynamics. Inorg Chem 16:511–522. https://doi.org/10.1021/ic50169a002

44. Lin Z, Bytheway I (1996) Stereochemistry of Seven-Coordinate Main Group and d^0 Transition Metal Molecules. Inorg Chem 35:594–603. https://doi.org/10.1021/ic950271o

45. Kandan R, Prabhakara Reddy B, Panneerselvam G, Nagarajan K (2016) Calorimetric measurements on rare earth titanates: RE2TiO5 (RE = Sm, Gd and Dy). J Therm Anal Calorim 124:1349–1355. https://doi.org/10.1007/s10973-016-5272-6

46. Kamal Warshi M, Mishra V, Sagdeo A, Mishra V, Kumar R, Sagdeo PR (2018) Synthesis and characterization of $RFeO_3$: experimental results and theoretical prediction. Advances in Materials and Processing Technologies 4:558–572. https://doi.org/10.1080/2374068X.2018.1483680

47. Kumar A, Mishra V, Warshi MK, Sati A, Sagdeo A, Kumar R, Sagdeo PR (2019) Possible evidence of delocalized excitons in Cr-doped PrFeO3: An experimental and theoretical realization. Journal of Physics and Chemistry of Solids 130:230–235. https://doi.org/10.1016/j.jpcs.2019.03.012

48. Mishra V, Sati A, Warshi MK, Phatangare AB, Dhole S, Bhoraskar VN, Ghosh H, Sagdeo A, Mishra V, Kumar R, Sagdeo PR (2018) Effect of electron irradiation on the optical properties of $SrTiO_3$: An experimental and theoretical investigations. Mater Res Express 5:036210. https://doi.org/10.1088/2053-1591/aab6f5

49. Misra S, Kalaswad M, Zhang D, Wang H (2020) Dynamic tuning of dielectric permittivity in BaTiO3 via electrical biasing. null 8:321–327. https://doi.org/10.1080/21663831.2020.1757527

50. Sagdeo PR, Anwar S, Lalla NP (2006) Strain induced coexistence of monoclinic and charge ordered phases in La1-xCaxMnO3. Phys Rev B 74:214118. https://doi.org/10.1103/PhysRevB.74.214118

51. Sagdeo PR, Lalla NP, Narlikar AV, Prabhakaran D, Boothroyd AT (2008) Strain-induced first-order orbital flip transition and coexistence of charge-orbital ordered phases in $Pr_{0.5}Ca_{0.5}MnO_3$. Phys Rev B 78:174106. https://doi.org/10.1103/PhysRevB.78.174106

52. House JE (2012) Inorganic Chemistry. Academic Press

53. Pavitra E, Raju GSR, Varaprasad GL, Chodankar NR, Rao MVB, Rao NM, Park JY, Han Y-K, Huh YS (2021) Desired warm white light emission from a highly photostable and single-component

Gd2TiO5:Dy3+/Eu3+ nanophosphors for indoor illuminations. Journal of Alloys and Compounds 875:160019. https://doi.org/10.1016/j.jallcom.2021.160019

54. Jafar M, Balhara A, Sawant P, Sudarshan K, Gupta SK (2023) High concentration quenching, improved PLQY and high color purity of novel Gd2TiO5:Eu3+ triggered by complete solubility of dopant. Optical Materials 142:114059. https://doi.org/10.1016/j.optmat.2023.114059

55. GOODMAN G (1963) Electrical Conduction Anomaly in Samarium-Doped Barium Titanate. Journal of the American Ceramic Society 46:48–54. https://doi.org/10.1111/j.1151-2916.1963.tb13770.x

56. Zhi J, Chen A, Zhi Y, Vilarinho PM, Baptista JL (1999) Incorporation of Yttrium in Barium Titanate Ceramics. Journal of the American Ceramic Society 82:1345–1348. https://doi.org/10.1111/j.1151-2916.1999.tb01921.x

57. Kageyama K, Takahashi J (2004) Tunable Microwave Properties of Barium Titanate-Based Ferroelectric Glass-Ceramics. Journal of the American Ceramic Society 87:1602–1605. https://doi.org/10.1111/j.1551-2916.2004.01602.x

58. Wu YJ, Wang N, Wu SY, Chen XM (2011) Transparent Barium Strontium Titanate Ceramics Prepared by Spark Plasma Sintering. Journal of the American Ceramic Society 94:1343–1345. https://doi.org/10.1111/j.1551-2916.2011.04507.x

59. Pan T-M, Lin J-C, Wu M-H, Lai C-S (2009) Structural properties and sensing performance of high-k Nd2TiO5 thin layer-based electrolyte–insulator–semiconductor for pH detection and urea biosensing. Biosensors and Bioelectronics 24:2864–2870. https://doi.org/10.1016/j.bios.2009.02.018

60. Lee JD (2008) Concise Inorganic Chemistry, 5th Ed. John Wiley & Sons

61. Shaik S, Hiberty PC (2011) A primer on qualitative valence bond theory – a theory coming of age. WIREs Comput Mol Sci 1:18–29. https://doi.org/10.1002/wcms.7

62. Cooper DL, Gerratt Joseph, Raimondi Mario (1991) Applications of spin-coupled valence bond theory. Chem Rev 91:929–964. https://doi.org/10.1021/cr00005a014

63. Bethe H (1929) Termaufspaltung in Kristallen. Annalen der Physik 395:133–208. https://doi.org/10.1002/andp.19293950202

64. Van Vleck JH (1932) Theory of the Variations in Paramagnetic Anisotropy Among Different Salts of the Iron Group. Phys Rev 41:208–215. https://doi.org/10.1103/PhysRev.41.208

65. Lüthi B (1980) Crystal field effects in rare earth systems. Journal of Magnetism and Magnetic Materials 15–18:1–8. https://doi.org/10.1016/0304-8853(80)90922-1

66. Tsuchida R (1938) Absorption Spectra of Co-ordination Compounds. I. Bulletin of the Chemical Society of Japan 13:388–400. https://doi.org/10.1246/bcsj.13.388

67. Persson I (2010) Hydrated metal ions in aqueous solution: How regular are their structures? Pure and Applied Chemistry 82:1901–1917. https://doi.org/10.1351/PAC-CON-09-10-22

68. Aughterson RD, Zaluzec NJ, Lumpkin GR (2021) Synthesis and ion-irradiation tolerance of the Dy2TiO5 polymorphs. Acta Materialia 204:116518. https://doi.org/10.1016/j.actamat.2020.116518

69. Shepelev YuF, Petrova MA (2008) Crystal structures of Ln2TiO5 (Ln = Gd, Dy) polymorphs. Inorganic Materials 44:1354–1361. https://doi.org/10.1134/S0020168508120170

70. Lang M, Lian J, Zhang J, Zhang F, Weber WJ, Trautmann C, Ewing RC (2009) Single-ion tracks in Gd 2 Zr 2 − x Ti x O 7 pyrochlores irradiated with swift heavy ions. Phys Rev B 79:224105. https://doi.org/10.1103/PhysRevB.79.224105

71. Lian J, Chen J, Wang LM, Ewing RC, Farmer JM, Boatner LA, Helean KB (2003) Radiation-induced amorphization of rare-earth titanate pyrochlores. Phys Rev B 68:134107. https://doi.org/10.1103/PhysRevB.68.134107

72. Lian J, Wang L, Chen J, Sun K, Ewing RC, Matt Farmer J, Boatner LA (2003) The order–disorder transition in ion-irradiated pyrochlore. Acta Materialia 51:1493–1502. https://doi.org/10.1016/S1359-6454(02)00544-X

73. Minervini L, Grimes RW, Sickafus KE (2000) Disorder in Pyrochlore Oxides. Journal of the American Ceramic Society 83:1873–1878. https://doi.org/10.1111/j.1151-2916.2000.tb01484.x

74. Tracy CL, Lang M, Zhang J, Zhang F, Wang Z, Ewing RC (2012) Structural response of A2TiO5 (A = La, Nd, Sm, Gd) to swift heavy ion irradiation. Acta Materialia 60:4477–4486. https://doi.org/10.1016/j.actamat.2012.05.005

75. Tracy CL, Lang M, Zhang F, Trautmann C, Ewing RC (2015) Phase transformations in Ln 2 O 3 materials irradiated with swift heavy

ions. Phys Rev B 92:174101. https://doi.org/10.1103/PhysRevB.92.174101

76. Aughterson R (2023) The in situ 1 MeV Kr - irradiation study of amorphisation resistance for the Ln2TiO5 (Ln = Lanthanides and Yttrium) Series. A review. Nuclear Instruments and Methods in Physics Research Section B: Beam Interactions with Materials and Atoms 538:144–156. https://doi.org/10.1016/j.nimb.2023.02.026

77. Pan T-M, Lee J-D, Shu W-H, Chen T-T (2006) Structural and electrical properties of neodymium oxide high-k gate dielectrics. Applied Physics Letters 89:232908. https://doi.org/10.1063/1.2402237

78. Pan T-M, Lin C-W (2010) Structural and Sensing Characteristics of Dy_2 O_3 and Dy_2 TiO_5 Electrolyte−Insulator−Semiconductor pH Sensors. J Phys Chem C 114:17914–17919. https://doi.org/10.1021/jp107733u

79. Pan T-M, Huang M-D, Lin W-Y, Wu M-H (2010) A urea biosensor based on pH-sensitive Sm2TiO5 electrolyte–insulator–semiconductor. Analytica Chimica Acta 669:68–74. https://doi.org/10.1016/j.aca.2010.04.045

80. Lin CF, Kao CH, Lin CY, Liu CS, Liu YW (2019) Comparison Between Performances of In2O3 and In2TiO5-Based EIS Biosensors Using Post Plasma CF4 Treatment Applied in Glucose and Urea Sensing. Sci Rep 9:3078. https://doi.org/10.1038/s41598-019-39012-9

81. Pan T-M, Huang M-D, Lin C-W (2010) Thin Sm[sub 2]TiO[sub 5] Film Electrolyte–Insulator–Semiconductor for pH Detection and Urea Biosensing. J Electrochem Soc 157: J275. https://doi.org/10.1149/1.3439676

82. Cao R, Huang Z, Lan B, Li L, Yi X, Luo Z, Liao C, Wang J (2022) Adjustable luminescence properties of Eu3+ and Bi3+ codoped Ca3Zn3Te2O12 phosphor. Materials Research Bulletin 152:111851. https://doi.org/10.1016/j.materresbull.2022.111851

83. Zhou B, Tao L, Chai Y, Lau SP, Zhang Q, Tsang YH (2016) Constructing Interfacial Energy Transfer for Photon Up- and Down-Conversion from Lanthanides in a Core–Shell Nanostructure. Angewandte Chemie 128:12544–12548. https://doi.org/10.1002/ange.201604682

84. Sailaja P, Mahamuda Sk, Dedeepya G, Alzahrani JS, Swapna K, Venkateswarlu M, Rao AS, Alrowaili ZA, Olarinoye IO, Al-Buriahi MS (2024) Effect of Eu3+ ions concentration on visible red luminescence and radiative shielding properties of SrO–Al2O3–

BaCl2–B2O3– TeO2 glasses. Radiation Physics and Chemistry 216:111467. https://doi.org/10.1016/j.radphyschem.2023.111467

85. Zhu H, Lin CC, Luo W, Shu S, Liu Z, Liu Y, Kong J, Ma E, Cao Y, Liu R-S, Chen X (2014) Highly efficient non-rare-earth red emitting phosphor for warm white light-emitting diodes. Nat Commun 5:4312. https://doi.org/10.1038/ncomms5312

86. Töreli SB, Kafadar VE, Emen FM, Öztürk E, Altınkaya R (2025) Synthesis and Photoluminescence Properties of Eu^{3+} -Activated $Ba_2 Cd(BO_3)_2$ Red-Emitting Phosphors for Near-Ultraviolet Excited White Light-Emitting Diodes. Luminescence 40:e70135. https://doi.org/10.1002/bio.70135

87. Soni AK, Rai VK, Mahata MK (2017) Yb 3+ sensitized Na 2 Y 2 B 2 O 7 :Er 3+ phosphors in enhanced frequency upconversion, temperature sensing and field emission display. Materials Research Bulletin 89:116–124. https://doi.org/10.1016/j.materresbull.2017.01.009

88. Jang HS, Yang H, Kim SW, Han JY, Lee S, Jeon DY (2008) White Light-Emitting Diodes with Excellent Color Rendering Based on Organically Capped CdSe Quantum Dots and $Sr_3 SiO_5:Ce^{3+}$,Li^+ Phosphors. Advanced Materials 20:2696–2702. https://doi.org/10.1002/adma.200702846

89. Li P, Wang Z, Guo Q, Yang Z, Li X, Teng F (2015) Luminescence, energy transfer and thermal stability of LiBaB9O15:Sm3+, Eu3+ for white LEDs. Materials Research Bulletin 70:789–794. https://doi.org/10.1016/j.materresbull.2015.06.006

90. Sailaja P, Mahamuda Sk, Dedeepya G, Alzahrani JS, Swapna K, Venkateswarlu M, Rao AS, Alrowaili ZA, Olarinoye IO, Al-Buriahi MS (2024) Effect of Eu3+ ions concentration on visible red luminescence and radiative shielding properties of SrO–Al2O3–BaCl2–B2O3– TeO2 glasses. Radiation Physics and Chemistry 216:111467. https://doi.org/10.1016/j.radphyschem.2023.111467

91. Pianassola M SOLID STATE SYNTHESIS OF MULTICOMPONENT RARE-EARTH OXIDE CERAMICS

92. Gupta M, Rambadey OV, Sagdeo PR (2022) Probing the effect of R-cation radii on structural, vibrational, optical, and dielectric properties of rare earth (R=La, Pr, Nd) aluminates. Ceramics International 48:23072–23080. https://doi.org/10.1016/j.ceramint.2022.04.285

93. Yadav A (2024) A Review on Synthesis Methods of Materials Science and Nanotechnology. Adv Mater Lett 15:0–0. https://doi.org/10.5185/amlett.2024.031758

94. Aykol M, Montoya JH, Hummelshøj J (2021) Rational Solid-State Synthesis Routes for Inorganic Materials. J Am Chem Soc 143:9244–9259. https://doi.org/10.1021/jacs.1c04888

95. Bianchini M, Wang J, Clément RJ, Ouyang B, Xiao P, Kitchaev D, Shi T, Zhang Y, Wang Y, Kim H, Zhang M, Bai J, Wang F, Sun W, Ceder G (2020) The interplay between thermodynamics and kinetics in the solid-state synthesis of layered oxides. Nat Mater 19:1088–1095. https://doi.org/10.1038/s41563-020-0688-6

96. Huo H, Bartel CJ, He T, Trewartha A, Dunn A, Ouyang B, Jain A, Ceder G (2022) Machine-learning rationalization and prediction of solid-state synthesis conditions. https://doi.org/10.48550/ARXIV.2204.08151

97. Gupta M, Rambadey OV, Shirbhate SC, Acharya S, Sagdeo A, Sagdeo PR (2022) Probing the Signature of Disordering and Delocalization of Oxygen Vacancies and Anti-Site Defects in Doped $LaAlO_3$ Solid Electrolytes. J Phys Chem C 126:20251–20262. https://doi.org/10.1021/acs.jpcc.2c06473

98. Cowley JM (1995) Diffraction physics, 3. rev. ed., 1. impr. Elsevier, Amsterdam

99. Compton AH (1923) A Quantum Theory of the Scattering of X-rays by Light Elements. Phys Rev 21:483–502. https://doi.org/10.1103/PhysRev.21.483

100. Langford JI, Boultif A, Auffrédic J P and Louër D (1993) The use of pattern decomposition to study the combined X-ray diffraction effects of crystallite size and stacking faults in ex-oxalate zinc oxide. J. Appl Cryst 26:22–33. https://doi.org/10.1107/S0021889892007684

101. Yadav E, Harisankar S, Soni K and Mavani KR (2021) Effects of Cu-doping on the vibrational and electronic properties of epitaxial PrNiO3 thin films. Vib Spectrosc 112:103185. https://doi.org/10.1016/j.vibspec.2020.103185

102. Sati A, Kumar, Mishra V, Warshi K, Pokhriyal P, Sagdeo A and Sagdeo PR (2021) Temperature-dependent dielectric loss in BaTiO3: Competition between tunnelling probability and electron-phonon interaction. Mater Chem Phys 257:123792. https://doi.org/10.1016/j.matchemphys.2020.123792.

103. Iwashita N (2016) X-ray Powder Diffraction. In: Materials Science and Engineering of Carbon. Elsevier, pp 7–25.

104. Falsafi SR, Rostamabadi H, Jafari SM (2020) X-ray diffraction (XRD) of nanoencapsulated food ingredients. In: Characterization of Nanoencapsulated Food Ingredients. Elsevier, pp 271–293.

105. Cullity B D (1956) Elements of X-ray diffraction. Reading, Mass.

106. David Zook J (1976) A simple model for diffuse reflection. Optics Communications 17:77–82. https://doi.org/10.1016/0030-4018(76)90183-8

107. Bauman RP, Asendorf RH (1963) *Absorption Spectroscopy*. Physics Today 16:62–64. https://doi.org/10.1063/1.3050810

108. Wendlandt WW (1968) Modern Aspects of Reflectance Spectroscopy. Springer US, Boston, MA

109. Da Costa GM, Barrón V, Mendonça Ferreira C, Torrent J (2009) The use of diffuse reflectance spectroscopy for the characterization of iron ores. Minerals Engineering 22:1245–1250. https://doi.org/10.1016/j.mineng.2009.07.003

110. Degenhard WE (1968) Instruments for Reflectance Spectroscopy. In: Wendlandt WW (ed) Modern Aspects of Reflectance Spectroscopy. Springer US, Boston, MA, pp 143–157

111. Kortüm G (1969) Regular and Diffuse Reflection. In: Kortüm G (ed) Reflectance Spectroscopy: Principles, Methods, Applications. Springer, Berlin, Heidelberg, pp 5–71

112. Law DP, Blakeney AB, Tkachuk R (1996) The Kubelka–Munk Equation: Some Practical Considerations. Journal of Near Infrared Spectroscopy 4:189–193. https://doi.org/10.1255/jnirs.89

113 Kortüm G (1969) Experimental Testing of the “Kubelka-Munk” Theory. In: Kortüm G (ed) Reflectance Spectroscopy: Principles, Methods, Applications. Springer, Berlin, Heidelberg, pp 170–216

114. Yang L, Kruse B (2004) Revised Kubelka–Munk theory I Theory and application. J Opt Soc Am A 21:1933. https://doi.org/10.1364/JOSAA.21.001933

115. Ferraro JR, Nakamoto K, Brown CW (2003) Introductory Raman spectroscopy, 2nd ed. Academic Press, Amsterdam Boston

116. Cowley RA (1965) Raman scattering from crystals of the diamond structure. J Phys France 26:659–667. https://doi.org/10.1051/jphys:019650026011065900

117. Gerrard DL, Bowley HJ (1989) Instrumentation for Raman Spectroscopy. In: Gardiner DJ, Graves PR (eds) Practical Raman Spectroscopy. Springer Berlin Heidelberg, Berlin, Heidelberg, pp 55–76

118. Gardiner DJ, Graves PR (1989) Practical Raman Spectroscopy. Springer Berlin Heidelberg, Berlin, Heidelberg

119. Gulamova DD, Turdiev ZhSh (2009) Properties of oxide compounds, obtained by molten phase synthesis via action of concentrated solar radiation. Applied Solar Energy 45:38–44. https://doi.org/10.3103/S0003701X09010113

120. Zhang J, Lang M, Ewing RC, Devanathan R, Weber WJ, Toulemonde M (2010) Nanoscale phase transitions under extreme conditions within an ion track. J Mater Res 25:1344–1351. https://doi.org/10.1557/JMR.2010.0180

121. Park S, Tracy CL, Zhang F, Palomares RI, Park C, Trautmann C, Lang M, Mao WL, Ewing RC (2018) Swift-heavy ion irradiation response and annealing behavior of A2TiO5 (A = Nd, Gd, and Yb). Journal of Solid State Chemistry 258:108–116. https://doi.org/10.1016/j.jssc.2017.09.028

122. Ray WE (1971) The lanthanons as nuclear control materials. Nuclear Engineering and Design 17:377–396. https://doi.org/10.1016/0029-5493(71)90100-2

123. Wang Z, Zhu C, Wang H, Wang M, Liu C, Yang D, Li Y (2023) Preparation and irradiation stability of A2B2O7 pyrochlore high-entropy ceramic for immobilization of high-level nuclear waste. Journal of Nuclear Materials 574:154212. https://doi.org/10.1016/j.jnucmat.2022.154212

124. Lumpkin GR, Aughterson RD (2021) Perspectives on Pyrochlores, Defect Fluorites, and Related Compounds: Building Blocks for Chemical Diversity and Functionality. Front Chem 9:778140. https://doi.org/10.3389/fchem.2021.778140

125. Ewing RC, Weber WJ, Lian J (2004) Nuclear waste disposal—pyrochlore (A2B2O7): Nuclear waste form for the immobilization of plutonium and “minor” actinides. Journal of Applied Physics 95:5949–5971. https://doi.org/10.1063/1.1707213

126. Lau GC, McQueen TM, Huang Q, Zandbergen HW, Cava RJ (2008) Long- and short-range order in stuffed titanate pyrochlores. Journal of Solid State Chemistry 181:45–50. https://doi.org/10.1016/j.jssc.2007.10.025

127. Jiang Y, Smith JR, Robert Odette G (2010) Prediction of structural, electronic and elastic properties of Y2Ti2O7 and Y2TiO5. Acta Materialia 58:1536–1543. https://doi.org/10.1016/j.actamat.2009.10.061

128. Li N, Xiao HY, Zu XT, Wang LM, Ewing RC, Lian J, Gao F (2007) First-principles study of electronic properties of La2Hf2O7 and Gd2Hf2O7. Journal of Applied Physics 102:063704. https://doi.org/10.1063/1.2779262

129. Zhang J, Wang YQ, Tang M, Sun C, Yin DM, Li N (2015) Helium irradiation induced micro-swelling and phase separation in pyrochlore Lu2Ti2O7. Nuclear Instruments and Methods in Physics Research Section B: Beam Interactions with Materials and Atoms 342:179–183. https://doi.org/10.1016/j.nimb.2014.09.036

130. Austin DA, Cole M, Stennett MC, Corkhill CL, Hyatt NC (2021) A preliminary investigation of the molten salt mediated synthesis of Gd2TiO5 'stuffed' pyrochlore. MRS Advances 6:149–153. https://doi.org/10.1557/s43580-021-00057-6

131. Blackman AG, Schenk EB, Jelley RE, Krenske EH, Gahan LR (2020) Five-coordinate transition metal complexes and the value of τ_5: observations and caveats. Dalton Trans 49:14798–14806. https://doi.org/10.1039/d0dt02985h

132. Xiao HY, Gao F, Weber WJ (2009) *Ab initio* investigation of phase stability of Y 2 Ti 2 O 7 and Y 2 Zr 2 O 7 under high pressure. Phys Rev B 80:212102. https://doi.org/10.1103/PhysRevB.80.212102

133. Seymour KC, Hughes RW, Kriven WM (2015) Thermal Expansion of the Orthorhombic Phase in the Ln $_2$ TiO $_5$ System. J Am Ceram Soc 98:4096–4101. https://doi.org/10.1111/jace.13821

134. Seymour KC, Ribero D, McCormack SJ, Kriven WM (2016) Relationship Between the Orthorhombic and Hexagonal Phases in Dy_2 TiO_5. J Am Ceram Soc 99:3739–3744. https://doi.org/10.1111/jace.14354

135. Wojtaszek K, Błachucki W, Tyrała K, Nowakowski M, Zając M, Stępień J, Jagodziński P, Banaś D, Stańczyk W, Czapla-Masztafiak J, Kwiatek WM, Szlachetko J, Wach A (2021) Determination of Crystal-Field Splitting Induced by Thermal Oxidation of Titanium. J Phys Chem A 125:50–56. https://doi.org/10.1021/acs.jpca.0c07955

136. Prasanna R, Gold-Parker A, Leijtens T, Conings B, Babayigit A, Boyen H-G, Toney MF, McGehee MD (2017) Band Gap Tuning via Lattice Contraction and Octahedral Tilting in Perovskite Materials for Photovoltaics. J Am Chem Soc 139:11117–11124. https://doi.org/10.1021/jacs.7b04981

137. Rodríguez-Carvajal J (1993) Recent advances in magnetic structure determination by neutron powder diffraction. Physica B: Condensed Matter 192:55–69. https://doi.org/10.1016/0921-4526(93)90108-I

138. Rietveld HM (1969) A profile refinement method for nuclear and magnetic structures. J Appl Crystallogr 2:65–71. https://doi.org/10.1107/S0021889869006558

139. Paufler P (1995) R. A. Young (ed.). The Rietveld Method. International Union of Crystallography. Oxford University Press 1993. 298 p. Price £ 45.00. ISBN 0–19–855577–6. Cryst Res Technol 30:494–494. https://doi.org/10.1002/crat.2170300412

140. Mason B, Berry LG (1968) ELEMENTS OF MINERALOGY, Reprint. W.H. Freeman, San Francisco

141. Klein C, Hurlbut CS, Dana JD (1985) Manual of mineralogy: (after James D. Dana), 20th ed. Wiley, New York

142. Dana JD (1911) The system of mineralogy of James Dwight Dana. 1837-1868. New York : J. Wiley

143. Momma K, Izumi F (2011) *VESTA 3* for three-dimensional visualization of crystal, volumetric and morphology data. J Appl Crystallogr 44:1272–1276. https://doi.org/10.1107/S0021889811038970

144. Hongu H, Yoshiasa A, Teshima A, Isobe H, Sugiyama K, Arima H, Nakatsuka A, Momma K, Miyawaki R (2018) Crystal structure refinement and chemical formula of prosopite, $CaAl_2F_4[(OH)_{4-x}F_x]$ x = 0.0–1.0. Journal of Mineralogical and Petrological Sciences 113:152–158. https://doi.org/10.2465/jmps.170418

145. Kuribayashi T, Nagase T, Nozaki T, Ishibashi J, Shimada K, Shimizu M, Momma K (2019) Hitachiite, $Pb_5Bi_2Te_2S_6$, a new mineral from the Hitachi mine, Ibaraki Prefecture, Japan. MinMag 83:733–739. https://doi.org/10.1180/mgm.2019.45

146. Stein HS, Soedarmadji E, Newhouse PF, Dan Guevarra, Gregoire JM (2019) Synthesis, optical imaging, and absorption spectroscopy data for 179072 metal oxides. Sci Data 6:9. https://doi.org/10.1038/s41597-019-0019-4

147. Picollo M, Aceto M, Vitorino T (2019) UV-Vis spectroscopy. Physical Sciences Reviews 4:20180008. https://doi.org/10.1515/psr-2018-0008

148. Kortüm G (1969) Reflectance Spectra Obtained by Attenuated Total Reflection. In: Kortüm G (ed) Reflectance Spectroscopy: Principles, Methods, Applications. Springer, Berlin, Heidelberg, pp 309–336

149. Kortüm G (1969) Reflectance Spectroscopy. Springer, Berlin, Heidelberg

150. Kortüm G (1969) Regular and Diffuse Reflection. In: Kortüm G (ed) Reflectance Spectroscopy: Principles, Methods, Applications. Springer Berlin Heidelberg, Berlin, Heidelberg, pp 5–71

151. Boudreaux EA, Englert JP (1968) Diffuse Reflectance Spectroscopy — A Quantitative Technique for Characterizing Ligand Field Spectra. In: Wendlandt WW (ed) Modern Aspects of Reflectance Spectroscopy. Springer US, Boston, MA, pp 47–52

152. (2024) [PDF] Theory and Applications of Diffuse Reflectance Spectroscopy by Audrey L. Companion · 10.1007/978-1-4684-8691-9_19 · OA.mg. https://oa.mg/work/10.1007/978-1-4684-8691-9_19. Accessed 14 Jan 2024

153. Giannozzi P, Andreussi O, Brumme T, Bunau O, Buongiorno Nardelli M, Calandra M, Car R, Cavazzoni C, Ceresoli D, Cococcioni M, Colonna N, Carnimeo I, Dal Corso A, de Gironcoli S, Delugas P, DiStasio RA, Ferretti A, Floris A, Fratesi G, Fugallo G, Gebauer R, Gerstmann U, Giustino F, Gorni T, Jia J, Kawamura M, Ko H-Y, Kokalj A, Küçükbenli E, Lazzeri M, Marsili M, Marzari N, Mauri F, Nguyen NL, Nguyen H-V, Otero-de-la-Roza A, Paulatto L, Poncé S, Rocca D, Sabatini R, Santra B, Schlipf M, Seitsonen AP, Smogunov A, Timrov I, Thonhauser T, Umari P, Vast N, Wu X, Baroni S (2017) Advanced capabilities for materials modelling with Quantum ESPRESSO. J Phys Condens Matter 29:465901. https://doi.org/10.1088/1361-648X/aa8f79

154. Giannozzi P, Baroni S, Bonini N, Calandra M, Car R, Cavazzoni C, Ceresoli D, Chiarotti GL, Cococcioni M, Dabo I, Dal Corso A, De Gironcoli S, Fabris S, Fratesi G, Gebauer R, Gerstmann U, Gougoussis C, Kokalj A, Lazzeri M, Martin-Samos L, Marzari N, Mauri F, Mazzarello R, Paolini S, Pasquarello A, Paulatto L, Sbraccia C, Scandolo S, Sclauzero G, Seitsonen AP, Smogunov A, Umari P, Wentzcovitch RM (2009) QUANTUM ESPRESSO: a modular and open-source software project for quantum simulations of materials. J Phys: Condens Matter 21:395502. https://doi.org/10.1088/0953-8984/21/39/395502

155. Heyd J, Scuseria GE, Ernzerhof M (2003) Hybrid functionals based on a screened Coulomb potential. The Journal of Chemical Physics 118:8207–8215. https://doi.org/10.1063/1.1564060

156. Perdew JP, Burke K, Ernzerhof M (1996) Generalized Gradient Approximation Made Simple. Phys Rev Lett 77:3865–3868. https://doi.org/10.1103/PhysRevLett.77.3865

157. Karlický F, Zbořil R, Otyepka M (2012) Band gaps and structural properties of graphene halides and their derivates: A hybrid functional study with localized orbital basis sets. The Journal of Chemical Physics 137: https://doi.org/10.1063/1.4736998

158. Kumar R, Mishra V, Dixit T, Sarangi SN, Samal D, Miryala M, Nayak PK, Rao MSR (2023) Investigating the effect of H+-ion irradiation on layered α-MoO3 flakes by defect engineering.

Applied Physics Letters 123:151104. https://doi.org/10.1063/5.0166452

159. Boultif A, Louër D (2004) Powder pattern indexing with the dichotomy method. J Appl Crystallogr 37:724–731. https://doi.org/10.1107/S0021889804014876

160. Ahrens LH (1952) The use of ionization potentials Part 1. Ionic radii of the elements. Geochimica et Cosmochimica Acta 2:155–169. https://doi.org/10.1016/0016-7037(52)90004-5

161. Whittaker EJW, Muntus R (1970) Ionic radii for use in geochemistry. Geochimica et Cosmochimica Acta 34:945–956. https://doi.org/10.1016/0016-7037(70)90077-3

162. Addison AW, Rao TN, Reedijk J, Van Rijn J, Verschoor GC (1984) Synthesis, structure, and spectroscopic properties of copper (II) compounds containing nitrogen–sulphur donor ligands; the crystal and molecular structure of aqua[1,7-bis(N-methylbenzimidazol-2′-yl)-2,6-dithiaheptane] copper (II) perchlorate. J Chem Soc, Dalton Trans 1349–1356. https://doi.org/10.1039/DT9840001349

163. Klein A, Neugebauer M, Krest A, Lüning A, Garbe S, Arefyeva N, Schlörer N (2015) Five Coordinate Platinum(II) in [Pt(bpy)(cod)(Me)][SbF6]: A Structural and Spectroscopic Study. Inorganics 3:118–138. https://doi.org/10.3390/inorganics3020118

164. Muetterties EL, Guggenberger LJ (1974) Idealized polytopal forms. Description of real molecules referenced to idealized polygons or polyhedra in geometric reaction path form. J Am Chem Soc 96:1748–1756. https://doi.org/10.1021/ja00813a017

165. Kortüm G (1969) Reflectance Spectroscopy. Springer Berlin Heidelberg, Berlin, Heidelberg

166. Mishra V, Warshi MK, Sati A, Kumar A, Mishra V, Sagdeo A, Kumar R, Sagdeo PR (2018) Diffuse reflectance spectroscopy: An effective tool to probe the defect states in wide band gap semiconducting materials. Materials Science in Semiconductor Processing 86:151–156. https://doi.org/10.1016/j.mssp.2018.06.025

167. Dolgonos A, Mason TO, Poeppelmeier KR (2016) Direct optical band gap measurement in polycrystalline semiconductors: A critical look at the Tauc method. Journal of Solid State Chemistry 240:43–48. https://doi.org/10.1016/j.jssc.2016.05.010

168. Miglio A, Heinrich CP, Tremel W, Hautier G, Zeier WG (2017) Local Bonding Influence on the Band Edge and Band Gap Formation in Quaternary Chalcopyrites. Advanced Science 4:1700080. https://doi.org/10.1002/advs.201700080

169. Wendlandt WW (1968) High Temperature Reflectance Spectroscopy and Dynamic Reflectance Spectroscopy. In: Wendlandt WW (ed) Modern Aspects of Reflectance Spectroscopy. Springer US, Boston, MA, pp 53–69

170. Kortüm G (1969) Phenomenological Theories of Absorption and Scattering of Tightly Packed Particles. In: Kortüm G (ed) Reflectance Spectroscopy: Principles, Methods, Applications. Springer, Berlin, Heidelberg, pp 103–169

171. Myrick ML, Simcock MN, Baranowski M, Brooke H, Morgan SL, McCutcheon JN (2011) The Kubelka-Munk Diffuse Reflectance Formula Revisited. Applied Spectroscopy Reviews 46:140–165. https://doi.org/10.1080/05704928.2010.537004

172. Simmons EL (1975) Diffuse reflectance spectroscopy: a comparison of the theories. Appl Opt 14:1380. https://doi.org/10.1364/AO.14.001380

173. Companion AL (1965) Theory and Applications of Diffuse Reflectance Spectroscopy. In: Davis EN (ed) Developments in Applied Spectroscopy. Springer US, Boston, MA, pp 221–234

174. Scafetta MD, Cordi AM, Rondinelli JM, May SJ (2014) Band structure and optical transitions in $LaFeO_3$: theory and experiment. J Phys: Condens Matter 26:505502. https://doi.org/10.1088/0953-8984/26/50/505502

175. Jones RO (2015) Density functional theory: Its origins, rise to prominence, and future. Rev Mod Phys 87:897–923. https://doi.org/10.1103/RevModPhys.87.897

176. Assadi MHusseinN, Hanaor DAH (2013) Theoretical study on copper's energetics and magnetism in TiO2 polymorphs. Journal of Applied Physics 113:233913. https://doi.org/10.1063/1.4811539

177. Evans R, Oettel M, Roth R, Kahl G (2016) New developments in classical density functional theory. J Phys: Condens Matter 28:240401. https://doi.org/10.1088/0953-8984/28/24/240401

178.Niu H, Gou H, Ewing RC, Lian J (2012) First principles investigation of structural, electronic, elastic and thermal properties of rare-earth-doped titanate Ln2TiO5. AIP Advances 2: https://doi.org/10.1063/1.4739276

179. Xiao HY, Zu XT, Gao F, Weber WJ (2008) First-principles study of energetic and electronic properties of A2Ti2O7 (A=Sm, Gd, Er) pyrochlore. Journal of Applied Physics 104:073503. https://doi.org/10.1063/1.2986156

180. Niu H, Gou H, Ewing RC, Lian J (2012) First principles investigation of structural, electronic, elastic and thermal properties of rare-earth-doped titanate Ln2TiO5. AIP Advances 2:. https://doi.org/10.1063/1.4739276

181. Singh P, Choudhuri I, Rai HM, Mishra V, Kumar R, Pathak B, Sagdeo A, Sagdeo PR (2016) Fe doped $LaGaO_3$: good white light emitters. RSC Adv 6:100230–100238. https://doi.org/10.1039/C6RA21693E

182. Yue H, Fang K, Chen T, Jing Q, Guo K, Liu Z, Xie B, Mao P, Lu J, Tay FEH, Tan I, Yao K (2023) First-Principle Study on Correlate Structural, Electronic and Optical Properties of Ce-Doped BaTiO3. Crystals 13:255. https://doi.org/10.3390/cryst13020255

183. Sultan NM, Albarody TMB, Obodo KO, Baharom MB (2023) Effect of Mn+2 Doping and Vacancy on the Ferromagnetic Cubic 3C-SiC Structure Using First Principles Calculations. Crystals 13:348. https://doi.org/10.3390/cryst13020348

184. Sun M, Hao Y, Ren Q, Zhao Y, Du Y, Tang W (2016) Tuning electronic and magnetic properties of blue phosphorene by doping Al, Si, As and Sb atom: A DFT calculation. Solid State Communications 242:36–40. https://doi.org/10.1016/j.ssc.2016.04.019

185. Vandenborre MT, Husson E, Chatry JP, Michel D (1983) Rare-earth titanates and stannates of pyrochlore structure; vibrational spectra and force fields. J Raman Spectroscopy 14:63–71. https://doi.org/10.1002/jrs.1250140202

186. Aughterson RD, Lumpkin GR, Smith KL, Cairney JM (2020) Novel complex ceramic oxides, $Ln_2 TiO_5$ (Ln = La, Sm, Gd, Tb, Dy, Ho, Er, and Yb), for polyphase nuclear waste-forms. J Am Ceram Soc 103:5536–5545. https://doi.org/10.1111/jace.17318

187. Nain R, Bansal L, Sagdeo PR, Kumar R (2024) Utilizing rare earth titanates to improve performance of solid-state electrochromic device. Nano Express

188. Muthuraman M, Dhas NA, Patil KC (1994) Combustion synthesis of oxide materials for nuclear waste immobilization. Bull Mater Sci 17:977–987. https://doi.org/10.1007/BF02757574

189. Xu J, Xi R, Xu X, Zhang Y, Feng X, Fang X, Wang X (2020) A2B2O7 pyrochlore compounds: A category of potential materials for clean energy and environment protection catalysis. Journal of Rare Earths 38:840–849. https://doi.org/10.1016/j.jre.2020.01.002

190. Garbout A, Bouattour S, Botelho Do Rego AM, Ferraria A, Kolsi AW (2007) Synthesis, Raman and X-ray diffraction investigations

of rubidium-doped Gd1.8Ti2O6.7 pyrochlore oxide via a sol–gel process. Journal of Crystal Growth 304:374–382. https://doi.org/10.1016/j.jcrysgro.2007.03.021

191. Kao C-H, Chen H, Lin SP (2011) The Comparison of the High-k Sm[sub 2]O[sub 3] and Sm[sub 2]TiO[sub 5] Dielectrics Deposited on the Polycrystalline Silicon. Electrochem Solid-State Lett 14:G9. https://doi.org/10.1149/1.3519812

192. Pramudita JC, Aughterson R, Dose WM, Donne SW, Brand HEA, Sharma N (2015) Using in situ synchrotron x-ray diffraction to study lithium- and sodium-ion batteries: A case study with an unconventional battery electrode (Gd_2TiO_5). J Mater Res 30:381–389. https://doi.org/10.1557/jmr.2014.311

193. Seymour K (2015) Thermal Expansion and Phase Transformation Behavior in the Rare-Earth Titanate System

194. Schlapp R, Penney WG (1932) Influence of Crystalline Fields on the Susceptibilities of Salts of Paramagnetic Ions. II. The Iron Group, Especially Ni, Cr and Co. Phys Rev 42:666–686. https://doi.org/10.1103/PhysRev.42.666

195. Zhang Y, Xu X (2020) Machine learning optical band gaps of doped-ZnO films. Optik 217:164808. https://doi.org/10.1016/j.ijleo.2020.164808

196. Zhang Y, Xu X (2020) Machine Learning Band Gaps of Doped-TiO_2 Photocatalysts from Structural and Morphological Parameters. ACS Omega 5:15344–15352. https://doi.org/10.1021/acsomega.0c01438

197. Apostolova I, Apostolov A, Wesselinowa J (2022) Band Gap Tuning in Transition Metal and Rare-Earth-Ion-Doped TiO2, CeO2, and SnO2 Nanoparticles. Nanomaterials 13:145. https://doi.org/10.3390/nano13010145

198. Khan I, Saeed K, Zekker I, Zhang B, Hendi AH, Ahmad A, Ahmad S, Zada N, Ahmad H, Shah LA, Shah T, Khan I (2022) Review on Methylene Blue: Its Properties, Uses, Toxicity and Photodegradation. Water 14:242. https://doi.org/10.3390/w14020242

199. Apostolova I, Apostolov A, Wesselinowa J (2022) Band Gap Tuning in Transition Metal and Rare-Earth-Ion-Doped TiO2, CeO2, and SnO2 Nanoparticles. Nanomaterials 13:145. https://doi.org/10.3390/nano13010145

200. Kotnana G, Jammalamadaka SN (2015) Band gap tuning and orbital mediated electron-phonon coupling in $HoFe_{1-x}Cr_xO_3$ (0 \le

x \le 1). Journal of Applied Physics 118:124101. https://doi.org/10.1063/1.4931155

201. Arif N, Zafar MN, Batool M, Humayun M, Iqbal MA, Younis M, Li L, Li K, Zeng Y-J (2024) Recent advances and perspectives on iron-based photocatalysts. J Mater Chem C 12:12653–12691. https://doi.org/10.1039/D4TC01062K

202. Parayil RT, Singh P, Sudarshan K, Mohapatra M, Devi P, Gupta SK (2025) Band gap and structural engineering to achieve excellent photocatalysis in A2B2O7 type composition. Inorganic Chemistry Communications 174:113965. https://doi.org/10.1016/j.inoche.2025.113965

203. Jafar M, Balhara A, Sawant P, Sudarshan K, Gupta SK (2023) High concentration quenching, improved PLQY and high color purity of novel Gd2TiO5:Eu3+ triggered by complete solubility of dopant. Optical Materials 142:114059. https://doi.org/10.1016/j.optmat.2023.114059

204. Zhang Y, Xu X (2023) Gaussian process modeling of doped-lanthanum manganites Curie temperature from compositions and ionic radii. Solid State Communications 360:115025. https://doi.org/10.1016/j.ssc.2022.115025

205. Li Z, Liang Z, Wan J, Liu L, Wu C, Wang P, Jiang X, Lin Z, Liu H (2025) Different p-block elements induce C_3 [111] octahedral distortion in titanium to generate an intense nonlinear effect. Chem Sci 16:3329–3335. https://doi.org/10.1039/D4SC06620K

206. Wang H, Cui W, Lin W, Yang J, Zhao W, Sang X (2024) Theoretical and Experimental Investigation on 3d Transition Metal Anisotropic Diffusion in van Der Waals Layered Sb_2 Te_3. J Phys Chem C 128:6859–6867. https://doi.org/10.1021/acs.jpcc.4c00145

207. Arillo MA, López ML, Pico C, Veiga ML, Jiménez-López A, Rodríguez-Castellón E (2001) Surface characterisation of spinels with Ti(IV) distributed in tetrahedral and octahedral sites. Journal of Alloys and Compounds 317–318:160–163. https://doi.org/10.1016/S0925-8388(00)01339-6

208. Zolnhofer EM, Wijeratne GB, Jackson TA, Fortier S, Heinemann FW, Meyer K, Krzystek J, Ozarowski A, Mindiola DJ, Telser J (2020) Electronic Structure and Magnetic Properties of a Titanium (II) Coordination Complex. Inorg Chem 59:6187–6201. https://doi.org/10.1021/acs.inorgchem.0c00311

209. Nain R, Mishra V, Sagdeo PR (2024) Influence of Fe substitution on the structural and optical properties of Gd2TiO5 ceramic. Journal of Materials Science: Materials in Electronics 35:1172. https://doi.org/10.1007/s10854-024-12954-1

210. Gupta M, Rambadey OV, Sagdeo A, Sagdeo PR (2022) Investigating the structural, vibrational, optical, and dielectric properties in Mg-substituted LaAlO3. J Mater Sci: Mater Electron 33:13352–13366. https://doi.org/10.1007/s10854-022-08273-y

211. Hanawalt JD, Rinn HW, Frevel LK (1986) Chemical Analysis by X-Ray Diffraction: Classification and Use of X-Ray Diffraction Patterns. Powder Diffr 1:2–14. https://doi.org/10.1017/S0885715600011490

212. Bunaciu AA, Udriştioiu EG, Aboul-Enein HY (2015) X-Ray Diffraction: Instrumentation and Applications. Critical Reviews in Analytical Chemistry 45:289–299. https://doi.org/10.1080/10408347.2014.949616

213. Rietveld HM (1967) Line profiles of neutron powder-diffraction peaks for structure refinement. Acta Cryst 22:151–152. https://doi.org/10.1107/S0365110X67000234

214. Singh P, Choudhuri I, Rai HM, Mishra V, Kumar R, Pathak B, Sagdeo A, Sagdeo PR (2016) Fe doped $LaGaO_3$: good white light emitters. RSC Adv 6:100230–100238. https://doi.org/10.1039/c6ra21693e

215. (2016) UV-visible-NIR reflectance spectrophotometry in cultural heritage: Background paper. Anal Methods 8:5894–5896. https://doi.org/10.1039/C6AY90112C

216. Kresse G, Hafner J (1993) *Ab initio* molecular dynamics for liquid metals. Phys Rev B 47:558–561. https://doi.org/10.1103/PhysRevB.47.558

217. Kresse G, Joubert D (1999) From ultrasoft pseudopotentials to the projector augmented-wave method. Phys Rev B 59:1758–1775. https://doi.org/10.1103/PhysRevB.59.1758

218. Hewat A, David WIF, Van Eijck L (2016) Hugo Rietveld (1932–2016). J Appl Crystallogr 49:1394–1395. https://doi.org/10.1107/s1600576716012061

219. Rodriguez-Carvajal J (2001) Recent developments of the program FULLPROF, commission on powder diffraction. IUCr Newsl 26:

220. Rietveld HM (1967) Line profiles of neutron powder-diffraction peaks for structure refinement. Acta Cryst 22:151–152. https://doi.org/10.1107/S0365110X67000234

221. Momma K, Izumi F (2011) *VESTA 3* for three-dimensional visualization of crystal, volumetric and morphology data. J Appl Crystallogr 44:1272–1276. https://doi.org/10.1107/S0021889811038970

222. Mishra V, Warshi MK, Sati A, Kumar A, Mishra V, Kumar R, Sagdeo PR (2019) Investigation of temperature-dependent optical properties of TiO2 using diffuse reflectance spectroscopy. SN Appl Sci 1:241. https://doi.org/10.1007/s42452-019-0253-6

223. Hecht HG (1968) The Present Status of Diffuse Reflectance Theory. In: Wendlandt WW (ed) Modern Aspects of Reflectance Spectroscopy. Springer US, Boston, MA, pp 1–26

224. Alcaraz De La Osa R, Iparragirre I, Ortiz D, Saiz JM (2020) The extended Kubelka–Munk theory and its application to spectroscopy. ChemTexts 6:2. https://doi.org/10.1007/s40828-019-0097-0

225. Edström P (2007) Examination of the revised Kubelka-Munk theory: considerations of modeling strategies. J Opt Soc Am A 24:548. https://doi.org/10.1364/JOSAA.24.000548

226. Myrick ML, Simcock MN, Baranowski M, Brooke H, Morgan SL, McCutcheon JN (2011) The Kubelka-Munk Diffuse Reflectance Formula Revisited. Applied Spectroscopy Reviews 46:140–165. https://doi.org/10.1080/05704928.2010.537004

227. Souri D, Tahan ZE (2015) A new method for the determination of optical band gap and the nature of optical transitions in semiconductors. Appl Phys B 119:273–279. https://doi.org/10.1007/s00340-015-6053-9

228. Pankove JI (1975) Optical Processes in Semiconductors. Courier Corporation

229. Rosencher E, Vinter B (2002) Optoelectronics. Cambridge University Press

230. Paques-Ledent MTh (1976) Infrared and Raman studies of M2TiO5 compounds (M = rare earths and Y): Isotopic effect and group theoretical analysis. Spectrochimica Acta Part A: Molecular Spectroscopy 32:1339–1344. https://doi.org/10.1016/0584-8539(76)80177-8

231. Prucnal S, Berencén Y, Wang M, Grenzer J, Voelskow M, Hübner R, Yamamoto Y, Scheit A, Bärwolf F, Zviagin V, Schmidt-Grund R, Grundmann M, Żuk J, Turek M, Drożdziel A, Pyszniak K, Kudrawiec R, Polak MP, Rebohle L, Skorupa W, Helm M, Zhou S (2018) Strain and Band-Gap Engineering in Ge - Sn Alloys via P Doping. Phys Rev Applied 10:064055. https://doi.org/10.1103/PhysRevApplied.10.064055

232. Monserrat B, Vanderbilt D (2016) Temperature Effects in the Band Structure of Topological Insulators. Phys Rev Lett 117:226801. https://doi.org/10.1103/PhysRevLett.117.226801

233. Shah WH, Alam A, Javed H, Rashid K, Ali A, Ali L, Safeen A, Ali MR, Imran N, Sohail M, Chambashi G (2023) Tuning of the band gap and dielectric loss factor by Mn doping of Zn1-xMnxO nanoparticles. Sci Rep 13:8646. https://doi.org/10.1038/s41598-023-35456-2

234. Li S, Lin Y, Tang S, Feng L, Li X (2021) A review of rare-earth oxide films as high k dielectrics in MOS devices — Commemorating the 100th anniversary of the birth of Academician Guangxian Xu. Journal of Rare Earths 39:121–128. https://doi.org/10.1016/j.jre.2020.10.013

235. Saxena R, Kangsabanik J, Kumar A, Shahee A, Singh S, Jain N, Ghorui S, Kumar V, Mahajan AV, Alam A, Kabra D (2020) Contrasting temperature dependence of the band gap in CH 3 NH 3 Pb X 3 (X = I , Br , Cl) : Insight from lattice dilation and electron-phonon coupling. Phys Rev B 102:081201. https://doi.org/10.1103/PhysRevB.102.081201

236. Singh S, Li C, Panzer F, Narasimhan KL, Graeser A, Gujar TP, Köhler A, Thelakkat M, Huettner S, Kabra D (2016) Effect of Thermal and Structural Disorder on the Electronic Structure of Hybrid Perovskite Semiconductor CH_3 NH_3 PbI_3. J Phys Chem Lett 7:3014–3021. https://doi.org/10.1021/acs.jpclett.6b01207

237. Varshni YP (1967) Temperature dependence of the energy gap in semiconductors. Physica 34:149–154. https://doi.org/10.1016/0031-8914(67)90062-6

238. Möglich P, Rompe R (1940) Über Energieumwandlung im Festkörper. Zeitschrift für Physik 115:707–728. https://doi.org/10.1007/BF01325648

239. Möglich F, Rompe R (1942) Über den Einfluß der Absorptionsspektrum von Isolatoren. Zeitschrift für Physik 119:472–481. https://doi.org/10.1007/BF01339784

240. Seiwert R (1950) Thermische Verschiebung der langwelligen Grenze der Grundgitterbasorption von Cadmiumsulfid. Annalen der Physik 441:241–252. https://doi.org/10.1002/andp.19494410127

241. Fan HY (1951) Temperature Dependence of the Energy Gap in Semiconductors. Phys Rev 82:900–905. https://doi.org/10.1103/PhysRev.82.900

242. Cheeseman IC (1952) The Structure of the Long Wave Absorption Edge of Insulating Crystals. Proc Phys Soc A 65:25–32. https://doi.org/10.1088/0370-1298/65/1/304

243. Radkowsky A (1948) Temperature Dependence of Electron Energy Levels in Solids. Phys Rev 73:749–761. https://doi.org/10.1103/PhysRev.73.749

244. Bardeen J (1937) Conductivity of Monovalent Metals. Phys Rev 52:688–697. https://doi.org/10.1103/PhysRev.52.688

245. Cohen ML (1962) Electron-Phonon Self-Energies in Many-Valley Semiconductors. Phys Rev 128:131–133. https://doi.org/10.1103/PhysRev.128.131

246. Tsang YW, Cohen ML (1971) Calculation of the Temperature Dependence of the Energy Gaps in PbTe and SnTe. Phys Rev B 3:1254–1261. https://doi.org/10.1103/PhysRevB.3.1254

247. Dey P, Paul J, Bylsma J, Karaiskaj D, Luther JM, Beard MC, Romero AH (2013) Origin of the temperature dependence of the band gap of PbS and PbSe quantum dots. Solid State Communications 165:49–54. https://doi.org/10.1016/j.ssc.2013.04.022

248. Querales-Flores JD, Cao J, Fahy S, Savić I (2018) Temperature effects on the electronic band structure of PbTe from first principles. https://doi.org/10.48550/ARXIV.1809.02643

249. Querales-Flores JD, Cao J, Fahy S, Savić I (2019) Temperature effects on the electronic band structure of PbTe from first principles. Phys Rev Materials 3:055405. https://doi.org/10.1103/PhysRevMaterials.3.055405

250. Yu R, Bozin ES, Abeykoon M, Sangiorgio B, Spaldin NA, Malliakas CD, Kanatzidis MG, Billinge SJL (2018) Emphanitic anharmonicity in PbSe at high temperature and anomalous electronic properties in the Pb Q (Q = S , Se , Te) system. Phys Rev B 98:144108. https://doi.org/10.1103/PhysRevB.98.144108

251. Allen PB, Cardona M (1983) Temperature dependence of the direct gap of Si and Ge. Phys Rev B 27:4760–4769. https://doi.org/10.1103/PhysRevB.27.4760

252. Guenzer CS, Bienenstock A (1971) Unsuccessful Brooks-Yu type calculation of the HgTe bandgap temperature dependence. Physics Letters A 34:172–174. https://doi.org/10.1016/0375-9601(71)90812-7

253. Fornasini P, Grisenti R (2015) On EXAFS Debye-Waller factor and recent advances. J Synchrotron Rad 22:1242–1257. https://doi.org/10.1107/S1600577515010759

254. Keffer C, Hayes TM, Bienenstock A (1968) PbTe Debye-Waller Factors and Band-Gap Temperature Dependence. Phys Rev Lett 21:1676–1678. https://doi.org/10.1103/PhysRevLett.21.1676

255. Keffer C, Hayes TM, Bienenstock A (1970) Debye-Waller Factors and the PbTe Band-Gap Temperature Dependence. Phys Rev B 2:1966–1976. https://doi.org/10.1103/PhysRevB.2.1966

256. Bhosale J, Ramdas AK, Burger A, Muñoz A, Romero AH, Cardona M, Lauck R, Kremer RK (2012) Temperature dependence of band gaps in semiconductors: Electron-phonon interaction. Phys Rev B 86:195208. https://doi.org/10.1103/PhysRevB.86.195208

257. Bardeen J, Shockley W (1950) Deformation Potentials and Mobilities in Non-Polar Crystals. Phys Rev 80:72–80. https://doi.org/10.1103/PhysRev.80.72

258. Gopalan S, Lautenschlager P, Cardona M (1987) Temperature dependence of the shifts and broadenings of the critical points in GaAs. Phys Rev B 35:5577–5584. https://doi.org/10.1103/PhysRevB.35.5577

259. Rambadey OV, Kumar A, Sagdeo PR (2021) Investigating the correlation between the Urbach energy and asymmetry parameter of the Raman mode in semiconductors. Phys Rev B 104:245205. https://doi.org/10.1103/PhysRevB.104.245205

260. Kumar A, Rambadey OV, Rai H, Sagdeo PR (2022) Role of Laser Excitation Wavelength and Power in the Fano Resonance Scattering in $RFe_{0.50}Cr_{0.50}O_3$ (R = Sm, Er, and Eu): A Brief Raman Study. J Phys Chem C 126:5403–5410. https://doi.org/10.1021/acs.jpcc.1c09537

261. Olguín D, Cardona M, Cantarero A (2002) Electron–phonon effects on the direct band gap in semiconductors: LCAO calculations. Solid State Communications 122:575–589. https://doi.org/10.1016/S0038-1098(02)00225-9

262. Saran R, Heuer-Jungemann A, Kanaras AG, Curry RJ (2017) Giant Bandgap Renormalization and Exciton–Phonon Scattering in Perovskite Nanocrystals. Advanced Optical Materials 5:1700231. https://doi.org/10.1002/adom.201700231

263. Monserrat B, Needs RJ (2014) Comparing electron-phonon coupling strength in diamond, silicon, and silicon carbide: First-principles study. Phys Rev B 89:214304. https://doi.org/10.1103/PhysRevB.89.214304

264. Warshi MK, Gautam K, Kumar A, Sagdeo A, Kim J-H, Sagdeo PR (2024) Unusual Lattice Dilation and Strong Electron–Phonon

Coupling in Erbium Ferrite Perovskite. J Phys Chem C 128:9652–9661. https://doi.org/10.1021/acs.jpcc.4c02279

265. Glagovskii ÉM, Kuprin AV, Pelevin LP, Konovalov ÉE, Starkov OV, Levakov EV, Postnikov AYu, Lisitsa FD (1999) Immobilization of high-level wastes in stable mineral-like materials in a self-propagating high-temperature synthesis regime. At Energy 87:514–518. https://doi.org/10.1007/BF02673211

266. Nain R, Mishra V, Mishra V, Sagdeo PR (2025) Experimental and first-principles investigation on the optical properties of Eu and Fe-substituted Gd2TiO5. Journal of Materials Science: Materials in Electronics 36:466. https://doi.org/10.1007/s10854-025-14543-2

267. Risovany VD, Varlashova EE, Suslov DN (2000) Dysprosium titanate as an absorber material for control rods. Journal of Nuclear Materials 281:84–89. https://doi.org/10.1016/S0022-3115(00)00129-X

268. Alonizan NH (2022) Elucidation of photocatalytic degradation mechanism of an organic pollutant based on Gd2−xTi2−xFexO7 nanomaterials under simulated visible light. Eur Phys J Plus 137:715. https://doi.org/10.1140/epjp/s13360-022-02919-w

269. Ali I, Suhail M, Alothman ZA, Alwarthan A (2018) Recent advances in syntheses, properties and applications of TiO_2 nanostructures. RSC Adv 8:30125–30147. https://doi.org/10.1039/C8RA06517A

270. Sati A, Mishra V, Kumar A, Warshi M, Sagdeo A, Kumar R, Sagdeo P (2019) Effect of structural disorder on the electronic and phononic properties of Hf doped BaTiO3. Journal of Materials Science Materials in Electronics 30:9498–9506. https://doi.org/10.1007/s10854-019-01281-5

271. Matsubara M, Saniz R, Partoens B, Lamoen D (2017) Doping anatase TiO_2 with group V-b and VI-b transition metal atoms: a hybrid functional first-principles study. Phys Chem Chem Phys 19:1945–1952. https://doi.org/10.1039/C6CP06882K

272. Siddhapara KS, Shah DV (2014) Experimental Study of Transition Metal Ion Doping on TiO₂ with Photocatalytic Behavior. j nanosci nanotechnol 14:6337–6341. https://doi.org/10.1166/jnn.2014.8833

273. Xie K, Jia Q, Wang Y, Zhang W, Xu J (2018) The Electronic Structure and Optical Properties of Anatase TiO2 with Rare Earth Metal Dopants from First-Principles Calculations. Materials 11:179. https://doi.org/10.3390/ma11020179

274. Kumar A, Sati A, Mishra V, Warshi MK, Kumar R, Sagdeo PR (2019) Charge neutral crystal field transitions: A measure of electron–phonon interaction. Journal of Physics and Chemistry of Solids 135:109102. https://doi.org/10.1016/j.jpcs.2019.109102

275. Zhang J, Zhang F, Lang M, Lu F, Lian J, Ewing RC (2013) Ion-irradiation-induced structural transitions in orthorhombic Ln2TiO5. Acta Materialia 61:4191–4199. https://doi.org/10.1016/j.actamat.2013.03.045

276. Jaswanth A, Kaleemulla S (2025) Synthesis of CdO nanoparticles using facile solid-state reaction and systematic study on their physical properties. Chem Pap 79:2053–2063. https://doi.org/10.1007/s11696-025-03904-0

277. McCusker LB, Von Dreele RB, Cox DE, Louër D, Scardi P (1999) Rietveld refinement guidelines. J Appl Crystallogr 32:36–50. https://doi.org/10.1107/S0021889898009856

278. Hewat A, David WIF, Van Eijck L (2017) Hugo Rietveld (1932–2016). Neutron News 28:19–20. https://doi.org/10.1080/10448632.2017.1265352

279. Roisnel T, Rodríquez-Carvajal J (2001) WinPLOTR: A Windows Tool for Powder Diffraction Pattern Analysis. MSF 378–381:118–123. https://doi.org/10.4028/www.scientific.net/MSF.378-381.118

280. Aceto M, Calà E, Gulino F, Gullo F, Labate M, Agostino A, Picollo M (2022) The Use of UV-Visible Diffuse Reflectance Spectrophotometry for a Fast, Preliminary Authentication of Gemstones. Molecules 27:4716. https://doi.org/10.3390/molecules27154716

281. Kortüm G (1969) Regular and Diffuse Reflection. In: Kortüm G (ed) Reflectance Spectroscopy: Principles, Methods, Applications. Springer Berlin Heidelberg, Berlin, Heidelberg, pp 5–71

282. Poh AH, Jamaludin MF, Fadzallah IA, Nik Ibrahim NMJ, Yusof F, Adikan F, Moghavvemi M (2019) Diffuse reflectance spectroscopic analysis of barium sulfate as a reflection standard within 173–2500 nm: From pure to sintered form. Journal of Near Infrared Spectroscopy 27:393–401. https://doi.org/10.1177/0967033519868241

283. Xu Z, He Z, Song Y, Fu X, Rommel M, Luo X, Hartmaier A, Zhang J, Fang F (2018) Topic Review: Application of Raman Spectroscopy Characterization in Micro/Nano-Machining. Micromachines 9:361. https://doi.org/10.3390/mi9070361

284. Orlando A, Franceschini F, Muscas C, Pidkova S, Bartoli M, Rovere M, Tagliaferro A (2021) A Comprehensive Review on

Raman Spectroscopy Applications. Chemosensors 9:262. https://doi.org/10.3390/chemosensors9090262

285. Allen PB, Cardona M (1981) Theory of the temperature dependence of the direct gap of germanium. Phys Rev B 23:1495–1505. https://doi.org/10.1103/PhysRevB.23.1495

286. Gao Q, Jiao Y, Sun Q, Sprenger JAP, Finze M, Sanson A, Liang E, Xing X, Chen J (2024) Giant Negative Thermal Expansion in Ultralight $NaB(CN)_4$. Angewandte Chemie 136:e202401302. https://doi.org/10.1002/ange.202401302

287. Goodwin AL, Calleja M, Conterio MJ, Dove MT, Evans JSO, Keen DA, Peters L, Tucker MG (2008) Colossal Positive and Negative Thermal Expansion in the Framework Material Ag_3 $[Co(CN)_6]$. Science 319:794–797. https://doi.org/10.1126/science.1151442

288. Wu S-G, Cui W, Ruan Z-Y, Ni Z-P, Tong M-L (2025) Switchable colossal anisotropic thermal expansion in a spin crossover framework. Chem Sci 16:8845–8852. https://doi.org/10.1039/D4SC08032G

289. Allen PB, Heine V (1976) Theory of the temperature dependence of electronic band structures. J Phys C: Solid State Phys 9:2305–2312. https://doi.org/10.1088/0022-3719/9/12/013

290. Watanabe H, Yamada N, Okaji M (2004) Linear Thermal Expansion Coefficient of Silicon from 293 to 1000 K. International Journal of Thermophysics 25:221–236. https://doi.org/10.1023/B:IJOT.0000022336.83719.43

291. Guenzer CS, Bienenstock A (1973) Temperature Dependence of the HgTe Band Gap. Phys Rev B 8:4655–4667. https://doi.org/10.1103/PhysRevB.8.4655

292. Palankovski V, Kaiblinger-Grujin G, Selberherr S (1999) Study of dopant-dependent band gap narrowing in compound semiconductor devices. Materials Science and Engineering: B 66:46–49. https://doi.org/10.1016/S0921-5107(99)00118-X

293. Riis-Jensen AC, Lu J, Thygesen KS (2020) Electrically controlled dielectric band gap engineering in a two-dimensional semiconductor. Phys Rev B 101:121110. https://doi.org/10.1103/PhysRevB.101.121110

294. Andriotis AN, Menon M (2015) Band gap engineering via doping: A predictive approach. Journal of Applied Physics 117:125708. https://doi.org/10.1063/1.4916252

295. Balasurendran J, Balhara A, Jafar M, Sudarshan K, Bahadur J, Gupta SK (2024) Contrasting Role of Ca2+ on the Gd2tio5:Eu3+

Light Emission Under Charge Transfer and F-F Band Excitation: Interplay of Oxygen Vacancies and Structural Distortion

296. Kumar A, Warshi MK, Mishra V, Sati A, Banik S, Sagdeo A, Kumar R, Sagdeo PR (2019) Optical spectroscopy: An effective tool to probe the origin of dielectric loss in Cr doped PrFeO3. Ceramics International 45:8585–8592. https://doi.org/10.1016/j.ceramint.2019.01.177

297. Sati A, Kumar A, Mishra V, Warshi K, Sagdeo A, Anwar S, Kumar R, Sagdeo PR (2019) Direct correlation between the band gap and dielectric loss in Hf doped BaTiO3. Journal of Materials Science: Materials in Electronics 30:8064–8070. https://doi.org/10.1007/s10854-019-01128-z

298. Frei RW (1976) Diffuse reflectance spectroscopy; applications, standards, and calibration (with special reference to chromatography). J RES NATL BUR STAN SECT A 80A:551. https://doi.org/10.6028/jres.080A.055

299. Thibault F, Ferri D (2023) Diffuse reflectance infrared spectroscopy of adsorbates in liquid phase. Talanta 264:124734. https://doi.org/10.1016/j.talanta.2023.124734

300. Kortüm G (1969) Introduction. In: Kortüm G (ed) Reflectance Spectroscopy: Principles, Methods, Applications. Springer, Berlin, Heidelberg, pp 1–4

301. Makuła P, Pacia M, Macyk W (2018) How To Correctly Determine the Band Gap Energy of Modified Semiconductor Photocatalysts Based on UV–Vis Spectra. J Phys Chem Lett 9:6814–6817. https://doi.org/10.1021/acs.jpclett.8b02892

302. Klein J, Kampermann L, Mockenhaupt B, Behrens M, Strunk J, Bacher G (2023) Limitations of the Tauc Plot Method. Adv Funct Materials 33:2304523. https://doi.org/10.1002/adfm.202304523

303. Sagdeo A, Gautam K, Sagdeo PR, Singh MN, Gupta SM, Nigam AK, Rawat R, Sinha AK, Ghosh H, Ganguli T, Chakrabarti A (2014) Large dielectric permittivity and possible correlation between magnetic and dielectric properties in bulk BaFeO3−δ. Applied Physics Letters 105:042906. https://doi.org/10.1063/1.4892064

304. Gupta M, Rambadey OV, Aggarwal R, Sagdeo PR (2025) Exploring electronic Raman scattering in La-doped Ce O 2: Laser energy and power-dependent Raman spectroscopy. Phys Rev B 111:235208. https://doi.org/10.1103/stgz-lbd3

305. Fano U (1961) Effects of Configuration Interaction on Intensities and Phase Shifts. Phys Rev 124:1866–1878. https://doi.org/10.1103/PhysRev.124.1866

306. Kumar K, Rambadey OV, Sagdeo PR (2024) Contribution of individual phonon to the band gap renormalization in semiconductors. Phys Scr 99:075932. https://doi.org/10.1088/1402-4896/ad5050

307. Rambadey OV, Kumar K, Nain R, Kumar A, Sagdeo PR, Chamberlin PM, Adu KW (2024) Shedding light on evolution of Raman line shape with probing laser power: Light-induced perturbation in electron–phonon coupling. The Journal of Chemical Physics 161:034202. https://doi.org/10.1063/5.0189327

308. Quan Y, Yue S, Liao B (2021) Impact of Electron-Phonon Interaction on Thermal Transport: A Review

309. Lihm J-M, Poncé S, Park C-H (2024) Self-consistent electron lifetimes for electron-phonon scattering. Phys Rev B 110:L121106. https://doi.org/10.1103/PhysRevB.110.L121106

310. Cody GD, Tiedje T, Abeles B, Brooks B, Goldstein Y (1981) Disorder and the Optical-Absorption Edge of Hydrogenated Amorphous Silicon. Phys Rev Lett 47:1480–1483. https://doi.org/10.1103/PhysRevLett.47.1480

311. Guenzer CS, Bienenstock A (1973) Temperature Dependence of the HgTe Band Gap. Phys Rev B 8:4655–4667. https://doi.org/10.1103/PhysRevB.8.4655

312. Kumar K, Rambadey OV, Sagdeo PR (2023) Deconvolution of Phonon–Phonon and Electron–Phonon Interactions from Phonon Line Width in Zr-Substituted BaTiO3. J Phys Chem C 127:22164–22176. https://doi.org/10.1021/acs.jpcc.3c05388

313. Buchner M, Höfler K, Henne B, Ney V, Ney A (2018) Tutorial: Basic principles, limits of detection, and pitfalls of highly sensitive SQUID magnetometry for nanomagnetism and spintronics. Journal of Applied Physics 124:161101. https://doi.org/10.1063/1.5045299

314. Krause H-J, Kreutzbruck M v. (2002) Recent developments in SQUID NDE. Physica C: Superconductivity 368:70–79. https://doi.org/10.1016/S0921-4534(01)01142-X

315. Malik SK, Kundaliya DC, Kale RD (2005) High temperature magnetic ordering in La2RuO5. Solid State Communications 135:166–169. https://doi.org/10.1016/j.ssc.2005.04.016

316. Riegg S, Günther A, Von Nidda H-AK, Loidl A, Eremin MV, Reller A, Ebbinghaus SG (2012) Spin-singlet dimerization in La 2 RuO 5 investigated using magnetic susceptibility and specific heat measurements. Phys Rev B 86:115125. https://doi.org/10.1103/PhysRevB.86.115125

317. Eyert V, Ebbinghaus SG, Kopp T (2006) Orbital Ordering and Spin-Ladder Formation in La 2 RuO 5. Phys Rev Lett 96:256401. https://doi.org/10.1103/PhysRevLett.96.256401

----End---